Flexible Piezoelectric Nanocomposite Energy Harvester for Extreme Temperature Applications

by

Alireza Nafari

A dissertation submitted in partial fulfillment
of the requirements for the degree of
Doctor of Philosophy
(Aerospace Engineering)
in the University of Michigan
2019

Doctoral Committee:

Professor Henry A. Sodano, Chair
Assistant Professor John Huron
Professor Daniel J. Inman
Associate Professor Veera Sundararaghavan

Alireza Nafari

anafari@umich.edu

ORCID iD: 0000-0002-5921-8763

Dedication

This dissertation is dedicated to my beloved parents who I miss dearly.

Acknowledgments

I would like to thank Professor Henry Sodano for being my advisor and for providing me with the opportunity to be a part of his research in the Multiscale Adaptive Sensors and Structures (MASS) Laboratory at the University of Florida and the University of Michigan. Dr. Sodano's guidance is how I developed a specialized knowledge in this field. Without his advice and critique, my technical skills and professional development would not have evolved as it has. I am especially grateful for his determination to motivate his students to meet high expectations and work ethic standards. I would also like to thank my committee members Dr. Daniel Inman, Dr. John Heron, and Dr. Veera Sundararaghavan for their support and contribution to my dissertation.

For their consistent support and flawless teamwork, I would like to thank my past lab mates, Dr. Mohammad Malakooti, Dr. Chris Bowland, Dr. Zhi Zhou, Dr. Brendan Patterson, Dr. Jiajun Lin, as well as my current lab mates, Mr. Jalal Nasser, Ms. Lori Groo, Ms. Kelsey Steinke, and Ms. Lisha Zhang. I wish to express my gratitude for being blessed with consistent support and flawless teamwork. A special thanks to Dr. Mohammad Malakooti, for his mentoring and friendship; working together was an effectively rewarding experience.

I would like to thank my friends, without whom I could not have successfully completed my studies. And last but definitely not least, for their unwavering love and emotional support throughout my PhD studies, I would like to thank my family. I love and miss you all dearly.

TABLE OF CONTENTS

Dedication ii

Acknowledgments iii

List of Figures ix

List of Tables xvi

Abstract xvii

Chapter 1: Introduction 1

1.1. Motivations 1

1.2. History of Piezoelectricity 4

1.3. Piezoelectric Ceramics 5

1.4. Piezoelectric constitutive equations 8

1.5. Basics of electromechanical coefficients and their measurements 10

1.5.1. Dielectric coefficient (κ_{ij}) 11

1.5.2. Piezoelectric strain coefficient (d_{ij}) 11

1.5.3. Piezoelectric voltage coefficient (g_{ij}) 13

1.5.4. Piezoelectric coupling coefficient (k_{ij}) 13

1.6. Historic outline of piezoelectric energy harvesters 15
1.7. Choice of piezoelectric material 18
1.7.1. Zinc oxide (ZnO) 18
1.7.2. Lead zirconate titanate (PZT) 18
1.7.3. Barium titanate (BTO) 20
1.8. Use of piezoelectric composite materials 21
1.9. Inclusion alignment 23
1.10. Piezoelectric composite modeling 28
1.11. Summary of contributions 32
1.12. Dissertation overview 33
Chapter 2: Modeling of a Piezoelectric Nanocomposite 36
2.1. Introduction 36
2.2. Theoretical modeling 38
2.2.1. Constitutive Equations 38
2.2.2. Mean field micromechanics 40
2.2.3. Simulation results 48
2.3. Finite element modeling (FEM) 52
2.3.1. Aligned inclusions 55
2.3.2. Randomly oriented inclusions 59

2.4. Conclusions 66

Chapter 3: Controlled Synthesis of Barium Titanate and Lead Titanate Nanowires 67

3.1. Introduction 67

3.2. Summary of various methods for synthesis of one-dimensional ferroelectric nanostructures 67

3.2.1. Sol-gel template methods 68

3.2.2. Molten salt methods 69

3.2.3. Electrospinning Methods 69

3.2.4. Nanosolid-state reaction methods 69

3.2.5. Sintering methods 70

3.2.6. Nonoxide material routes 70

3.2.7. Hydrothermal methods 71

3.3. Synthesis methods of piezoelectric nanowires for energy harvesting 71

3.3.1. Hydrothermal synthesis of sodium titanate ($Na_2Ti_3O_7$) nanowires 72

3.3.2. Hydrothermal synthesis of barium titanate ($BaTiO_3$) Nanowires 73

3.3.3. Hydrothermal synthesis of lead titanate ($PbTiO_3$) Nanowires 77

3.4. Conclusions 79

Chapter 4: Model Verification and Device Characterization 80

4.1. Introduction 80

4.2. Nanocomposite fabrication method 81

4.3. Measurement setups 83

4.3.1. Measurement setup for calculation of electromechanical coefficients 83

4.3.2. Measurement setup for energy harvesting characterization 85

4.4. Model Validation and Discussion 86

4.5. Conclusions 104

Chapter 5: Extreme Temperature Energy Harvesting 105

5.1. Introduction 105

5.2. High temperature piezoelectric materials 106

5.3. High temperature energy harvester based on vertically aligned arrays of PTO nanowires 109

5.3.1. Synthesis procedure 109

5.3.2. Fabrication of the energy harvester device 112

5.3.3. Electrical Characterization 113

5.4. High temperature flexible energy harvester using freestanding PTO nanowires . 117

5.4.1. Heat resistant matrix 117

5.4.2. Polyimide synthesis 118

5.4.3. Fabrication of high temperature flexible energy harvester 123

5.4.4. Electromechanical modeling and Electrical characterization 124

5.5. Conclusions 130

Chapter 6: Conclusions 132

6.1. Summary of the findings and contributions 132

6.2. Recommendations for future work 134

References 136

List of Figures

Figure 1-1: Crystal structure of a perovskite (piezoelectric) material. (a) Before polarization (above Curie temperature) and (b) after polarization (bellow Curie temperature). 6

Figure 1-2: Poling process of a perovskite material. (a) Prior to poling the dipole moment in various domains are randomly oriented. (b) By applying a DC voltage while the sample is being heated, the dipoles align themselves in the direction of electric field. (c) After removing the electric field and heat, the dipoles maintain their general direction and which result in a net permanent polarization in the direction of electric field. 7

Figure 1-3: (a) A poled piezoelectric material with upward polarity. (b and c) Piezoelectric effect where an application of tensile or compressive force induce a voltage difference across the material. (d and e) Converse piezoelectric effect where, by applying a voltage difference across the material, a mechanical strain is induced. 8

Figure 1-4: A piezoelectric material with a net downward dipole moment and two electrodes. ... 9

Figure 1-5: A typical piezoceramic configured in 33 mode. 12

Figure 1-6: An open-circuited piezoelectric transducer under a force in direction. 13

Figure 1-7: Various piezoelectric based energy harvesters. (a) The first ZnO-based energy harvester composed of vertically aligned nanowires. The device was excited by an AFM tip to bend individual nanowires and was able to generate up to 9 mV [64]. (b) Schematic and SEM image of the first practical ZnO-based energy harvester which was excited by ultrasonic wave through a zigzag-shaped top electrode. The design of the electrode allowed for bending of multiple nanowires and hence resulted in enhanced current output [64]. (c) Schematic of a single ZnO finewire attached to a flexible substrate which lead to further development of flexible energy harvesters [69]. (d) Schematic and SEM image of a fully flexible energy harvester composed of

BTO nanowires dispersed in PDMS matrix [70]. (e) Schematic of a direct write method for fast fabrication of flexible energy harvesters with controlled alignment of BTO nanowires which show a significant output power improvement when the nanowires are aligned in the direction of applied stress (0°) compared to that of casted nanocomposite [72]. 17

Figure 1-8: Phase diagram of PZT materials. Depending on the Zr content, the Curie temperature (T_c) ranges from 220 °C to 490 °C [1]..... 20

Figure 1-9: Optical image of the ink-jet nozzle while printing a triangular honeycomb composite, and the schematic of the printing process. The schematic shows the progressive alignment of high aspect ratio fillers within the nozzle due to a high-shear environment..... 26

Figure 1-10: (a) The alignment of cellulose fibrils due to a shear high shear environment inside the nozzle during four-dimensional ink-jet printing. The anisotropic swelling properties of the fibrils result in higher Young's modulus in the longitudinal direction compared to that of transverse direction. The optical image of the composite show that using this printing method the fibrils' alignment can be closely controlled resulting in complex geometrical microstructure for the composite (scale bars are 200 μm). (b) Complex printed geometries evolving in time by tailoring localized time-changing anisotropic swelling properties into the composite (scale bars are 5 mm) [126]..... 27

Figure 1-11: Connectivity types for diphasic composite materials [107]..... 29

Figure 2-1: Simulated piezoelectric strain coefficient of a nanocomposite made of active BTO nanowires and PDMS matrix. (a) d_{33} and (b) d_{31} coefficients are normalized with respect to piezoelectric strain coefficients of the bulk BTO material. 50

Figure 2-2: Simulated piezoelectric coupling coefficient of a nanocomposite made of active BTO nanowires and PDMS matrix. (a) k_{33} and (b) k_{31} coefficients are normalized with respect to piezoelectric coupling coefficients of the bulk BTO material. 51

Figure 2-3: Simulated stiffness coefficient of a nanocomposite made of active BTO nanowires and PDMS matrix. (a) C_{33} and (b) C_{31} coefficients are normalized with respect to stiffness coefficients of the bulk BTO material. 52

Figure 2-4: A sample RUC with a constraint of periodicity satisfied..... 53

Figure 2-5: (a) Body centered cubic lattice structure with AR = 10 inclusions which allows for geometrical repetition of the RRVE in all there axes. (b) Meshed RRVE with tetrahedron elements. 55

Figure 2-6: FEM results for calculation of d_{33} coefficient. (a) Voltage distribution along the RRVE (y = b/2 plane). (b) Vertical displacement distribution in the RRVE. 58

Figure 2-7: Simulated results of Mori-Tanaka approach and FEM. (a) d_{33}, (b) d_{31} (c) k_{33}, and (d) k_{31} coefficients are normalized with respect to piezoelectric coefficients of the bulk BTO material. 59

Figure 2-8: (a) A cylinder in 3D space can be uniquely defined by the position of its center of mass and two Euler angles (b) Flow chart of the RSA procedure. (c) The expansion of RVE in order to decrease the volume fraction. By increasing the length of the **C** vector according to Eq. (2-39), an RRVE with lower volume fraction and similar orientation of fibers is obtained. 61

Figure 2-9: Schematic of the projection method. (a) Two non-intersecting objects with non-intersecting projections on to the line **D**. (b) Two intersecting objects with intersecting projections on to the line **D**..... 62

Figure 2-10: A typical RRVE generated using RSA method consisting of 150 random, non-overlapping fibers with AR = 10. 64

Figure 2-11: Three RRVEs with different amount of maximum allowable misalignment for their inclusions. 64

Figure 2-12: The effect of misalignment on the normalized d_{33} coefficient..... 65

Figure 3-1: Free-standing sodium titanate ($Na_2Ti_3O_7$) nanowires with various length and diameter. Reaction temperatures: (a) 150 °C, (b) 180 °C, (c) 210 °C, and (d) 240 °C. Scale bars are (10 µm). 73

Figure 3-2: Free-standing Barium titanate ($BaTiO_3$) nanowires with various length and diameter. Precursors ($Na_2Ti_3O_7$) were prepared at various reaction temperatures: (a) 150 °C, (b) 180 °C, (c) 210 °C, (d) 240 °C. Scale bars are (10 µm). 74

Figure 3-3: the distribution of $BaTiO_3$ nanowires aspect ratio with various precursors ($Na_2Ti_3O_7$), prepared at various reaction temperatures: (a) 150 °C, (b) 180 °C, (c) 210 °C, (d) 240 °C. 75

Figure 3-4: (a) SEM micrograph, (b) AFM topography scan, (c) XRD pattern and (d) EDS spectrum of the as synthesized $BaTiO_3$ nanowires. 77

Figure 3-5: Synthesized $PbTiO_3$ nanowires characterization. (a) SEM, (b) AFM topography, (c) EDS spectra and (d) XRD pattern associated with JCPDS Card No. 06-0452..... 78

Figure 4-1: (a) Experimental setup used for direct write of the nanocomposite. (b) Schematic illustration of a single layer direct printing process with nanowires aligned in the 3-direction. (c) SEM micrograph of the fabricated BTO nanowire/PDMS nanocomposites with varying degrees of alignment, controlled by adjusting the viscosity of the nanocomposite ink using toluene..... 82

Figure 4-2: DMA test setup for measurement of the d_{31} coupling coefficient which enables the application of a controlled strain while the force is measured..... 84

Figure 4-3: (a) AFM test setup. (b) The displacement measurement during the application of a unipolar voltage to a nanocomposite containing 20 WF% BTO nanowires..... 85

Figure 4-4: Measurement setup along with schematics and samples of the energy harvester devices. Mechanical excitation is applied by an electromechanical shaker and the input acceleration is measured using an accelerometer. 86

Figure 4-5: Comparison between the effective d_{31} coefficients calculated using Mori-Tanaka method, FEM and experimental measurement using DMA for nanocomposites with aligned and randomly oriented nanowires with varying aspect ratios. 89

Figure 4-6: Comparison between the effective d_{33} coefficients calculated using Mori-Tanaka method, FEM and experimental measurement using DMA for nanocomposites with aligned and randomly oriented nanowires with varying aspect ratios. 91

Figure 4-7: Comparison between the effective ε_{33} coefficients calculated using the Mori-Tanaka method, FEM and experimental measurement using the LCR meter for nanocomposites with aligned and randomly oriented nanowires with varying aspect ratios. 92

Figure 4-8: (a) Output power measurements of nanocomposite energy harvesters with aligned nanowires across varying load resistance. (b) AC voltage (V) and current (I) passing through a load resistor. 94

Figure 4-9: (a) Calculated normalized dielectric constant and piezoelectric strain coefficient based on the Mori-Tanaka method. (b) Comparison between the effective g_{31} coefficients calculated using the Mori-Tanaka method, FEM and experimental measurement along with corresponding measured power at various weight fractions. 97

Figure 4-10: Frequency response function (FRF) of output open circuit voltage (V_{oc}) and short circuit current (I_{sc}) of (a) type I and (b) type II energy harvesters. 99

Figure 4-11: V_{oc} and I_{sc} characterization of (a) type I and (b) type II energy harvesters with sin-wave excitation at resonance. 100

Figure 4-12: The RMS values of V_{oc} and I_{sc} characterization of (a) type I and (b) type II energy harvesters with sin-wave excitation at resonance. 101

Figure 4-13: The FRF response of three nanocomposites with varying degrees of alignment (scale bars are 5 μm). 103

Figure 5-1: SEM micrographs of vertically aligned nanowire arrays: (a) top-view of $Na_2Ti_3O_7$ nanowires (b) side-view of $Na_2Ti_3O_7$ nanowires (c) top-view of PTO nanowires (d) side-view of PTO nanowires (Scale bars are 5μm). (e) An energy dispersive spectrum of PTO nanowires showing Pb, Ti and O peaks (f) XRD pattern of PTO nanowires (JCPDS Card No. 06-0452, red ovals denote the PTO peaks and green squares denote the small PbO peaks). 111

Figure 5-2: Schematics of (a) the fabricated energy harvester device, (b) the designed setup to test the device at high temperatures with (c) the equivalent electrical circuit of the device. 113

Figure 5-3: (a) The open circuit voltage of the PTO nanowire arrays energy harvester device at various temperatures with (b) corresponding peak-to-peak values of open circuit voltage. (c) The short circuit current of the PTO nanowire arrays energy harvester device at various temperatures with (d) corresponding peak-to-peak values of short circuit current. 115

Figure 5-4: (a) The peak to peak and RMS values of the voltage across and (b) current passing through the load resistor. (c) Power characterization of the energy harvester device at various temperatures. 117

Figure 5-5: Common heat resistant polymers. (a) polybenzoxazole, (b) polybenzimidazole, (c) polybenzthiazole, and (d) polyimide. 118

Figure 5-6: A two-step chemical reaction for synthesizing Kapton polyimide [316]. 119

Figure 5-7: Reaction mechanism for formation of aromatic imide [275]. 120

Figure 5-8: (a) Heat treatment process for imidization of poly(amic) acid. (b) FTIR spectra of the as synthesized and commercial Kapton polyimide. 121

Figure 5-9: (a) As-synthesized poly(amic) acid. (b) A sample of imidized poly(amic) acid (Kapton, brown) with printed graphite electrode (black). (c) SEM micrographs of the printed graphite electrode on the surface of Kapton polyimide film (laser parameters: 3.2 W, 1000 DPI). 123

Figure 5-10: PTO nanowires/polyimide nanocomposite with (a) aligned (direct write method) and (b) randomly oriented nanowires (casting method) 124

Figure 5-11: Interpolated (a) stiffness and (b) piezoelectric stress coefficients of PTO as a function of temperature based on Eqs. (5-3) and (5-4) [331,332]. (c) Dielectric coefficient of PTO vs. temperature (adapted from Ref. [333]). 126

Figure 5-12: (a) The tensile modulus and (b) dielectric constant of the synthesized polyimide Kapton. 127

Figure 5-13: Normalized d_{31} coefficients of PTO nanowires/polyimide nanocomposite energy harvester at various volume fractions, aspect ratios, and temperatures. 128

Figure 5-14: The power output characterization of PTO nanowires/polyimide nanocomposite energy harvester at various volume fractions, aspect ratios, alignment and temperatures. 130

List of Tables

Table 1-1: Change of notation rules..... 10

Table 1-2: Electrical performance of various BTO based composite energy harvesters..... 23

Table 2-1: Divisions and their corresponding weights for Gaussian quadrature procedure..... 48

Table 2-2: Material properties of the barium titanate nanowires, and PDMS. $S_0 = 10^{-12}$ m^2/N; $d_0 = 10^{-12}$ C/N; κ_0 = 8.85E-12 F/m; $\rho_0 = 10^3$ kg/m^3 48

Table 2-3: Mechanical and electrical boundary conditions for calculation of effective stiffness matrix and piezoelectric strain and coupling coefficients..... 57

Table 4-1: Material properties of the barium titanate nanowires [216,217], and PDMS [214,215]. $S_0 = 10^{-12}$ m^2/N; $d_0 = 10^{-12}$ C/N; κ_0 = 8.85E-12 F/m; $\rho_0 = 10^3$ kg/m^3. 88

Table 5-1: High temperature piezoelectric materials and their electromechanical properties.... 108

Abstract

Piezoelectric materials are currently among the most promising building blocks for sensing, actuation and energy harvesting systems. However, these materials are limited in many applications due to their lack of machinability as well as their inability to conform to curved surfaces. One method to mitigate this issue is through additive manufacturing (direct printing) of piezoelectric nanocomposites, where piezoelectric nanomaterials are embedded in a polymer matrix. With the advent of additive manufacturing it is now possible to realize directly printed nanocomposites with tailored microstructure. Although significant progress has been made in this area, parameters such as filler morphology, alignment and volume fraction are critical aspects that heavily influence the nanocomposites' electromechanical response and have not been adequately modeled.

A primary objective of this study is to develop and experimentally validate micromechanical and finite element models that allow the study of the electroelastic properties of a directly printed nanocomposite containing piezoelectric inclusions. Furthermore, the dependence of these properties on geometrical features such as aspect ratio and active phase alignment are investigated. In particular, the core focus of this work is to demonstrate how the alignment of piezoelectric nanowires in the nanocomposite starting from randomly oriented to purely aligned can improve the electroelastic properties of a printed nanocomposite. This work provides the first experimental validation of theoretical and FEM models through measurement of the electroelastic properties of the nanocomposites containing piezoelectric nanowires inside a polymeric matrix. Moreover, this dissertation presents a novel approach for harvesting ambient mechanical energy at extreme environments. Many miniature electronic sensors and actuators in aerospace applications risk breakdown due to their operation in extreme temperature conditions, as cooling and protecting them prove to be challenging due to space and weight limitations. Therefore, as a second objective of this investigation, a flexible energy harvester capable of withstanding extreme temperatures (< 250 °C) is developed using a direct write approach that can provide useful electrical energy from

ambient vibrations. The research presented in this dissertation can provide a robust tool for the analysis and design of two phase piezoelectric nanocomposite energy harvesters able to operate under a spectrum of conditions ranging from ambient to extreme temperatures.

Chapter 1: Introduction

1.1. Motivations

Piezoelectric materials are among the most popular and commercially used functional materials for converting mechanical energy to electrical energy and vice versa. Typically, they are divided into two categories, namely, lead-containing and lead-free materials. Lead-containing materials such as lead titanate ($PbTiO_3$), lead zirconate titanate ($Pb_xZr_{1-x}TiO_3$, PZT), and many other chemically doped versions of these materials exhibit superior piezoelectric performance [1-3]. However, due to environmental and biological problems associated with the use of lead, such materials are limited in applications, spurring the development of many types of lead-free piezoelectric materials such as zinc oxide (ZnO), barium titanate ($BaTiO_3$), polyvinylidene fluoride (PVDF). These materials exhibit many advantages including strong piezoelectricity, easy synthesis, low-cost production, simple structure and sustainability for mass production in many applications, thus providing a route to gradual replacement of all lead-containing piezoelectric materials [4-12]. Over the past decade, significant progress in the research and development of piezoelectric based sensors and energy harvesters has been made. Piezoelectric energy harvesters have shown promising abilities for harvesting ambient mechanical energy and converting it into electrical energy via nanometer-scale materials. Compared to conventional batteries, piezoelectric energy harvesters are more environmentally friendly and can sustain electrical energy for longer times. Therefore, they have been considered as a key component in energy conversion transducers [13-18]. However, these devices have not been used particularly in extreme temperature applications.

High-temperature electronics is an area of research offering interesting materials and design challenges and one of significant industrial importance. The evolution of high temperature electronic materials, devices, circuits, and systems can be attributed to the energy crisis of 1974, when geothermal exploration was deemed a probable solution [19]. During this time, geothermal

and oil-well logging industries needed sensors and electronic systems that could withstand higher operational temperatures for deep drilling in the earth's crust. Additionally, the aerospace and aircraft industries have particularly challenging temperature requirements; engineers find it difficult to protect sensitive electronic systems in a cool, remote place while optimizing space and weight to minimums. Electronic controls must reside directly inside jet engines because of reliability and noise requirements, so sensors must survive temperatures of 500-1000°C while allowing mission lifetimes up to 100,000 hours [20]. In the automotive industry, the number of sensors and actuators in electronics continues to increase each year. Ceramic and semiconductor sensors keep track of temperature, oxygen pressure, and preignition knock and are used in conjunction with microprocessor-based controls to enhance the efficiency and dependability of internal combustion engines. Of course, operation at higher temperatures also makes combustion engines more efficient. Research on utilizing ceramic components in diesel engines has led to higher operating temperatures, resulting in an increase in fuel efficiency of up to 65%, as well as a decrease in exhaust pollution [21]. Therefore, not only the sensors and actuators that work in these environments have to withstand high temperatures, but they also have to be powered by either batteries or energy harvesters. However, a battery’s efficiency drops significantly at higher temperatures and in some applications the electronic devices are too remote to easily access. Hence, powering these devices via piezoelectric energy harvesters is a viable solution.

Although piezoelectric materials in their bulk form exhibit high coupling coefficients and linear response over a large span of excitation frequencies, they are typically very brittle and cannot be conformed to curved surfaces. One proposed method to solve this problem is to use nanocomposites which incorporate piezoelectric powders in the form of high aspect ratio nanowires in a polymer matrix. Piezoelectric nanocomposites provide mechanical compliance and flexibility due to the properties of the polymer matrix [22-26]. While the multiphase nature of a nanocomposite makes the accurate prediction of electromechanical properties challenging, it also provides the capacity to create a larger design space which can be capitalized upon in order to achieve a new set of electromechanical properties not found in bulk materials.

Generally, there are two main approaches for modeling of a piezoelectric nanocomposite: continuum mechanics and the finite element method (FEM). Continuum mechanics based approaches have been developed as a practical modeling scheme for nanocomposites. For

example, Odegard *et al.* proposed a model for predicting the elastic properties of a nanocomposite containing aligned fibers and hollow nanotubes [27]. Halpin and Tsai proposed an equation for calculating the Young's modulus of a nanocomposite, which takes into account the effect of volume fraction, geometry of the fillers and relative modulus of the constituents, but not piezoelectricity [28]. Dunn and Taya developed the first continuum mechanics based approach for solving coupled electroelastic behavior of piezoelectric composite materials [29]. Although the models have been shown to provide valid methods for calculating the overall properties of a nanocomposite, their application is limited due to certain assumptions and simplifications applied to the model formulation. For instance, the Mori-Tanaka and Halpin-Tsai methods are formulated by assuming a single inclusion in the nanocomposite and neglecting the relative distribution of fillers and their potential interactions [28,30-33].

To avoid some of the assumptions made in the continuum mechanics methods, numerical approaches based on FEM have been developed to calculate the overall properties of nanocomposites. In FEM, a representative volume element (RVE) or a repeating unit cell (RUC) is used for numerical homogenization of the heterogeneous medium of the nanocomposite. Since RVE/RUC volumes are modeled in lieu of the entire nanocomposite, their selection as well as their corresponding properties play a crucial role in the accuracy of the results. Maxwell *et al*. employed the RVE concept to calculate the electromechanical properties of a three-phase piezoelectric nanocomposites containing PZT nanoparticles and single walled carbon nanotubes (SWCNTs) in a polyimide matrix [34]. The authors developed an experimental framework to validate their FEM results and showed that only under certain conditions, such as in low volume fraction cases, their model could be verified. Further FEM and micromechanics models were then developed by Andrews *et al.* to study the effect of aspect ratio and orientation of the piezoelectric nanowires on the piezoelectric properties. [24]. All of the aforementioned studies have been used to predict the performance of a piezoelectric nanocomposite based on the material and geometrical properties of the constituent parts. However, none have been employed in the design of a material which utilizes geometric control over the constituents to achieve properties which exceed the bulk properties of the piezoelectric phase.

In this dissertation, we study the role of aspect ratio and orientation of the fillers in a piezoelectric nanocomposite energy harvester by employing the Mori-Tanaka method and FEM.

The results are then validated by electrical characterization of nanocomposite energy harvesters. To validate our models, a range of nanocomposites with synthesized barium titanate (BTO) [35-37] nanowires dispersed in a polydimethylsiloxane (PDMS) matrix were prepared with controlled alignment using a direct write method. The piezoelectric energy harvesting performance of the nanocomposites were then assessed by measuring the piezoelectric coefficients of the nanocomposites. This is the first validated model that inspects the effect of filler properties on the piezoelectric properties and energy harvesting performance of the nanocomposite. It is shown that the aforementioned models can be used to accurately predict various piezoelectric coefficients. The results demonstrate that the alignment and increased aspect ratio of the nanowires in the energy harvester can significantly enhance the power output of the device. Finally, towards the end of this dissertation, a new class of thermally stable piezoelectric nanocomposites based on lead titanate nanowires are developed that can provide electrical energy at temperatures exceeding 250 °C. Then the models were modified to account for the effects of temperature and it is shown that they can be verified by experimental data.

1.2. History of Piezoelectricity

Piezoelectricity phenomenon was first studied by Pierre and Jacques Curie in 1880 [38]. While conducting a variety of experiment on different crystals, they discovered that some crystals such as quartz, tourmaline, cane sugar, Rochelle salt, and topaz exhibit a surface charge when they were mechanically stressed. At the time, the scientific community realized the significance of this discovery and coined the term “piezoelectricity” to describe this phenomenon. The word “piezo” means “to press” in Greek, therefore, piezoelectricity can be translated to the electricity generated by pressure. Although the piezoelectricity effect is credited to Curie brothers, the converse piezoelectric effect wasn’t reported by them. Later in 1881, using thermodynamics laws and mathematics, Lippmann predicted that it is possible to strain a piezoelectric crystal by applying a voltage difference across the crystal [39]. Subsequently within the next 30 years, and prior to world war one, research on piezoelectric crystals were considered as a credible scientific activity. These studies resulted in the discovery of asymmetric nature of piezoelectric crystals, reversible exchange of electrical and mechanical energies using piezoelectric materials and the use of thermodynamics to describe different aspects of piezoelectricity.

The first engineering application of piezoelectric materials appeared during World War I where Paul Langevin from France fabricated a mosaic of thin quartz crystals and glued them between two steel plates (electrodes). The system had a resonance frequency of about 50 KHz and was used to transmit an ultrasonic signal into the water and measure the time for the reflected sound wave to reach the water surface. Basically, this was the first sonar where they used piezoelectric materials to measure the depth of the ocean. The invention of sonars where perfected in the few years between World War I and II and the use of piezoelectric crystals were further expanded. For example, quartz crystals were used to develop frequency stabilizers for vacuum tube oscillators. [40] Ultrasonic transducers based on piezoelectric crystals were also used for measurement of material properties. It is worth mentioning that many of the classic applications of piezoelectric materials such as transducers, accelerometers and microphones that we are familiar with today were first developed in this period. During World War II a significant amount of research was performed on the piezoelectric materials by different sides of the war which resulted in the development of piezo ceramics and synthesis or formation of very high dielectric material used in capacitors. These studies later lead to the invention of powerful sonars, sensitive headphones, ceramic phono cartridges and piezo-ignition systems [40].

1.3. Piezoelectric Ceramics

A piezoelectric ceramic is a volume of perovskite crystal where a small tetravalent metal ion like titanium (Ti^{+4}) or zirconium (Zi^{+4}) is placed inside a lattice of larger divalent metal (like lead, Pb^{+2}) and oxygen (O^{+2}) ions, as shown in Figure 1-1. Traditionally, the perovskite crystals were prepared by mixing of the appropriate ratio of the fine metal oxide powders and sintered (using heat) to form a dense structure. The product is then cooled down and formed into specific shapes like disks, rods, and plates, before subsequently applying two electrodes on either side of the crystal to form a piezoelectric transducer.

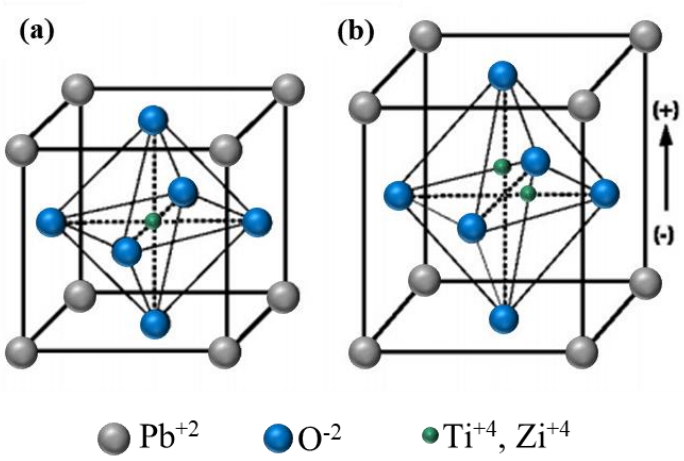

Figure 1-1: Crystal structure of a perovskite (piezoelectric) material. (a) Before polarization (above Curie temperature) and (b) after polarization (bellow Curie temperature).

Above a critical temperature, known as “Curie temperature”, all perovskite structures exhibit a simple symmetrical cubic structure with no dipole moment (Figure 1-1a). On the other hand, bellow the Curie temperature, the ions in the structure settle in a lower energy state with a tetragonal crystal structure (Figure 1-1b). Because this structure has an inherent charge asymmetry, a dipole moment forms in the crystal, thus inducing piezoelectricity. In other word, a perovskite structure with symmetrical cubic crystal shows no piezoelectricity due to the symmetric nature of the charges in the structure. Bellow Curie temperature, the adjoining dipoles form regions of local alignment called “domains”, where the alignment gives a net dipole moment to the domain and therefore a net polarization. It should be noted that even bellow Curie temperature, the direction of each domain’s dipole moment is random and the material as a whole does not exhibit a net polarization (Figure 1-2a). By applying a DC voltage across the structure (poling process), the randomly oriented domain dipoles align themselves with the direction of applied electric field in the material (Figure 1-2b). Usually the poling process is implemented at an elevated temperature, often slightly below Curie temperature to increase the mobility of the domains for alignment. Subsequently, the temperature is lowered while the electric field is being applied and finally after reaching room temperature, the electric field is removed. As shown in Figure 1-2c when the electric field is removed, the dipoles more or less keep their general orientation, hence the whole material exhibit a remnant dipole moment with permanent micrometer range elongation.

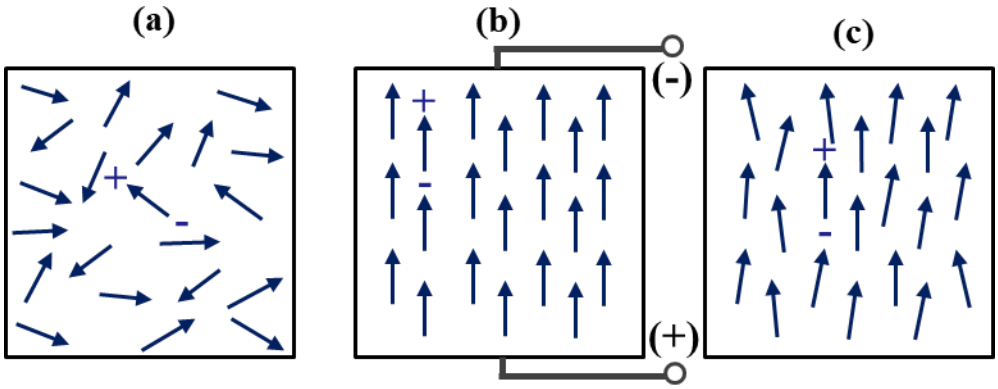

Figure 1-2: Poling process of a perovskite material. (a) Prior to poling the dipole moment in various domains are randomly oriented. (b) By applying a DC voltage while the sample is being heated, the dipoles align themselves in the direction of electric field. (c) After removing the electric field and heat, the dipoles maintain their general direction and which result in a net permanent polarization in the direction of electric field.

The working mechanism of a piezoelectric ceramic can be explained using Figure 1-3. After the poling process, a permanent net vertical (upward) polarization occur in the ceramic (Figure 1-3a). By applying a tensile or compressive force along the polarization direction, the dipole moment across the ceramic changes which creates opposite net charge and a potential difference across the ceramic. According to Figure 1-3b when a compressive or tensile strain is applied in the direction of polarization, or perpendicular to it, respectively, a voltage is generated with the same polarity as the poling voltage. On the other hand, as shown in Figure 1-3c when a tensile or compressive strain is applied in the direction of polarization, or perpendicular to that, respectively, a voltage is generated with the opposite polarity as the poling voltage. Therefore, it can be seen that a piezoelectric ceramic can convert the mechanical energy to electrical energy. It should be noted that because the voltage generated is linearly proportional to the applied strain (up to a specific strain), a piezoelectric device can be configured into a linear sensor or energy harvester.

Piezoelectric materials can be used in a different mode where by application of a voltage difference (or equivalently, electric field) across the material, it can deform. Specifically when the applied voltage has the same polarity, or opposite polarity, the material elongates or shortens, respectively (Figure 1-3 d and e). Therefore, by applying an alternating (AC) voltage to a piezoelectric device, it is possible to induce cyclical expansion and shrinkage, and thus making an

actuator (also known as converse piezoelectric effect). In such a mode the energy conversion is from electrical to mechanical.

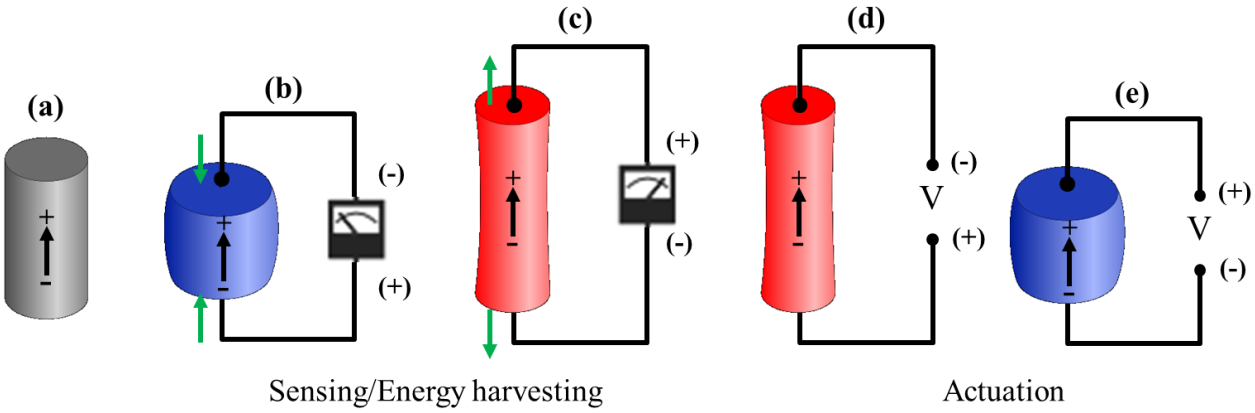

Figure 1-3: (a) A poled piezoelectric material with upward polarity. (b and c) Piezoelectric effect where an application of tensile or compressive force induce a voltage difference across the material. (d and e) Converse piezoelectric effect where, by applying a voltage difference across the material, a mechanical strain is induced.

1.4. Piezoelectric constitutive equations

Piezoelectric effect can be considered by the interaction between the state variables in mechanical and electrical energy domains. The constitutive equations that describes this phenomenon was first standardized by IEEE, and are widely accepted in the scientific community [41]. This standard considers a linear piezoelectric material, a valid assumption in the case of low electric fields and mechanical stress conditions. However, under high stress or electric fields they tend to exhibit strong nonlinearity which result in hysteresis and creep effects [42]. Here, we assume that the piezoelectric material is operated in the linear range and that these effects are negligible.

The constitutive equations that describe the piezoelectric effect is based on superposition principle. The total apparent strain in a piezoelectric material is the sum of mechanical strains and induced electrical strains that are due to applied electric fields. As shown in Figure 1-4 the coordinate axes are referred to as 1, 2, and 3. Traditionally, axis 3 is aligned in the direction of dipole moment and perpendicular directions to axis 3 are assigned as axes 1, and 2 (right hand rule is satisfied).

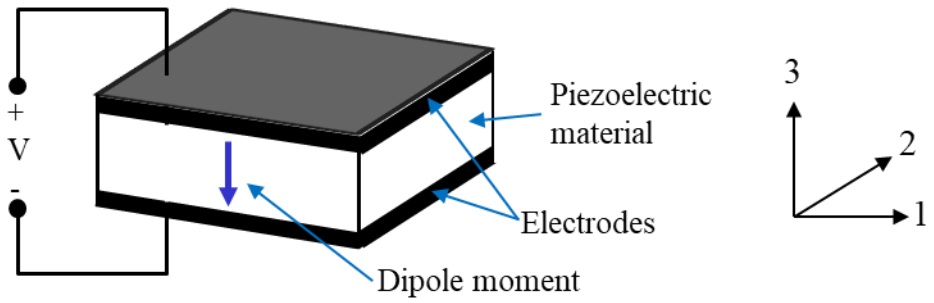

Figure 1-4: A piezoelectric material with a net downward dipole moment and two electrodes.

Using the Einstein indicial notation, the piezoelectric equations can be written as [41,43]:

$$\begin{cases} \sigma_{ij} = C^{E}_{ijmn}\varepsilon_{mn} - e_{mij}E_m \\ D_i = e_{imn}\varepsilon_{mn} + \kappa^{\varepsilon}_{im}E_m \end{cases}, \tag{1-1}$$

where in Eq. (1-1) the electric field, E_m, and elastic strain, ε_{mn} are independent variables and electric displacement, D_i, and stress, σ_{ij} are the dependent variables. The remaining constants C_{ijmn}, κ_{im}, and e_{mij}, represent the elastic moduli, the dielectric constant and the piezoelectric stress coefficient, respectively. The subscript i, j, m, and n are spatial indices, and the superscript E, ε, and σ represent the measurement in constant electric, strain, and stress fields, respectively. In Eq. (1-1) the first line describes the piezoelectric effect while the second line describes the converse piezoelectric effect. It should be noted that electric field and electric displacement are related. i.e.

$$D_i = \varepsilon_0 E_i + P_i, \tag{1-2}$$

where P and $\varepsilon_0 = 8.854 \times 10^{-12} F/m$ denote the polarization vector, and the permittivity of free space. Eq. (1) can be written in another form, i.e.:

$$\begin{cases} \varepsilon_{ij} = S^{E}_{ijmn}\sigma_{mn} + d_{mij}E_m \\ D_i = d_{imn}\sigma_{mn} + \kappa^{\sigma}_{im}E_m \end{cases}, \tag{1-3}$$

in which S_{ijmn}, and d_{mij} are the compliance moduli and piezoelectric strain coefficient. Similar to Eq. (1-1), the first and second lines in Eq. (1-3) describe the piezoelectric and converse piezoelectric effects, respectively.

Eqs. (1-1) and (1-3) are tensor equations but it is possible to employ them in matrix formulations which significantly simplify the calculations. For that, the following change of notation is implemented [41]

$$X_{ijmn} \equiv X_{pq}, \text{ and } Y_{ij} \equiv Y_p. \tag{1-4}$$

where X, and Y are two 4th and 2nd order general tensors. Using this change of indicial notation fourth, and second order tensors can be represented by a matrix and a vector, respectively. The transformation of notations for i, j, m, n = 1, 2, 3, 4, and p, q = 1, 2 is shown in Table 1-1. It should be noted that when the matrix notation is used, the transformation properties of the original tensors become unclear, and therefore the tensor indices must be employed when coordinate transformations are needed.

Table 1-1: Change of notation rules.

ij or *kl*	*p* or *q*
11	1
22	2
33	3
23 or 32	4
31 or 13	5
12 or 21	6

1.5. Basics of electromechanical coefficients and their measurements

This section describes the physical meaning and basics of some of the important piezoelectric coefficients along with their measurement methods. These methods are implemented in chapters 3,4, and 5 to calculate the various electromechanical coefficients [44].

1.5.1. Dielectric coefficient (κ_{ij})

The dielectric coefficient κ_{ij} represent the charge per unit area in the i-axis due to an electric field applied in the j-axis. In most piezoelectric materials, a field applied along the j-axis causes electric displacement only in that direction. The relative dielectric constant, defined as the ratio of the absolute permittivity of the material by permittivity of free space, is denoted by ε_0 = 8.85 E-12 F/m.

1.5.2. Piezoelectric strain coefficient (d_{ij})

In general, it is customary to define the polarization direction as the 3-direction (i.e. along the thickness direction or Z axis). The 1-direction represents one of axes in the perpendicular plane to the polarization direction (3-direction). A mechanical stress or electrical field that is applied either along the direction of polarization (3-direction) or at right angles to it (1-direction) constitute the two most commonly used operating modes of piezoelectric transducers (energy harvester or sensor), termed as 33 (axial mode) and 31 (bender or lateral mode), respectively. Figure 1-5 represent a typical poled piezoceramic with the dipole moment aligned in the 3-direction and 1 and 2-directions are aligned toward the length and width of the material. It should be noted that, sensing or energy harvesting from other modes of operation of the piezoelectric material is also possible; however, these two operating modes cover the majority of the configurations used for sensing and energy harvesting [45].

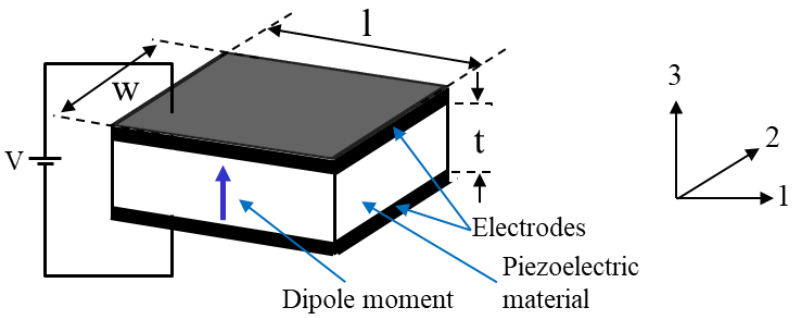

Figure 1-5: A typical piezoceramic configured in 33 mode.

The piezoelectric coefficient d_{ij} is the ratio of the strain in the j-axis to the electric field applied along the i-axis, when all external stresses are held constant. In Figure 1-5, a voltage of V is applied to a piezoceramic in the 3-direction (33 mode). This generated electric field can be calculated as

$$E_3 = \frac{V}{t}. \tag{1-5}$$

where t is the thickness. The electric field, E_3 lead to

$$\varepsilon_3 = \frac{\Delta l}{l}. \tag{1-6}$$

in which

$$\Delta l = \frac{d_{31} V l}{t}, \tag{1-7}$$

and

$$\Delta t = d_{33} V. \tag{1-8}$$

The piezoelectric constant d_{31} is usually a negative number (an important exception is PVDF [46,47]), because application of a positive electric field lead to a positive and negative strains in 3-direction, and 1-direction, respectively. Another interpretation of d_{ij} is the ratio of short circuit charge per unit area flowing between connected electrodes perpendicular to the j-direction to the stress applied in the i-direction.

1.5.3. Piezoelectric voltage coefficient (g_{ij})

The piezoelectric voltage coefficient g_{ij} signifies the electric field developed along the i-axis when the piezoceramic is stressed along the j-axis. According to Figure 1-6 the applied force F is in the 1-direction, which result in a voltage difference along the 3-direction, i.e.

$$\mathrm{V} = \frac{g_{31}F}{w}. \tag{1-9}$$

where w is the width of the piezoelectric material. Another interpretation of g_{ij} is the ratio of strain developed along the j-axis to the charge (per unit area) deposited on electrodes perpendicular to the i-axis.

$$\Delta l = \frac{g_{31}Q}{w}. \tag{1-10}$$

It can be shown that voltage coefficient can also be calculate by the following relation:

$$g_{31} = \frac{d_{ij}}{\kappa ii}. \tag{1-11}$$

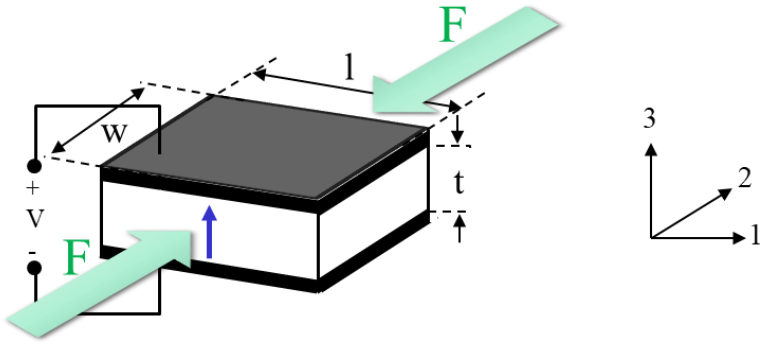

Figure 1-6: An open-circuited piezoelectric transducer under a force in direction.

1.5.4. Piezoelectric coupling coefficient (k_{ij})

The piezoelectric coupling coefficient (k_{ij}) demonstrate the ability of the piezoceramic material to transform electrical and mechanical energies (both as energy harvester/sensor or actuator). In k_{ij}, the i index indicate that the electrodes are perpendicular to i-direction and the

stress or strain is applied in j-direction. For instance, if the material is mechanically strained in 1-direction, as a result of an electric field in 3-direction, and while being under no other external stresses, then the ratio between stored mechanical energy and applied electrical energy is k_{13}^2. There are several ways to measure k_{ij} experimentally. One way is to apply a force to the material, while leaving it open circuited, and allow the material deform like a spring. The deformation, Δz, can be measured and the work done by the applied force can be calculated as

$$\mathrm{W}_{Mech} = \frac{F\Delta z}{2}. \tag{1-12}$$

Due to the piezoelectric effect, this lead to accumulation of electric charges on the electrodes (Q). By considering the piezoceramic as a capacitor with capacitance C_p, the stored electrical energy is given by

$$\mathrm{W}_{Elec} = \frac{Q^2}{2C_p}. \tag{1-13}$$

Therefore,

$$\mathrm{k}_{33} = \sqrt{\frac{\mathrm{W}_{Elec}}{\mathrm{W}_{Mech}}} = \frac{\mathrm{Q}}{\sqrt{F\Delta z C_p}}. \tag{1-14}$$

The coupling coefficient can be written in terms of other piezoelectric coefficients, i.e.

$$\mathrm{k}_{ij}^2 = \frac{\mathrm{d}_{ij}^2}{\mathrm{S}_{jj}^E \mathrm{k}_{ii}^\sigma} = g_{ij} d_{ij} E_p. \tag{1-15}$$

where E_p is the Young's modulus of the piezoelectric material. It should be noted that when a force is applied to a piezoelectric material, depending on whether it is open-circuited or short-circuited, different Young's moduli should be expected. For example, a short-circuited piezoceramic device will appear to be "less stiff". This is due to the fact that upon the application of a force, the electric charges of opposite polarities accumulated on the electrodes cancel each other. Subsequently, no electrical energy can be stored in the piezoelectric capacitor. Denoting short-circuit stiffness and open-circuit stiffness respectively as K_{sc} and K_{oc}, it can be shown that they are related to the piezoelectric coupling coefficient by

$$\frac{K_{oc}}{K_{sc}} = \frac{1}{1-k^2}. \quad (1\text{-}16)$$

1.6. Historic outline of piezoelectric energy harvesters

Over the past few decades the fields of microelectromechanical (MEMS) and portable electronics such as wireless sensors have been growing rapidly. Since these devices are designed to carry in situ power with limited lifespan, such as batteries. However, replacing the batteries can be problematic and difficult in cases where the device is not easily accessible and can die at any time. For example, global positioning system (GPS) sensors that are used to track animals in the wild can be easily retrieved for battery replacement. Therefore, it is desirable to utilize the "free" ambient mechanical energy in the surroundings of the sensor. The mechanical energy is then transformed to electrical energy which can be used to power small wireless electronics. Many approaches have been implemented to make use of this free energy. For example the energy harvesting based on piezoelectric [48], photovoltaic [49], pyroelectric [50], capacitive [51], magnetic [52], triboelectric [53], and thermoelectric [54] effects have been proposed.

In the past couple of decades, piezoelectric based energy harvesters have been developing rapidly. Unlike many conventional harvesters, they have the capability of transforming small mechanical disturbances in the environment in to useful electrical energy. The mechanical energy density presented in the environment can reach to up to an order of 10 mW/cm^2 which is only second to that of solar energy (10-100 mW/cm^2) [18]. Researchers have used many piezoelectric materials including ZnO [18], CdS [55], GaN [56], NaNbO3 [57], PVDF[58], $BaTiO_3$ [59], PZTs [60], and InN [61] for this purpose.

The first piezoelectric energy harvester which used vertically aligned arrays of ZnO nanowires was developed by Z. Wang in 2006 [62]. The working mechanism of the device is shown in Figure 1-7a. The tip of the nanowires were deformed by a week atomic force microscope machine (AFM) tip force which resulted in bending of the nanowires and consequently a potential difference between upper and lower ends of the nanowires. AC current was generated by external circuit to convert mechanical energy of the AFM tip to electrical energy. This demonstration paved a way to develop "self-generating" nano-devices that can generate electrical energy under the action of an external forces using nanometer-scale piezoelectric materials [63].

Although the measurement of electric output of a single strained nanowire is promising, for practical applications it is essential to collect the power from an array of nanowires. In 2007 the Z. Wang group developed the first piezoelectric nanogenerator excited by ultrasonic waves which could drive AC current through an external load continuously [64]. This work established a route toward solving the engineering problems associated with effective usage of nanogenerators. A schematic of this nanogenerator is shown in Figure 1-7b. The device consists of vertically grown ZnO nanowire arrays on a fixed substrate with a zigzag-shaped electrode (platinum coated silicon wafer) on top of the nanowires. The physical configuration of the device allows for bending of the nanowires and in-turn generation of piezoelectric voltage when a sound pressure is applied to the top electrode. A number of other devices were fabricated using the same zigzag electrode configuration such as those formed by gold-coated ZnO nanowires [65-68].

Although the first energy harvester based on piezoelectric nanowires in 2006 could only generate up to 9 mV output, it did pave a way toward more efficient devices with enhanced outputs. In 2009 Yang *et al.* developed a flexible piezoelectric energy harvester based on a single horizontal ZnO "Fine wire" with a length and diameter of 200 μm and 4 μm, respectively, that could generate up to 65 mV output voltage when bended (Figure 1-7c) [69]. Later in 2014, Zhou *et al.* reported a flexible nanocomposite energy harvester consisting of hydrothermally grown freestanding PZT nanowires and polydimethylsiloxane (PDMS) matrix. The configuration of the device made full use of piezoelectric properties of the inorganic nanowires and flexibility of organic polymer matrix. The open circuit voltage and short circuit current output of the energy harvester devices was reported to be up to 7 V and 120 nA, respectively (Figure 1-7d) [70].

In 2017, Alluri *et al.* demonstrated a piezoelectric composite composed of BTO and PDMS for scavenging biomechanical energy. They reported high open circuit voltage and short circuit current of up to 126.3 V and 77.6 μA, respectively [71]. This demonstration allowed for powering portable electronic devices with continuous power supply. Later in 2018, Malakooti *et al.* used a 3D printing method to fabricate piezoelectric nanocomposite energy harvester with controlled alignment using direct write method. They showed that using this method, they can incorporate highly aligned BTO nanowires in polylactic acid (PLA) polymer and enhance the output of the device by aligning the nanowires in the direction of applied stress. Using the direct write method, they proved that the power output of the device can be improved about 400% compared to that of

casted composite with randomly oriented nanowires (Figure 1-7e) [72]. It can be then seen that the design of the piezoelectric energy harvesters have evolved from a single nanowire with mV range output to more than 100 V in about a decade, therefore enabling self-powered portable electronic devices.

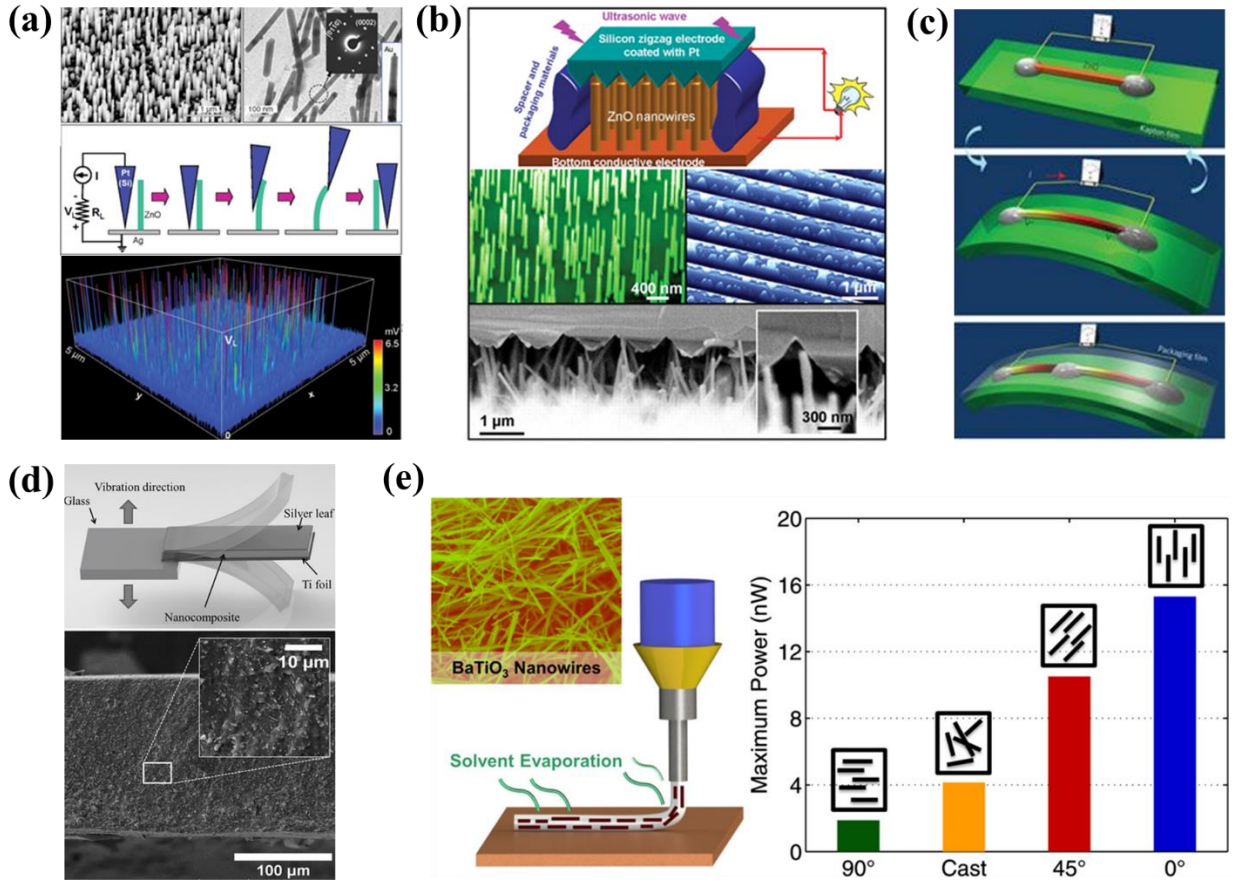

Figure 1-7: Various piezoelectric based energy harvesters. (a) The first ZnO-based energy harvester composed of vertically aligned nanowires. The device was excited by an AFM tip to bend individual nanowires and was able to generate up to 9 mV [64]. (b) Schematic and SEM image of the first practical ZnO-based energy harvester which was excited by ultrasonic wave through a zigzag-shaped top electrode. The design of the electrode allowed for bending of multiple nanowires and hence resulted in enhanced current output [64]. (c) Schematic of a single ZnO finewire attached to a flexible substrate which lead to further development of flexible energy harvesters [69]. (d) Schematic and SEM image of a fully flexible energy harvester composed of BTO nanowires dispersed in PDMS matrix [70]. (e) Schematic of a direct write method for fast fabrication of flexible energy harvesters with controlled alignment of BTO nanowires which show a significant output power improvement when the nanowires are aligned in the direction of applied stress (0°) compared to that of casted nanocomposite [72].

1.7. Choice of piezoelectric material

There are many options for choosing the appropriate piezoelectric material. For example, zinc oxide, lead zirconate titanate, barium titanate, and Polyvinylidene fluoride. Each of these materials have their own advantages and disadvantages as well as various application which are discussed in the following sections.

1.7.1. Zinc oxide (ZnO)

ZnO was one of the very first piezoelectric material to be studied and it was used in many energy harvesting applications due to its beneficial piezoelectric, semiconducting, and optical properties. ZnO has a simple chemical composition, crystal structure, and easy to control synthesis processes for development of various sizes and morphologies. In earlier studies, the vertically aligned ZnO nanowires with high aspect ratio were bent by an AFM tip to generate spontaneous polarization in the nanowire resulting in temporally stored electrical energy that could be harvested using an external circuit [62]. In this study Wang *et al.* demonstrated the first energy harvester prototype based on ZnO nanowires which was able to generate about 9 mV open circuit voltage. Since then, significant amount of research has been dedicated to improving the preparation of the nanowires and its piezoelectric properties, as well as optimization of the energy harvester's structure. For instance, Yang *et al.* developed an energy harvester based on a single laterally packaged ZnO finewire on a flexible substrate [69]. By periodic bending of the substrate a uniaxial tension was developed in the nanowire resulting in a potential difference between two ends of the nanowire. They demonstrated that a single finewire with a diameter and length of 4 and 200 μm, respectively, can generate open circuit voltage and short circuit current of up to 50 mV and 750 pA, respectively. This flexible design allowed for an efficient way to convert irregular mechanical excitations to electrical energy. Later, in 2010 Xu *et al.* improved on Yang's design by integrating 700 rows of laterally packaged ZnO nanowires on a flexible substrate to generate 1.26 V and 28.8 nA at a low strain of only 0.19% which can be used for recharging an AA battery [73].

1.7.2. Lead zirconate titanate (PZT)

As mentioned before, ZnO has many desirable features, but due to its relatively low piezoelectric coefficients, it cannot meet the necessary power requirement of many

microelectronic devices. Therefore, it is essential to use alternate materials such as PZTs. For many years, PZT based nanogenerators have been popular due to their high piezoelectric coefficient, dielectric constant and crystallinity [74,75]. Lin *et al.* [76] reported a hydrothermal synthesis method for scalable growth of vertically aligned PZT nanowire arrays that was later used for energy harvesting applications by Malakooti *et al.* [77]. They showed that PZT nanowire based functionally graded interface can improve the power output of the energy harvester by more 7 times compared to that of a PZT film.

Similar to the work of Yang *et al.* [69] a flexible self-powered (ultraviolet) UV sensor based on a single PZT nanowire was fabricated by Bai *et al.* [78] and able to produce 0.12 V and 1.1 nA under the application of only 20 με tensile strain. Qi *et al.* designed and fabricated a nanogenerator based on highly crystalline PZT nanoribbons which were sputtered on a magnesium oxide (MgO) substrate by radio frequency (RF) sputtering method. Then the nanoribbons where transferred on to a flexible PDMS silica gel and their piezoelectricity where evaluated by AFM measurements. They demonstrated high d_{31} and d_{33} piezoelectric coefficients of up to 79 and 101 pm/V, respectively. Moreover, they used the PZT nanoribbons to fabricate a 1 cm^2 nanogenerator that was able to produce 0.25 V and 40 nA [79]. As another example, Zhang *et al.* incorporated freestanding PZT nanowires into PDMS polymer to form a piezoelectric composite and was able to generate up to 2.7 V and reach a power density of 51.8 $\mu W/cm^2$ [80]. Based on this brief overview it can be conclude that PZT-based nanogenerator can outperform the ZnO-based nanogenerators due to the higher piezoelectric coefficients of PZTs. However, due to environmental and biological concerns regarding the toxic effect of lead in PZTs, the development of lead-free piezoelectric materials with high piezoelectric coefficients is essential [81].

PZTs have great advantages such as high coupling coefficient and well-known synthesis processes to achieve scalable and inexpensive nanowires. However, depending on the elemental Zr content in the material, its Curie temperature (T_c) ranges from 220 °C to 490 °C. As shown in Figure 1-8 [1], the highest possible temperature that a PZT material can maintain its tetragonal crystal structure and accordingly its piezoelectricity is 490 °C which correspond to pure lead titanate ($PbTiO_3$ or PTO) with no Zr. This is crucial because for energy harvesting using piezoelectric materials at extrema temperatures, one should choose a high Curie temperature material with stable crystal structure.

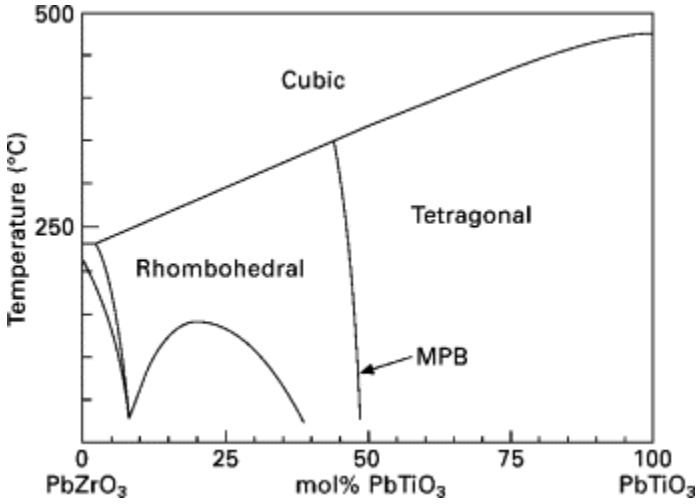

Figure 1-8: Phase diagram of PZT materials. Depending on the Zr content, the Curie temperature (T_c) ranges from 220 °C to 490 °C [1].

Many high Curie temperature materials have been developed. Quartz (SiO_2) is the oldest known piezoelectric material with T_c = 573 °C [82], however it has poor piezoelectric properties such as low piezoelectric strain coefficient. Other often used single-crystal piezoelectric material with high Curie temperature include lithium niobate ($LiNbO_3$) with T_c = 1165 °C and lithium tantalite ($LiTaO_3$) with T_c = 601 °C [83]. Although both materials exhibit high electromechanical coupling coefficient at room temperature, they suffer from high conductivity and strong pyroelectric effects at extreme temperatures [84]. Other materials with high Curie temperatures include bismuth titanate ($Bi_4Ti_3O_{12}$ with T_c = 685 °C), bismuth niobate titanate (Bi_3TiNbO_9 with T_c = 940 °C), lead metaniobate ($PbNb_2O_6$ with T_c = 560 °C) [84]. Although all of these materials can potentially be used in extreme temperature energy harvesting applications, their synthesis methods require complex and expensive processes. Moreover, these materials are usually synthesized into 2D films rather than 1D nanostructures like nanowires. Therefore in this research, a new method for synthesizing PTO nanowires is developed. Then the PTO nanowires are incorporated into polyimide polymer to fabricate extreme temperature composite energy harvester (please refer to chapter 5 for more information).

1.7.3. Barium titanate (BTO)

To date, various lead-free materials such as barium titanate ($BaTiO_3$) [85], bismuth titanate [86], sodium potassium niobate [87], potassium bismuth titanate [88] and so on have been

developed as an alternative to lead-containing piezoelectric materials such as PZTs. For instance, Huan *et al.* fabricated an energy harvester based on sodium potassium niobate particles and multiwall carbon nanotubes (MWCNTs) that was able to produce open circuit voltage and close circuit current of up to 3.5 V and 0.3 μA under mechanical stress of 0.1 MPa, respectively. In this study they used sodium potassium niobate particles due to their high Curie temperature (high temperature stability), and electromechanical coupling coefficients [89].

BTO is the most well-known lead-free piezoelectric material with excellent ferroelectric, dielectric and piezoelectric properties and hence is the best alternative to lead-containing materials. Koka *et al.* used an inexpensive two-step hydrothermal reaction method to synthesize vertically aligned barium titanate on conductive fluorine doped tin oxide (FTO) glass [85]. The nanogenerator was completed by boding a strip of indium foil, thus creating a conductive cantilever beam on top of nanowires. They reported open circuit voltage and short circuit current of up to 0.312 V and 0.9 nA, respectively. It was also demonstrated that under similar excitation method a nanogenerator with similar size but based on ZnO nanowires can produce less than 16 times lower power compared to that of BTO based nanogenerator. Feenstra *et al.* used an electrospinning method to synthesize ultra-high aspect ratio BTO fibers with diameters between 0.5 and 1 μm [90]. By mixing the BTO fibers with epoxy they prepared a piezocomposite which was shown to have significantly higher electromechanical coupling coefficient compared to that of a similar piezocomposite made of BTO particles. With that, they experimentally demonstrated for the first time that an increase in the aspect ratio of the piezoelectric inclusions in a polymer matrix can remarkably improve the piezoelectric properties of the piezocomposite.

1.8. Use of piezoelectric composite materials

As mentioned before, most piezoelectric materials are made of inorganic ceramics which are brittle and have low mechanical stability, therefore they cannot easily conform to curved surfaces. Researchers have proposed to disperse inorganic piezoelectric particles with organic polymers to fabricate a composite energy harvester. This configuration not only provide excellent piezoelectric properties but also lead to high mechanical flexibility due to the use of elastomeric matrix. Moreover, the polymer can efficiently transfer the mechanical strain to the piezoelectric inclusions inside the composite. The use of composite material for fabricating piezoelectric energy harvesters

has many advantages such as flexibility, lower internal leakage, cost effectiveness, ease of processing, eco-friendliness, adaptability to large mechanical forces, and ease of large-scale fabrication.

In the literature, many piezoelectric composite energy harvester composed of BTO inclusions and PDMS [71,91-96], as well as PVDF [97,98], P(VDF-TrFE) [99-101], P(VDF-HFP) [102], P(VDF-HFP) [103,104], and PVC [105] polymers have been reported. Table 1-2 compares the performance of various BTO based composite energy harvesters with different polymeric matrix materials as the polymer. It should be noted that some studies suggest that the piezoelectricity of composite materials can outperform that of bulk piezoelectric material. For example, Bent *et al.* [106] reported a composite made of PZT fibers that exhibits enhanced in-plane actuation properties compared to bulk PZTs. Safari *et al.* [107] and Smith *et al.* [108] reported that 1-3 piezoelectric composites have a higher electromechanical coupling coefficient than that of conventional piezoceramic PZT.

Table 1-2: Electrical performance of various BTO based composite energy harvesters.

Piezoelectric material	Polymer matrix	Open circuit voltage (V)	Short circuit current (μA)
$BaTiO_3$ (BTO)	PDMS [109]	6	0.3
	PDMS [71]	126.3	77.6
	PVDF [98]	35	0.6
	PVDF [97]	7.99	1.01
	P(VDF-TrFE) [99]	14	4
	P(VDF-TrFE) [101]	9.8	0.69
	P(VDF-HFP) [103]	75	15
	P(VDF-HFP) [102]	110	22
	PVC [105]	0.9	0.01

1.9. Inclusion alignment

From the discussion provided in section 1.7, it is evident that the use of composite materials can improve both electrical and mechanical properties of a piezoelectric energy harvester. However, further improvement can be made by alignment of the piezoelectric inclusions (nanowires, nanorods, nanoribbon, etc.). It has been shown both theoretically and experimentally that by engineering the inclusions to have high degree of alignment, one can fabricate piezoelectric composites with significantly improved properties. For example, using micromechanical modeling and FEM, Andrews *et al.* demonstrated that a nanocomposite with aligned piezoelectric particles have approximately two times higher piezoelectric strain and coupling coefficients compared to that of randomly oriented particles [24]. Systematic experiments were performed by Yan *et al.* to show the effect of alignment in BTO/PDMS composites. They demonstrated enhanced dielectric properties as well as higher open circuit voltage and short circuit current by alignment of electrospun BTO fibers in PDMS [110].

The alignment of nanowires in composite can be achieved using many methods such as dielectrophoresis [111-114], strain-release assembly [115], microfluidics [116,117], blown-bubble films [118,119], Langmuir–Blodgett technique [120,121], uniaxial strain assembly [122], and shear force assisted methods [123-129]. The dielectrophoretic effect is based on the dipole-dipole

interactions that are induced between particles in a suspension by an electric field. These interactions result in the formation of chains or fibrils parallel to the applied electric field direction. Tomer [111] used a dielectrophoresis assembly approach to fabricate an anisotropic composite with BTO particles as the active material and silicone elastomer thermoset polymer as the matrix. In another study, Bowen *et al.* showed that using this method they can engineer anisotropy inside their composite containing various filler materials in a thermoset polyurethane matrix. Dielectrophoresis has also been used to orient colloidal dispersions of nanometer-scale rod-shaped gold particles in an electro-optical cell [130] and to align carbon nanotubes between electrically biased electrodes on a glass substrate [131].

Self-release assembly method is a simple approach for alignment of the nanowires in a stretchable substrate. The nanowires are assembled through the stretch and then release of the substrate, leading to the nanowires aligning themselves in the transverse direction, and thus increasing the area coverage of the nanowires inside the substrate. Using this method, Xu *et al.* demonstrated an effective way to align silver (Ag) and silicon (Si) nanowires in PDMS [115]. In microfluidic approach such as the one reported by Huang *et al.* the inclusions are aligned using a fluid flow via hierarchical assembly of the nanostructures with some control over the separation and spatial location of the inclusions [116]. Alternatively, the blown-bubble approach is a simple method for large-area assembly of inclusions with control over their orientation and density. It relies on expanding a bubble from a homogenous suspension of inclusions [118,119], which can be used both on rigid and flexible substrates. The Langmuir–Blodgett approach has been used to align nanowires with controlled spacing. In this technique, surfactant-wrapped nanowires are slowly compressed on an aqueous subphase to yield uniaxially-aligned nanowires which produces aligned nanowires with controlled spacing down to close-contact [120,121]. In the uniaxial assembly method, the composite containing randomly oriented inclusions inside a thermoplastic matrix is heated and stretched. Subsequently, it is cooled down to room temperature while being stretched. Tang *et al.* [122] used this method to align PZT nanowires in PDMS matrix and showed that the energy density and dielectric permittivity of the piezocomposite can be significantly improved due to the alignment.

However, each of these fabrication approaches have major drawbacks. In all self-alignment methods, such as microfluidics, Langmuri-Blodgett, and bubble blown techniques, the alignment

of the inclusions is only possible on the surface of the substrates. The uniaxial strain assembly technique is only applicable to composites with thermoplastic matrices in order to provide the necessary filler mobility for the assembly of the inclusions. Furthermore, this method often leads to non-uniform strain along the sample which limits its usage to small, planar applications. The field assisted methods such as dielectrophoretic technique have similar disadvantages. Moreover, these methods are only limited to small composite materials since extremely high electric and magnetic fields are required to align the inclusions in a bulk composite material. Another restriction of this method is that the fillers must respond to the field before the matrix polymerization. Therefore, a new process for fabrication of bulk composites with high anisotropy properties with controlled filler alignment is needed.

A relatively new approach for alignment of the inclusions in the matrix is called the direct-write technique, which unlike other methods of composite fabrication that were discussed so far, it provides material flexibility, inexpensive fabrication, and the ability to construct arbitrary and complex 3D structures. The direct-write method describes a fabrication process which utilize a computer-controlled stage (in all X, Y, and Z directions) that moves based on a predefined pattern and deposits the material via a nozzle [132]. Various direct-write techniques have been introduced, and can be categorized into droplet-based approaches such as hot-melt printing [133] and ink-jet printing [134-137], and filamentary-based approaches such as micropen writing [138], robocasting [139,140] (or robotic deposition [141-144]), and fused deposition [145,146]. Several ink designs have been employed such as polymer melts [146], waxes [133,147], concentrated polyelectrolyte complexes [144,148,149], colloidal gels [142,150], dilute colloidal fluids [134-136], and highly shear thinning colloidal suspensions, [138-140]. These inks solidify by gelation [123,138,143], liquid evaporation [134-137,139,140], temperature [145,146] or solvent-induced phase change [144,148,149]. It should be noted that for ink-jet printing method, two criteria have to be met: (1) after printing the ink solvent should evaporate quickly, and within the same time span as printing process; (2) the rheological properties of the ink, such as its viscosity should be tunable for controlled alignment of the inclusions in the composite ink, while maintaining a self-supporting structure.

Compton *et al.* reported an epoxy-based ink-jet printing technique where they 3D printed a cellular composite with controlled alignment of high aspect ratio reinforcement fillers. Using this

method, they demonstrated that the printed structure have up to 10 times higher Young's modulus compared to that of 3D printed polymers without inclusions, while comparable strength values were maintained (Figure 1-9) [125]. Due to the high-shear environment inside the nozzle, the fillers progressively arrange themselves parallel to the nozzle which result in aligned fillers in the "written" composite. The shear force in the nozzle is at its maximum in the vicinity of the nozzle's inner wall and increase with reduction of the nozzle diameter [72,126]. Therefore, by reducing the diameter of the nozzle or increasing the viscosity of the ink, higher filler alignment can be achieved. However, reducing the nozzle's diameter has an adverse effect, namely, it can increase the chance of nozzle clogging due to agglomeration of high aspect ratio fillers in the nozzle.

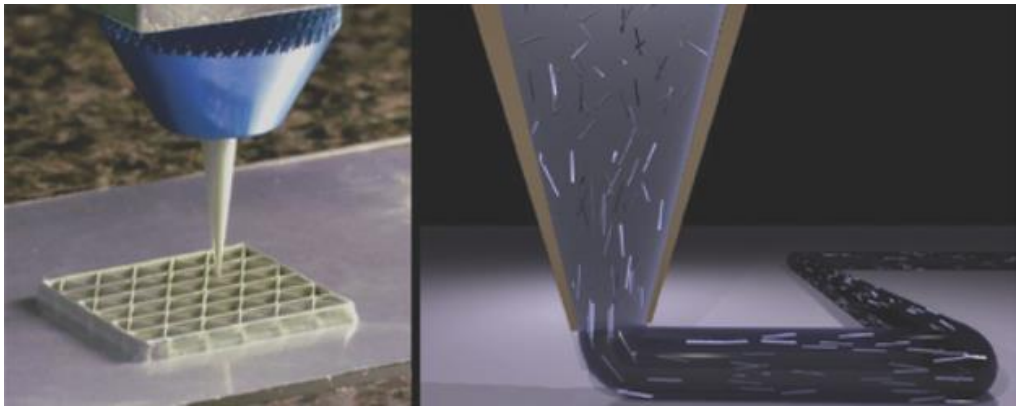

Figure 1-9: Optical image of the ink-jet nozzle while printing a triangular honeycomb composite, and the schematic of the printing process. The schematic shows the progressive alignment of high aspect ratio fillers within the nozzle due to a high-shear environment.

Gladman *et al.* demonstrated a botanic-system inspired 4D printing method, where they printed composite hydrogel architectures with localized, anisotropic swelling behavior, controlled by alignment of cellulose fibrils along prescribed four-dimensional printing pathways (Figure 1-10a) [126]. This design allows for bilayer architectures that are patterned in space and time, i.e. the localized swelling anisotropy induces complex shape changes when immersed in water (Figure 1-10b). The efficiency of the four-dimensional printing relies heavily on the ability of defining the elastic and swelling anisotropies deterministically. This is accomplished by local control of the orientation of cellulose fibrils within the hydrogel composite. Similar to the work of Compton *et al.* [125] and Malakooti *et al.* [72] the fibrils undergo a shear assisted alignment as the ink flows through the nozzle. Therefore, anisotropic stiffness and swelling behavior can be achieved in the longitudinal direction (along the nozzle and printing path) compared to the transverse direction.

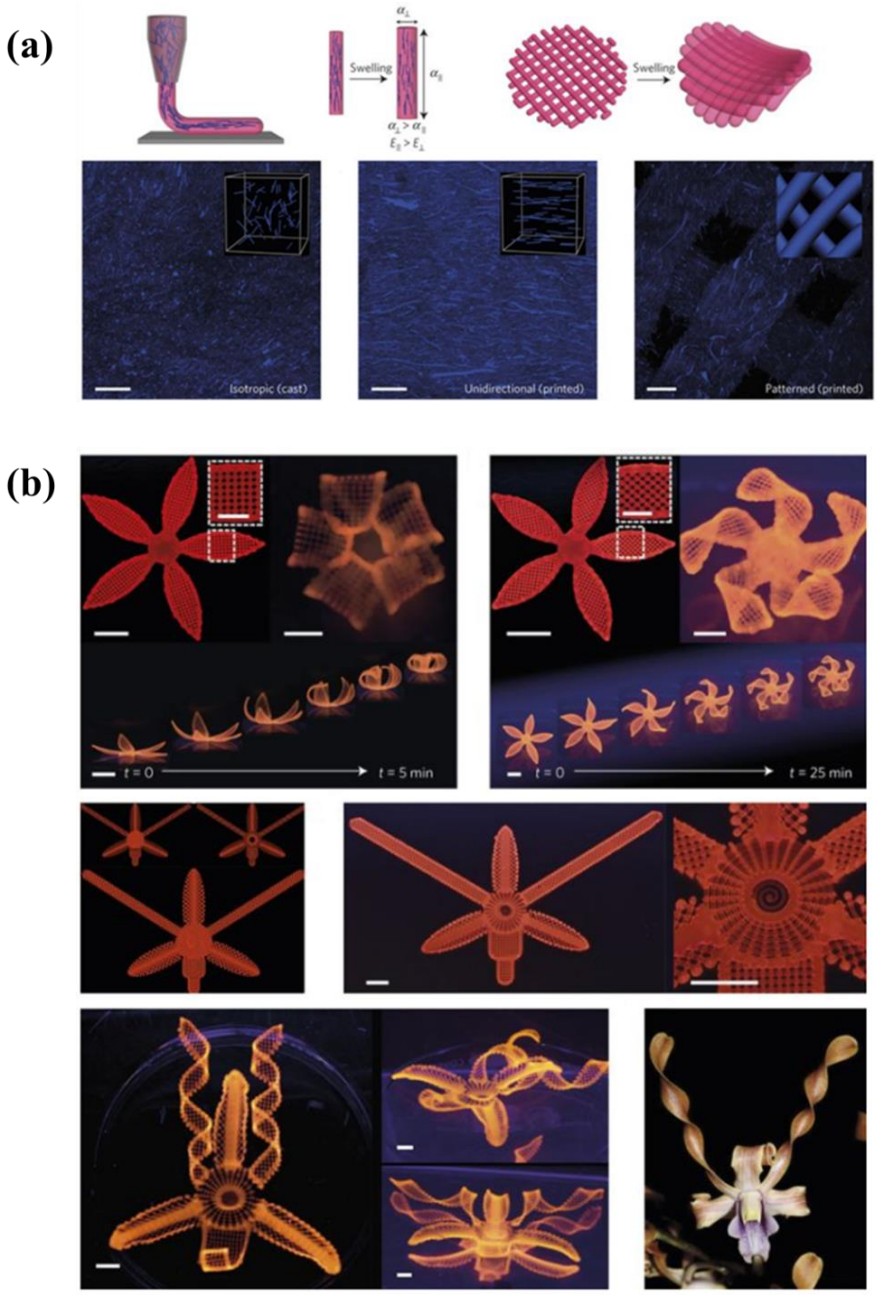

Figure 1-10: (a) The alignment of cellulose fibrils due to a shear high shear environment inside the nozzle during four-dimensional ink-jet printing. The anisotropic swelling properties of the fibrils result in higher Young's modulus in the longitudinal direction compared to that of transverse direction. The optical image of the composite show that using this printing method the fibrils' alignment can be closely controlled resulting in complex geometrical microstructure for the composite (scale bars are 200 μm). (b) Complex printed geometries evolving in time by tailoring localized time-changing anisotropic swelling properties into the composite (scale bars are 5 mm) [126].

1.10. Piezoelectric composite modeling

In 1978 Newnham pioneered the micromechanical modeling of piezocomposite through his connectivity theory which was derived based on arrangement of different constituents in the material [151]. The way composite constituent materials are connected within a composite significantly affects the effective composite material properties; therefore, it is natural to aim to accurately model the composites in the way they are connected. In this theory, and as seen in Figure 1-11, there are ten important connectivity patterns in diphasic solids, i.e. 0-0, 0-1, 0-2, 0-3, 1-1, 2-1, 2-2, 2-3, 1-3, and 3-3 (the number of connectivity pattern for a *n*-phase composite is given by $(n+3)!/(3!n!)$ [152]). Classifying composites with this developed connectivity system has become a conventional process and has been adapted by many researchers. Among these connectivities, 0-3 and 1-3 composites are the most widely studied due to their simplicity in modeling and fabrication as well as the high coupling that could be achieved by these designs. For example, a 1-3 (or sometimes referred to as 3-1) has one phase (matrix) that is self-connected in 3-dimensional layers and the other phase (piezoelectric component) is self-connected in one dimensional chains [153]. This design gives the composite a high electromechanical coupling in the same direction as the piezoelectric connectivity. The 1-3 piezocomposites are usually produced with the aim of obtaining a combination of mechanical and piezoelectric properties which are desirable in electromechanically transducing applications such as piezoelectric energy harvesters or sensors. The 0-3 composites contain piezoelectric materials that are physically connected in zero directions imbedded in an epoxy matrix that has connectivity in all three directions. In other words, this type of composites contains piezoelectric particles (zero dimension) in a uniform matrix which encompasses the particles in all 3 directions. This type of piezoelectric composite is by far the easiest to fabricate and apply to complex engineering systems. Since the piezoceramic material is simply added and mixed with the polymer, 0-3 composites may be fabricated with existing equipment used to fabricate other polymer composites, such as plastic injectors and hot-presses.

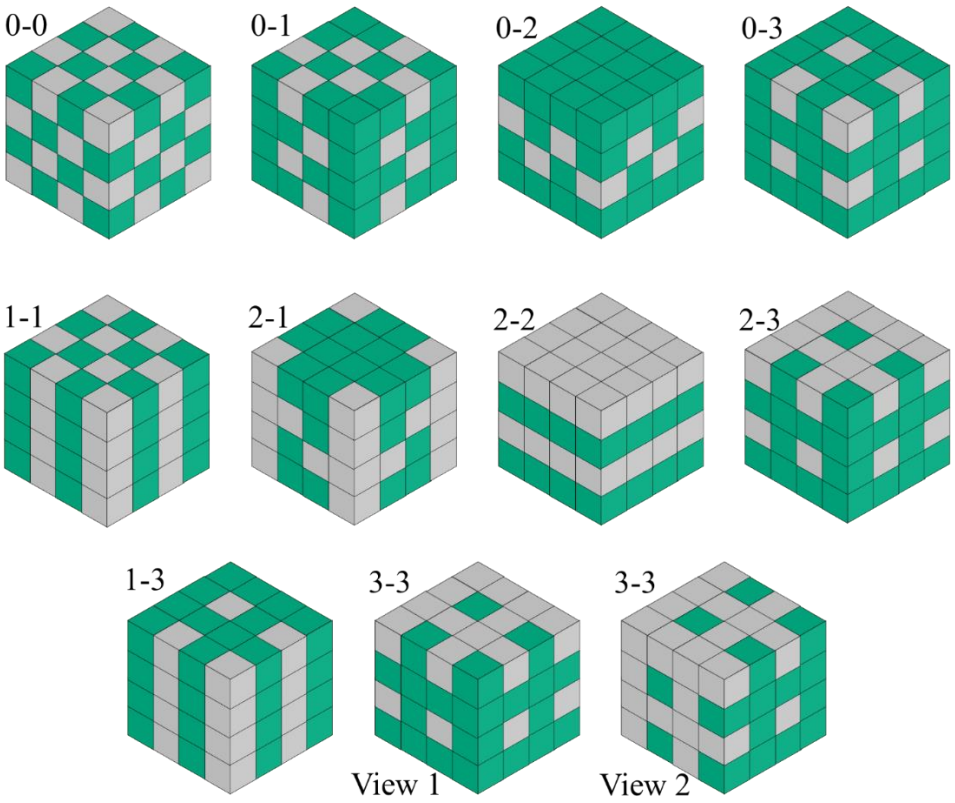

Figure 1-11: Connectivity types for diphasic composite materials [107].

In order to assess the overall properties of piezocomposites, several micromechanical models have been conceived. In all these models the aim is to predict the effective properties and responses of heterogeneous media which are derived from the properties of the constituent species and microstructural morphologies. The micromechanical models are formulated based on the assumption that a heterogeneous material is considered as a statistically homogeneous medium and the overall field variables, such as stress, strain and electric fields of the heterogeneous body can be estimated by a volume-averaged scheme over some representative volume. The reprehensive volume has to be small relative to the specimen size but large relative to the micro scale and thus on average is typical of the entire composite.

Early works on connectivity theory and modeling of 0-3 and 1-3 piezocomposites can be found in refs. [154] and [155], respectively. Using connectivity theory Banno derived the dielectric and piezoelectric constants of a composite containing PZT and $PbTiO_3$ particles in chloroprene rubber matrix [154]. A different approach was taken by Smith and Auld in the study of continuous

fiber-reinforced piezoelectric composites. Using a similar method, they showed that a tradeoff exist in between a composite's material properties such as desirable lower acoustic impedance and high electromechanical coupling coefficient and the two cannot be optimized at the same time [155]. In each of these methods, however, a simplifying assumption of either a constant stress or strain field in the composite has been made which leads to the use of Voigt or Reuss type estimates [156].

In 1991 Zhou *et al.* modeled the coupled electroelastic fields in piezocomposite by using continuum mechanics and electric dipoles, which at the time was a novel approach [157]. Later in 1992, Wang incorporated the thorough solutions for the coupled electroelastic fields in a piezoelectric inclusion into the analysis of the properties of piezocomposite materials [158]. However, his approach is only valid for low concentrations of piezoelectric inclusions (dilute limit) because the interaction between the inclusions at higher concentrations is not considered in this approach.

The most popular micromechanics models to receive attention over the past few decades are dilute, self-consistent, differential and the Mori-Tanaka schemes. In the dilute approximation, it is assumed that the interaction between the inclusions can be disregarded and that the properties of the piezocomposite can be approximated by considering the problem of a single particle embedded in a continuous matrix phase [159]. The self-consistent model which was first devised by Hershey [160] and Kroner [161] is based on a vibrational principle and is particular for the case where the volume fraction of the inclusions is relatively large. The differential scheme is based on the idea that a piezocomposite can be constructed explicitly from an initial material through a series of incremental additions [159]. The work of Mori and Tanaka, which originally was developed to calculate the mean stress in a matrix of material containing precipitates with eigenstrains, has been a topic of interest for many studies [33]. In 1991 an interesting aspect of these models were reported by Benveniste *et al.* in which they provided the mathematical basis for these models to result in symmetric elastic moduli, an absolute necessity for any micromechanical model [162]. For each of these methods, it is common to use the well-formulated stress and strain concentration factors that are acquired by solving the mathematical problem of a single embedded inclusion in an infinite medium Eshelby's solution for the stress-strain fields in an ellipsoidal inclusion have been used [163]. Eshelby's solution is based on the assumption that under a uniform load, the

stress and strain fields are uniform in the inclusion, simplifying the problem of obtaining the volume averaged fields. Moreover, this solution allows for modeling of a variety of geometries for the ellipsoidal inclusions such as spherical particles (flakes), continuous fibers and short fibers.

Until 1991, the dilute, self-consistent, differential and Mori-Tanaka methods had been only applied to a number of models involving uncoupled mechanical and electrical behavior of composites with great success [159,164,165]. In 1992, Dunn and Taya expanded the Eshelby's tensor to encompass piezoelectricity; and a year later they used these methods to solve the coupled electroelastic problem involved in piezocomposites [166]. Therefore, they were able to generalize all the previously mentioned methods to solve coupled electrical and mechanical systems. Their results were implemented based on matrix formulations which led to convenient numerical calculations of the effective electrostatic moduli of a piezoelectric composite.

In 1993, Nan and Jin proposed the effective medium theory, where they were able to predict the electromechanical property of a piezoelectric composite using Dunn and Taya's method [166] and then compare their results to experimental data. They showed that increasing the length of PZT particles in a composite can increase the effective electromechanical coefficients [167,168]. Aboudi used the cells model to predict the effective piezoelastic, dielectric pyroelectric and thermal-expansion constants of multiphase piezocomposites and compared the results with Dunn and Taya's method for a similar piezocomposite [169]. Later, Odegard generalized the Mori-Tanaka and self-consistent approaches to propose a new model which, in certain cases, provided more accurate results and was easier to implement [27]. The effects of geometrical parameters of the inclusions such as aspect ratio were studied by Andrews *et al.* They showed that by increasing the aspect ratio of inclusions the coupling coefficient of the piezocomposite increased significantly [24]. By building on previous electromechanical models such as Dunn and Taya's method, the non-linear and field dependent responses of piezoelectric composite were studied by Tan *et al*., [170] and Muliana *et al*. [171]. These studies presented a multi-scale formulation for solving the coupled thermos-electro-mechanical deformations and heat conduction in a smart cantilever beam. Although significant progress has been made toward effective electromechanical modeling of piezocomposites, a lack of comprehensive studies with experimental verification on the effect of geometrical properties of piezoelectric inclusions still exists.

1.11. Summary of contributions

The design and fabrication of any piezoelectric nanocomposite energy harvester require a comprehensive model to predict piezoelectric properties such as piezoelectric strain, voltage and coupling coefficients, and dielectric constant. This dissertation demonstrate a micromechanical model based on the Mori-Tanaka approach which is used for calculation of all piezoelectric coefficients. This model shows that the piezoelectric properties of a nanocomposite energy harvester are closely related to that of its fillers microstructure such as geometrical properties and alignment. Particularly, the effect of filler aspect ratio, alignment and gradual deviation from complete alignment is studied. To verify the micromechanical model, a FEM analysis is performed using COMSOL Multiphysics software. A robust model with complete freedom over material properties, filler aspect ratio and degree of alignment (including randomly oriented fillers) is developed and the results are compared to the micromechanical model. The results show that the micromechanical model can be verified by FEM over a large portion of filler weight fractions.

The FEM and micromechanical models are then verified experimentally. First, a direct write 3D printing approach using shear assisted technique is developed. This technique allows for fast and inexpensive fabrication of nanocomposite energy harvesters with piezoelectric nanowires. Then, various nanocomposite with assorted volume fractions, and aspect ratio of BTO nanowires in PDMS are fabricated. The alignment of the nanowires is controlled by adjusting the viscosity of nanocomposite ink and through modifying the printing parameters. Comparison between the models and experimental measurements shows that the experimental procedure developed here can verify the models, confirming the ability to fabricate high performance nanocomposite energy harvesters using this technique.

Finally the effects of energy harvesters' operating temperature on electromechanical properties of the nanocomposite is incorporated in to the models. The electromechanical coefficients of a nanocomposite containing lead titanate nanowires and polyimide matrix are calculated and compared to experimental data. For practical applications of energy harvesting at extreme temperatures a new piezoelectric material is developed. With the goal of synthesizing piezoelectric nanowires with high Curie temperature (T_c), lead titanate was chosen due to its high temperature stability (T_c = 490° C). Lead titanate has a significantly higher T_c compared to many

perovskite materials such as PZTs (230 °C < T_c < 490 °C) and barium titanate (T_c = 125° C). Therefore, lead titanate can retain its piezoelectricity at high temperature which allows for energy harvesting even at extreme temperatures. This dissertation demonstrates the first synthesis of freestanding lead titanate nanowires using a two-step inexpensive hydrothermal reaction where sodium titanate nanowires were first used as precursor. It is shown that the aspect ratio of the freestanding lead titanate nanowires can be controlled by adjusting reaction parameters such as reaction time, temperature, and the concentration of reacting species in the hydrothermal reaction process. Moreover, vertically aligned lead titanate nanowire arrays were grown on oxidized titanium foil using a similar two-step hydrothermal reaction with vertically aligned sodium titanate nanowire arrays as their precursor. As with freestanding nanowires, it is shown that the morphology and the length of these nanowires can be controlled by adjusting the reaction parameters. Both freestanding and vertically aligned lead titanate nanowires are used as the basis of extreme temperature energy harvesting.

Using the synthesized lead titanate nanowires, two types of energy harvester suitable for working at extreme temperatures are developed. First as a feasibility test, vertically aligned arrays of lead titanate nanowires are synthesized to fabricate a cantilever beam-based energy harvester capable of providing electrical power at temperatures exceeding 300 °C. Although this device demonstrates the potentiality of lead titanate nanowires for energy harvesting at extreme temperatures, it is not suitable for applications where a flexible device is needed. Therefore, free-standing lead titanate nanowires are developed to be incorporated in a polymeric nanocomposite for development of flexible energy harvesters. This requires a thermally stable polymeric matrix, hence Kapton polyimide was synthesized to be used as the matrix. Using a direct write method as described before, these nanocomposites are printed with control over the nanowires' alignment. It is shown that this type of energy harvesters can provide output at temperatures of up to 250 °C. The performances of these energy harvesters are then compared to those predicted by developed models to verify their sanity at various temperatures.

1.12. Dissertation overview

Chapter 2, develops a micromechanics model based on the Mori-Tanka approach and FEM are provided that are used for calculation of overall properties of a nanocomposite based on the

properties of its constituents. First the micromechanics approach is formulated using the Mori-Tanaka and Eshelby's inclusion theories, and the effects of inclusions' geometrical features such as aspect ratio and alignment was illustrated. Then, the results are validated using FEM performed in COMSOL Multiphysics software. It is shown that the FEM method provided in chapter 2 can predict the piezoelectric performance of a diphase nanocomposite with aligned and randomly oriented inclusions. Finally, the effects of inclusion misalignment is quantified via calculation of the nanocomposite's piezoelectric strain coefficients with different degrees of misalignment.

In Chapter 3, two hydrothermal methods are developed to synthesize free-standing barium titanate and lead titanate nanowires. A template-assisted method is employed where first sodium titanate nanowires with control over morphology are synthesized and then converted to final product, namely barium titanate ($BaTiO_3$) and lead titanate ($PbTiO_3$) nanowires. The inexpensive, scalable method used in this chapter allows for synthesis of $BaTiO_3$ and $PbTiO_3$ nanowires with various aspect ratios. These nanowires are used for fabrication of nanocomposite energy harvesters.

An additive manufacturing process is developed in Chapter 4 which enables to fabrication of piezoelectric nanocomposite with control over alignment of the nanowires. Using this method, the alignment can be varied and therefore a wide range of model conditions formulated in Chapter 2 are validated through experimental data. By comparing the Mori-Tanaka and FEM models with experimental measurement of the piezoelectric strain coefficient, it is shown that aspect ratio and alignment of the nanowires are dictating factors in the overall piezoelectric properties of nanocomposites and can be tailored to enable high coupling.

A novel method for energy harvesting using piezoelectric nanowires is provided in Chapter 5. First, the feasibility of this task is proven by synthesizing ultra-long arrays of lead titanate nanowires and fabrication a non-flexible cantilever-based energy harvester. It is illustrated that the energy harvester can provide voltage and power outputs at temperatures as high as 375 °C. Then after confirming that lead titanate can be used as high temperature piezoelectric material, the freestanding nanowires developed in chapter 2 is used to fabricate flexible nanocomposite energy harvester for high temperature applications. The nanocomposite is fabricated using the additive manufacturing process developed in chapter 4 and it is demonstrated that the energy harvester is

thermally stable and can generate constant output at temperatures ranging from ambient temperature to 250 °C.

Finally in Chapter 6, a summary of the finding and contributions of this work along with recommendations for future work are provided.

Chapter 2: Modeling of a Piezoelectric Nanocomposite

2.1. Introduction

The development and application of active materials to a variety of host structures is a continually evolving field due to their use in a vast range of applications spanning energy harvesting [172,173], sensing [174,175], and actuation [172,176]. The most prominent of these active materials are piezoelectric [177,178], piezoresistive [179,180], electrostrictive [181,182], shape memory alloys [183,184], and magnetorheological fluids [185,186]. Piezoelectric materials are among the most popular "*smart*" materials due their fast response to dynamic systems with high electromechanical coefficients. However, when applied in the monolithic form piezoelectric materials are very brittle with low fracture toughness, making them susceptible to accidental breakage and poorly suited for applications in non-flat surfaces [187-189]. One solution is to embed piezoelectric materials in a polymer matrix [190], which results in the production of a nanocomposite that offers enhanced flexibility and robustness to damage as well as the ability to be conformed to curved surfaces. However, when compared to monolithic form, reported nanocomposites have a significantly lower electromechanical coupling coefficient, making them inadequate for many engineering applications. Recent work has shown that the use of higher aspect ratio piezoelectric fillers could enable greater electromechanical coupling coefficients at the same volume fraction as their equiaxial counterparts [3,24,58,190-195]. For instance, Feenstra and Sodano have reported a 300% increase in coupling by the use of high aspect ratio electrospun fibers instead of spherical nanoparticles [90].

The integration of high aspect ratio fillers into the polymer matrix leads to anisotropic properties that cannot be easily optimized through experimental approaches. Many theoretical models have been proposed to show the effective electroelastic properties of a nanocomposite. For instance, models such as the dilute approximation [196], the conditional moments method [197], and the differential scheme [29] are all based on averaging procedures and take into account

features of the arrangement of the inclusions and their electromechanical interactions. Generally, these methods are only applicable to low volume fraction composites and cannot be applied to composites with a high concentration of inclusions. Other approaches such as the Voigt [198] and Reuss approximations [199] have been proposed that allow for computation of the lower and upper limits of the actual electromechanical coefficients, respectively [200]. Another approach for calculating the effective electroelastic coupling coefficients of a nanocomposite is the Mori-Tanaka method [159]. In this approach, interaction between the fillers is taken into account and hence is applicable to higher filler concentrations. It is formulated based on the assumption of a finite number of inclusions in an infinite matrix and explains the relations between fillers. This method is among the most powerful and accurate approaches in predicting the electromechanical properties of a piezoelectric nanocomposite, and unlike the dilute approximation, it can produce accurate results in a wide range of volume fractions [201].

Despite the effectiveness of the Mori-Tanaka method in producing explicit and closed form solutions for the electromechanical properties of a nanocomposite, some limitations remain. For instance, it is demonstrated that for a more than two-phase composite with different inclusion morphologies, the Mori-Tanaka method can produce asymmetric stiffness matrices which are not physically possible [31,202]. Moreover, this method requires knowledge of the Eshelby's tensor, which has only been formulated for certain specific geometries of inclusions [203]. To overcome these issues, finite element modeling (FEM) has been used to calculate the effective electromechanical properties of nanocomposites with arbitrary geometry of inclusions and arrangements. It is based on the assumption that the nanocomposite can be approximated by a unit cell (RVE) with geometric periodicity and a number of inclusions which are representative of the whole nanocomposite [203]. A significant advantage of FEM methods over micromechanics approaches is that it imposes no restrictions on the size, spatial distribution or connectivity of the inclusions in the nanocomposite.

In this chapter, using a micromechanical model and FEM, the role of the filler aspect ratio and orientation on the overall piezoelectric performance of a nanocomposite is studied. The material is first simulated using the Mori-Tanaka approach for nanocomposites with aligned fillers. Then using tensor transformation rules, their properties in all possible discretized 3D Euler angles is calculated and averaged for prediction of electroelastic properties of a nanocomposite with

randomly oriented fillers [204]. It is shown that the piezoelectric strain coefficients of a nanocomposite with aligned nanowires are significantly higher than that of one with randomly aligned nanowires. This model is then validated through FEM and demonstrates that the alignment and aspect ratio of the nanowires play major roles in the overall piezoelectric properties of the nanocomposite. Later in chapter 4 the FEM and micromechanical model provided in this chapter is experimentally verified. This is the first experimental verification of the Mori-Tanaka model on nanocomposites with high aspect ratio fillers. Model validation is carried out by measurement of d_{31} and d_{33} coefficients of various directly printed nanocomposite [58] with different volume fractions of barium titanate (BTO) nanowires in polydimethylsiloxane (PDMS) matrix. The experimental procedure is applied through an additive manufacturing direct write approach, which enables alignment to be varied and therefore a wide range of model conditions to be validated. By comparing the Mori-Tanaka and FEM models with experimental measurement of piezoelectric strain coefficients, it is shown that aspect ratio and alignment of the nanowires are dictating factors of the overall properties of piezoelectric nanocomposites and can be tailored to enable high coupling.

2.2. Theoretical modeling

2.2.1. Constitutive Equations

The piezoelectric constitutive equations which describe the coupled interaction between mechanical and electrical variables can be expressed as [205]

$$\sigma_{ij} = C_{ijmn}\varepsilon_{mn} + e_{nij}(-E_n), \tag{2-1}$$

$$D_i = e_{imn}\varepsilon_{mn} - \kappa_{in}(-E_n). \tag{2-2}$$

in which the electric field, E_n, and elastic strain, ε_{mn} are independent variables and electric displacement, D_i, and stress, σ_{ij} are the dependent variables. The remaining constants C_{ijmn}, κ_{in}, and e_{nij}, represent the elastic moduli measured in a constant electric field, the dielectric constant measured in constant strain field and the piezoelectric stress coefficient, respectively.

In the absence of free charges and body forces, the stress and electric displacement in Eqs. (2-1) and (2-2) should satisfy the equations of equilibrium, namely,

$$\sigma_{ij,i} = 0, \tag{2-3}$$

$$D_{i,i} = 0. \tag{2-4}$$

where, the Einstein indicial notation were used. Using the compatibility equations, E_n and ε_{mn} can be related to electric potential, Φ and elastic displacement, u as

$$\varepsilon_{mn} = \frac{1}{2}\left(u_{m,n} + u_{n,m}\right) \tag{2-5}$$

$$E_n = -\Phi_{,n}. \tag{2-6}$$

In a 3-dimensional space, Eqs. (2-1)-(2-6) describe a set of 22 equations with 22 unknowns σ_{ij}, ε_{mn}, u_i, D_i, E_i and Φ. Using a notation first introduced by Barnett and Lothe [206], Eqs. (2-1)-(2-6) can be unified to a single shorthand equation, namely,

$$\Sigma_{iJ} = E_{iJMn} Z_{Mn} \tag{2-7}$$

in which the stress–electric displacement Σ_{iJ} is represented by

$$\Sigma_{iJ} = \begin{cases} \sigma_{ij} & J = 1,2,3 \\ D_i & J = 4 \end{cases} \tag{2-8}$$

and the electroelastic moduli are defined as

$$E_{iJMn} = \begin{cases} C_{ijmn} & J = 1,2,3; \quad M = 1,2,3 \\ e_{nij} & J = 1,2,3; \quad M = 4 \\ e_{imn} & J = 4; \quad M = 1,2,3 \\ -\kappa_{in} & J = 4; \quad M = 4 \end{cases} \tag{2-9}$$

similarly, the elastic-strain electric field Z_{Mn} is expressed as

$$Z_{Mn} = \begin{cases} \varepsilon_{mn} & M = 1,2,3 \\ -E_n & M = 4 \end{cases} \tag{2-10}$$

using Eqs. (2-3), (2-4) and (2-7), the equation of equilibrium can be obtained as

$$\left(E_{iJMn}U_{M,n}\right)_{,i} = 0. \tag{2-11}$$

Based on Eq. (2-9) the electroelastic moduli matrix can be written as [205]

$$\boldsymbol{E} = \begin{bmatrix} \underset{(6\times6)}{\boldsymbol{C}} & \underset{(6\times3)}{\boldsymbol{e'}} \\ \underset{(3\times6)}{\boldsymbol{e}} & \underset{(3\times3)}{-\boldsymbol{\kappa}} \end{bmatrix}. \tag{2-12}$$

By extracting $\boldsymbol{e}$ matrix from Eq. (2-12), the piezoelectric strain coefficient matrix ($\boldsymbol{d}$) can be calculated as

$$\boldsymbol{d^T} = \boldsymbol{C^{-1}e}. \tag{2-13}$$

Using the Voigt notations the Eq. (2-7) can be reformulated as a matrix equation where Z_{Mn} and Σ_{Mn} are 9×1 column vectors and E_{iJMn} is a 9×9 matrix. The mapping of the variables to the new notation is as follows:

$$\begin{array}{lll} (11) \rightarrow 1 & (22) \rightarrow 2 & (33) \rightarrow 3 \\ (23) \rightarrow 4 & (13) \rightarrow 5 & (12) \rightarrow 6 \\ (14) \rightarrow 7 & (24) \rightarrow 8 & (34) \rightarrow 9 \end{array} \tag{2-14}$$

2.2.2. Mean field micromechanics

A simple method for calculation of the effective mechanical and piezoelectric properties of a composite based on the geometry of the fillers is the use of mean field micromechanics. Typically, a mean field micromechanics formulations involve a concentration tensor, which relates the averaged fields in the separate phases (fibers or matrix) to the corresponding macroscopic fields.

2.2.2.1. The Mori-Tanaka method

A well-known mean field micromechanics method is the Mori-Tanaka approach [159]. It approximates the behavior of composites that contain reinforcements at non-dilute volume fractions via dilute inhomogeneities that are subjected to effective matrix fields rather than the macroscopic fields. For calculation of the overall properties of heterogeneous inclusions, the

properties and volume fraction of each phase are defined and put into a model proposed by Dunn and Taya [207]. For a two-phase composite material with electroelastic matrix, they proposed an effective electrostatic modulus (E_c), namely,

$$E_c = E_m + \phi_a(E_a - E_m)\lambda_a. \tag{2-15}$$

in which λ_a, ϕ_a, and E_a, are the concentration tensor, volume fraction and the electroelastic properties of the active phase, respectively. E_m represents the electroelastic properties of the matrix. The concentration tensor plays a critical role in the overall electromechanical properties of the composites. Mori and Tanaka suggested a simple relation for calculating λ_a from the dilute concentration tensor [27,207], defined as,

$$\lambda_a = \lambda_a^{dil}\left[(1-\phi_a)I + \phi_a\lambda_a^{dil}\right]^{-1}. \tag{2-16}$$

in which the dilute concentration tensor, λ_a^{dil} can be expressed as

$$\lambda_a^{dil} = [I + SE_m^{-1} + (E_a - E_m)]^{-1}. \tag{2-17}$$

where S denotes the Eshelby's tensor which is a function of Poisson ratio of the matrix and the inclusion morphology. Here we assume that for the case of piezoelectric nanowires, both can be generalized as ellipsoidal inclusions [24,208]. It should be noted that in Eq. (2-17), if inclusions of the active phase have different orientations in space, orientation averaging must be used to consider the effect of the inclusions' alignment on the effective elastic properties of composites. In this situation, $\langle\lambda_{\boldsymbol{a}}\rangle$ is used instead of λ_a in Eq. (2-17), where angle brackets $\langle°\rangle$ show an average over all possible orientations and we have [209]:

$$\langle\lambda_a\rangle = \frac{1}{4\pi}\int_{-\varphi_0}^{\varphi_0}\int_{-\theta_0}^{\theta_0}\lambda_a(\theta,\varphi)\times\sin\theta d\theta d\varphi, \tag{2-18}$$

where θ_0, and φ_0 are the range of angles for which the inclusions can orient themselves in space. The components of the fourth-order tensor λ_a in the local coordinate system ($\lambda_{a\,ijkl}$) are transformed to the global coordinate system ($\lambda_{a\,mnrs}$) by:

$$\lambda_{a\,ijkl} = Q_{im}Q_{jn}Q_{kr}Q_{ls}\lambda_{a\,mnrs}, \tag{2-19}$$

where $\boldsymbol{Q}$ is defined in terms of the Euler angles, (θ, φ) , as follow:

$$\boldsymbol{Q} = \begin{bmatrix} \cos\theta\cos\varphi & -\sin\varphi & \sin\theta\cos\varphi \\ \cos\theta\sin\varphi & \cos\varphi & \sin\theta\sin\varphi \\ -\sin\theta\cos\varphi & \sin\theta\sin\varphi & \cos\theta \end{bmatrix}. \tag{2-20}$$

Using the averaging method provided in Eq. (2-18), the Eshelby's tensor for a nanocomposite containing randomly oriented fillers can be calculated. Then by applying the Mori-Tanaka method (Eqs. (2-15) to (2-17)), the stiffness tensor of the composite ($\boldsymbol{E^c}$) can be estimated. $\boldsymbol{E^c}$ contains the main electromechanical coefficients of the composite such as structural stiffness, piezoelectric stress and dielectric constants, i.e.

$$\boldsymbol{E^c} = \begin{bmatrix} C_{11} & C_{12} & C_{13} & C_{14} & C_{15} & C_{16} & e_{11} & e_{21} & e_{31} \\ C_{12} & C_{22} & C_{23} & C_{24} & C_{25} & C_{26} & e_{12} & e_{22} & e_{32} \\ C_{13} & C_{23} & C_{33} & C_{34} & C_{35} & C_{36} & e_{13} & e_{23} & e_{33} \\ C_{14} & C_{24} & C_{34} & C_{44} & C_{45} & C_{46} & e_{14} & e_{24} & e_{34} \\ C_{15} & C_{25} & C_{35} & C_{45} & C_{55} & C_{56} & e_{15} & e_{25} & e_{35} \\ C_{16} & C_{26} & C_{36} & C_{46} & C_{56} & C_{66} & e_{16} & e_{26} & e_{36} \\ e_{11} & e_{12} & e_{13} & e_{14} & e_{15} & e_{16} & \kappa_{11} & 0 & 0 \\ e_{21} & e_{22} & e_{23} & e_{24} & e_{25} & e_{26} & 0 & \kappa_{22} & 0 \\ e_{31} & e_{32} & e_{33} & e_{34} & e_{35} & e_{36} & 0 & 0 & \kappa_{33} \end{bmatrix}. \tag{2-21}$$

where C_{ij}, e_{ij}, ε_{ii} are the coefficients of elastic moduli, piezoelectric stress coefficients and permittivity constants matrices, respectively. By considering the relation between piezoelectric strain coefficients ($\boldsymbol{d}$) and piezoelectric stress coefficients ($\boldsymbol{d} = \boldsymbol{C}^{-T}\boldsymbol{e}^{T}$), the g_{31} piezoelectric voltage coefficient can be calculated as

$$g_{31} = \frac{d_{31}}{\kappa_{33}}. \tag{2-22}$$

2.2.2.2. The Eshelby's tensor

The Eshelby's tensor is widely used in micromechanics models for calculation of bulk composite properties. It was first introduced by Eshelby [163] to calculate the strain and stress fields in a composite with ellipsoidal inclusion. Dunn and Taya [207] expanded the Eshelby's tensor for predicting the coupled behavior of piezoelectric composites. They created a set of constraint tensors that represent both stress and electric fields within the ellipsoidal inclusions

resulting from the restriction of the surrounding matrix. These tensors are expressed in four integral equations for which the closed form solutions have only been identified for the case of infinitely long aligned fibers [210], spheroidal inclusions [211], and polygons [212]. To calculate the constraint tensors of finite aspect ratio fibers, a method similar to Andrews, *et al*. [208] and Gavazzi *et al*. [213] was adopted for numerically calculating the Eshelby's tensor using Gaussian quadrature which discretizes the integrals into a weighted summation of a finite number of function values.

The 4th order piezoelectric Eshelby's tensor is given by the following 4 integral equations [207]:

$$S_{mnab} = \frac{1}{8\pi}\Big[C_{ijab}\int_{-1}^{1}\int_{0}^{2\pi}\big[G_{mjin}(z) + G_{njim}(z)\big]\,d\sigma\,d\psi - e_{iab}\int_{-1}^{1}\int_{0}^{2\pi}[G_{m4in}(z) + G_{n4im}(z)]\,d\sigma\,d\psi\Big], \tag{2-23a}$$

$$S_{mn4b} = \frac{1}{8\pi}\Big[e_{bij}\int_{-1}^{1}\int_{0}^{2\pi}\big[G_{mjin}(z) + G_{njim}(z)\big]\,d\sigma\,d\psi + k_{ib}\int_{-1}^{1}\int_{0}^{2\pi}[G_{m4in}(z) + G_{n4im}(z)]\,d\sigma\,d\psi\Big], \tag{2-23b}$$

$$S_{4nab} = \frac{1}{4\pi}\Big[C_{ijab}\int_{-1}^{1}\int_{0}^{2\pi}G_{4jin}(z)\,d\sigma\,d\psi - e_{iab}\int_{-1}^{1}\int_{0}^{2\pi}G_{44in}(z)\,d\sigma\,d\psi\Big], \tag{2-23c}$$

$$S_{4n4b} = \frac{1}{4\pi}\Big[e_{bij}\int_{-1}^{1}\int_{0}^{2\pi}G_{4jin}(z)\,d\sigma\,d\psi + k_{ib}\int_{-1}^{1}\int_{0}^{2\pi}G_{44in}(z)\,d\sigma\,d\psi\Big]. \tag{2-23d}$$

in which *m*, *n*, *a*, and *b* are indices, and $G_{MJin}(z)$ is given as

$$G_{MJin}(z) = z_i z_n K_{MJ}^{-1}(z), \tag{2-24}$$

where

$$K_{MJ} = z_i z_n E_{iMJn}, \tag{2-25}$$

and

$$z_1 = \frac{(1-\psi^2)^{\frac{1}{2}}\cos\sigma}{a_1}, \tag{2-26a}$$

$$z_2 = \frac{(1-\psi^2)^{\frac{1}{2}}\sin\sigma}{a_2}, \tag{2-26b}$$

$$z_3 = \frac{\sigma}{a_3}, \tag{2-26c}$$

Dunn and Taya [207] showed that the piezoelectric Eshelby's tensor has a solution (Eq. (2-23)) for infinitely long fibers, circular cylindrical inclusions and ribbon–like inclusions. For a two-dimensional elliptical inclusion (aspect ratio: $\alpha = {a_2}/{a_1}, a_3 \to \infty$) in a transversely isotropic matrix, the nonzero components of the *S* tensors are given by:

$$S_{1111} = \frac{\alpha}{2(\alpha+1)^2}\left[\frac{2C_{11}+C_{12}}{C_{11}} + 2(\alpha+1)\right], \tag{2-27a}$$

$$S_{1212} = S_{2121} = S_{1221} = S_{2112} = \frac{\alpha}{2(\alpha+1)^2}\left[\frac{\alpha^2+\alpha+1}{\alpha} - \left(\frac{C_{12}}{C_{11}}\right)\right], \tag{2-27b}$$

$$S_{1313} = S_{3131} = S_{1331} = S_{3113} = \frac{\alpha}{2(\alpha+1)}, \tag{2-27c}$$

$$S_{1122} = \frac{\alpha}{2(\alpha+1)^2}\left[\frac{(2\alpha+1)C_{12}-C_{11}}{C_{11}}\right], \tag{2-27d}$$

$$S_{1133} = \frac{C_{13}}{C_{11}}\frac{\alpha}{\alpha+1}, \tag{2-27e}$$

$$S_{1143} = \frac{e_{31}}{C_{11}}\frac{\alpha}{\alpha+1}, \tag{2-27f}$$

$$S_{2211} = \frac{\alpha}{2(\alpha+1)^2}\left[\frac{(\alpha+2)C_{12}-C_{11}}{C_{11}}\right], \tag{2-27g}$$

$$S_{2222} = \frac{\alpha}{2(\alpha+1)^2}\left[\frac{2C_{11}+C_{12}}{C_{11}} + \frac{\alpha+2}{\alpha}\right], \tag{2-27i}$$

$$S_{2323} = S_{3232} = S_{2332} = S_{3223} = \frac{1}{2(\alpha+1)}, \tag{2-27j}$$

$$S_{2233} = \frac{C_{13}}{C_{11}} \frac{1}{\alpha+1}, \tag{2-27k}$$

$$S_{2243} = \frac{e_{31}}{C_{11}} \frac{1}{\alpha+1}, \tag{2-27l}$$

$$S_{4141} = \frac{\alpha}{\alpha+1}, \tag{2-27m}$$

$$S_{4242} = \frac{1}{\alpha+1}. \tag{2-27n}$$

Hence, for a circular cylindrical inclusion ($\alpha = 1$), the nonzero components of the Eshelby's tensor reduce to

$$S_{1111} = S_{2222} = \frac{5C_{11}+C_{12}}{8C_{11}}, \tag{2-28a}$$

$$S_{1212} = S_{2121} = S_{1221} = S_{2112} = \frac{3C_{11}-C_{12}}{8C_{11}}, \tag{2-28b}$$

$$S_{1313} = S_{3131} = S_{1331} = S_{3113} = S_{2323} = S_{3232} = S_{2332} = S_{3223} = \frac{1}{4}, \tag{2-28c}$$

$$S_{1122} = S_{2211} = \frac{3C_{12}-C_{11}}{8C_{11}}, \tag{2-28d}$$

$$S_{1133} = S_{2233} = \frac{C_{13}}{2C_{11}}, \tag{2-28e}$$

$$S_{1143} = S_{2243} = \frac{e_{31}}{2C_{11}}, \tag{2-28f}$$

$$S_{4141} = S_{4242} = \frac{1}{2}. \tag{2-28g}$$

For a ribbon-like inclusion ($\alpha_2 \gg \alpha_1$), the nonzero components of the constraint tensors reduce to:

$$S_{1111} = \frac{3C_{11}+C_{12}}{2C_{11}}\alpha, \tag{2-29a}$$

$$S_{1212} = S_{2121} = S_{1221} = S_{2112} = \frac{1}{2} - \frac{C_{11}+C_{12}}{2C_{11}}\alpha, \tag{2-29b}$$

$$S_{1313} = S_{3131} = S_{1331} = S_{3113} = \frac{\alpha}{2}, \tag{2-29c}$$

$$S_{1122} = -\frac{C_{11}-C_{12}}{2C_{11}}\alpha, \tag{2-29d}$$

$$S_{1133} = \frac{C_{13}}{C_{11}}\alpha, \tag{2-29e}$$

$$S_{1143} = \frac{e_{31}}{C_{11}}\alpha, \tag{2-29f}$$

$$S_{2211} = \frac{2C_{12}-C_{11}}{2C_{11}}\alpha, \tag{2-29g}$$

$$S_{2222} = 1 - \frac{C_{11}-C_{12}}{2C_{11}}\alpha, \tag{2-29h}$$

$$S_{2323} = S_{3232} = S_{2332} = S_{3223} = \frac{1-\alpha}{2}, \tag{2-29i}$$

$$S_{2233} = \frac{C_{13}}{C_{11}}(1-\alpha), \tag{2-29j}$$

$$S_{2243} = \frac{e_{31}}{C_{11}}(1-\alpha), \tag{2-29k}$$

$$S_{4141} = \alpha, \tag{2-29l}$$

$$S_{4242} = 1 - \alpha. \tag{2-29m}$$

In the case of cylindrical inclusions with finite length (finite aspect ratio) the Eshelby's tensor (Eq. (2-23)) doesn't have an analytical solution and can only be solved numerically. First, using Gaussian quadrature, the integrals are discretized to summations, i.e.

$$\int_{-1}^{1} f(x')\,dx' = \sum_{i=1}^{n} A_i f(x'_i), \tag{2-30}$$

where *x* and *x'* are two general variables (dependent), i.e.

$$x' = \frac{b-a}{2}x + \frac{b+a}{2}, \tag{2-31}$$

therefore,

$$dx' = \frac{b-a}{2}\,dx. \tag{2-32}$$

The discretization of a general integral is given by

$$\frac{b-a}{2}\int_a^b f\left(\frac{b-a}{2}x + \frac{b+a}{2}\right)dx = \frac{b-a}{2}\sum_{i=1}^{n} A_i f\left(\frac{b-a}{2}x_i + \frac{b+a}{2}\right). \tag{2-33}$$

Using this method, the Eq. (2-23) can be written as

$$S_{mnab} = \frac{1}{8\pi}\Big[C_{ijab}\int_{-1}^{1}\int_{0}^{2\pi}\big[G_{mjin}(z) + G_{njim}(z)\big]\,d\sigma\,d\psi - e_{iab}\int_{-1}^{1}\int_{0}^{2\pi}[G_{m4in}(z) + G_{n4im}(z)]\,d\sigma\,d\psi\Big], \tag{2-23a}$$

$$S_{mn4b} = \frac{1}{8\pi}\Big[e_{bij}\int_{-1}^{1}\int_{0}^{2\pi}\big[G_{mjin}(z) + G_{njim}(z)\big]\,d\sigma\,d\psi + k_{ib}\int_{-1}^{1}\int_{0}^{2\pi}[G_{m4in}(z) + G_{n4im}(z)]\,d\sigma\,d\psi\Big], \tag{2-23b}$$

$$S_{4nab} = \frac{1}{4\pi}\Big[C_{ijab}\int_{-1}^{1}\int_{0}^{2\pi} G_{4jin}(z)\,d\sigma\,d\psi - e_{iab}\int_{-1}^{1}\int_{0}^{2\pi} G_{44in}(z)\,d\sigma\,d\psi\Big], \tag{2-23c}$$

$$S_{4n4b} = \frac{1}{4\pi}\Big[e_{bij}\int_{-1}^{1}\int_{0}^{2\pi} G_{4jin}(z)\,d\sigma\,d\psi + k_{ib}\int_{-1}^{1}\int_{0}^{2\pi} G_{44in}(z)\,d\sigma\,d\psi\Big]. \tag{2-23d}$$

where p, and q are the indices and P and Q are the number divisions for each integral. The discretization points used for the provided Gaussian quadrature are denoted as σ and ψ with their corresponding weights as W_σ and W_ψ. Table 2-1 show the list of divisions (n divisions) and weights for n = 2 to n = 16.

Table 2-1: Divisions and their corresponding weights for Gaussian quadrature procedure.

$n = 2$		$n = 4$		$n = 8$		$n = 16$	
$\pm x_i$	$W_{\sigma_q} or\ W_{\psi_p}$	$\pm x_i$	$W_{\sigma_q} or\ W_{\psi_p}$	$\pm x_i$	$W_{\sigma_q} or\ W_{\psi_p}$	$\pm x_i$	$W_{\sigma_q} or\ W_{\psi_p}$
0.5774	1.0000	0.3400	0.6521	0.1834	0.3627	0.0950	0.1895
		0.8611	0.3479	0.5255	0.3137	0.2816	0.1826
				0.7967	0.2224	0.4580	0.1692
				0.9603	0.1012	0.6179	0.1496
						0.7554	0.1246
						0.8656	0.0952
						0.9446	0.0623
						0.9894	0.0272

2.2.3. Simulation results

This section presents a case study for prediction of the electromechanical properties of a piezoelectric composite. In this study, a composite material containing aligned BTO nanowires incorporated in an infinite matrix medium made of PDMS is considered. The electrometrical properties of these materials are presented in Table 2-2 [214-217]. Once the Gaussian quadrature method is employed and the Eshelby's tensor (S) for piezoelectric inclusions with finite aspect ratio is calculated (Eq. (2-36)), it was incorporated into Eqs. (2-17) – (2-19). Then, the effective electromechanical coefficient of the composite (E_c) is calculated. After calculation of E_c, the piezoelectric strain coefficients can be easily calculated based on Eqs. (2-12) and (2-13).

Table 2-2: Material properties of the barium titanate nanowires, and PDMS. $S_0 = 10^{-12}$ m^2/N; $d_0 = 10^{-12}$ C/N; κ_0 = 8.85E-12 F/m; $\rho_0 = 10^3$ kg/m^3

	S_{11}/S_0	S_{12}/S_0	S_{13}/S_0	S_{33}/S_0	S_{44}/S_0	S_{66}/S_0	d_{31}/d_0	d_{33}/d_0	d_{15}/d_0	κ_{11}/κ_0	κ_{33}/κ_0	ρ/ρ_0
BTO	7.38	-1.39	-4.41	13.1	16.4	7.46	-33.72	93.95	560.7	1450	1450	6.03
PDMS	4.88E5	-1.2E5	-1.2E5	4.88E5	6.10E5	6.10E5	0.0	0.0	0.0	2.4	2.4	0.97

The resulting effective piezoelectric strain coefficients (d_{33} and d_{31}) of the active nanocomposite are plotted in Figures (2-1a) and (2-1b), respectively, with reference to the various volume fractions and aspect ratio (AR) of the nanowires. It should be noted that these figures depict the normalized value of the coefficients. All values in Figure 2-1 are normalized with respect to the piezoelectric strain coefficients of the bulk BTO material. For example, a value of 0.5 in Figure 2-1a correspond to $d_{33} = 0.5 \times 93.95$ pC/N = 46.98 pC/N (Table 2-2). Figure 2-1 emphasizes the effects of nanowires aspect ratio. For example, it shows that for a nanocomposite with aligned BTO nanowires and AR = 40, the piezoelectric strain coefficient of the nanocomposite is only slightly less than a similar nanocomposite with continuous fibers (AR $\rightarrow \infty$). This fact is very important because it shows that for having a highly efficient nanocomposite energy harvester with high piezoelectric strain coefficients, there is no need for fabrication of fiber-like inclusions rather nanowire-shape inclusions with AR $\approx$ 40 suffice. It also shows that at AR $\leq$ 20, an increase in aspect ratio results in a significant improvement in both d_{33} and d_{31}. Namely, at V_f = 0.4, a nanocomposite with AR = 10 has more than 15 times higher piezoelectric strain coefficient compared to that of a nanocomposite with AR = 1. This fact is crucial because it is well known that the maximum V_f possible for a spherical particle or a cylindrical inclusion with AR = 1 is 0.74, and 0.78, respectively. Therefore, according to Figure 2-1, the maximum theoretically attainable piezoelectric strain coefficient for these particles is only about 10% of the bulk material value.

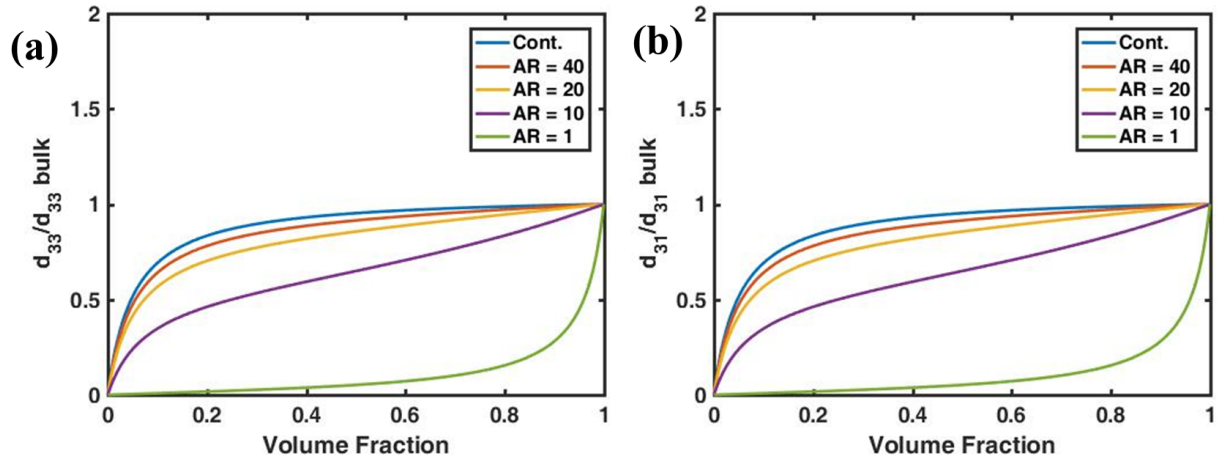

Figure 2-1: Simulated piezoelectric strain coefficient of a nanocomposite made of active BTO nanowires and PDMS matrix. (a) d_{33} and (b) d_{31} coefficients are normalized with respect to piezoelectric strain coefficients of the bulk BTO material.

By calculating the piezoelectric coupling coefficient (k_{ij}) using Eq. (1-15), the effect of aspect ratio on both k_{31} and k_{33} can be observed. Figure 2-2 shows the normalized value of these coefficients with respect to the bulk piezoelectric coupling coefficients of BTO. These figures further highlight the importance of aspect ratio. It shows that compared to d_{ij}, the increase in k_{ij} coefficients due to aspect ratio occurs at lower volume fractions. For example, at $V_f = 0.1$, the k_{33} and k_{31} of a piezoelectric nanocomposite with AR = 10 is 15.3 and 10.1, times higher than that of a nanocomposite with AR = 1, respectively.

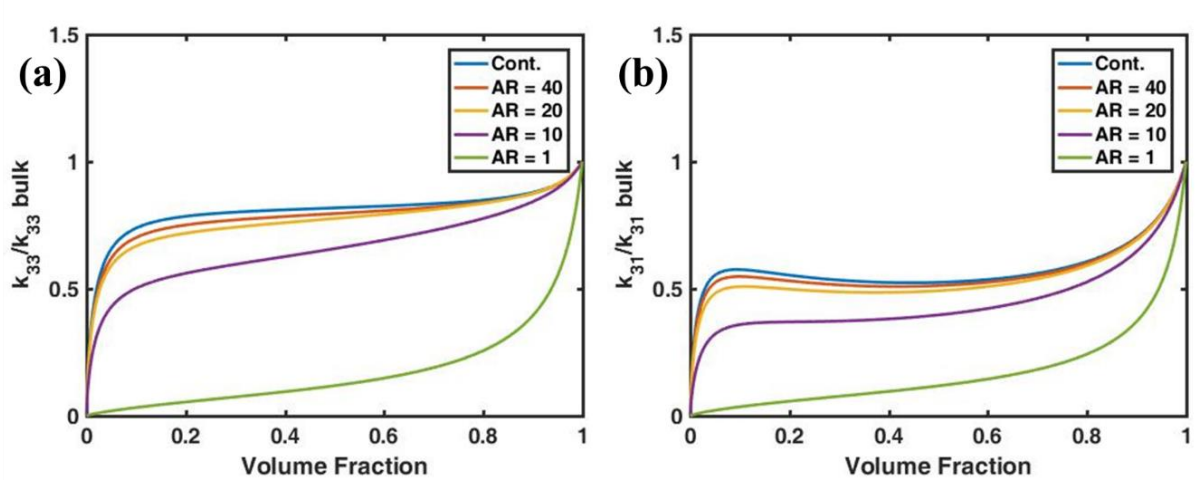

Figure 2-2: Simulated piezoelectric coupling coefficient of a nanocomposite made of active BTO nanowires and PDMS matrix. (a) k_{33} and (b) k_{31} coefficients are normalized with respect to piezoelectric coupling coefficients of the bulk BTO material.

The d_{ij} coefficient, relates the induced polarization to the applied stress in the material and therefore specifies the performance of the material as a sensor or energy harvester. The k_{ij} coefficient defines the ratio of the energy that is transferred between the mechanical and electrical domains in a loading cycle. This parameter can provides a relative "efficiency" for the material. Both of these coefficients are heavily affected by aspect ratio, therefore to fabricate a high performance and efficient piezoelectric energy harvester, high aspect ratio nanowires are desirable.

By comparing Figures 2-1 and 2-2, it is evident that although the normalized values of d_{33} and d_{31} are very similar, the normalized values of k_{33} and k_{31} are not. Figure 2-2 shows that k_{31} coefficient exhibit a local maxima for all aspect ratios except for AR = 1. This fact be explained by the definition of normalized k_{31} and k_{33}, namely,

$$\widehat{k_{31}} = \frac{\widehat{d_{31}}}{\widehat{\kappa_{33}}}\sqrt{\widehat{C_{11}}} \tag{2-35a}$$

$$\widehat{k_{33}} = \frac{\widehat{d_{33}}}{\widehat{\kappa_{33}}}\sqrt{\widehat{C_{33}}} \tag{2-35b}$$

in which the normalized values are denoted with the hat operator "^". According to Figure 2-1, the normalized values of d_{33} and d_{31} ($\widehat{d_{33}}$and $\widehat{d_{31}}$) are identical. Therefore, by comparing Eqs. (2-35a) and (2-35b), it is evident that the only difference is in the values of $\widehat{C_{33}}$ and $\widehat{C_{31}}$. According to

Figure 2-3, the normalized C_{33} coefficient is significantly higher than that of C_{11}, resulting in higher normalized k_{33} values compared to that of k_{31}.

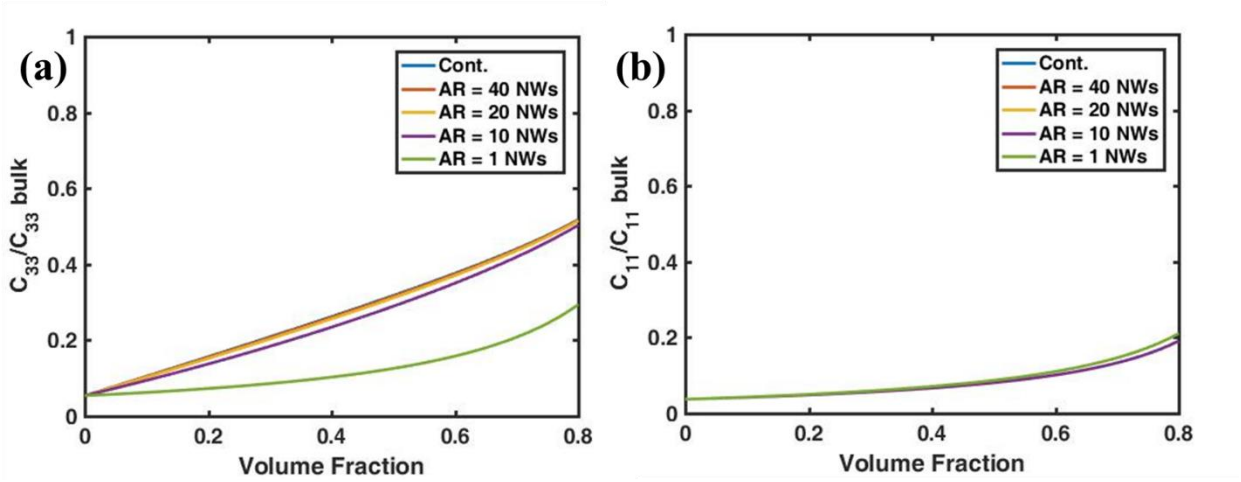

Figure 2-3: Simulated stiffness coefficient of a nanocomposite made of active BTO nanowires and PDMS matrix. (a) C_{33} and (b) C_{31} coefficients are normalized with respect to stiffness coefficients of the bulk BTO material.

In the next section, the results presented in section 2.2.3 are validated through finite element modeling (FEM). In chapter 3, after discussing the fabrication process for developing a piezoelectric composite energy harvester with control inclusion alignment, the results of both micromechanics and FEM is validated through experimental data.

2.3. Finite element modeling (FEM)

The finite element method (FEM) is considered as a versatile tool for the modeling and simulation of a wide range of engineering problems. Computational limitations and modeling complexities of the FEM impose limits on the maximum number of elements, which are used for introducing the geometries in the model. In this way, composite material simulations are limited to modeling only a small section of the system. In order to implement a numerical method, a representative modeling volume from the real medium is required. Based on the literature, two sets of modeling volumes have been studied and implemented, namely representative volume element (RVE) and repeating unit cell (RUC). However, sometimes these two methods are used interchangeably.

The RUC method is suitable for modeling crystalline materials, such as those found in molecular dynamics simulations, and modeling regularly distributed particles in a heterogeneous media. Based on the RUC definition, if a particle in the medium is cut by a boundary face in the model, the remaining volume of that particle must continue from the opposite side (Figure 2-4). This feature is referred to as the Constraint of Periodicity (CoP). The CoP must be implemented to guarantee the regeneration of the entire composite before deformation by regular arrangement of RUCs [218-220]. Furthermore, the FEM simulation should result in deformed RUCs which cover the entire medium without any gap or overlap between the particles. By applying proper constraints on the boundaries, such repeatability of the deformed medium can be guaranteed. These constraints are usually called periodic boundary conditions (PBCs). Together, the CoP and PBCs guarantee the periodicity of the system before and after deformation, respectively.

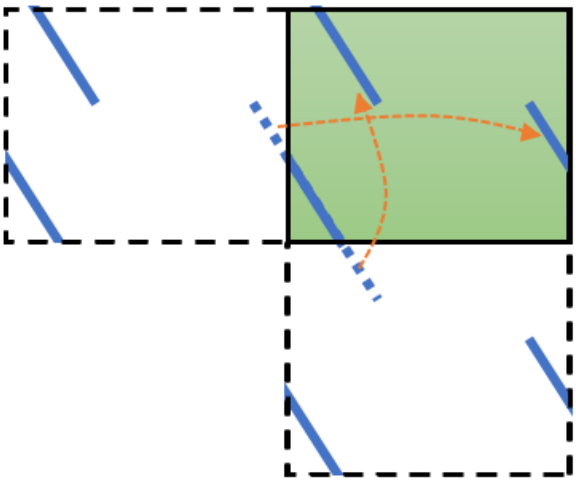

Figure 2-4: A sample RUC with a constraint of periodicity satisfied.

On the other hand, the concept of RVE is suitable for modeling a piezoelectric composite with randomly oriented inclusions. In this case, a few options is available for designing the RVE since for this kind of composites a unique RVE geometry does not exist. Therefore, it is expected that each choice of RVE lead to slightly different results. Intuitively, increasing the size of RVE and the number of inclusions in it, result in more statistically identical modeling volumes which consequently result in less disagreement between the results. However, the size of RVE cannot be increased freely due to limited computational memory and time [221]. As a solution, researchers have developed a concept called repeating RVE (RRVE) which is used for modeling a

heterogeneous media while imposing the periodic boundary conditions on the RVEs. This concept can help reduce the size of RVE and thus, reduce the size effects, and the computational time and power required for the calculations [222].

A well-known approach for calculation of effective electromechanical coefficients of a piezoelectric composite using FEM is through energy approach. The total elastic strain energy, U_s, of any geometry (RRVE) can be calculated as

$$U_s = \frac{1}{2} V \bar{C}_{ijkl} \bar{\varepsilon}_{ij} \bar{\varepsilon}_{kl}, \tag{2-36}$$

where V is the total volume and $\bar{C}_{ijkl}$, $\bar{\varepsilon}_{ij}$ are the equivalent stiffness, and mechanical strain tensors within the RRVE. Similarly, by treating the RRVE as a capacitor, the total electric energy stored in the piezoelectric composite is given by

$$U_e = \frac{1}{2} V \bar{\kappa} E^2, \tag{2-37}$$

where $\bar{\kappa}$, and E are the equivalent dielectric constant and electric field in the material. The effective piezoelectric strain coefficient ($\bar{d}_{nij}$) can be determined from the following stress-free equation:

$$\bar{\varepsilon}_{ij} = \bar{d}_{nij} E_{n.} \tag{2-38}$$

In the next section, the details of RVE/RUC generation for modeling of a piezoelectric composite with aligned and randomly oriented inclusions are presented. Then, using Eqs. (2-36) – (2-38), the result of FEM performed in COMSOL Multiphysics software is studied. This software was chosen for FEM analysis due to the following advantages: (1) easy, seamless interface between different physics fields such as structural mechanics, electrostatic and piezoelectric fields; (2) ability to modify the governing equations, and (3) flexibility in solver selection using direct, iterative, or mixed solvers, and segregated or fully-coupled solutions. Moreover, due to the multiphysics nature of this software, it allows for more sophisticated calculations by adding more physical modules to the program, such as the microelectromechanical (MEMS) module which can be used for more accurate modeling of piezoelectric nanocomposite energy harvesters.

2.3.1. Aligned inclusions

To model a piezoelectric composite with aligned fillers, a body centered cubic lattice RRVE is considered (Figure 2-5a). This geometry can be systematically configured to account for various inclusion aspect ratios and volume fractions. Poizat *et al.* proved that a body centered cubic lattice structure can simulate piezoelectric strain coefficients for a large range of aspect ratios accurately, whereas a simple cubic lattice structure is only reliable for aspect ratios above 1000 [223]. It should be noted that body centered cubic structure is normally referred to a geometry where a sphere is in the middle of the lattice cell. However, here we are referring to the relative geometrical placements of the short inclusions' centers. The design of this RRVE allows for repeating geometry of the inclusions in all *x*, *y*, and *z* directions. Figure 2-5 depicts an RRVE with AR = 10. Inclusions are aligned in poling direction (3-direction). For adjusting the aspect ratio, the RRVE was simulated with inclusions of the same radius and different lengths accordingly.

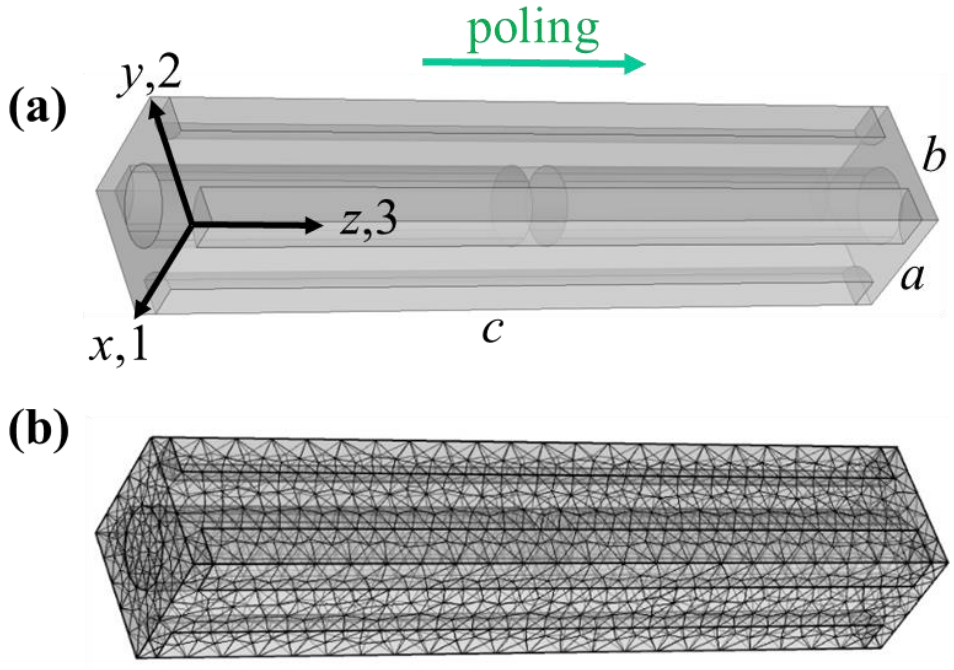

Figure 2-5: (a) Body centered cubic lattice structure with AR = 10 inclusions which allows for geometrical repetition of the RRVE in all there axes. (b) Meshed RRVE with tetrahedron elements.

Modeling of the RRVE in COMSOL is accomplished using the boundary conditions listed in Table 2-3. This table lists all mechanical and electrical boundary conditions for calculating various

coefficients such as the elements of stiffness matrix, and piezoelectric strain and coupling coefficients are given (φ, and ε° represent the voltage and strain on the walls of RRVE). After applying the appropriate boundary conditions, the RRVE was meshed with tetrahedron elements with 4 nodes (Figure 2-5b) with each node having three spatial, and one electrical potential degrees of freedom.

Table 2-3: Mechanical and electrical boundary conditions for calculation of effective stiffness matrix and piezoelectric strain and coupling coefficients.

Parameter	Mechanical boundary conditions	Electrical boundary conditions
C_{11}	$u_1\,(x = 0) = 0$	$\varphi = 0$
	$u_1\,(x = a) = \varepsilon°$	
C_{33}	$u_3\,(z = 0) = 0$	$\varphi = 0$
	$u_3\,(z = c) = \varepsilon°$	
C_{23}	$u_2\,(y = 0) = 0$	$\varphi = 0$
	$u_2\,(y = b) = \varepsilon°$	
	$u_3\,(z = 0) = 0$	
	$u_3\,(z = c) = \varepsilon°$	
C_{12}	$u_1\,(x = 0) = 0$	$\varphi = 0$
	$u_1\,(x = a) = \varepsilon°$	
	$u_2\,(y = 0) = 0$	
	$u_2\,(y = b) = \varepsilon°$	
C_{44}	$u_1\,(y = 0) = 0$	$\varphi = 0$
	$u_2\,(y = 0) = 0$	
	$u_3\,(y = 0) = 0$	
	$u_3\,(y = b) = \varepsilon°$	
C_{66}	$u_1\,(x = 0) = 0$	$\varphi = 0$
	$u_2\,(x = 0) = 0$	
	$u_3\,(x = 0) = 0$	
	$u_2\,(x = a) = \varepsilon°$	
d_{31}	$u_1\,(x = 0) = 0$	$\varphi\,(z = 0) = 0$
		$\varphi\,(z = c) = \varphi°$
d_{33}	$u_3\,(z = 0) = 0$	$\varphi\,(z = 0) = 0$
		$\varphi\,(z = c) = \varphi°$
k_{11}	$u_1\,(x = 0) = 0$	$\varphi\,(x = 0) = 0$
		$\varphi\,(x = a) = \varphi°$
k_{33}	$u_3\,(z = 0) = 0$	$\varphi\,(z = 0) = 0$
		$\varphi\,(z = c) = \varphi°$

Figures 2-6a and 2-6b show the potential and vertical displacement fields within the RRVE, respectively. In this simulation which was used to calculate the effective d_{33} coefficient, periodic electrical and mechanical boundary conditions on the walls of the RVE were assumed. The bottom end of the RRVE ($z = 0$) was assumed to have zero displacement and be electrically grounded ($\varphi = 0$) while free boundary condition with a uniform potential ($\varphi = 1$ V) was considered for the top side ($z = c$). Because the calculations assume the RRVE is poled downward, a uniform potential at $z = c$ resulted in contraction of the RRVE due to the piezoelectricity of the inclusions (Figure2-6b). By finding the ratio of maximum displacement of the top side to the applied voltage ($\varphi = 1$ V), the piezoelectric strain coefficient, d_{33}, can be calculated. All other coefficients were calculated similarly, by imposing the appropriate boundary condition listed in Table 2-3.

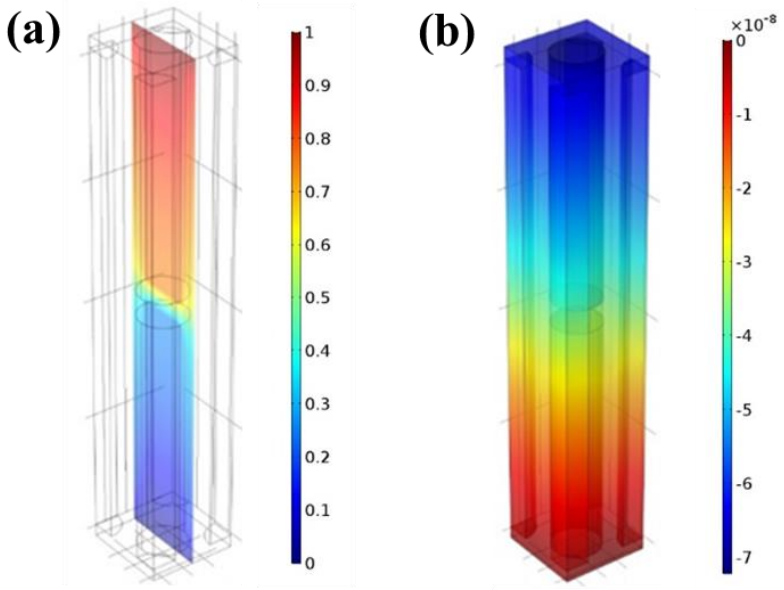

Figure 2-6: FEM results for calculation of d_{33} coefficient. (a) Voltage distribution along the RRVE ($y = b/2$ plane). (b) Vertical displacement distribution in the RRVE.

Figures 2-7 shows the result of FEM analysis along with the micromechanics results presented in 2.2.3. It shows that the two models agree well and the results are reliable. The FEM was only implemented on volume fractions bellow 0.4 due to geometrical limitations of the RRVE. In section 2.3.2, a novel approach for modeling of a piezoelectric composite with randomly oriented inclusions is provided.

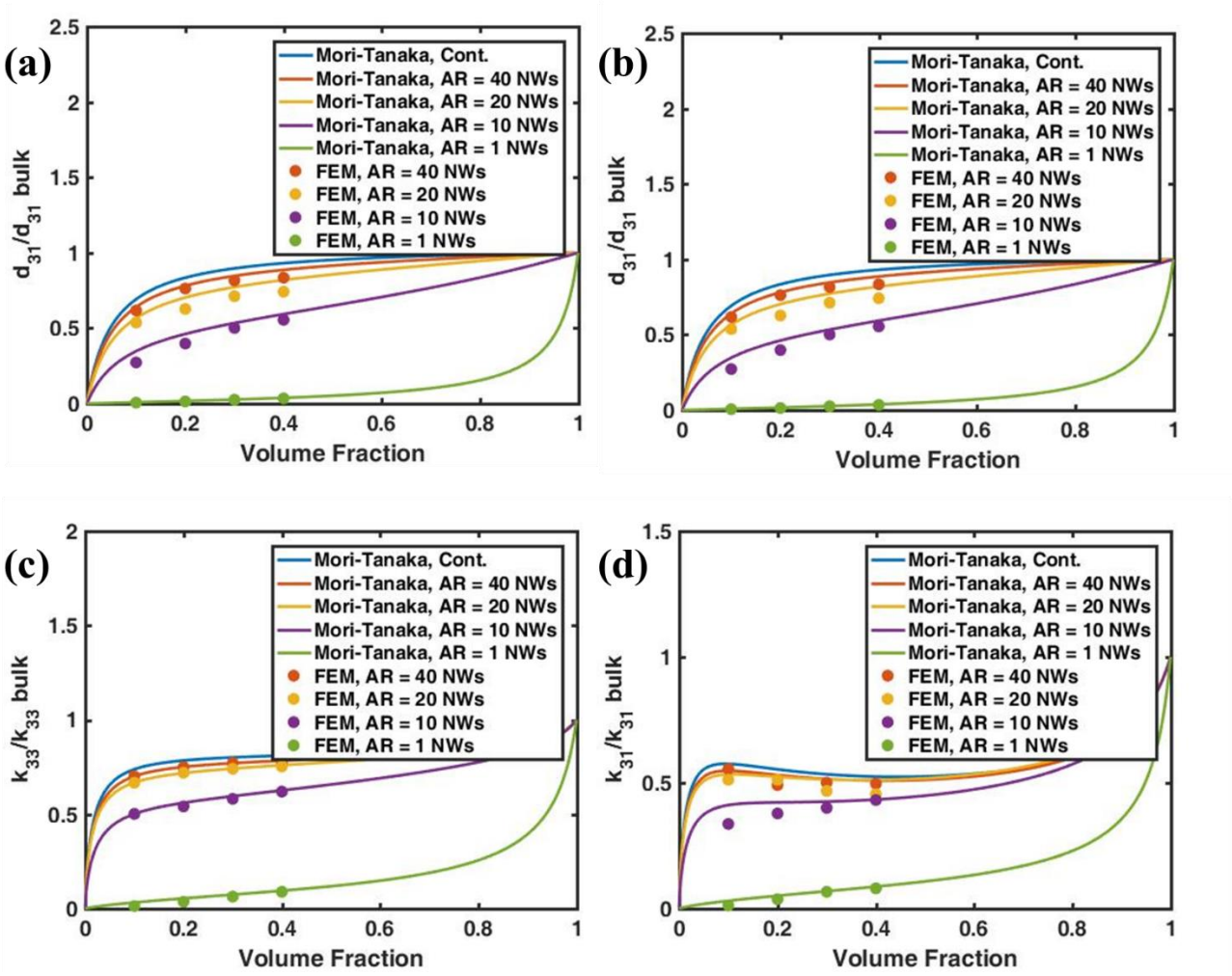

Figure 2-7: Simulated results of Mori-Tanaka approach and FEM. (a) d_{33}, (b) d_{31} (c) k_{33}, and (d) k_{31} coefficients are normalized with respect to piezoelectric coefficients of the bulk BTO material.

2.3.2. Randomly oriented inclusions

In this section, FEM is implemented to calculate the electromechanical properties of RRVEs with randomly distributed and oriented inclusions. The size of the RRVE is adjusted based on the geometry, volume fractions and number of perfect particles inside the RRVE. To accurately create the desired volume concentration of fillers inside the RRVE, it is constructed in a way to satisfy the periodicity criterion. To accurately model a RRVE with randomly oriented inclusions, a relatively large geometry that includes many inclusions is needed. However, since naturally it is not possible for two inclusions to have spatial overlap, a method is needed to generate randomly oriented inclusions with none having any intersection with others. For that, a procedure called

random sequential adsorption (RSA) is used to guarantee the generation of nonintersecting inclusions [224].

2.3.2.1. Generation of the RRVEs using RSA method

The RSA method [22,224] has been widely used for the study of composite materials with different shapes of active phases such as cylindrical [225-227], spherical [225,228], ellipsoidal [228], and sphero-cylindrical [225] shapes. Here, the RSA method is used to generate the geometry of an RRVE containing non-intersecting cylinders. In 3D space, a cylinder can be uniquely defined by its length, l, radius, a, its center of mass coordinate $\boldsymbol{C}$ and two Euler's angles, γ and θ, which define its axis orientation (Figure 2-8a). The RSA method for generating randomly distributed fibers in an RVE consists of adding fibers in a cube sequentially by choosing a random $\boldsymbol{C}$ vector and γ and θ angles based on a fiber orientation distribution function (ODF), $f(\gamma, \theta)$. In this method, l and a can be randomly selected according to a distribution function as well. Physically, the fibers in an RVE cannot intersect and therefore, any spatial overlap between the newly generated fiber and previously placed fibers is not allowed by the RSA method. To prevent stress concentrations between any two neighboring fibers, a minimum distance of $d_{min} = 0.1r$ is defined to disregard any new fiber that is closer than d_{min} to a neighboring fiber. If the newly generated fiber satisfies the non-overlapping and minimum distance conditions, it is added to the RVE and the volume fraction is increased accordingly. This process is continued until a predefined number of cycles or volume fraction ($V_{f\text{-}max}$) is reached. This process is summarized in the flow chart depicted in Figure 2-8b.

It is worth mentioning that the computational time for this process grows rapidly as the number of fibers or their aspect ratio is increased. Finally, when the desired volume fraction is reached the $\boldsymbol{C}$ coordinates and Euler angles of each fiber are stored and exported to COMSOL Multiphysics for FEM analysis. To simulate RVEs with a reduced volume fraction (i.e. $V'_f < V_{f-max}$), the RVE's dimensions and $\boldsymbol{C}$ coordinates of its fibers are expanded (Figure 2-8c) while preserving the orientation of the fibers, resulting in a smaller volume fraction. The RVE volume is increased without reorientation of the fillers and the properties of the new fibers can be expressed as

$$\boldsymbol{C'} = \boldsymbol{C}\left(\sqrt[3]{\frac{V_{f-max}}{V'_f}}\right), \gamma' = \gamma, \text{ and } \theta' = \theta. \tag{2-39}$$

where *C'*, *γ'*, and *θ'* are the center of mass vector, and axis orientation angles of the RVE with reduced volume fraction, respectively.

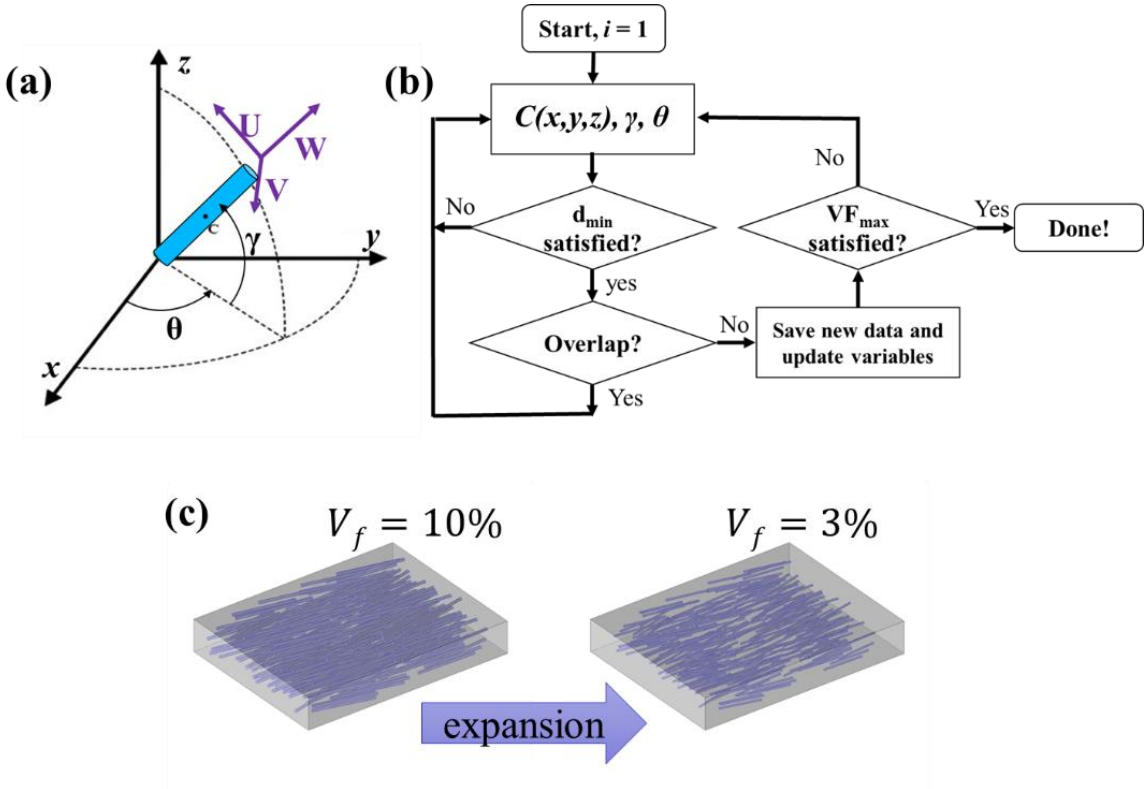

Figure 2-8: (a) A cylinder in 3D space can be uniquely defined by the position of its center of mass and two Euler angles (b) Flow chart of the RSA procedure. (c) The expansion of RVE in order to decrease the volume fraction. By increasing the length of the ***C*** vector according to Eq. (2-39), an RRVE with lower volume fraction and similar orientation of fibers is obtained.

2.3.2.2. Conditions for non-overlapping fibers

Checking against the overlap of two random cylindrical fibers in an RRVE is a complicated and computationally expensive task [229]. Here, the projection method [230] was used to disregard intersecting fibers. In this method, the idea is that any two convex objects have no intersection if there exists a line for which the intervals of the projection of the two objects onto that line do not overlap. Therefore, if a line is found in which the projection of the two convex objects on to the line intersect, then the two objects intersect (Figure 2-9).

If such a line can be found, it is called a separating axis. It can be shown that linear translation of a separating axis is also a separating axis [230]. Therefore, for simplicity it is sufficient to only consider the lines passing through the origin. The sufficient condition for non-overlapping fibers is the existence of a separating axis out of all possible 3D directions which form a unit sphere centered at the origin. To find this axis, it is computationally more efficient to start from some known directions which are described in the section 2.3.2.3.

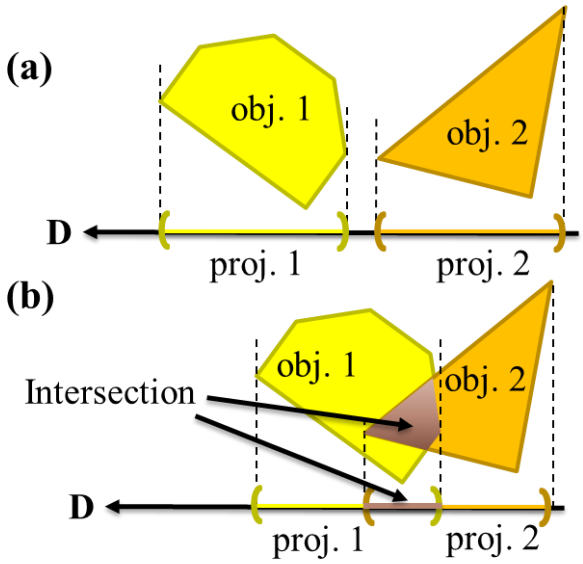

Figure 2-9: Schematic of the projection method. (a) Two non-intersecting objects with non-intersecting projections on to the line **D**. (b) Two intersecting objects with intersecting projections on to the line **D**.

2.3.2.3. Separating axis

To find a separating axis, the cylindrical inclusions have to be uniquely defined in 3D space. Any point $\boldsymbol{X_i}$ on the surface of the cylinder i can be expressed by two dummy variables such as t and α, namely,

$$\boldsymbol{X_i}(\alpha, t) = \boldsymbol{C_i} + (a\cos\alpha)\boldsymbol{U_i} + (a\sin\alpha)\boldsymbol{V_i} + t\boldsymbol{W_i}, \quad \alpha\epsilon[0,2\pi), |t| \leq \frac{l}{2}, i = 1,2 \qquad (2\text{-}40)$$

in which a, l, and $\boldsymbol{W_i}$ are radius, length and the unit vector representing the axis of cylinder i, respectively. $\boldsymbol{U_i}$ and $\boldsymbol{V_i}$ are any two-unit vectors that satisfy $\boldsymbol{W_i} = \boldsymbol{U_i} \times \boldsymbol{V_i}$ (Figure 2-8a). The projection of any point on the surface of a cylinder, Eq. (2-40), on a line $\boldsymbol{D}$ is given by

$$\lambda_i(\alpha, t) = \boldsymbol{D}.\boldsymbol{X_i}(\alpha, t)_i = \boldsymbol{D}.\boldsymbol{C_i} + (a\cos\alpha)\boldsymbol{D}.\boldsymbol{U_i} + (a\sin\alpha)\boldsymbol{D}.\boldsymbol{V_i} + t\boldsymbol{D}.\boldsymbol{W_i} \quad (2\text{-}41)$$

the maximum value of λ_i is given by

$$\lambda_{i(max)}(\boldsymbol{D}) = \boldsymbol{D}.\boldsymbol{C_i} + a\sqrt{|\boldsymbol{D}|^2 - (\boldsymbol{D}.\boldsymbol{W_i})^2} + l/2|\boldsymbol{D}.\boldsymbol{W_i}|. \quad (2\text{-}42)$$

Similarly, the minimum value of λ_i is given by

$$\lambda_{i(min)}(\boldsymbol{D}) = \boldsymbol{D}.\boldsymbol{C_i} - a\sqrt{|\boldsymbol{D}|^2 - (\boldsymbol{D}.\boldsymbol{W_i})^2} - l/2|\boldsymbol{D}.\boldsymbol{W_i}|. \quad (2\text{-}43)$$

Therefore, the projection of cylinder *i* onto line $\boldsymbol{D}$ is the following interval

$$I_i = \left[\lambda_{i(min)}(\boldsymbol{D}) - \lambda_{i(max)}(\boldsymbol{D})\right], \quad i = 1, 2. \quad (2\text{-}44)$$

This shows that if the projection interval of the two cylinders (I_1 and I_2) do not intersect, the corresponding two cylinders do not overlap. To check for separation of the two cylinders represented by sets of ($\boldsymbol{W_1}$, $\boldsymbol{C_1}$) and ($\boldsymbol{W_2}$, $\boldsymbol{C_2}$), first the axes of the two cylinders and their mutual perpendicular direction ($\boldsymbol{W_1}$, $\boldsymbol{W_2}$, and $\boldsymbol{W_1} \times \boldsymbol{W_2}$) are checked. If none of those directions satisfy the non-intersecting criteria, all other perpendicular directions to $\boldsymbol{W_1}$ or $\boldsymbol{W_2}$ are checked (these directions form a unit circle around each cylinder). Finally, if no separating axis between the two cylinders is found, inspection continues for any separation vector that lies between $\boldsymbol{W_i}$ (i = 1, 2) and its corresponding unit circle around $\boldsymbol{W_i}$.

Using the method described in section 2.3.2.1 various RVEs with different volume fractions, aspect ratio, and degree of alignment can be generated. Figure 2-10 shows a typical RVE generated based on the as-described RSA method. This RVE consist of 150 fibers with aspect ratio AR = 10 and volume fraction of 10%. These fibers have a radius of a = 1 and length of l = 20 (arbitrary units) which are distributed randomly across the volume of RVE. The in-plane and out-of-plane angle of the axis of these fibers are chosen randomly in the $0 < \theta \leq 2\pi$ and $-\pi/12 < \gamma \leq \pi/12$ ranges, respectively. It is worth mentioning that for the case of a printed nanocomposite, an RVE with $\theta = \gamma = 0$ was used to simulate aligned fibers. Similarly, for fully randomly oriented nanowires composites, $0 < \theta \leq 2\pi$ and $-\pi/2 < \gamma \leq \pi/2$ were chosen as these encompass all possible orientation of nanowires in 3D.

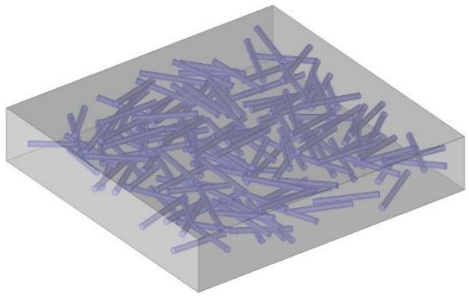

Figure 2-10: A typical RRVE generated using RSA method consisting of 150 random, non-overlapping fibers with AR = 10.

2.3.2.4. The effect of misalignment

In this section, the effects of misalignment of the inclusions is studied. For that, using the methods described in sections 2.3.2.1 and 2.3.2.2 a variety of RRVEs with varying amount in-planar misalignment (θ) was generated. According to Figure 2-11, for θ = 0 all inclusions are aligned in 3-direction, and for θ = 15 the inclusions are randomly oriented in the RRVE with the maximum in-plane misalignment of up to 15°. Similarly, for θ = 30 although each individual inclusion was oriented randomly, the maximum allowable misalignment was set to 30°.

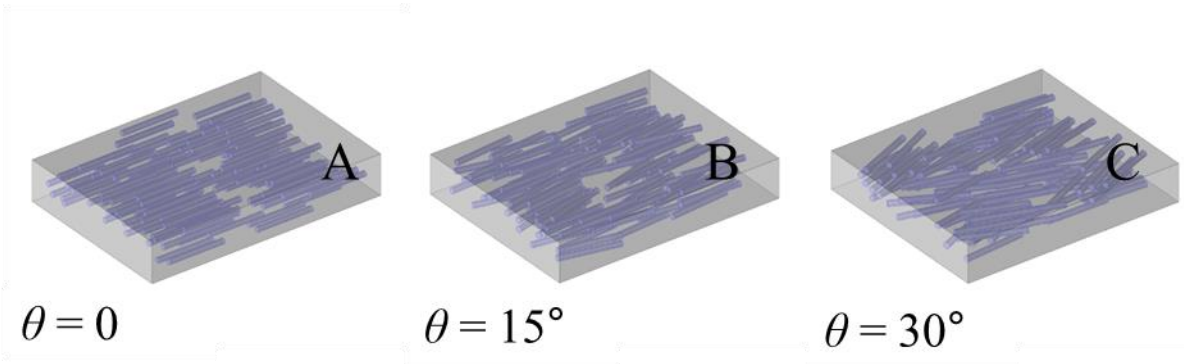

Figure 2-11: Three RRVEs with different amount of maximum allowable misalignment for their inclusions.

Using the same boundary conditions that was given in Table 2-3, the effective piezoelectric strain coefficients for various weight fractions and aspect ratios are calculated (Figure 2-12). It shows that as expected the piezoelectric strain coefficient increase rapidly with volume fraction and aspect ratio, however, the maximum values does not correspond to aligned inclusions (θ = 0°).

Rather depending on the volume fraction and aspect ratio the maximum d_{33} or d_{31} correspond to $15° \leq \theta \leq 20°$. This fact can be explained by considering that increase in misalignment (θ) leads to more compliant RRVE and therefore an increase in the apparent d_{33} or d_{31} coefficient of the composite. By comparing the RRVEs provided in Figure 2-11, it is evident that the nanocomposites with $\theta = 15°$ and $\theta = 30°$ have significantly higher compliance compared to that of the nanocomposite with $\theta = 0°$. It is because the inclusions (BTO) have much higher stiffness than the polymer matrix, and when they are aligned in the direction of applied force in horizontal direction, they resist deformation more than those of $\theta = 15°$ and $\theta = 30°$.

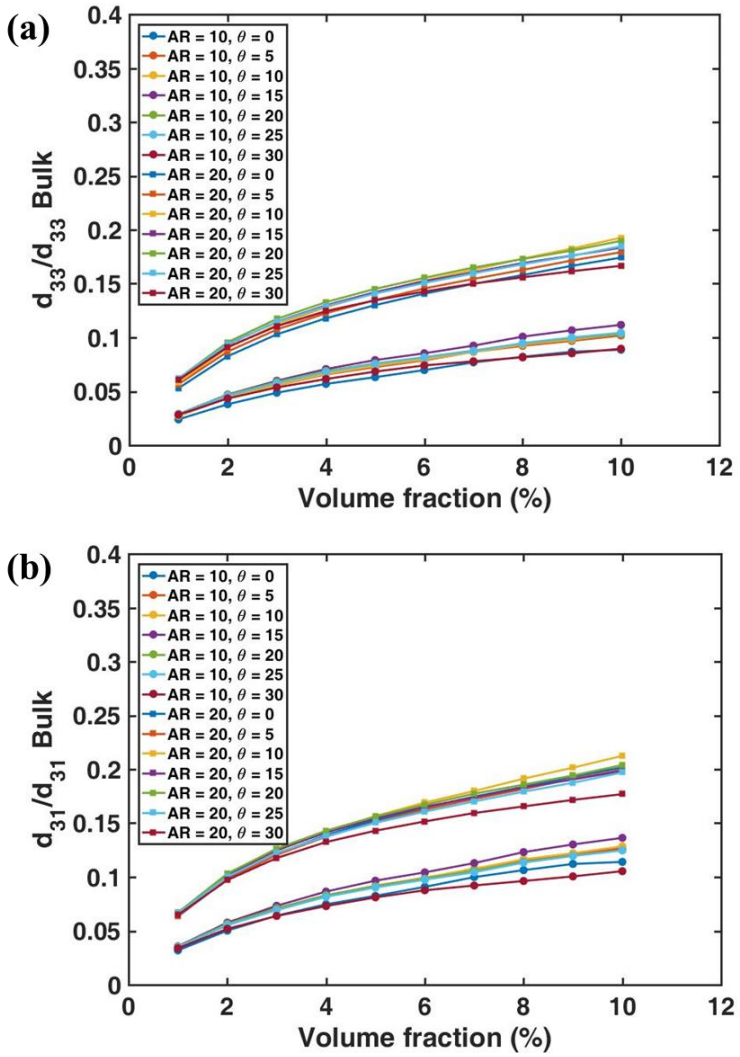

Figure 2-12: The effect of misalignment on the normalized d_{33} coefficient.

This fact can be further demonstrated by considering two identical RRVEs as shown in Figure 2-11; A (θ = 0°), and B (θ = 15°) with similar inclusion geometric features (AR = 10, V_f = 10%), and electromechanical properties and matrix Young's moduli $E_{m,A}$ and $E_{m,B}$, respectively. Based on the FEM results (Figure 2-12), if $E_{m,A} = E_{m,B}$ then the d_{31} and d_{33} coefficients of the nanocomposite B are 20% and 26% higher than that of nanocomposite A, respectively. However, if $E_{m,B} = 1.42\ E_{m,A}$ condition was set in the models then the two nanocomposite will have equal overall Young's modulus and d_{31} and d_{33} coefficients of the nanocomposite A will be 11% and 13% higher than that of nanocomposite B. The effects of inclusions' misalignment will be experimentally verified in chapter 4.

2.4. Conclusions

Piezoelectric nanocomposites have many advantages over monolithic materials, such as high fracture toughness and conformability to curved surfaces. However, the electromechanical coupling is often too small to enable effective use in sensing and actuation applications. To resolve this issue, researchers have adopted the use of piezoelectric inclusions in a polymer matrix and have shown that electromechanical properties of a nanocomposite can improve significantly by incorporating high aspect ratio fibers in the nanocomposite. In this chapter, we validated a micromechanics model based on the Mori-Tanka approach with a robust FEM which were used to predict the electromechanical strain coefficients of a nanocomposite with nanowire inclusions. Using a modified RSA method, different RVEs with aligned and randomly distributed, nonintersecting nanowires were generated and COMSOL Multiphysics software was used for calculation of the piezoelectric strain coefficients. The results of both models demonstrated that for all aspect ratio nanowires, the nanocomposites with aligned nanowires have significantly higher piezoelectric strain coefficients compared to that of randomly oriented nanowires. For instance, alignment of the nanowires with AR = 10 in a 40 %WF nanocomposite exhibit more than 100% enhancement in d_{31} and d_{33} coefficients. And it was realized that using high aspect ratio nanowires (AR = 40) even at low weight fractions, the nanocomposites exhibit enhanced piezoelectric performance. Furthermore, the effects of inclusions' misalignment were studied and it was determined that nanocomposite with misalignment less than 20°, can outperform that of aligned inclusions.

Chapter 3: Controlled Synthesis of Barium Titanate and Lead Titanate Nanowires

3.1. Introduction

Novel approaches for synthesis and characterization of free-standing barium titanate ($BaTiO_3$) and lead titanate ($PbTiO_3$) nanowires are developed in this chapter. These synthesis methods utilize a two-step hydrothermal reaction. In the first step, precursor sodium titanate ($Na_2Ti_3O_7$) nanowires are synthesized followed by a second hydrothermal reaction, which preserves the structural integrity and morphology of the nanowires, while converting them to either $BaTiO_3$ or $PbTiO_3$ nanowires. $BaTiO_3$ or $PbTiO_3$ nanowires are synthesized in the second hydrothermal reaction, in which the nanowires are kept in an aqueous solution containing Ba^{+2} or Pb^{+2} ions, respectively. This synthesis method in which results in single crystalline nanowires is scalable, relatively inexpensive and enables control over the geometry and morphology of the nanowires. These nanowires will be used as active component of the nanocomposite energy harvesters that will be fabricated in the following chapters and used to validate the models developed in Chapter 2.

3.2. Summary of various methods for synthesis of one-dimensional ferroelectric nanostructures

Ferroelectric materials have been studied for their excellent ferroelectric [231,232], pyroelectric [233,234], piezoelectric [235,236], and other interesting features such as electro-acousto-optic [237] and mechanic-electric-thermal [238] coupling, switching characteristics [239], and non-linear optical [240] properties. Although monolithic ferroelectric materials present a high level of reliability and sensitivity, they are usually brittle and incompatible with semiconductors or metals. They are also prone to fatigue and fracture under mechanical or electrical loads, further limiting their applications. Over the past couple of decades, many efforts have been made to mitigate these problems. For example, dimension reduction strategies, doping modification [241,242], and synthesis process optimizations [190,243] are among the most effective ways to

enhance the performance of these ferroelectric materials. Dimensional reduction strategies [244,245] are generally the most cost-effective and viable solution for this purpose.

One-dimensional (1D) ferroelectric nanostructures such as nanotubes, nanofibers, nanobelts, nanorods and nanowires have been studied intensively in the past decade. Reducing the size of ferroelectric nanostructures to less than 200 nm in one dimension results in new physical phenomena that only occur during down-scaling [246]. Compared to bulk ferroelectric materials, this class of nanostructures has higher surface area and a greater amount of surface atoms which results in higher surface energy. These new characteristics provide the 1D ferroelectric materials with new specific properties such as changes in dielectric constant, polarization level, piezoelectric response, Curie temperature (T_c), coercive fields, etc. [247]. Furthermore, formation of single crystal ferroelectric materials can be facilitated by reducing the size and dimension of the material which significantly enhance the ferroelectric properties. Due to these beneficial features, 1D ferroelectric materials have been used in many engineering applications such as nanogenerators, sensors, microelectromechanical systems (MEMS), nonlinear optics, etc. Based on the target application and the composition of the materials, many synthesis methods have been developed to fabricate 1D ferroelectric materials. In the following section, a brief outline of the most widely-used synthesis methods to fabricate 1D ferroelectric nanostructures is presented.

3.2.1. Sol-gel template methods

Sol-gel synthesis method is based on the hydrolysis and condensation reaction of molecular precursors such as metal alkoxides and inorganic salts. In this procedure, a suspension of colloidal particles (the sol) is formed which then evolve and aggregate to form a gel-like diphasic system containing both solid and liquid phases [3]. Subsequently, the gel is thermally treated to synthesize the desired material. Over the past decade, this method has evolved into a powerful approach for synthesizing inorganic materials and has many advantages over other conventional methods. For instance, this method generally requires lower temperatures and result in high quality materials. Moreover, by mixing precursor solutions a homogenous multi-component system can be obtained which facilitate chemical doping in the final material.

3.2.2. Molten salt methods

The molten salt method, which was originally derived from the flux method, has been used for single crystal bulk materials. In this method, the reactants are dissolved in a high temperature molten salt, which acts as a medium for preparing dissoluble complex oxides from its constituent materials, such as oxides and carbonates. The nucleation and growth of these complex oxides can be controlled by adjusting the reaction temperature and the concentration of the materials [248]. Typical examples of salts used in this method are chlorides and sulfates. In many cases, eutectic mixtures of salts are used to reduce the melting point temperature. For example, eutectic mixtures of alkaline hydroxides with low melting points, such as KOH and NaOH (K/Na ratio = 48.5:51.5, melting point = 150 °C), have been used to synthesize complex oxide nanostructures [249].

3.2.3. Electrospinning Methods

Electrospinning is one of the most commonly used methods to produce composite, ceramic or polymeric nanofibers. In this approach, a DC voltage is applied to a fine metallic needle, which is then used to eject a uniform stream of precursor solution or melt. Due to electrostatic forces between the needle and a grounded surface close to it, the droplet that forms at the tip of the needle is deformed into a conical shape called a Taylor cone. When the solution's properties (such as its viscosity) are tuned, a stable jet of material is formed. This material undergoes whipping and drawing resulting in thin fibers with nanoscale diameters [90,250]. The electrospinning approach can be utilized to fabricate nano/microfibers with different compositions. Organic nanofibers can be directly synthesized from the electrospinning processes, but inorganic nanofibers must undergo a post-calcination procedure after electrospinning process.

3.2.4. Nanosolid-state reaction methods

Solid-state reaction approach is an important method for synthesizing inorganic powders in which during the reaction two or more compounds are mixed and reacted in the solid state at high temperatures. This method has been used in many industries including electronic ceramics, high temperature ceramics, and even super conducting materials [251]. The nanosolid-state reaction method is originally derived from the solid-state reaction method, which is used to synthesize nanostructured materials. Usually, crystalline nanostructures such as nanoparticles, nanowires, and

nanobelts include a secondary phase which covers the nanostructure and forms a shell-core structure. By applying heat, a new phase evolves from solid-state reaction between the shell and core. This new phase inherits the geometry and morphology of the core material. Thereby, the core acts as both the raw material and template for the shell core nanostructure. This approach is especially important for synthesizing nanostructures with crystallization features that are not suitable for use in morphology-controlled reactions. By applying a heat-treatment, a new crystalline phase forms from a solid-state reaction between the core and shell and inherits the morphology of the core. During the synthesis process, the core acts as a raw material as well as a template. This method can synthesize nanostructures with crystallization habits that are not suitable for use in morphologically controllable synthesis [252].

3.2.5. Sintering methods

High performance ferroelectric materials have been synthesized using sintering technologies such as spark plasma sintering [253,254], two-step sintering, and microwave sintering, which is attributed to the small grain size of the fabricated material. More specifically, the spark plasma sintering method has been increasingly used due to its clear advantages over conventional sintering methods, making it possible to sinter nanometric powders to near full densification with little grain growth. With the miniaturization of electronic devices and due to requirement of reducing the size effects on the properties of materials approaching nanoscale, this method is among the most popular approaches for synthesizing ferroelectric materials. [253-255]

3.2.6. Nonoxide material routes

To date, oxide-based perovskite materials have been the primary focus of most studies in ferroelectric nanostructures. Unfortunately, most of the previously mentioned methods are not suitable for synthesizing nonoxide-based materials due to their unique physical and chemical properties. However, other methods such as chemical vapor deposition (CVD) [256] and sonochemistry methods [257] have been utilized to synthesize 1D nonoxide ferroelectric nanostructures.

3.2.7. Hydrothermal methods

A widely used method to synthesize nanomaterials is hydrothermal method which involve a heterogeneous chemical reaction in aqueous solution above room temperature and high pressures (typically above 100 °C and 1 atm, respectively) [258]. The reactant solubility and reactivity are enhanced under these high temperature and pressure conditions which result in unusual reactions [259]. Usually hydrothermal approaches involve precursor synthesis and the reaction takes places in an autoclave kept in an oven at a certain temperature. In some cases, such as synthesizing lead titanate, the product must undergo a post-treatment to obtain the appropriate crystal structure [177,260]. This method allows for easy diffusion, homogenous nucleation of the reacting species, and formation of highly crystalline stoichiometric materials at relatively low temperatures.

3.3. Synthesis methods of piezoelectric nanowires for energy harvesting

As mentioned earlier in this chapter, 1D piezoelectric nanostructures have many advantages over their bulk counterparts in terms of their piezoelectricity. For instance, improved polarization level, piezoelectric response, Curie temperature (T_c), coercive fields, etc. [247]. They are also mechanically more robust, compliant, and more sensitive to small excitations levels. They are divided, usually based on their geometry, into several categories, namely, nanowires [72,193], nanotubes [91,261], nanobelts [262,263], and nanorods [264,265]. It is well-known that nanowires usually perform better than other morphologies in terms of energy harvesting which can be contributed to their superior compliance [266,267]. Based on how these nanowires are grown, they are categorized into free-standing nanowires [22,193] and vertically aligned arrays of nanowires [177,268]. The free-standing nanowires are usually grown hydrothermally and refer to individual nanowires dispersed in another material, such as polymers with no substrate to grow on. They are useful in fabrication of flexible polymeric nanocomposites [190]. The vertically aligned nanowires are often grown vertically on a substrate via hydrothermal reactions or CVD methods [269]. The devices made of these nanowires are usually less compliant than those of freestanding counterparts but since the nanowires are aligned in the direction of applied stress, they are more sensitive to small excitations [270]. In the next section, the details of synthesis methods for fabrication of the nanowires used in this dissertation is provided.

3.3.1. Hydrothermal synthesis of sodium titanate ($Na_2Ti_3O_7$) nanowires

First, a total of 0.5 g of titanium dioxide (TiO_2) was dispersed in 20 mL of a 10.3 M sodium hydroxide (NaOH) aqueous solution in a Teflon-lined stainless-steel autoclave by stirring for 15 min. Then, after sealing, the autoclave was heated at various temperatures (based on the targeted nanowire aspect ratio [271]) for 12 hours and then cooled down to room temperature. The resulting $Na_2Ti_3O_7$ precipitate was collected and washed with diluted hydrochloric acid (HCl), distilled water, and ethanol sequentially, and then dried in a vacuum oven at 85 °C for 12 h. The acid wash of $Na_2Ti_3O_7$ nanowires produces an ion exchange (Na^+ with H^+) which results in conversion to hydrogen titanate nanowires $H_2Ti_3O_7$ [23,177,178]. Figure 3-1 show the resulting nanowires with various length and diameter. The morphology of the nanowires is mostly dominated by the temperature and duration of the hydrothermal reaction. For example, higher reaction temperature results in longer nanowires with larger diameter; however, this effect is more dominant in the length of nanowires. Therefore, higher reaction temperature lead to higher aspect ratio nanowires. Figure 3-1a, b, c, and d show the scanning electron micrograph (SEM) of resulting nanowires synthesized at 150 °C, 180 °C, 210 °C, and 240 °C, respectively.

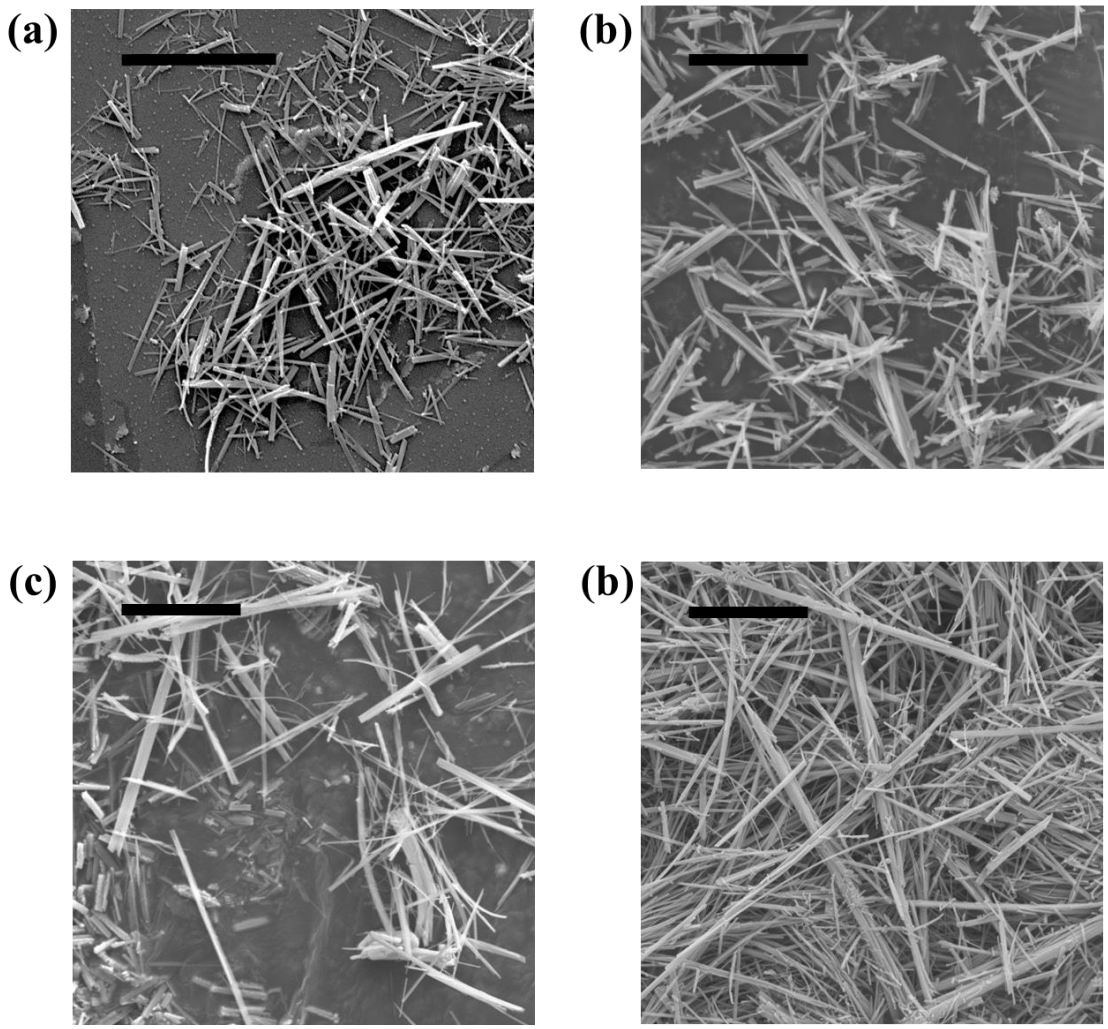

Figure 3-1: Free-standing sodium titanate ($Na_2Ti_3O_7$) nanowires with various length and diameter. Reaction temperatures: (a) 150 °C, (b) 180 °C, (c) 210 °C, and (d) 240 °C. Scale bars are (10 µm).

3.3.2. Hydrothermal synthesis of barium titanate ($BaTiO_3$) Nanowires

After synthesizing $H_2Ti_3O_7$ nanowires, they were used as precursor to synthesize $BaTiO_3$ nanowires. By preserving the morphology of the nanowires developed in section 3.3.1, they were transformed to $BaTiO_3$ nanowires using a second hydrothermal reaction. For that, 0.13 g of $H_2Ti_3O_7$ nanowires were dispersed in 20 mL aqueous solution of 0.05 M $Ba(OH)_2$. After saturating the Teflon-lined autoclave with Ar gas and adequate sealing, the autoclave was heated at 210 °C for 2 h and then cooled to room temperature. The $BaTiO_3$ nanowires precipitates were collected, washed several times with a 0.1 M aqueous solution of HCl, distilled water and ethanol, and then dried in a vacuum oven at 85 °C for 12 h.

Figure 3-2 shows the resulting $BaTiO_3$ nanowires that were transformed from their corresponding $Na_2Ti_3O_7$ nanowires - synthesized at 150 °C, 180 °C, 210 °C, and 240 °C with various length and diameter. It is clear that the nanowires preserved the morphology of the precursors. Figure 3-3 demonstrates the distribution of $BaTiO_3$ nanowires' aspect ratio in each SEM picture in Figure 3-2. It shows that the $BaTiO_3$ nanowires shown in Figure 3-2 a, b, c, and d have median aspect ratio of approximately, 10, 20, 30 and 40, respectively.

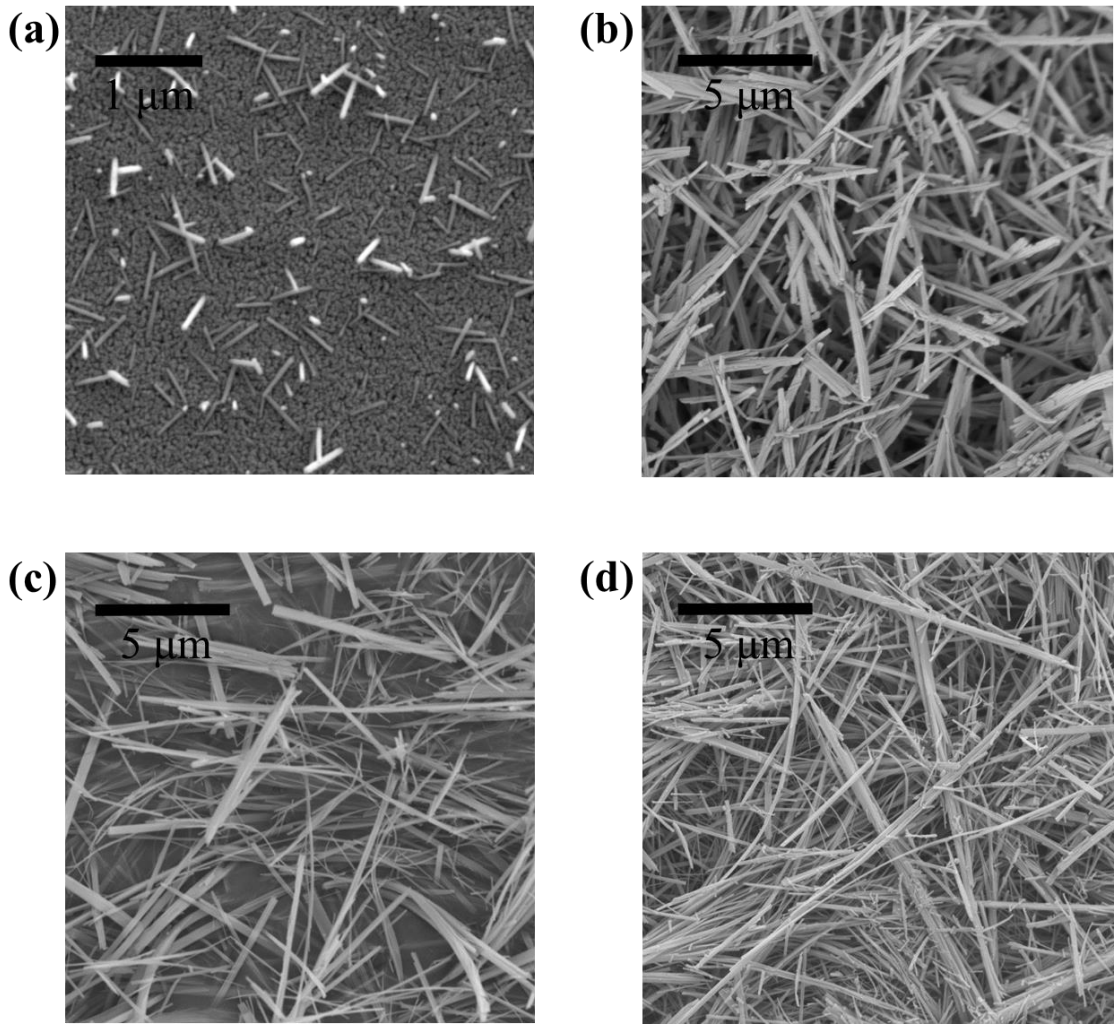

Figure 3-2: Free-standing Barium titanate ($BaTiO_3$) nanowires with various length and diameter. Precursors ($Na_2Ti_3O_7$) were prepared at various reaction temperatures: (a) 150 °C, (b) 180 °C, (c) 210 °C, (d) 240 °C. Scale bars are (10 μm).

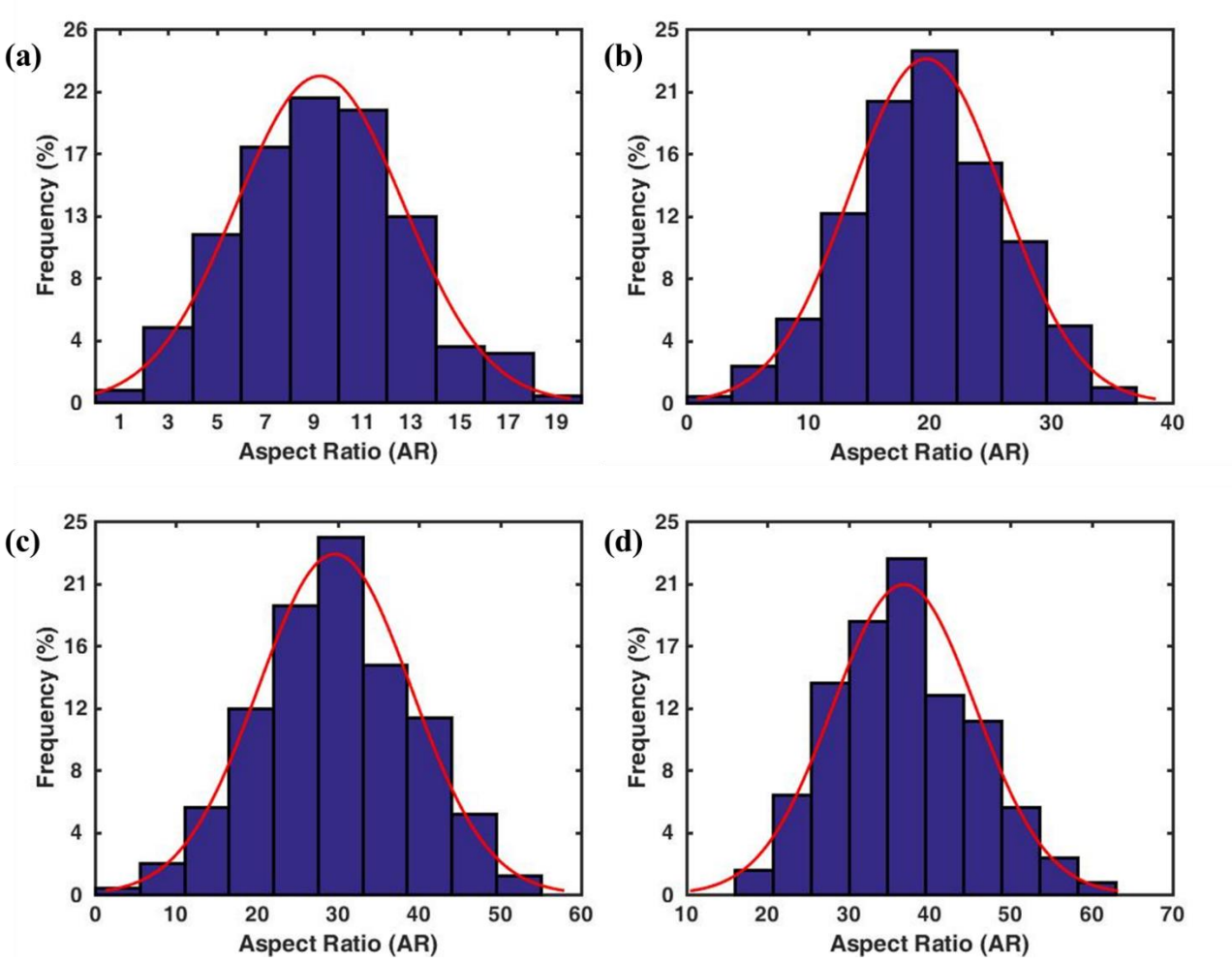

Figure 3-3: the distribution of $BaTiO_3$ nanowires aspect ratio with various precursors ($Na_2Ti_3O_7$), prepared at various reaction temperatures: (a) 150 °C, (b) 180 °C, (c) 210 °C, (d) 240 °C.

To better characterize the $BaTiO_3$ nanowires, a single nanowire was imaged with SEM and shown in Figure 3-4a, which displays straight nanowires with high aspect ratios. The nanowires' topography is further analyzed using atomic force microscope (AFM, Park Systems). The AFM scan of a single nanowire was performed in noncontact mode with a low scan speed (0.3 μm s^{-1}, Figure 3-4b). Figure 3-4c shows the X-ray diffraction (XRD) characterization of $BaTiO_3$ and hydrogen titanate precursor nanowires, which exhibit a crystalline structure of $BaTiO_3$ with no indication of by-product. This figure shows that after conversion to $BaTiO_3$, all characteristic peaks associated with hydrogen titanate have disappeared and the XRD pattern of the $BaTiO_3$ nanowires agrees well with the Joint Committee on Powder Diffraction Standards (JCPDS) Card No. 05–0626 corresponding to barium titanate. Using the XRD data provided in Figure 3-4c and Bragg's

law [272] the inter-planar spacing of the crystal (d-spacing) was calculated. According to Bragg's law:

$$2d_{hkl}(\sin\theta_{hkl}) = \lambda_0, \tag{3-1}$$

where θ is the x-ray incidence angle (Bragg angle), λ_0 = 1.54 Å (Cu K-alpha radiation) is the wavelength of characteristic x-rays, and *hkl* represent the plane indices. From the XRD data provided in Figure 1c and Eq. (3-1), the d_{110} can be calculated as

$$d_{110} = \frac{\lambda_0}{2(\sin\theta_{110})} = \frac{1.54\ \text{Å}}{2(\sin 15.8°)} = 2.828\ \text{Å}. \tag{3-2}$$

The d-spacing can also be calculated based on the geometry of the crystal structure, namely, for tetragonal crystal structure,

$$\left(\frac{1}{d_{hkl}}\right)^2 = \frac{h^2+k^2}{a^2} + \frac{l^2}{c^2}. \tag{3-3}$$

Based on Joint Committee on Powder Diffraction Standards (JCPDS) Card No. 05–0626, the tetragonal $BaTiO_3$ crystals have the following size: a = 3.994 Å and c = 4.038 Å. Using Eq. (3-3), the d-spacing can be calculated as d_{110} = 2.825 Å, which is approximately the value calculated by Eq. (3-2). This results show that the synthesized $BaTiO_3$ has a tetragonal crystal structure with d_{110} = 2.828 Å. The elemental composition of the nanowires was studied using energy dispersive x-ray spectroscopy (EDS) which confirmed the presence of Ba, Ti, and O peaks as shown in Figure 3-4d.

It should be noted that reaction parameters, such as chemical concentrations and temperatures, have a dominant effect on the morphology and efficiency of the conversion to $BaTiO_3$. Specifically, an increase in the concentration of $Ba(OH)_2$ and the temperature of the second hydrothermal reaction results in a higher degree of conversion to $BaTiO_3$. On the other hand, higher temperature and chemical concentration can change the nanowire morphology of the precursor. Therefore, obtaining pure $BaTiO_3$ nanowires with a range of aspect ratios from 10 to 40 requires a careful optimization of reaction parameters.

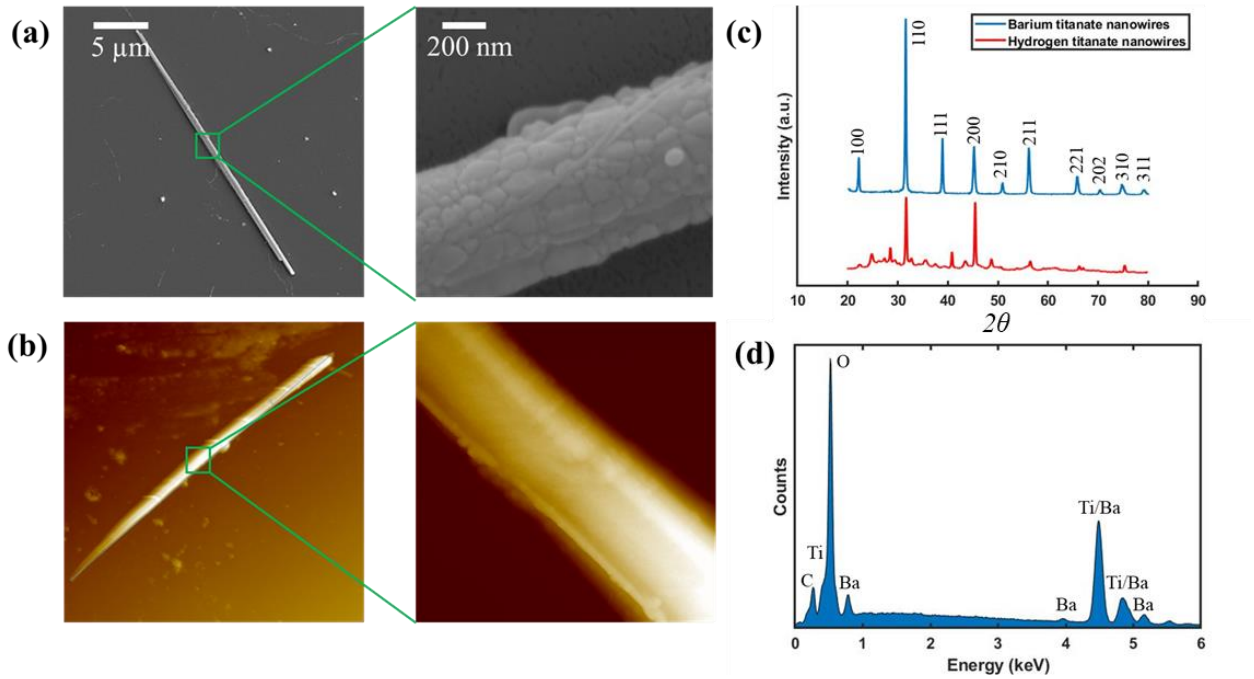

Figure 3-4: (a) SEM micrograph, (b) AFM topography scan, (c) XRD pattern and (d) EDS spectrum of the as synthesized $BaTiO_3$ nanowires.

3.3.3. Hydrothermal synthesis of lead titanate ($PbTiO_3$) Nanowires

Similar to the method discussed in section 3.3.1 where freestanding $BaTiO_3$ nanowires were synthesized, freestanding lead titanate **(**$PbTiO_3$) nanowires were also produced using sodium titanate nanowires precursor. After successfully growing sodium titanate nanowires and converting them to hydrogen titanate through ion exchange process (H^+ with Na^+, section 3.3.1.1), 0.644 g of the material was dispersed in a Teflon lined reactor. Then the reactor was filed with 50 ml aqueous solution of 0.01 M lead nitrate ($Pb(NO_3)_2$, Acros Organics, 99%) and 0.26 g potassium hydroxide (Alfa Aesar, flake, 85%). Then, the reactor was kept at 200 °C for 4 hours, during which the Pb^{+2} ions replaced H^+ ions in the crystal structure while preserving the nanowires' morphology. After the reaction, the product was filtered out and washed with dilute solution of HCl (0.2 M), to remove any unwanted byproducts such as lead oxide (PbO) and other salts. Subsequently, the nanowires were washed with DI water several times until neutral pH was reached. Finally, the nanowires were calcinated at 600 °C in a furnace for 5 hours. The calcination process is essential because it helps the material to reach a complete perovskite structure with added benefit of removing the unwanted hydroxyl groups in the structure [177,178,190].

Similar to synthesis of freestanding $BaTiO_3$ nanowires, the quality and purity of the $PbTiO_3$ final product highly depends on the reaction parameters. Among those, an increase in the reaction time and temperature, or concentration of reacting species, lead to higher purity of the $PbTiO_3$ nanowires but also can cause significant unwanted morphology transformation in the nanowires [190]. Therefore, balanced reaction parameters as mentioned earlier have to be employed. Figure 3-5a represents the SEM picture of as synthesized $PbTiO_3$ nanowires which are converted from $Na_2Ti_3O_7$ precursors grown at 240 °C. Figure 3-5b show the AFM topography scan of single $PbTiO_3$ nanowire. Figure 3-5c demonstrate the existence of Pb, Ti and O atoms in the crystal structure of $PbTiO_3$ nanowires using EDS characterization. And finally Figure 3-5d show the XRD spectrum of these nanowires confirming high purity $PbTiO_3$ with tetragonal crystal structure (JCPDS Card No. 06-0452).

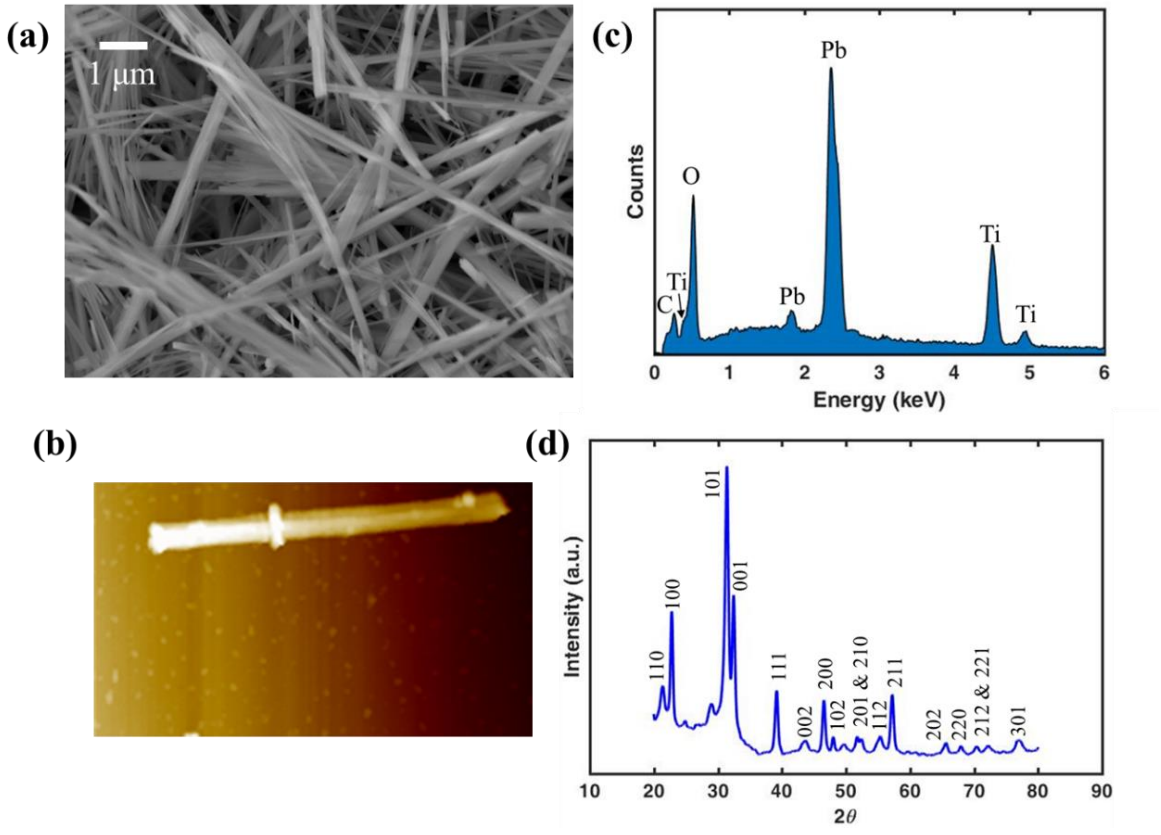

Figure 3-5: Synthesized $PbTiO_3$ nanowires characterization. (a) SEM, (b) AFM topography, (c) EDS spectra and (d) XRD pattern associated with JCPDS Card No. 06-0452.

3.4. Conclusions

In conclusion, two hydrothermal methods were provided that employ two-step reactions for synthesizing $BaTiO_3$ and $PbTiO_3$ nanowires with control over their purity, aspect ratio and morphology. Both types of nanowires were synthesized using a template assisted method where first $Na_2Ti_3O_7$ nanowires were synthesized as precursor. By controlling the reaction temperature and duration the length and diameter of $Na_2Ti_3O_7$ nanowires were engineered leading to controlled aspect ratios ranging from 10 to 45. Then, $Na_2Ti_3O_7$ were washed with HCl to substitute the Na^+ with H^+ ions in the crystal structure yielding $H_2Ti_3O_7$ nanowires. Subsequently, $H_2Ti_3O_7$ nanowires were converted to final product using a second hydrothermal reaction. In this reaction, $H_2Ti_3O_7$ nanowires were transformed to $BaTiO_3$ by an ion exchange process in which the H^+ ions were substituted with Ba^{+2} in an aqueous solution of $Ba(OH)_2$. Similarly, $H_2Ti_3O_7$ nanowires were converted to $PbTiO_3$ using another aqueous solution of $Pb(NO_3)_2$ in which ion exchange process resulted in substitution of Pb^{+2} with H^+ ions. The nanowires synthesized in this chapter will be used to fabricate piezoelectric nanocomposite energy harvesters in the following chapters.

Chapter 4: Model Verification and Device Characterization

4.1. Introduction

In this chapter, we study the role of aspect ratio and orientation of the fillers in a piezoelectric nanocomposite energy harvester by employing the Mori-Tanaka method and FEM. The results are then validated by electrical characterization of nanocomposite energy harvesters. The nanocomposites with controlled filler alignment are fabricated by an additive manufacturing method and the results show that the piezoelectric performance of the nanocomposite can be enhanced by increased aspect ratio of the filler and control over filler alignment using the direct write method. This is the first validated model that inspects the effect of filler properties on the overall piezoelectric voltage coefficient and the effect on energy harvester performance. The simulation results demonstrate that by using high aspect ratio fillers the g_{31} voltage coefficient can be enhanced by more than 500%, compared to that of the bulk material. Furthermore, it is shown that the g_{31} coefficient does not increase continuously with weight fraction (WF) of the fillers in the nanocomposite, i.e. depending on the aspect ratio of the fillers, there exist an optimum WF in which the highest possible g_{31} coefficient is realized. This fact is crucial in terms of the design and fabrication of high-performance energy harvesters and sensors and can be achieved using a low fraction of filler.

To validate our model, a range of nanocomposites with barium titanate (BTO) [35-37] nanowires dispersed in a polydimethylsiloxane (PDMS) matrix were prepared with controlled alignment using the direct write method. The piezoelectric energy harvesting performance of the nanocomposites were then assessed by measuring the g_{31} coefficients of the nanocomposites. It is shown that the models can be used to accurately predict the g_{31} coefficient and that the energy output of the nanocomposites is directly related to the voltage coefficient. The results demonstrate that increased aspect ratio of the nanowires in the energy harvester can significantly enhance both the power output and the voltage coefficient for the nanocomposites. The output power of the

nanocomposite energy harvester with aligned nanowires is compared to that of randomly oriented nanowires and it is shown that alignment of the nanowires can increase the power by a factor of three. However, it has been illustrated that a slight deviation from aligned nanocomposite can actually improve the piezoelectric strain coefficient and further misalignment reduce it until finally reaching its lowest value when the nanowires are completely randomly oriented. The results presented in this chapter can provide a robust tool for analyzing two phase piezoelectric nanocomposites energy harvesters with nanowire inclusions and can be used for the design of efficient piezoelectric energy harvesters or sensors.

4.2. Nanocomposite fabrication method

To validate the results of the FEM and micromechanics models, a variety of nanocomposites were prepared that contained different aspect ratios and weight fractions (WFs) of BTO nanowires. First, a 10 g solution of PDMS [273] (elastomer/curing agent ratio = 1:10) was mixed with the appropriate weight of BTO nanowires to achieve a desired WF of BTO/PDMS, ranging from 10% WF to 40% WF. A speed mixer (3500 RPM, 15 min, FlackTek Inc) was used to uniformly disperse the nanowires in the polymer solution. To remove any remaining nanowire agglomerations in the solution, the mixtures were further sonicated for 60 min in a bath sonicator, resulting in a homogeneous white nanocomposite solution that readily flowed. The uncured polymer nanowire suspensions were then degassed at room temperature under high vacuum for 15 min. Similarly, a variety of nanocomposite solutions containing commercially available BTO nanoparticles (spherical, 100 nm, Inframat Advanced Materials) were prepared to fabricate different WF nanocomposites with spherical inclusions. Here it is assumed that the nanowires with aspect ratio 1 can be approximated by spherical nanoparticles.

Following dispersion of the nanowires in the uncured polymer matrix, the solution was loaded in a syringe and applied to a heated borosilicate glass with a direct write system, [22,23,274] which enables the preparation of films with alignment based on the motion of the nozzle and the shear alignment that occurs in the nozzle. Figure 4-1a shows the custom-built Aerotech 3D printer equipped with a precision solution dispenser for direct writing of the nanocomposite onto borosilicate glass. Previously, it was shown that the high shear environment that exists in the nozzle causes the nanowires to align themselves in the nozzle and consequently become parallel

to the writing direction [22,23,274]. The shear forces in the nozzle are controlled by the viscosity of the nanocomposite solution and can be used to control nanowire alignment in the nanocomposite. Figure 4-1b illustrates a schematic of the writing process which shows that the nanowires within the printed nanocomposite align themselves in the writing path. For the sake of comparison, all nanocomposites were printed with a serpentine pattern (prepared using Slicer software) on a 3 cm by 0.8 cm area. Figure 4-1c demonstrates the effect of viscosity on the alignment of the nanowires in the nanocomposite. It shows that by increasing the amount of toluene in the solution, hence reducing the nanocomposites ink viscosity, it is possible to decrease the alignment of the nanowires.

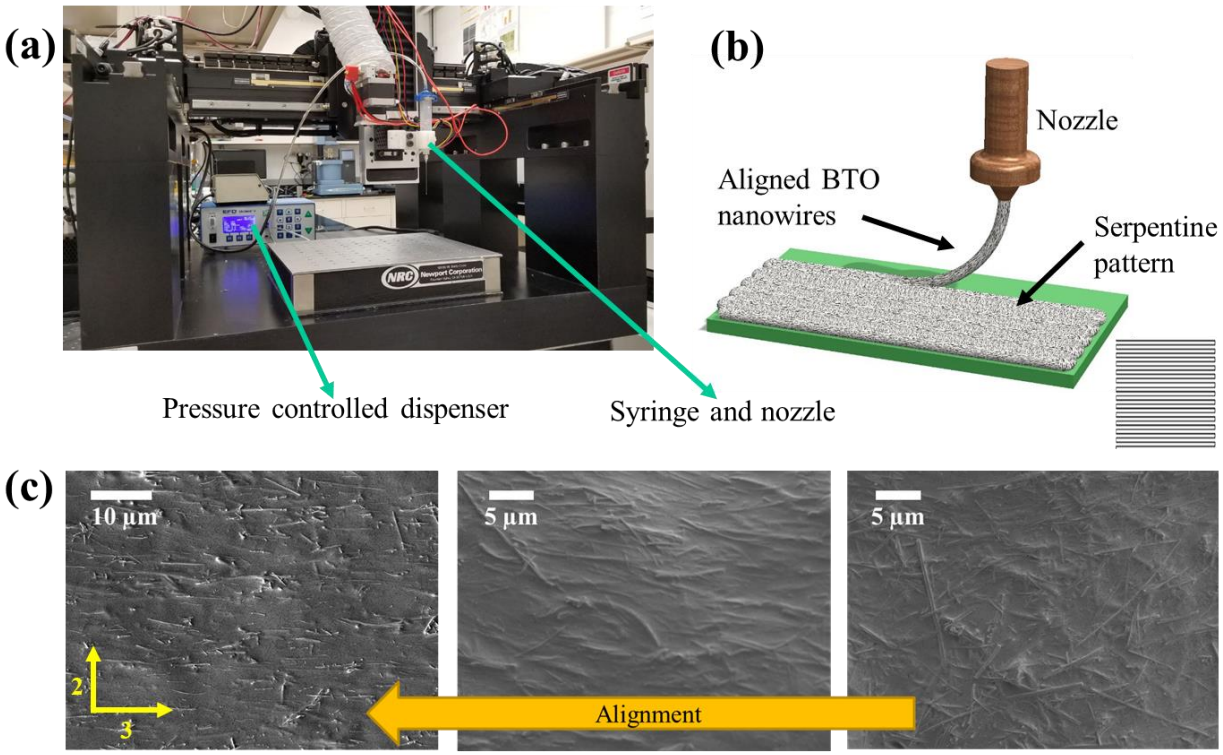

Figure 4-1: (a) Experimental setup used for direct write of the nanocomposite. (b) Schematic illustration of a single layer direct printing process with nanowires aligned in the 3-direction. (c) SEM micrograph of the fabricated BTO nanowire/PDMS nanocomposites with varying degrees of alignment, controlled by adjusting the viscosity of the nanocomposite ink using toluene.

After thermal curing of the nanocomposites at 100 °C in a vacuum oven, the nanocomposites were removed from the substrate and coated with 10 nm of gold on both sides as electrodes using a sputter coater. Because BTO nanowires in the nanocomposite are ferroelectric, poling is

essential. There are several ways to pole the samples, such as corona poling [193], self-poling process [235,275] or direct field poling [23,177]. Here the poling was accomplished by directly applying an electric field at 150 °C with 300 V for 1 hour. The samples were then cooled down to room temperature under the poling voltage. In section 4.4, the piezoelectric performance of nanocomposites with randomly oriented nanowires are compared to nanocomposites with aligned nanowires. It is shown, both numerically and experimentally, that the alignment of the nanowires can significantly increase the piezoelectric strain coefficient of the nanocomposite.

4.3. Measurement setups

4.3.1. Measurement setup for calculation of electromechanical coefficients

Following poling, the electromechanical coupling of each nanocomposite was measured using a dynamic mechanical analyzer (DMA, Q800, TA Instruments), with a preload of 0.5 N applied to the samples (Figure 4-2). The samples were then excited by a 5 Hz sinusoidal strain with 0.5% amplitude while the force and voltage were measured. Using this method, the d_{31} coefficient was calculated as [22,276]

$$d_{31} = \frac{CV}{F}\left(\frac{t}{L}\right), \tag{4-1}$$

where C, t, and L are the capacitance (measured by an LCR meter, Agilent E4980A), thickness and length of the nanocomposite, respectively. V (measured by an electrometer, Keysight B2985A) and F (measured by the DMA) are the RMS output voltage and input force exerted on the samples, respectively.

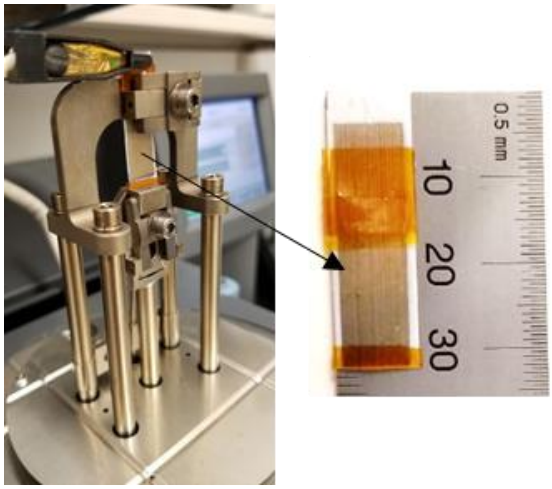

Figure 4-2: DMA test setup for measurement of the d_{31} coupling coefficient which enables the application of a controlled strain while the force is measured.

Another important characteristic of a piezoelectric nanocomposite energy harvester is its ability to generate charge on its electrodes, which can significantly affect its ability for driving current through an external load. This effect is closely related to the dielectric permittivity of the nanocomposite. Using the measured capacitance of the device and its geometrical dimensions, the dielectric permittivity can be calculated as

$$\varepsilon = \frac{C}{\varepsilon_0}\left(\frac{t}{A}\right), \tag{4-2}$$

where ε_0 = 8.85 x 10^{-12} F/m and represents the permittivity of the vacuum space.

In addition to the d_{31} piezoelectric strain coefficient, the d_{33} coefficient of the samples were also measured, however this measurement required the use of an atomic force microscope (AFM, XE-70, Park Systems). Initially, a variety of nanocomposites composed of 15 layers with a total thickness ~ 0.6 mm were printed. They were then cut perpendicular to the direction of the nanowires with a length of about 1 mm and bonded to an AFM puck using conductive silver paint, which served as the bottom electrode in AFM testing (small sample dimensions reduced the chance of a membrane effect). The top surface of the samples was also coated with silver paint to serve as a top electrode (Figure 4-3a). Following the poling process, the AFM pucks containing the nanocomposites were mounted on an AFM stage and a grounded conductive AFM tip (Pt, k = 40 N m^{-1}, f = 170 kHz) was brought into contact with the top electrode (contact mode). To ensure a

robust contact between the tip and top electrode a 1,500 nN force was applied to the tip (Figure 4-3a). Then, an externally supplied 1 Hz unipolar triangular wave voltage with varying amplitude was applied to the bottom electrode. Using this method, the AFM tip acted as a highly accurate displacement transducer. To reduce the thermal noise that affects the measurements, a band pass filter was used to improve the displacement signal to noise ratio (SNR). The application of the unipolar voltage to the samples through AFM, resulted in the movement of the top electrode due to piezoelectric properties of the nanocomposite. Figure 4-3b shows the piezoelectric displacement versus three separate unipolar voltages applied to a directly printed nanocomposite containing 20 %WF BTO nanowires. By measuring the slope of the curves in Figure 4-3b, the d_{33} piezoelectric strain coefficient can be calculated as 29 pm/V.

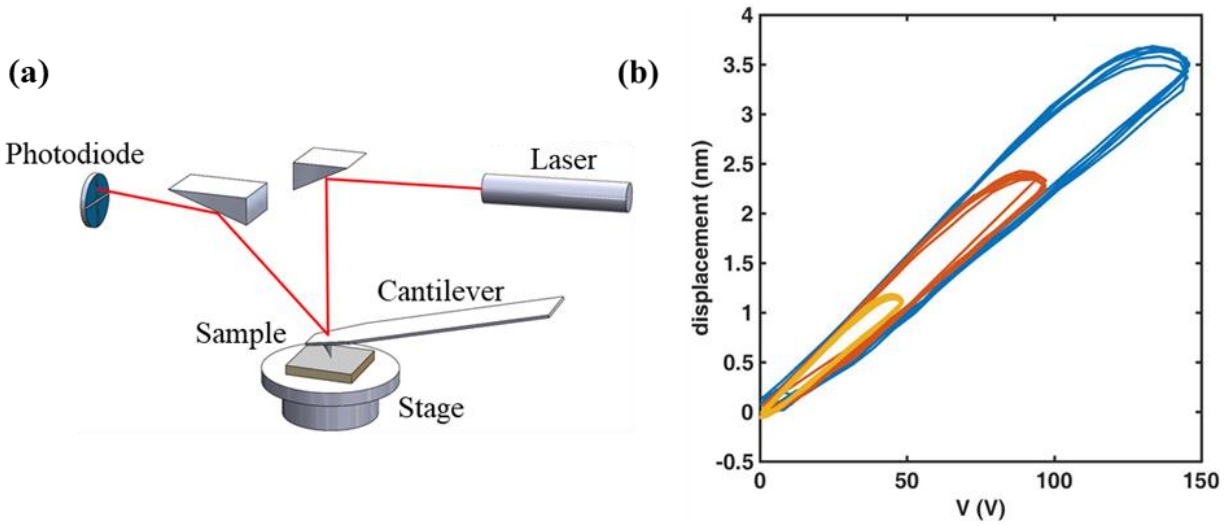

Figure 4-3: (a) AFM test setup. (b) The displacement measurement during the application of a unipolar voltage to a nanocomposite containing 20 WF% BTO nanowires.

4.3.2. Measurement setup for energy harvesting characterization

A well-known approach for characterization of piezoelectric based energy harvesters is by application of impulse excitation, which usually causes a large mechanical strain on the material and therefore leads to a high impulsive output [277-279]. Although this method can be used as a preliminary test for the energy harvester, it doesn't provide a meaningful electric characterization with reliable results. Hence, a more reliable excitation method is needed. Here, the flexible BTO nanowire/PDMS nanocomposite is printed onto a stainless-steel beam which acts as a cantilever

beam. The mechanical excitation input is provided by an electromagnetic shaker and the material is characterized by an input acceleration level measured by an accelerometer (Figure 4-4) [22,53,177,190,193,244].

Two types of energy harvesters with identical geometrical and material properties are considered for this test. For type I energy harvester, the nanocomposite is printed longitudinally, which results in aligned nanowires in the x-direction and for type II it is printed laterally leading to aligned nanowires in the y-direction (Figure 4-4). It is intuitively obvious that the type I energy harvester exhibits higher output response because the nanowires are aligned in the direction of bending stress caused by cantilever deformation. On the other hand, since in the type II energy harvester the nanowires are aligned perpendicular to the applied stress, lower output response is expected. This test further demonstrates the effect of nanowire alignment in the performance of the energy harvester.

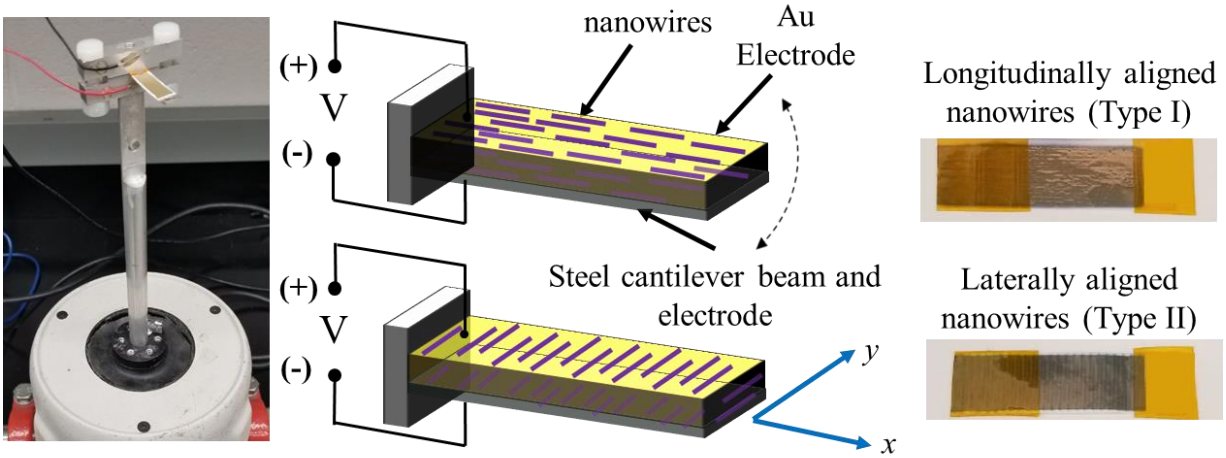

Figure 4-4: Measurement setup along with schematics and samples of the energy harvester devices. Mechanical excitation is applied by an electromechanical shaker and the input acceleration is measured using an accelerometer.

4.4. Model Validation and Discussion

The accuracy of the predicted piezoelectric strain coefficients (d_{31} and d_{33}) based on the Mori-Tanaka micromechanics model and the FEM method were assessed by comparing to the experimental results. For all results presented here, the material properties for the BTO (active

phase) and PDMS polymer matrix are shown in Table 4-1. All of the effective d_{31} and d_{33} coefficients are normalized with respect to the active constituent's bulk (BTO) d_{31} and d_{33} values, respectively. Therefore, a ratio of one would indicate that the coupling of the nanocomposite is equivalent to the bulk and thus would be perfectly efficient in the transfer of coupling from the filler to the nanocomposite.

Figure 4-5 represents the normalized effective d_{31} values of various aspect ratio (AR) fibers for aligned and randomly oriented nanowires. As anticipated, in all cases the d_{31} coefficients increased with an increase in the WF of the nanowires in the nanocomposite. As the aspect ratio increased from one, at any given WF, the morphology of the fibers slowly changed from spherical particles to continuous fibers at an aspect ratio of infinity. For lower AR fibers, the effect of an increase in AR on d_{31} enhancement was more significant and as the nanowires approached higher ARs, further increase in d_{31} slowed down. For instance, as shown in Figure 4-5 at WF = 40% the Mori-Tanka results for aligned nanowires predicted an 89%, 61%, and 10% increase in d_{31} when AR was changed from 1 to 10, from 10 to 20, and from 20 to 40, respectively. For the case of randomly oriented nanowires similar results can be inferred. Through a convergence study, it was established that the nanowires with AR greater than 100 can be considered as continuous fibers, which indicate that further increase in AR has little to no effect on the overall d_{31} coefficient [24,208].

From Figure 4-5 it is evident that for all cases, at any given WF, the aligned nanowires have higher d_{31} coefficients compared to randomly oriented nanowires. Moreover, it shows that this effect declines for lower AR nanowires. Specifically, for AR = 1 both randomly oriented and aligned nanowires have small and approximately equal d_{31} coefficients. This fact can be explained by considering the fibers with AR = 1 as spheres. It is clear that spheres have no preferred directions and random or aligned orientations have no effect on their electromechanical coefficients.

Figure 4-5 further demonstrate that the results of FEM and experimental measurements of d_{31} coefficients have good agreement with the Mori-Tanaka method. Each experimental data point consists of at least three samples with similar ARs and WFs. These results are the average value of the measured d_{31} coefficient, with corresponding error bars. It is evident that experimental data

for all cases follow the same trend as predicted by Mori-Tanaka and FEM methods. The experimental data clearly shows that, except for the case of AR = 1 and for a fixed WF, the direct print nanocomposite samples with aligned nanowires have significantly improved piezoelectric coefficients when compared to solution cast nanocomposites with randomly oriented nanowires. It should be noted that for the case of AR = 1 piezoelectric performance is independent of alignment, as the experimental data of either type of nanocomposite overlaps.

Table 4-1: Material properties of the barium titanate nanowires [216,217], and PDMS [214,215]. $S_0 = 10^{-12}$ m^2/N; $d_0 = 10^{-12}$ C/N; κ_0 = 8.85E-12 F/m; $\rho_0 = 10^3$ kg/m^3.

	S_{11}/S_0	S_{12}/S_0	S_{13}/S_0	S_{33}/S_0	S_{44}/S_0	S_{66}/S_0	d_{31}/d_0	d_{33}/d_0	d_{15}/d_0	κ_{11}/κ_0	κ_{33}/κ_0	ρ/ρ_0
BTO	7.38	-1.39	-4.41	13.1	16.4	7.46	-33.72	93.95	560.7	4366	132	6.03
PDMS	4.88E5	-1.2E5	-1.2E5	4.88E5	6.10E5	6.10E5	0.0	0.0	0.0	2.4	2.4	0.97

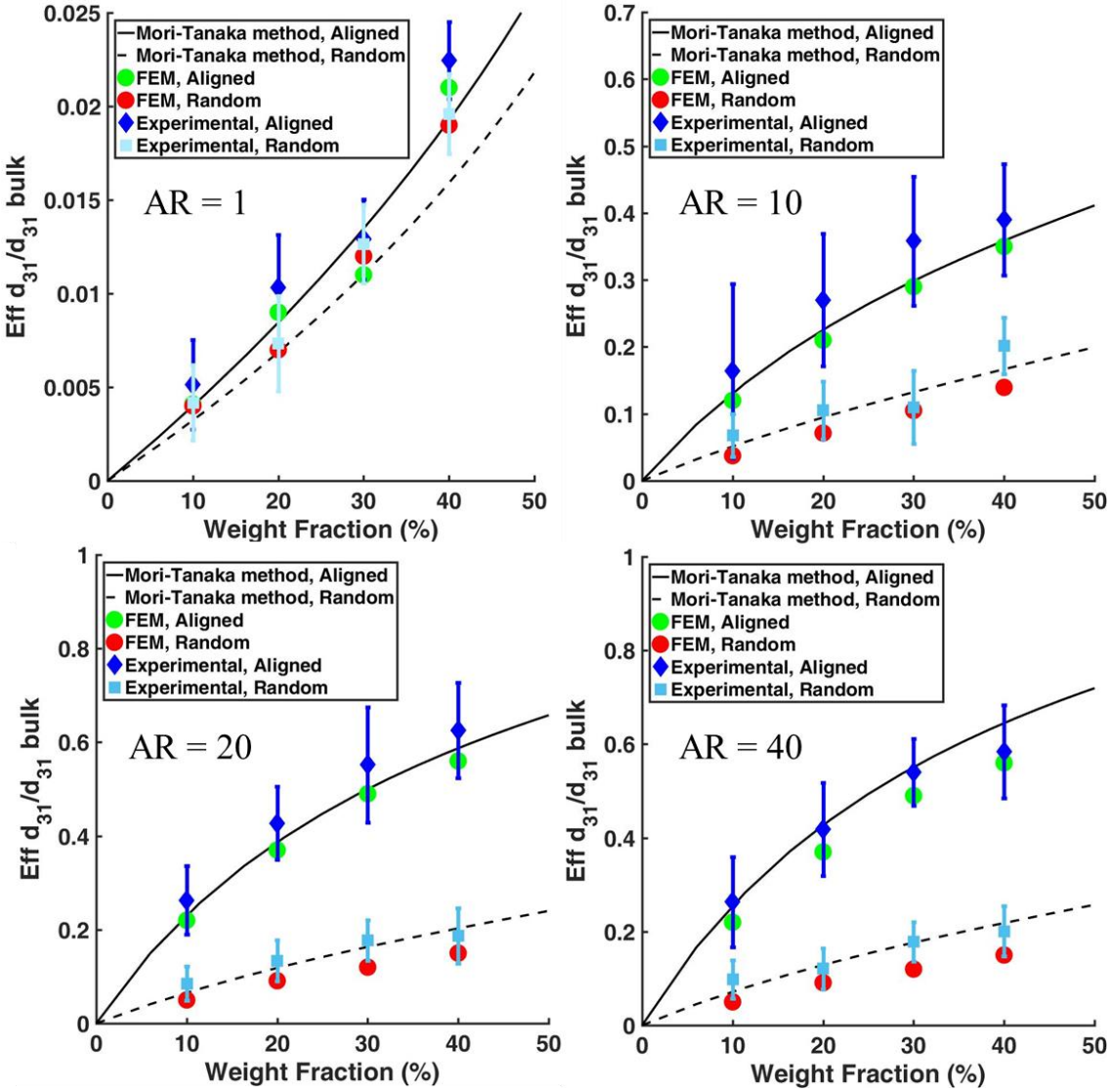

Figure 4-5: Comparison between the effective d_{31} coefficients calculated using Mori-Tanaka method, FEM and experimental measurement using DMA for nanocomposites with aligned and randomly oriented nanowires with varying aspect ratios.

Similarly, according to Figure 4-6 it is shown that the results of the Mori-Tanaka method, FEM and experimentally measured d_{33} values using AFM have a good agreement and for all aspect ratios. The d_{33} coefficient of directly printed nanocomposites with aligned nanowires have significantly higher values compared to that of random nanowires. However, in the case of AR = 1, due to symmetric nature of these nanowires, their alignment has no effect on increasing the overall d_{33} of the nanocomposites. Figure 4-6 also demonstrates that by incorporating high aspect ratio nanowires within the nanocomposite it is possible to achieve relatively high d_{33} values, even

at low weight fractions. For instance, a directly printed nanocomposite with 40% WF (equivalent to ~ 10% volume fraction) of BTO nanowires with AR = 40, d_{33} can reach up to 55% of the bulk value, which is equivalent to a coupling value of 51.67 pm/V. This value is the highest reported for a piezoelectric nanocomposite and was achieved through an additive manufacturing process. In summary from Figures 4-5 and 4-6 it can be inferred that aspect ratio and orientation of the nanowires are the main source of enhancement in piezoelectric performance of a nanocomposite.

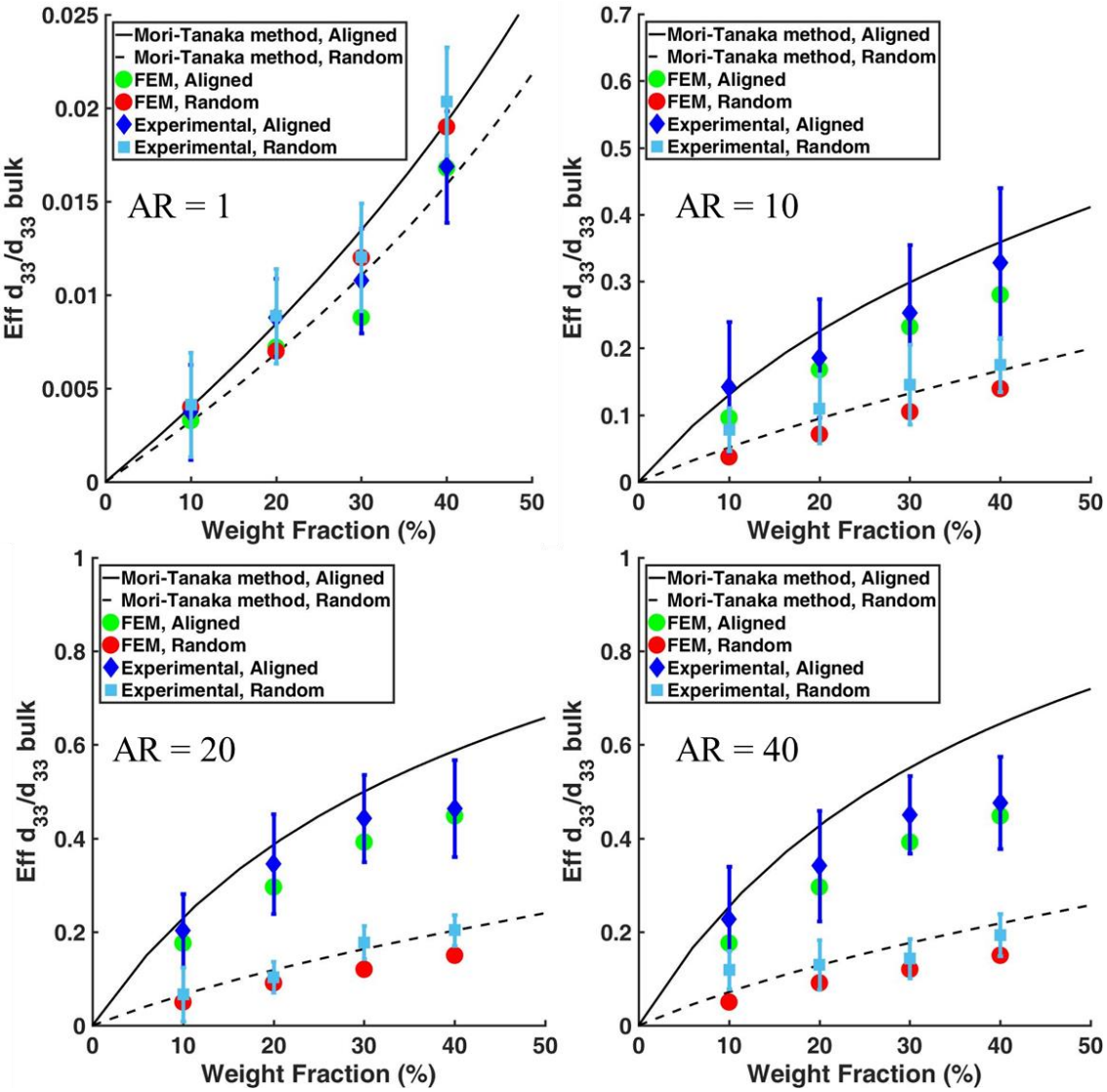

Figure 4-6: Comparison between the effective d_{33} coefficients calculated using Mori-Tanaka method, FEM and experimental measurement using DMA for nanocomposites with aligned and randomly oriented nanowires with varying aspect ratios.

The accuracy of the predicted dielectric constants and voltage coefficients based on FEM and the Mori-Tanaka micromechanics model were also examined by comparing the simulations to experimental results. Here, the effective ε_{33} of the nanocomposites is normalized with respect to the bulk dielectric permittivity of the active BTO nanowires. Therefore, a ratio of one would indicate that the value of the corresponding dielectric constant is equivalent to the bulk value, and all coefficients approach one as the WF approaches 100%. Figure 4-7 represents the ε_{33} constant of the nanocomposites containing various aspect ratio (AR) fibers with aligned and randomly

oriented nanowires. As anticipated in all cases, the ε_{33} constants increase with WF of the nanowires in the nanocomposites due to the higher dielectric constant of the BTO nanowires over the PDMS matrix. For lower AR fibers, the effect of an increase in AR on the enhancement of ε_{33} constants is more significant, but as it approaches higher ARs, further increases in the ε_{33} constant slows. For instance, as shown in Figure 4-7, the Mori-Tanaka results at WF = 40% for aligned nanowires, predicted 141%, 27%, and 9% increase in the ε_{33} constant when AR is changed from 1 to 10, 10 to 20, and from 20 to 40, respectively.

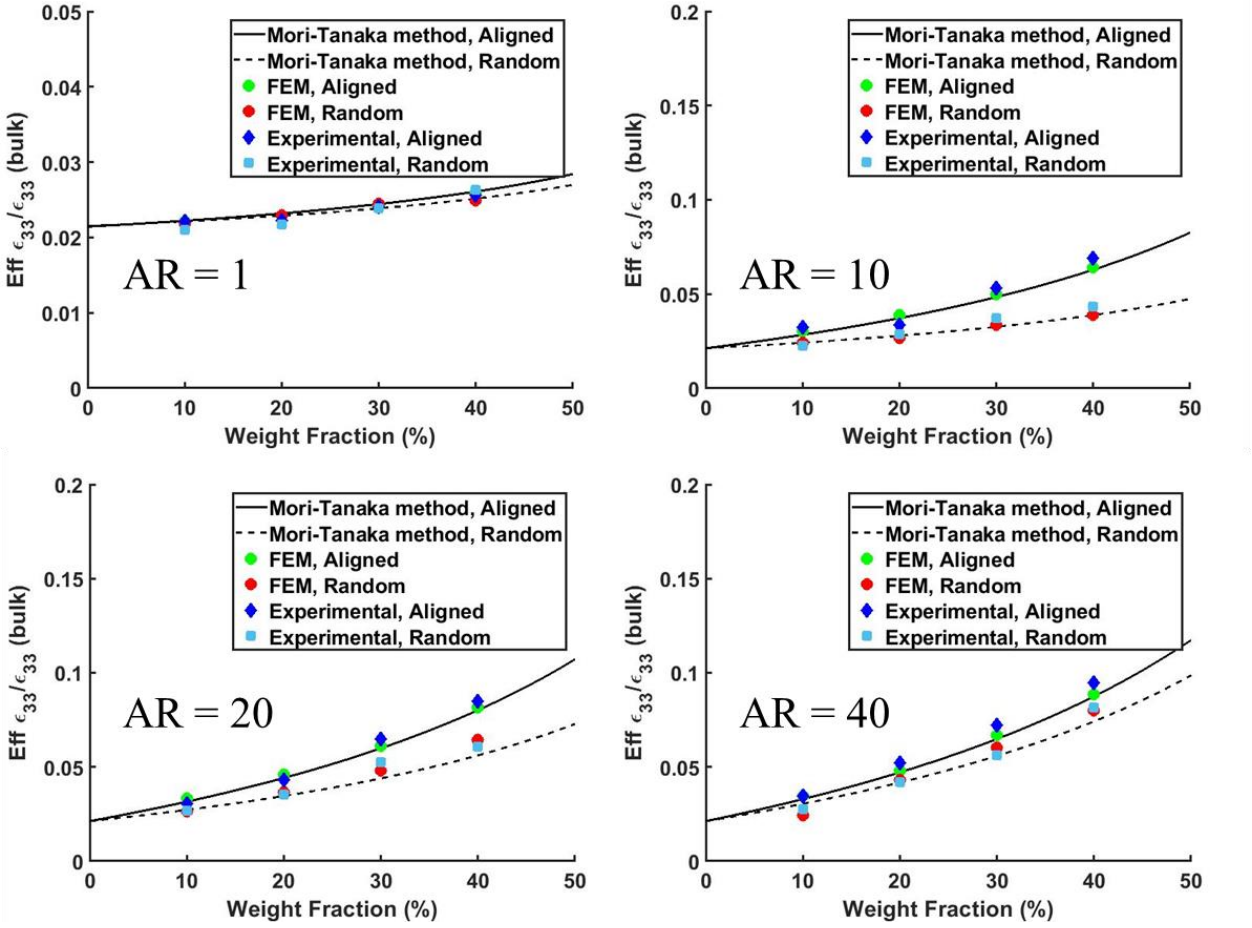

Figure 4-7: Comparison between the effective ε_{33} coefficients calculated using the Mori-Tanaka method, FEM and experimental measurement using the LCR meter for nanocomposites with aligned and randomly oriented nanowires with varying aspect ratios.

From Figure 4-7 it is evident that for all cases, at any given WF, the aligned nanowires have a higher ε_{33} constant compared to that of the randomly oriented nanowires. Moreover, it demonstrates that the results of experimental measurements of the ε_{33} constants have good

agreement with the FEM and the Mori-Tanaka method. The experimental data clearly shows that for a fixed WF, the direct write nanocomposite samples with aligned nanowires have significantly improved dielectric constant when compared to solution cast nanocomposites with randomly oriented nanowires.

A well-known approach to measure output power of an energy harvester is by measuring the voltage across a varying load resistor [22,53,177,178]. The AC power (P) delivered to a load can be calculated as

$$P = \frac{V_L^2}{R_L} = I_L^2 R_L, \tag{4-3}$$

in which V_L (measured by an electrometer) is the voltage across the load resistance (R_L) and the I_L is the current passing through it.

Figure 4-8a shows the power delivered across various load resistances for an energy harvester containing WF = 20% of aligned nanowires with different aspect ratios. For all aspect ratio cases, as the resistance increases from 200 kΩ to 10 MΩ, the power first increases rapidly and peaks at an optimal load resistance of $R_{opt} \approx 2$ MΩ, and then it declines slowly back to zero. According to Figure 4-8a, by increasing the aspect ratio of the nanowires from 1 to 40, a significant enhancement in delivered power can be achieved. Moreover, Figure 4-8a demonstrates that the optimal resistance for the highest power delivered to the load, decreases slightly as the aspect ratio increases. This can be explained by considering the fact that the optimal load resistance is proportional to the impedance of the device [85,244], i.e.

$$R_{opt} \propto \frac{1}{j\omega C} \tag{4-4}$$

where ω is the excitation frequency, C is the capacitance of the energy harvester and $j = \sqrt{-1}$. According to Eq. (4-4), R_{opt} is inversely proportional to capacitance of the device and capacitance is proportional to the dielectric constant, which increases with aspect ratio according to Figure 4-8a. Therefore, it is expectable that R_{opt} decreases slightly with increased aspect ratio. Figure 4-8b shows the AC voltage across the varying load resistor and the electrical current that passes through it. By increasing the load resistor from 0 to 10 MΩ, the voltage across the load resistor increase

rapidly from zero to approximately the open circuit voltage (~V_{oc}). At the same time, the current across the load resistor decreases from approximately the short circuit current (~I_{sc}) to zero when the load resistor reaches infinity. Figure 4-8b demonstrate that the open circuit voltage of the nanocomposites with AR = 40, 20, and 10 nanowires are 350, 262, and 180 mV, respectively. Moreover, the short circuit current of these nanocomposites is 191, 144, and 90 nA, respectively. These results further prove that by increasing the aspect ratio of the nanowires in the nanocomposite the output voltage and current can be improved.

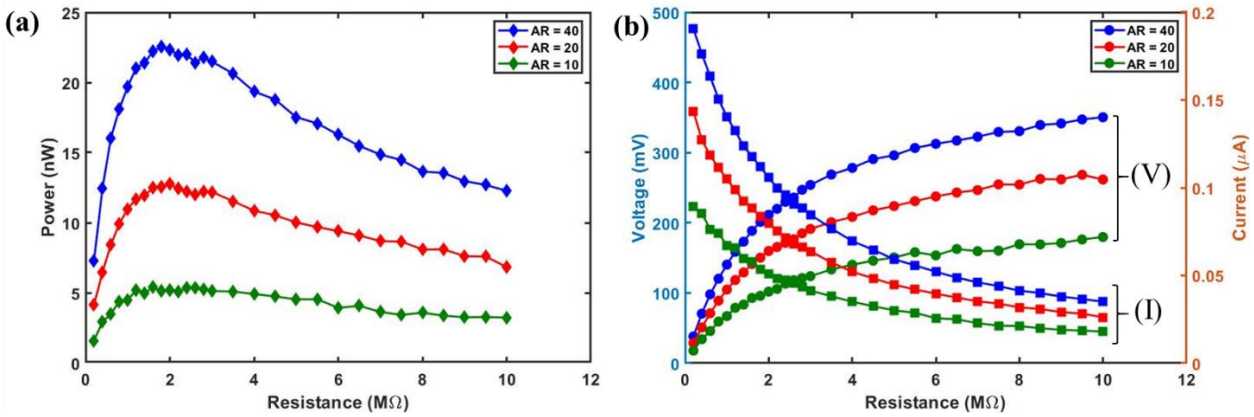

Figure 4-8: (a) Output power measurements of nanocomposite energy harvesters with aligned nanowires across varying load resistance. (b) AC voltage (V) and current (I) passing through a load resistor.

An important aspect of any energy harvester is its voltage coefficient (g, induced voltage under applied stress), which represents the material's figure of merit for piezoelectric energy harvesters. The piezoelectric voltage coefficient (g_{ij}) can be evaluated through either direct or converse piezoelectric effects using $g_{ij} = -(E_i/\sigma_j)_{\mathbf{D}}$ and $g_{ij} = (\varepsilon_j/D_i)_{\boldsymbol{\sigma}}$, respectively, which are equivalent thermodynamic definitions via Maxwell's relation. Since it is more convenient to implement the stress-free condition ($\boldsymbol{\sigma} = 0$) in the phase field simulation, the converse piezoelectric effect was employed to evaluate $g_{31} = \varepsilon_3/D_1 = d_{31}/\varepsilon_{33}$ through the piezoelectric strain coefficient d_{31} and dielectric constant ε_{33} (evaluated based on capacitance measurement).

Figure 4-9a shows the evolution of normalized dielectric constant (ε_{33}) and piezoelectric strain coefficient (d_{31}) for different ARs as the weight fraction increases (based on the Mori-Tanaka method). Similarly, the evolution of power and normalized voltage coefficient (g_{31}) for varying

ARs and weight fractions is depicted in Figure 4-9b. As shown in Figure 4-9a, for all nanocomposites with aligned and randomly oriented nanowires, the d_{31} coefficient increases more rapidly with increase in weight fraction than that of ε_{33}. Their ratio, which defines the voltage coefficient ($g_{31} = d_{31}/\varepsilon_{33}$), exhibits a local maxima for 20% < WF < 40%, depending on the AR of the nanowires. This fact is depicted in Figure 4-9b which shows as the WF of fibers increases, the g_{31} coefficients increase from its corresponding polymer matrix value to a maximum at a specific WF, and then decline to its corresponding bulk value at WF = 100%. For instance, the maximum g_{31} coefficient for nanowires with AR equal to 10, 20 and 40, coincide with WF = 35%, 27%, and 24%, respectively. This result indicates that the use of high AR nanowires can provide an energy harvester with a g_{31} coefficient greater than a bulk monolithic piezoelectric material, even when the majority of the nanocomposite is an inactive polymer phase. Furthermore, as the AR increases, the nanocomposites require less piezoelectric material to achieve the optimal g_{31} coefficient. This trend is crucial in designing an efficient energy harvester nanocomposite because nanocomposites with high aspect ratio nanowires have significantly higher g_{31} coefficient compared to the bulk piezoelectric material.

The voltage coefficient describes a materials capacity to function as an energy harvester and according to Figure 4-9b, it is evident that the g_{31} coefficients of aligned nanowires with any AR are significantly higher than that of randomly oriented nanowires. Therefore, it shows that the highest g_{31} coefficient can be achieved with high aligned ARs nanowires. Furthermore, given that the use of nanowires enables the g_{31} to be more than 3 times greater than that of bulk material, it can be expected that a nanocomposite energy harvester would greatly outperform bulk piezoelectric material. For instance, Figure 4-9b shows that for nanocomposites with WF = 30% and aligned nanowires with AR = 10, 20, and 40 the g_{31} coefficients are 3.5, 5.7, and 7.2 greater than that of bulk material ($g_{31(\text{bulk})}$ = -2.6E-3 V m/N). Due to the low curvature of the voltage coefficient curves around their maxima, it can be concluded that the g_{31} coefficients are relatively constant in the vicinity of their maxima. This fact is important since it indicates that for any AR there is a window of WFs that maximizes the g_{31} coefficients and gives the energy harvester designer some freedom when choosing the WF.

The results of FEM and experimental data for g_{31} coefficients presented in Figure 4-9b, demonstrate general agreement with the Mori-Tanaka method. While the experimental data

follows the same trend as the models, they slightly overestimate the g_{31} coefficients. This overestimation can be explained by consideration of the experimental data for dielectric constants shown in Figure 4-7. According to Figure 4-7, the underestimation of the ε_{33} coefficients in the models results in overestimation of the g_{31} coefficients.

The measured electrical power of the nanocomposites with aligned and randomly oriented nanowires with different ARs and WFs is depicted in Figure 4-9b. Each data point consists of an average of at least three samples' power measurement and its corresponding error bar. Figure 4-9b shows general agreement between the power and g_{31} coefficient trends. The aligned nanowires have significantly higher power output compared to that of the randomly oriented nanowires and this effect is even more significant at higher ARs. Specifically, the output powers of a nanocomposite containing aligned nanowires with AR = 10, 20, and 40 are 3.6, 3.2, and 3.4 times more than that of the randomly oriented nanowires, respectively. These results demonstrate that by increasing the voltage coefficient in the nanocomposite, via increasing nanowire AR and alignment, the output electrical power can be greatly enhanced and enables the energy harvester to be used for self-powered micro-electromechanical systems (MEMS) sensors.

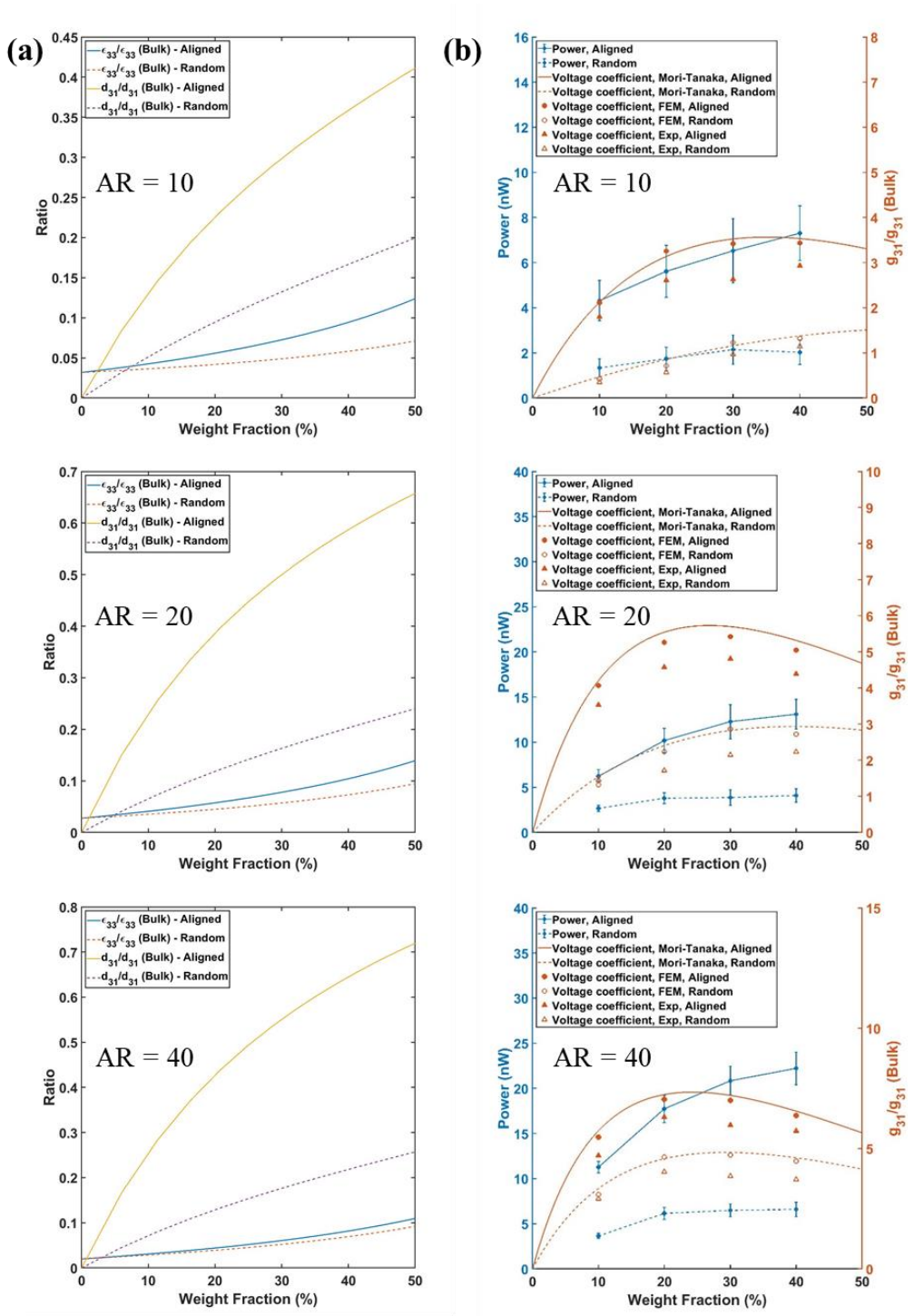

Figure 4-9: (a) Calculated normalized dielectric constant and piezoelectric strain coefficient based on the Mori-Tanaka method. (b) Comparison between the effective g_{31} coefficients calculated using the Mori-Tanaka method, FEM and experimental measurement along with corresponding measured power at various weight fractions.

Further electromechanical analysis of the energy harvester nanocomposites was performed by calculating the frequency response function (FRF) between the input acceleration and output voltage of the device. The FRF defines the relative magnitude and phase between the reference sensor (accelerometer) and output voltage. This produces an accurate measure of the input acceleration acting on the energy harvester, and the output piezoelectric voltage and current of the device. Two sets of nanocomposites composed of 30 wt% BTO nanowires (AR = 40) in PDMS matrix were prepared and bonded to stainless-steel cantilever beams. As mentioned in section 4.3.2, the first set of nanocomposites was printed longitudinally (type I) and the second set was printed laterally (type II). After poling the samples (with a similar method as mention in section 4.2) they were mounted on to an electromagnetic shaker and an amplified white noise signal was applied to the shaker. An accelerometer was mounted on the shaker and the output voltage and current of the fabricated energy harvester devices were measured using an electrometer. All input/output signals were acquired and generated through a data acquisition board (NI USB 4431) and analyzed using National Instrument Signal Express software.

Figure 4-10a shows the FRF between output open circuit voltage (V_{oc}) and short circuit current (I_{sc}) and input acceleration for the type I energy harvester and Figure 4-10b shows those of type II energy harvesters. Because both types of devices were fabricated with the same geometrical and material properties (same device dimensions, cantilever thickness and stiffness), both devices exhibit a resonance frequency around 31 Hz. It should be noted that the resonance frequencies on all FRF measurements coincide with the vibrational resonance frequency of the device (first resonance frequency), which results in maximum deformation and mechanical stress on the nanowires leading to the highest electrical outputs. According to Figure 4-10 all phase signals exhibit a 90° phase change at 31 Hz due to resonance. Figure 4-10 demonstrate the effects of inclusion's alignment on the energy harvesting performance of the devices. Based on this figure it is evident that at resonance, the type I energy harvester outperforms the type II by 6.3 dB V/g and 10.7 dB nA/g in V_{oc} and I_{sc}, respectively, proving the importance of nanowires' alignment in the direction of applied stress.

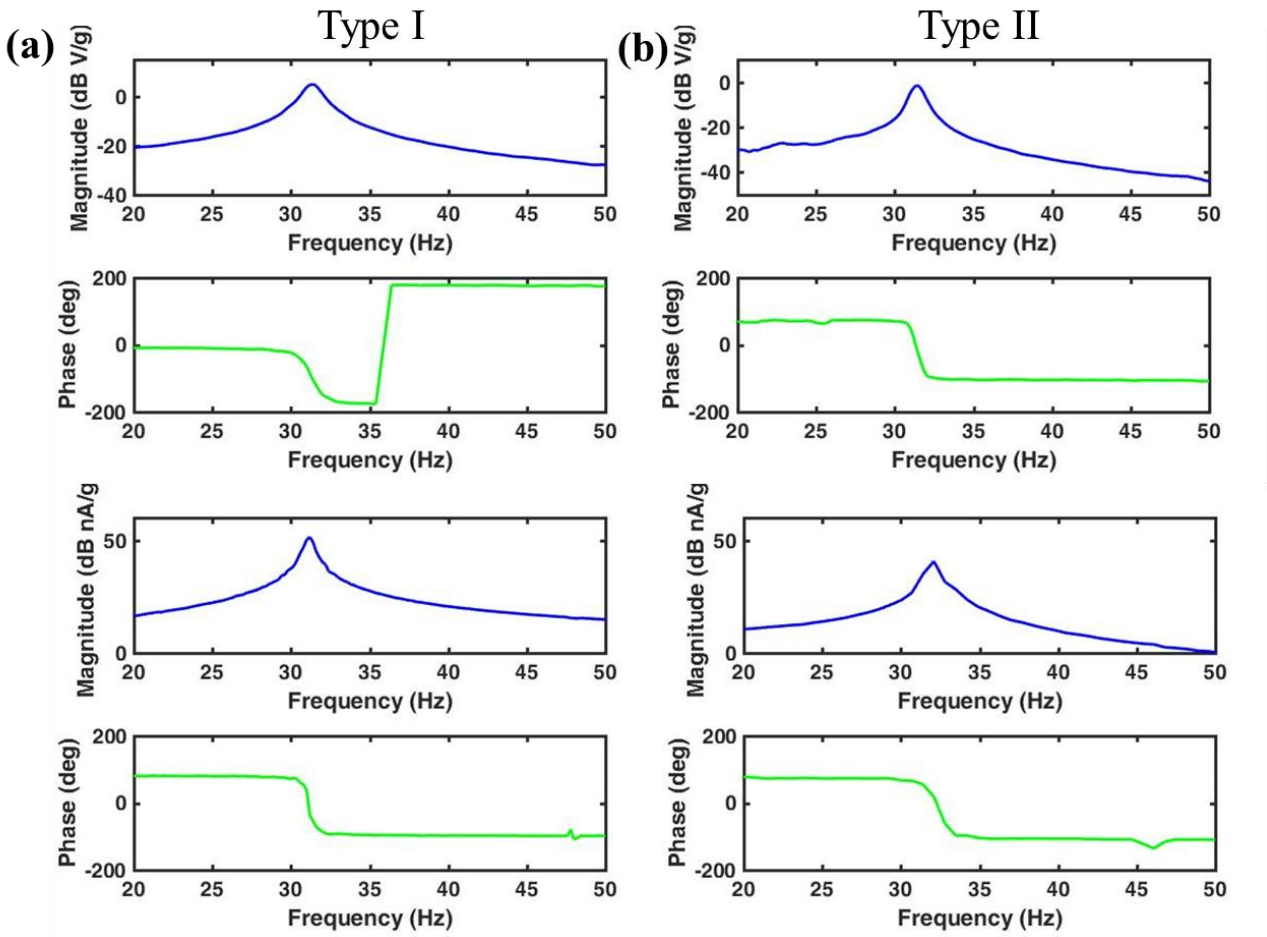

Figure 4-10: Frequency response function (FRF) of output open circuit voltage (V_{oc}) and short circuit current (I_{sc}) of (a) type I and (b) type II energy harvesters.

Further electrical characterization was performed on both types of devices. By applying sinusoidal excitations (at resonance) with varying amplitudes the V_{oc} and I_{sc} of the devices were measured. Figure 4-11 shows the output V_{oc} and I_{sc} of both types of devices when excited with 31 Hz sinusoidal accelerations with amplitude between 0.1 to 0.5 g (RMS). The 90° phase difference between input acceleration and output V_{oc} and I_{sc} due to resonance can be seen in Figure 4-11.

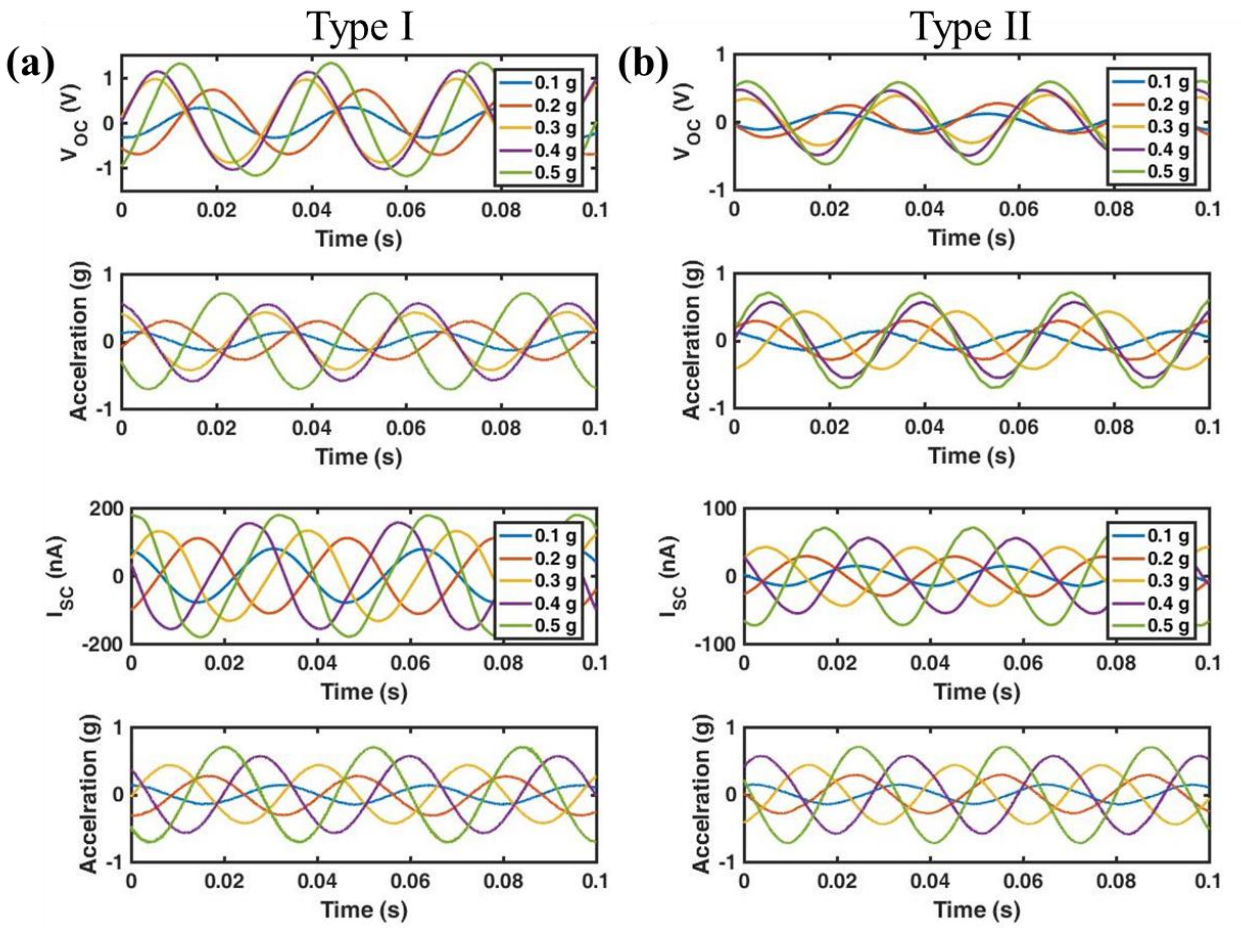

Figure 4-11: V_{oc} and I_{sc} characterization of (a) type I and (b) type II energy harvesters with sin-wave excitation at resonance.

Figure 4-12 demonstrates the root mean square (RMS) values of the V_{oc} and I_{sc} for both devices when excited by 31 Hz sin-wave input acceleration with varying levels. It shows relatively linear relationship between input and outputs of the devices when excited with up to 1 g RMS acceleration. Both figures 4-11 and 4-12 show that the type I device with nanowires aligned in the longitudinal direction of the cantilever have the higher output than that of the type II with nanowires aligned in the transverse direction.

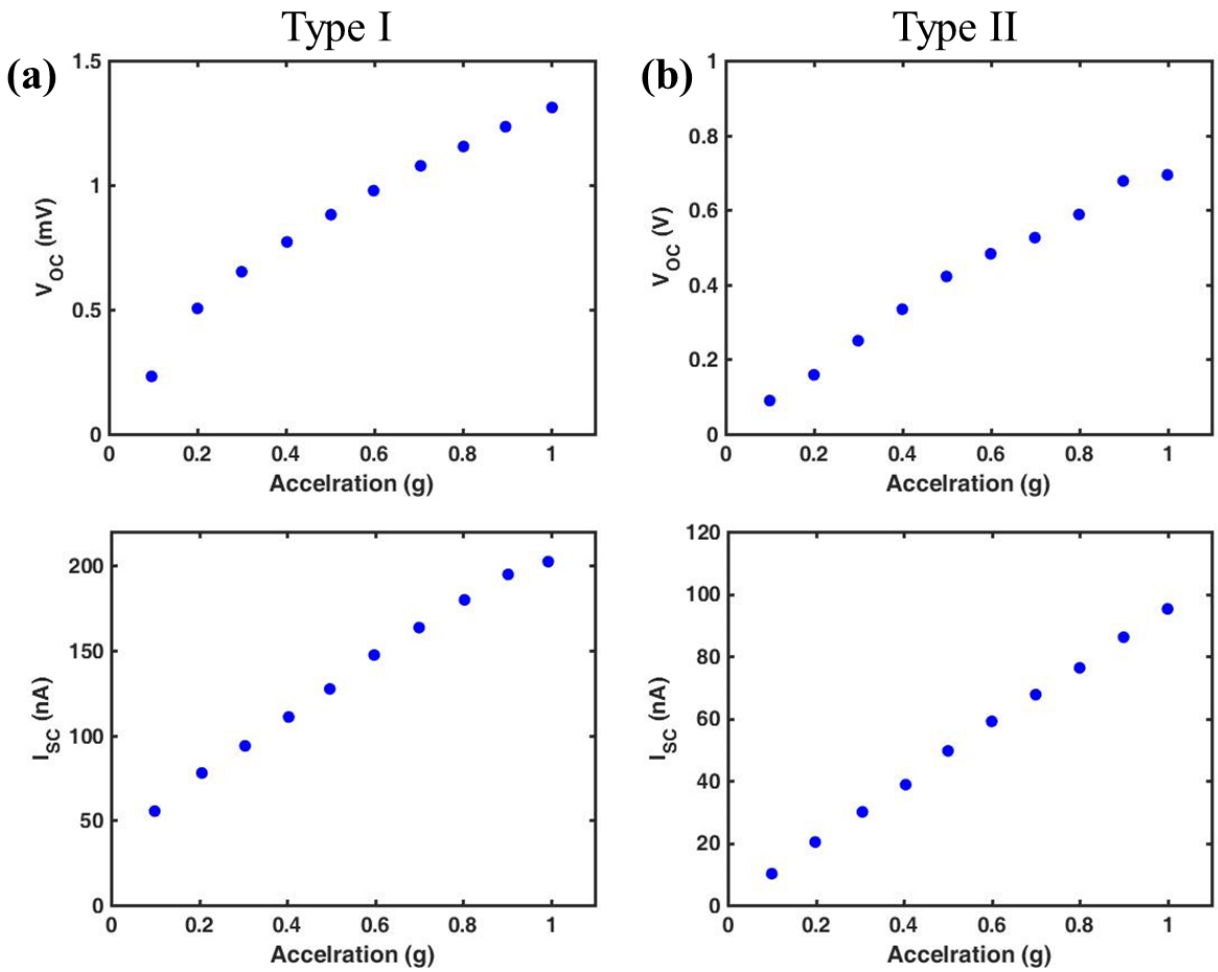

Figure 4-12: The RMS values of V_{oc} and I_{sc} characterization of (a) type I and (b) type II energy harvesters with sin-wave excitation at resonance.

In chapter 2, FEM was implemented to study the effect of inclusions gradual misalignment. It was found out that slight misalignment in the $15° \leq \theta \leq 20°$ range can increase the d_{31} coefficient significantly compared to an aligned nanocomposite. This effect was contributed to reduction in nanocomposite stiffness when misalignment was introduced which was numerically proven by an FEM case study analysis. Here, by comparing three different nanocomposites with varying degree of nanowires misalignment, the aforementioned effect is verified experimentally. As shown in Figure 4-13, the samples (denoted by A, B, and C) are arranged by their alignment (A: the most aligned, and C: the least aligned). The FRF of the output open circuit voltage of each sample is shown in Figure 4-13. According Figure 4-13, the magnitude of sample B's FRF is the highest among these samples (3.8 dB, and 12.2 dB higher than sample A and C, respectively). This result

show that a small amount of nanowires misalignment can dramatically improve the output voltage of the nanocomposite energy harvester. These findings were confirmed by DMA tests. By preparing six individual samples of each nanocomposite A, B, and C, the average d_{31} coefficients were calculated. As illustrated in Figure 4-13, nanocomposite A, B, and C's d_{31} coefficients are 14.55 pm/V, 17.33 pm/V and 5.42 pm/V, respectively. Therefore, it is demonstrated that by increasing the misalignment from sample A to B, 18% improvement in d_{31} coefficient can be achieved.

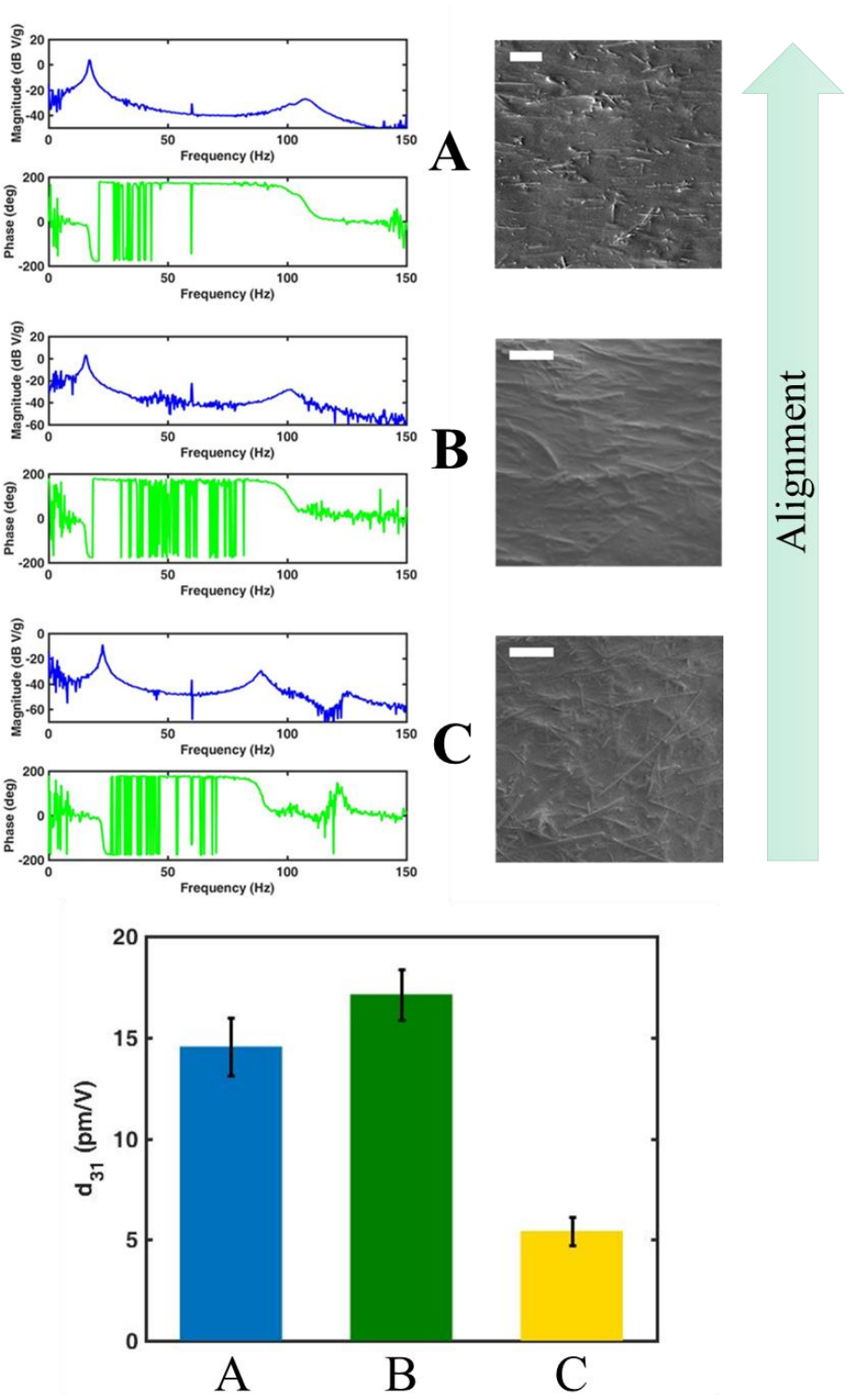

Figure 4-13: The FRF response of three nanocomposites with varying degrees of alignment (scale bars are 5 μm).

4.5. Conclusions

Piezoelectric nanocomposites have many advantages over monolithic materials and can be used to fabricate highly flexible energy harvesters; however, the coupling is generally too low for the use in most applications. To solve this issue, researchers have developed nanowire-based nanocomposite energy harvesters which provide flexibility and high coupling coefficients. In this chapter, the theoretical models developed in chapter 2 were experimentally tested by fabricating direct write nanocomposite energy harvesters. The model was formulated using the Mori Tanaka approach and was shown to have excellent agreement with the FEM. It was demonstrated that the aspect ratio and alignment of the active phase can significantly affect the performance of the nanocomposite in terms of piezoelectric strain and voltage coefficients, and voltage, current and power output. For instance, it was found out that by using nanowires with AR = 40, the voltage coefficient of the nanocomposite can outperform that of the bulk piezoelectric material by more than seven times due to the ability to vary the dielectric and coupling coefficients. It was also demonstrated that the g_{31} coefficient does not increase continuously with WF of the nanowires in the nanocomposite. Rather, depending on the aspect ratio of the nanowires, there is an optimum WF in which the highest possible g_{31} coefficient can be achieved. For example, the results showed that for nanocomposites with aligned nanowires with AR = 10, 20 and 40, the highest possible g_{31} coefficients coincide with WF = 35%, 27% and 24%, respectively. Further increase in WF results in a reduction of the g_{31} coefficient. The relationship between the g_{31} coefficient and power measurements was carried out on a variety of nanocomposite energy harvesters with different aspect ratio nanowires. The results show that the power delivered to a load resistor can be enhanced significantly by incorporating high aspect ratio nanowires in the nanocomposite. Specifically, it was demonstrated that the nanocomposite containing aligned nanowires with AR = 40 has more than 3 times higher power compared to that of a nanocomposite with AR = 10. The effects of slight nanowires misalignment that was presented in Chapter 3 were experimentally verified. It was experimentally shown that by allowing the nanowires to have a little amount of misalignment the output voltage and d_{31} coefficient can be improved. The results of this chapter can be used to establish a robust route for modeling of piezoelectric nanocomposite energy harvesters and mitigating the power constraints by using high AR nanowires.

Chapter 5: Extreme Temperature Energy Harvesting

5.1. Introduction

With the increasing demand for sensors to monitor the conditions in extreme environments, such as those found in turbine engines [280], oil and gas exploration [281], hypersonic aircraft rockets [282], etc., the development of energy harvesting devices that exhibit both a high coupling coefficient and high temperature stability is a necessity. However, to the best of the authors' knowledge, no demonstration of nanoscale piezoelectric based energy harvesters have been developed for use in extreme temperatures. ZnO is one of the most researched piezoelectric materials that can potentially be used in extreme environments. This is mostly due to its biocompatibility, ability to exhibit diverse configurations, and intrinsic piezoelectric properties [62,65,283]. However, it exhibits very small piezoelectric strain and coupling coefficients which makes it useless for high temperature engineering applications [85]. Other potential candidates for this purpose are ferroelectrics; however, ferroelectric materials exhibit a Curie temperature (T_c) at which point the material undergoes a phase change and produces a centrosymmetric cubic unit cell. Upon heating above the Curie temperature, the ceramic settles into the low energy state with zero net polarization thus losing its piezoelectricity and ability to generate useful electrical energy. Therefore, for energy harvesting in extreme environments, a high T_c material with decent piezoelectric performance is needed. Among the many ferroelectric materials, $PbTiO_3$ (PTO) is chosen for this research due to its high piezoelectricity at extreme temperatures (T_c = 490 °C) [272,284].

In this chapter first using a two-step synthesis method, vertically aligned ultra-long arrays of PTO nanowires are synthesized. Then, a non-flexible, non-composite energy harvester is developed to examine the feasibility of high temperature energy harvesting using PTO nanowires. The results show that it can withstand extreme temperatures above 300 °C while maintaining output voltage, current, and power. Next, after confirming the feasibility of PTO-based energy

harvesters in converting mechanical energy to electrical energy at temperatures above 300 °C, a flexible nanocomposite energy harvester based on freestanding PTO nanowires is developed. Unlike the previous nanocomposites that were discussed in Chapters 3 and 4, PDMS cannot be used as the matrix in high temperature applications, because it is a thermoplastic and easily decomposes in these conditions. Therefore a new polymeric matrix with superior thermal stability and flexibility with low dielectric loss is needed. Here, an aromatic polyimide is chosen as the matrix material since it satisfies all those conditions. Here, a novel approach is used to synthesized the poly(amic) acid precursor which is then mixed with PTO nanowires and imidized at elevated temperatures to produce a nanocomposite energy harvester which includes both an active phase (PTO) and polymer matrix able to withstand the extreme temperatures above 250 °C. The results show that the energy harvester can generate stable voltage and power at conditions ranging from room temperature to 250°C.

5.2. High temperature piezoelectric materials

Assorted piezoelectric materials have been thoroughly tested for high-temperature applications, including aluminum nitride (AlN), quartz (SiO_2), gallium orthophosphate ($GaPO_4$), langasite ($La_3Ga_5SiO_{14}$, LGS), lithium niobate ($LiNbO_3$), and lead titanate ($PbTiO_3$) [1,84,285,286]. Table 5-1 lists various piezoelectric materials that can be used at high temperatures along with their corresponding electromechanical properties. Each compound has its own characteristic advantages and disadvantages for use in high temperature applications. The most popular high temperature piezoelectric material, quartz, has a high mechanical quality factor, exceptional high-temperature stability, and high electrical resistivity ($>10^{17}\ \Omega$ at room temperature). The drawbacks of quartz include its low electromechanical and piezoelectric coefficients, α to β phase transition temperature at 573 °C, and high losses above 350 °C. These properties limit its use for high-temperature applications [20,287].

$LiNbO_3$ has high electromechanical coefficients and a reported T_c of about 1150 °C. However, its limited resistivity, chemical decomposition beginning at 300 °C, increased attenuation and intergrowth transition, and loss of oxygen to the environment limits the practical applications of Lithium niobate to around 600 °C. The use of lithium niobite is also constrained by its brief lifetime

at elevated temperatures because of its aforementioned decomposition (10 days at 400 °C and 0.1 days at 450 °C) [288-290].

$GaPO_4$ has both a high electrical resistivity and mechanical quality factor, similar to quartz, but it has higher electromechanical coupling and greater piezoelectric sensitivity up to the α to β phase transition (<970 °C). $GaPO_4$ crystals are characterized by fairly sharp resonances compared to other high-temperature piezoelectric materials [291]. The limitations of this material lie in its restriction to operation temperatures below 700 °C due to a decreased mechanical quality factor as a result of increased structural disorder [84,285].

Langasite crystals possess no phase transition preceding their melting point (1470 °C). These crystals have been researched extensively for high-temperature utilization, such as bulk acoustic wave (BAW) and surface acoustic wave (SAW) applications. One disadvantage of langasite is that its oxygen vacancies transport and diffuse in the lattice, limiting the performance of langasite sensors and resulting in low electrical resistivity and low quality factor at higher temperatures [292,293].

Aluminum nitride (AlN), a non-ferroelectric material that melts around 2200 °C, is another common high-temperature piezoelectric material. Thin films of AlN have been utilized as high frequency ultrasonic transducers and surface acoustic wave sensors, with the AIN maintaining its piezoelectric properties up to 1150 °C. However, mass production has continued to be an obstacle because of challenges in creating large quantities of high quality piezoelectric materials from AlN [294-296].

Lead titanate ($PbTiO_3$) is a member of the lead zirconate titanate (PZTs) family with the highest T_c of about 490°C and high piezoelectric strain coefficient and quality factor (Q). PZT has a perovskite structure and is a solid solution of tetragonal $PbTiO_3$ and orthorhombic $PbZrO_3$. There are a multitude of polarization directions available in this structure. Thus, compositions near the morphotropic phase boundary at approximately 53:47 $PbZrO_3$ to $PbTiO_3$ ratio are easily poled to a high remnant polarization and exhibit extremely high values of electromechanical coupling coefficients and electrical permittivity. However, the addition of $PbZrO_3$ to the $PbTiO_3$ crystal decrease the T_c up to 260 °C which limit its application at extreme temperatures. Therefore, several

modifications have been developed to optimize specific electrical and mechanical characteristics of $PbTiO_3$, similar to PZT. Many commercial compositions of $PbTiO_3$ are doped with samarium or calcium but this still lowers the T_c to around 240°C [1,286]. In this chapter, $PbTiO_3$ was chosen for high temperature energy harvesting applications due to its decent electromechanical properties, ability to form a nanowire structure using inexpensive hydrothermal reactions and high T_c.

Table 5-1: High temperature piezoelectric materials and their electromechanical properties.

	Material	T_c (°C)	κ/ε_0	Loss factor	Quality factor (Q)	k_{33}	d_{33} (pC/N)	Refs.
$PbZr_xTi_{1-x}O_3$	PZT4	328	1300	0.004	500	0.71	289	[297,298]
$PbZr_xTi_{1-x}O_3$	PZT8	300	1000	0.004	1000	0.64	225	[297,298]
$Pb(Zr,Ti)O_3$–$Pb(Sb,Mn)O_3$-Yb	PZT-PSM-Yb	250	550	-	1350	0.61	160	[299]
$Pb(Mg_{1/3}Nb_{2/3})O_3$–$PbTiO_3$	PMN–PT	175	2100	-	300	-	350	[300]
$0.3BiScO_3$–$0.6PbTiO_3$–0.1 $Pb(Mn_{1/3}Nb_{2/3})O_3$	BSPT-PMN	400	500	-	1000	-	80	[301]
$PbTiO_3$	PTO	490	190	-	1300	0.45	56	[272,284,298]
$KNbO_3$	KNO	417	48	-	7600	0.4	18.5	[297,298]
$LiNbO_3$	LNO	1150	30	-	10000	0.16	6	[297,298]
$Pb(Yb_{0.5}Nb_{0.5})O_3$-$x$$PbTiO_3$, x = 46	PYNT46	325	2500	0.01	70	0.9	2200	[302]
(1-x)$BiScO_3$-$x$$PbTiO_3$, x = 0.43	BSPT57	402	3000	0.04	70	0.9	1150	[303]
SiO_2	SiO_2	573	4.5	-	-	-	-	[304]
$(BaPb)Nb_2O_6$	BPN	400	300	-	-	0.3	85	[305]
$Na_{0.5}Bi_{4.5}Ti_4O_{15}$	NBT	600	140			0.15	8	[306]

5.3. High temperature energy harvester based on vertically aligned arrays of PTO nanowires

5.3.1. Synthesis procedure

A new synthesis method is developed to obtain nanowires with a length of 40 μm and an aspect ratio (AR) of 75 by utilizing an inexpensive two-step hydrothermal reaction. Through optimization of the synthesis parameters, the length and aspect ratio of the nanowires are engineered to obtain high deformability and compliance in order to increase the piezoelectric voltage. The synthesis method for obtaining ultra-long PTO nanowires consists of two separate hydrothermal reactions. In the first step, ultra-long arrays of $Na_2Ti_3O_7$ nanowires were grown on a titanium foil substrate (MTI Corporation, 99.9%, 100 μm thick). The substrates were cut in 1 cm^2 square sections and sonicated for 30 minutes in deionized (DI) water, acetone and 2-propanol solution with a 1:1:1 volume ratio, followed by a DI water rinse. Then the cleaned substrates were oxidized at 750 °C (15 °C/min) for 8 hours in a furnace and cooled down slowly to room temperature at a rate of 50 °C/hour. Next, two oxidized titanium foil substrates were immersed in a Teflon lined autoclave reactor (Parr Instrument Co.) filled with 30 ml (Fill Factor: 67%) of 12 M sodium hydroxide aqueous solution (97% Alfa Aesar). The reactor was then maintained at 210 °C in a convection oven for 8.5 hours and cooled down in ambient air. The resultant substrates containing high aspect ratio vertically aligned $Na_2Ti_3O_7$ nanowires were then washed gently with DI water. Then, the resulting nanowires were washed and soaked in a 0.2 M hydrochloric acid (Fisher, 30%). As a result, Na^+ ions were substituted with H^+ ions in the nanowires crystal structure yielding hydrogen titanate ($H_2Ti_3O_7$) nanowires [243]. To avoid nanowire tip wicking, reaction parameters were controlled so that the nanowire arrays were sufficiently rigid [307]. This hydrothermal reaction and ion exchange resulted in ultra-long, vertically aligned arrays of $H_2Ti_3O_7$ nanowires, which then act as the precursor for the next hydrothermal reaction.

In the second hydrothermal reaction, the H_2TiO_3 precursor substrate was immersed in a Teflon lined autoclave containing 20 ml CO_2 free DI water (Fill Factor: 44%), 0.662 g lead nitrate (Acros Organics, 99%) and 0.16 g potassium hydroxide (Alfa Aesar, flake, 85%). The solution was saturated with nitrogen and kept at 200 °C for 4 hours. During this reaction, Pb^{+2} ions replaced H^+ ions in the crystal structure while retaining the nanowires' morphology. The resultant ultra-long PTO nanowire arrays were then washed in a dilute 0.2M HCl solution to remove any unwanted byproducts, such as lead oxide (PbO) and other salts. Finally, the samples were covered with PbO

powder (MP Biomedicals, LLC) and heat treated at 600 °C in a furnace. This heat treatment is essential for two reasons. First, it anneals the nanowires creating a more thorough perovskite structure. Second, the high temperatures remove any hydroxyl groups resulting from the hydrothermal reaction that increase the nanowire conductivity thus screening the generated piezoelectric charges [190].

It should be noted that the concentration of reactants, reaction time, and temperature are the main contributors to the resultant nanowire morphology and degree of PTO conversion. Usually, an increase in these parameters will result in a more complete conversion but degrades the nanowire morphology. However, decreasing these parameters preserves the morphology of the precursor but results in incomplete conversion. Therefore, there is a trade-off between conversion efficiency and morphology preservation to consider when optimizing the conversion parameters.

Scanning electron micrographs (SEM, TESCAN VEGA3 LM) of the $Na_2Ti_3O_7$ and PTO nanowires are illustrated in Figure 5-1a and b, and Figure 5-1c and d, respectively. As shown in the figure, the average length of the nanowires is about 40 μm and the aspect ratio is about 75. From this figure, it is evident that the diameter of the PTO nanowires increased after substitution of Na^+ with H^+ and then Pb^{+2}. This is because Pb^{+2} ions have a larger atomic radii than Na^+ ions, and this conversion increases the size of the unit cell which results in swelling of the nanowires.

The Chemical composition of the PTO nanowires were analyzed using energy dispersive spectroscopy (EDS). EDS results are depicted in Figure 5-1e which demonstrate that the nanowires are composed of Pb, Ti, and O. Note that C peak is due to the carbon tape used for holding the sample. To confirm the conversion from $Na_2Ti_3O_7$ to PTO, the crystallographic structure of these nanowires is analyzed using x-ray diffraction. As shown in Figure 5-1f, the diffraction pattern of the nanowires match completely with perovskite PTO (Joint Committee on Powder Diffraction Standards, Card No. 06-0452). In this figure, the red ovals represent the PTO peaks and green squares represent the excessive PbO residue in the material. Further characterization was performed to analyze the phase transition behavior of the PTO nanowire arrays near Curie temperature. The tetragonal phase in PTO transfers to cubic phase around Curie temperature. This phase transition is associated with a change in specific heat constant of the material which can be measured using differential scanning calorimeter (DSC) [243,308].

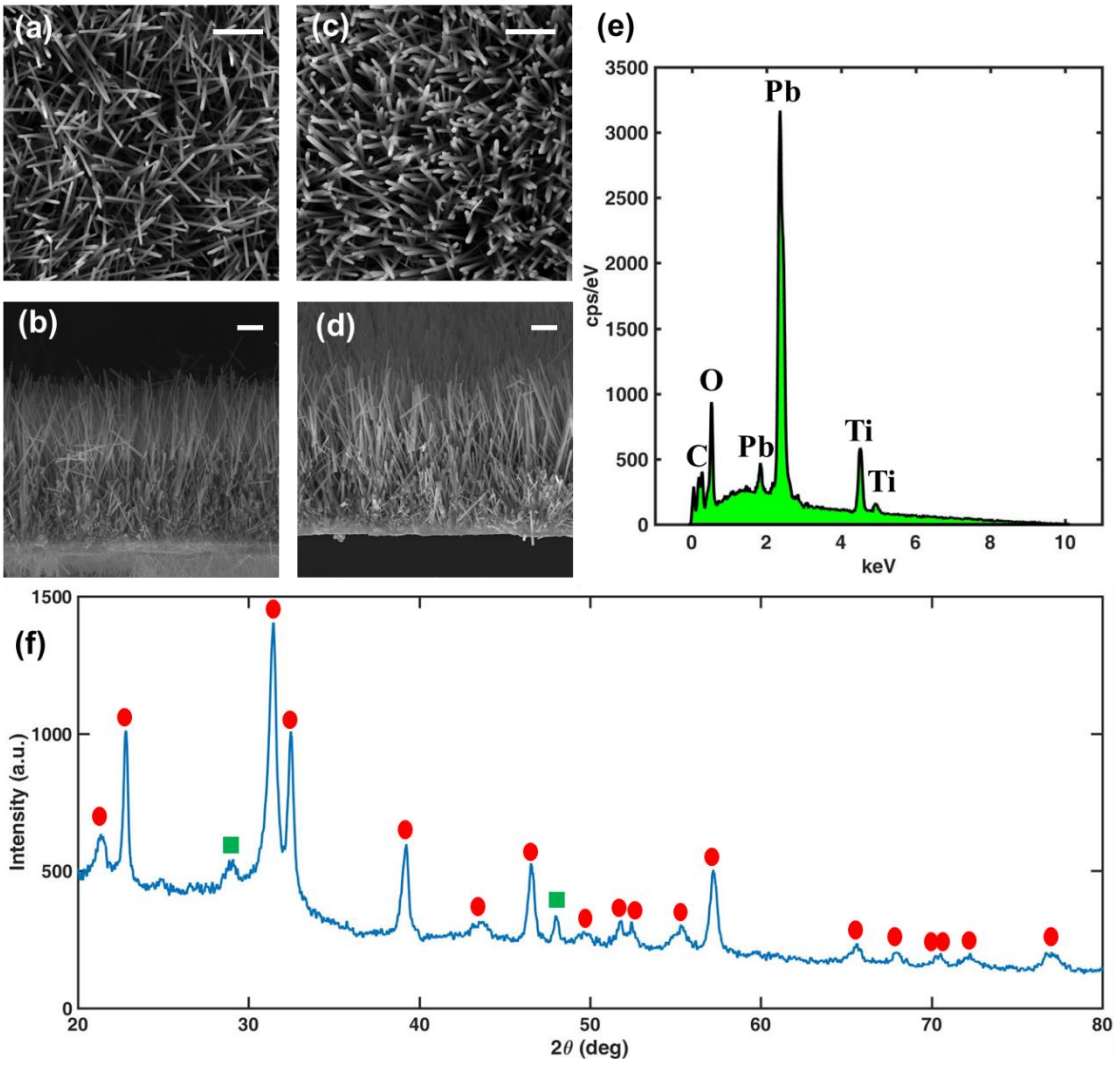

Figure 5-1: SEM micrographs of vertically aligned nanowire arrays: (a) top-view of $Na_2Ti_3O_7$ nanowires (b) side-view of $Na_2Ti_3O_7$ nanowires (c) top-view of PTO nanowires (d) side-view of PTO nanowires (Scale bars are 5µm). (e) An energy dispersive spectrum of PTO nanowires showing Pb, Ti and O peaks (f) XRD pattern of PTO nanowires (JCPDS Card No. 06-0452, red ovals denote the PTO peaks and green squares denote the small PbO peaks).

Upon successfully synthesizing the PTO NW array (described in Chapter 3), a resonating beam-based energy harvesting device is fabricated, and its application in harvesting vibrational energy at extreme temperatures above 300 °C is demonstrated through the characterization of open circuit voltage and power measurements. The resonating beam-based energy harvester allows for a lower resonance frequency which is well-suited for ambient vibration energy harvesting [85]. Using this device configuration, the feasibility of high temperature energy harvesting using PTO nanowires is tested. Upon successful fabrication of the non-flexible device and demonstration of

the PTO's capability to transform mechanical energy to electrical energy at temperatures above 300 °C, another flexible energy harvester based on PTO nanowires for extreme temperature applications is fabricated and characterized.

5.3.2. Fabrication of the energy harvester device

To fabricate the energy harvester device, a small piece of PTO NW arrays was removed from the oxidized titanium foil substrate by washing it with diluted HCl acid and subsequently soaking it in ethanol [244]. The oxidation layer under the NW array provided a support structure which allowed the NW array to stay intact during removal from the foil substrate. It was then transferred and bonded to a rectangular shim stock stainless steel beam (5 by 25 mm) using conductive silver paint (SPI Supplies). To increase the adhesion to the beam and conductivity of the silver paint, the stainless shim with the nanowire array was cured at 80 °C in a vacuum oven for 2 hours. The beam served as both the bottom electrode contacting the NWs and as a spring to transfer mechanical energy from the base acceleration to the NWs using an impact mechanism [85]. The beam can be effectively considered as a frequency conversion device to allow tuning of the beam's frequency to match that of the vibration in the harvester's environment, since an impact will excite the nanowires independent of their natural frequency. Furthermore, a thin layer of gold was sputtered (PELCO SC-7 Auto Sputter Coater) on a square piece of borosilicate glass (5 by 5 mm) and attached to the base of the device to serve as the top electrode for the NWs. Therefore, the NW arrays were sandwiched between the stainless steel beam and the gold sputtered glass as electrodes one and two, respectively. As shown in Figure 5-2a, both electrodes were assembled on a piece of borosilicate glass for handling and installing of the device on a permanent magnet shaker. Lastly, the output voltage wires were attached to the electrodes using silver paint and silver epoxy.

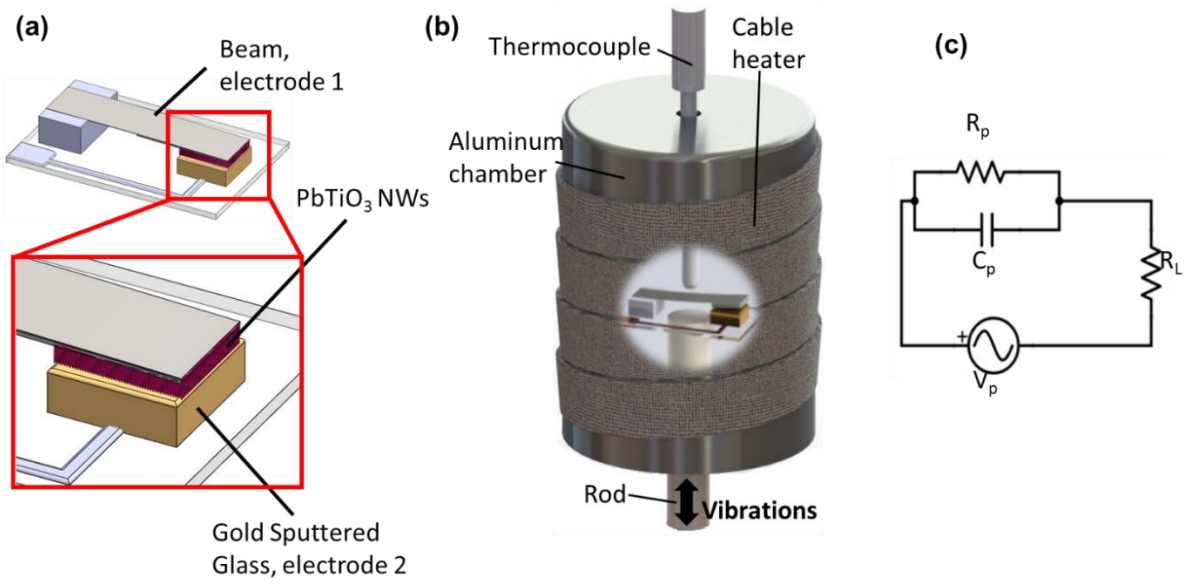

Figure 5-2: Schematics of (a) the fabricated energy harvester device, (b) the designed setup to test the device at high temperatures with (c) the equivalent electrical circuit of the device.

After device fabrication, the NW arrays were poled by applying an 89kV cm^{-1} DC electric field between the electrodes for 10 hours. Poling of the PTO dipoles is an essential step due to the random orientation created through the mentioned synthesis process. Poling aligns the dipoles in the direction of the source vibration and thus increases the efficiency of the mechanical to electrical energy conversion. It should be noted that there is a dense layer of PTO film near the base of the NWs that prevents breakdown or shorting during the poling process [236].

5.3.3. Electrical Characterization

The energy harvester is excited using a permanent magnet shaker (LDS, V408). The compressive force generated from the inertial force of the vibrating beam on the NWs results in charge generation through the direct piezoelectric effect, thus generating an alternating voltage that can be used in an external load [85,243]. The equivalent electrical circuit of the device is shown in Figure 5-2c. The piezoelectric voltage, V_p, is generated from a dynamic load on the NWs and is in series with the impedance of the device. Its impedance consists of the piezoelectric leakage resistance, R_p, and the capacitance of the device, C_p, which are connected in parallel. Here, R_p is ignored because it is two orders of magnitude higher than the impedance of the source capacitance ($X = 1/j\omega C_p$) [85]. V_L is the output voltage measured across the load resistor (R_L)

which was measured with a unity gain, high impedance (1TΩ) voltage follower (Linear Technologies LTC6240CS8 CMOS Op Amp) with a very low input bias current of 0.2 pA. All other input/output signals were generated and acquired through a data acquisition board (NI USB 4431) and analyzed using National Instrument Signal Express software.

Figure 5-2b illustrates the experimental setup for testing the performance of the energy harvesting device in a high temperature environment. The PTO energy harvester was bonded to a glass-mica ceramic rod using high temperature adhesive and coupled to the shaker. To test the device at higher temperatures, a heat cable (McMaster, 156 W) was wrapped around an aluminum cylinder which was fixed to the shaker body via insulating fire bricks. The heater was connected to a temperature controller (Omega, J type) and fed by a thermocouple (Omega, J type) that was inside the cylinder to adjust the temperature of the device and the air surrounding it. The aluminum cylinder has two functions. First, it acts as a high temperature chamber that maintains the temperature of the device, and second, when connected to the ground, it acts as a Faraday cage and attenuates the extrinsic power-line noise on the output of the device. The voltage follower was insulated from the heat and placed in close proximity to the device to decrease the effect of parasitic capacitance that could decrease the performance of the energy harvester [85,236].The PTO energy harvester was excited with a 187 Hz symmetric square wave, which coincides with the resonance frequency of the beam, and the open circuit voltage (V_{oc}) and short circuit current (I_{sc}) were measured while the temperature was increased from room temperature to 375 °C in 50 °C increments. At each increment, the device was maintained at the specified temperature for 30 minutes to ensure thermal equilibrium. As shown in Figure 5-3a, the device generated a peak value of 0.56 V for temperatures ranging from 25 °C to 300 °C, but beyond 300 °C, the output voltage decreases gradually. This decrease in output is due to the fact that the aligned dipoles start to orient randomly as the temperature approaches the Curie temperature [298], thus decreasing the piezoelectric performance of the device. Figure 5-3b shows similar behavior for the peak-to-peak value of the open circuit voltage at each temperature. As shown in Figure 5-3c and 5-3d, the I_{sc} exhibited similar trend as V_{oc}. These figures demonstrate that the fabricated device is capable of generating stable current ($I_{sc(pp)}$ = 5.2 µA) up to 350 °C. Beyond 350 °C, the I_{sc} start declining as the nanowires approach the Curie temperature.

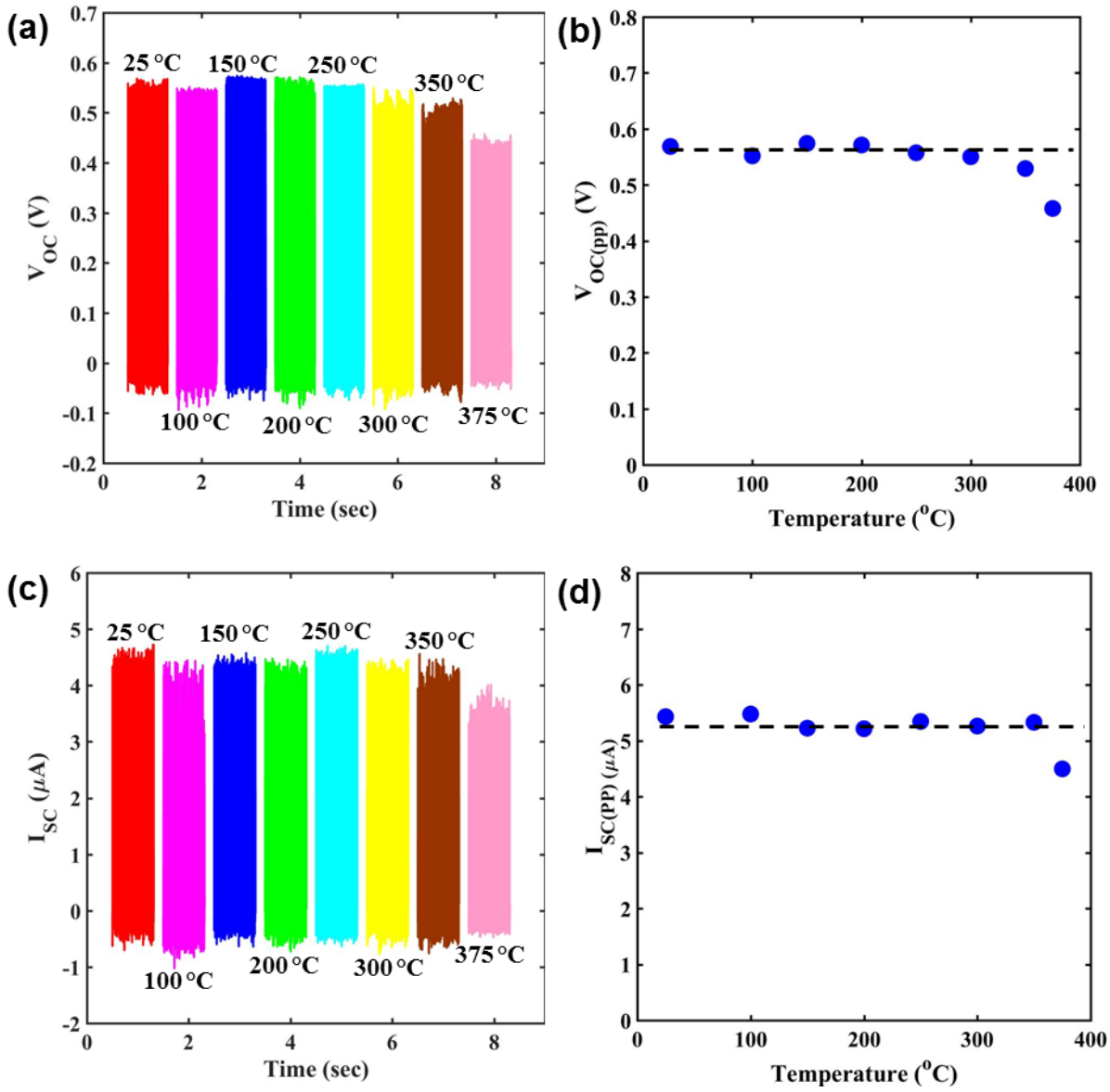

Figure 5-3: (a) The open circuit voltage of the PTO nanowire arrays energy harvester device at various temperatures with (b) corresponding peak-to-peak values of open circuit voltage. (c) The short circuit current of the PTO nanowire arrays energy harvester device at various temperatures with (d) corresponding peak-to-peak values of short circuit current.

Further performance characterization of the device is completed using through power measurements. By measuring the voltage across a varying load resistor, the AC power delivered to the load can be calculated according to Eq. 5-1 [190,236]:

$$P_L = I_L^2 R_L = \left(\frac{V_p}{Z_s + R_L}\right)^2 R_L = \frac{V_L^2}{R_L}, \tag{5-1}$$

in which P_L is the generated power, I_L is the electrical current passing through the load, and Z_s is the inherent impedance of the device, respectively. The power density can be calculated as

$$p_L = \frac{P_L}{A_{NWs}}, \tag{5-2}$$

where p_L is the power density and A_{NWs} is the area of the nanowire arrays ($A_{NWs} \approx 0.3$ cm^2). At each temperature, the voltage across the load (V_L) was measured to calculate the power. As shown in Figure 5-4a, peak to peak and root mean square (RMS) values of V_L increased with increasing load resistor and slowly saturates to the open circuit voltage of the energy harvester device. Similarly, according to Figure 5-4b, starting from the short circuit current, the peak to peak and RMS values of I_L decreased as the load resistor reached 3 MΩ. Using Eq. 5-1, the AC power from the device can be calculated. Figure 5-4c depicts the evolution of p_L with a varying load resistor (R_L). According to the figure, p_L increased rapidly as the load resistor increased from 10 KΩ to an optimal peak-to-peak power value of 22.3 mW m^{-2} (156 μW m^{-2} (RMS)) at a $R_{L(optimal)}$ of 200 kΩ in room temperature conditions. The output power then decreased beyond $R_{L(optimal)}$ as the load resistor traced up to 3 MΩ because the voltage across the load resistor saturates toward V_{OC}. Furthermore, as the temperature increased, the peak power delivered to the load resistor decreased to 13.0 mW m^{-2} (78.7 μW m^{-2} (RMS)) at 375 °C.

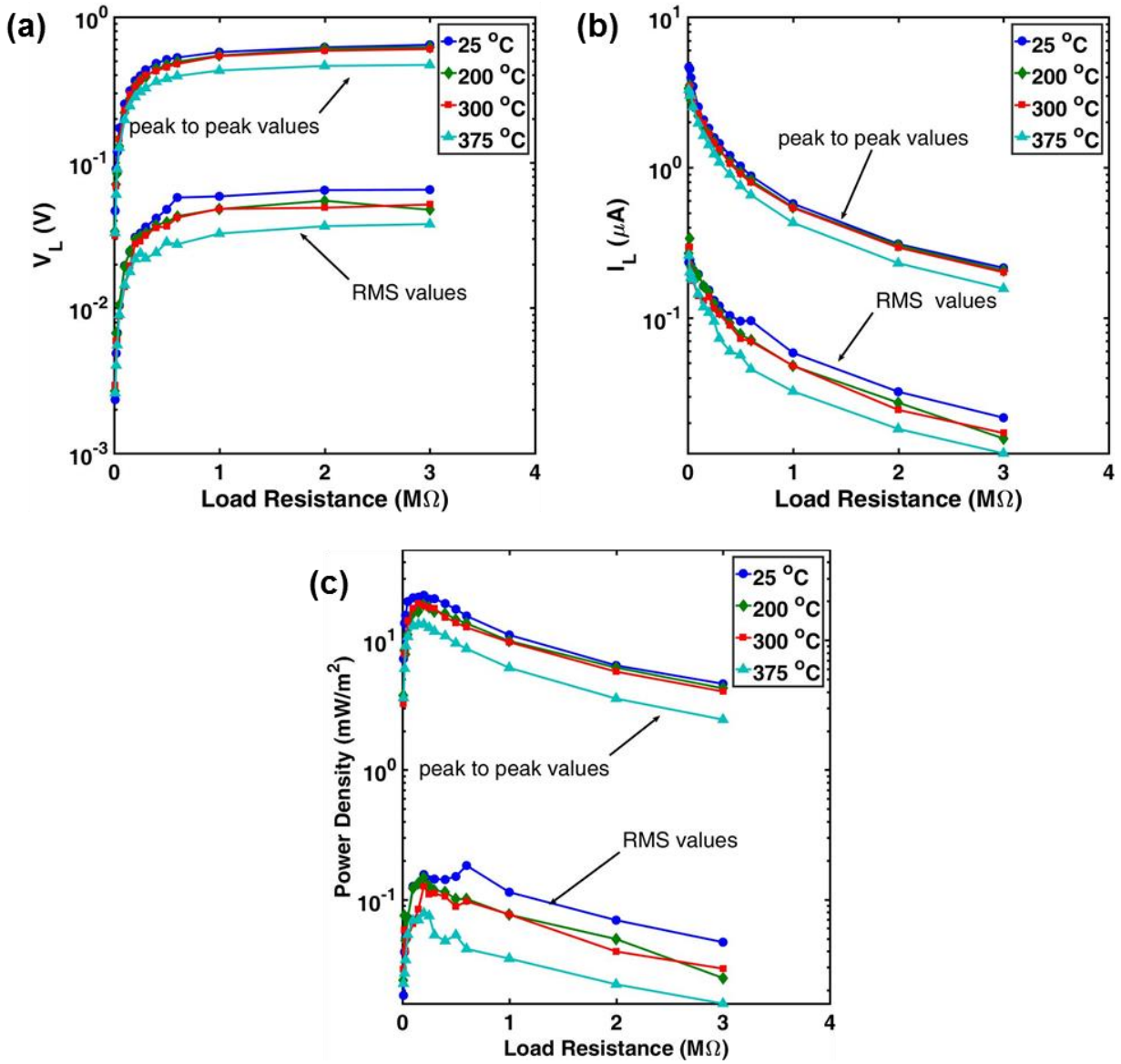

Figure 5-4: (a) The peak to peak and RMS values of the voltage across and (b) current passing through the load resistor. (c) Power characterization of the energy harvester device at various temperatures.

5.4. High temperature flexible energy harvester using freestanding PTO nanowires

5.4.1. Heat resistant matrix

A key component of any nanocomposite is the matrix material which is usually chosen among polymers. Polymers provide flexibility, conformability and a medium for transformation of the mechanical stress to the piezoelectric inclusions. To develop an energy harvester nanocomposite which can perform at extreme temperatures, a polymeric matrix material with superior heat

resistance is needed. Many polymers have been developed for high temperature applications. For example, polybenzoxazole, polybenzimidazole, and polybenzthiazole, which are not necessarily suitable for energy harvesting applications due to complex and expensive synthesis processes, low flexibility and high dielectric losses (Figure 5-5) [309-313]. Another well-known polymer with excellent thermal stability, deformability, and low dielectric loss is polyimide [314,315]. The chemistry of polyimides, a class of thermally stable polymers often based on stiff aromatic backbones, is quite expansive with several monomers and processes for synthesis available. There has been significant debate, however, on the different reaction mechanisms involved in different synthesis methods. The properties of polyimides can be modified significantly by minor variations in the structure. In the next section, a common method for synthesizing 'aromatic' polyimides is discussed, as they make up the primary category of such materials.

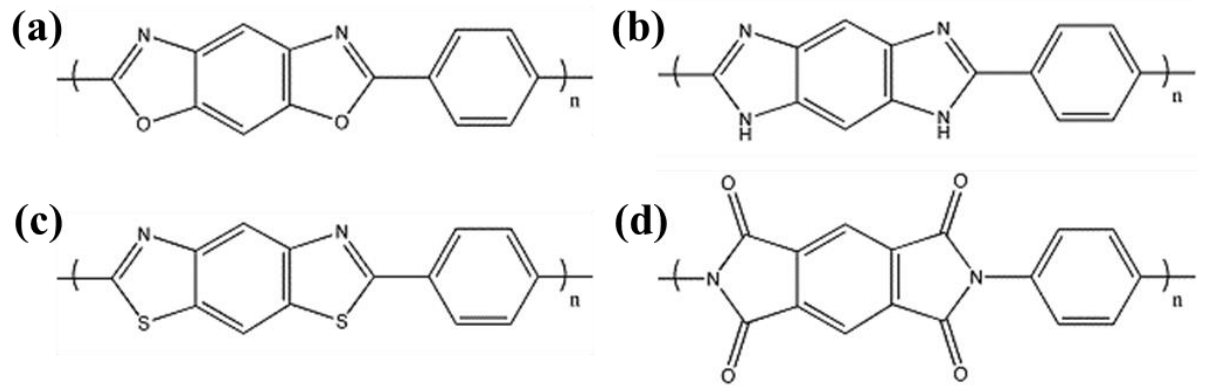

Figure 5-5: Common heat resistant polymers. (a) polybenzoxazole, (b) polybenzimidazole, (c) polybenzthiazole, and (d) polyimide.

5.4.2. Polyimide synthesis

The most common procedure in polyimide synthesis is the two-step poly(amic acid) process, developed at Dupont in the 1950s. A dianhydride and a diamine are reacted in ambient conditions in a dipolar aprotic solvent such as N,N-dimethylacetamide (DMAc) and Nmethylpyrrolidinone (NMP) resulting in the corresponding poly(amic acid). This poly(amic) acid is then cyclized into the final polyimide. Their planar aromatic and hetero-aromatic structures make most polyimides infusible and insoluble. Thus, they usually need to be processed from a solvent. This method enabled the first commercially significant polyimide, "Kapton", to become widely available.

According to Figure 5-6 the procedure for the most developed Kapton polyimide uses pyromellitic dianhydride (PMD) and 4,4'-oxydianiline (ODA) [316]. This seemingly simple process relies on several elementary reactions that are interrelated in a complex system. Many factors, including reaction conditions and the mode of monomer addition, can massively affect the course of these reactions. These small details determine whether high yield molecular weight polymers are produced, and thus whether the reaction is deemed successful [314].

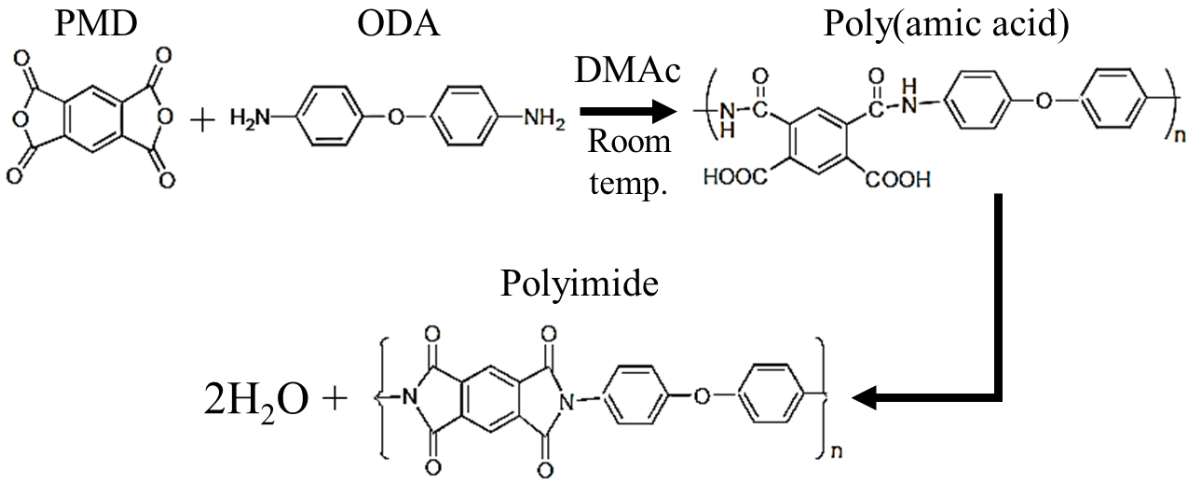

Figure 5-6: A two-step chemical reaction for synthesizing Kapton polyimide [316].

Addition of a dianhydride to a diamine in a dipolar aprotic solvent such as DMAc or NMP at ambient temperatures leads to the formation of the intermediate poly(amic acid) due to the nucleophilic attack of the amino group on the carbonyl carbon of the anhydride group. The scheme that is illustrated in Figure 5-7 involves a reversible reaction leading to the opening of the anhydride ring to form an amic acid group. However, the forward rate constant for the reaction is several orders of magnitude larger than the reverse reaction, and thus the reaction often appears irreversible if pure reagents are utilized. The formation of a high molecular weight product is also dependent on this large difference in the reaction rate constants and thus it becomes important to examine the driving forces favoring the forward reaction. For the reverse reaction to take place, the carboxyl proton needs to attack the adjacent poly(amic aid) group. Therefore, any reagent that hinders this reaction can decrease the rate of backward reaction and thus can shift the equilibrium to the right.

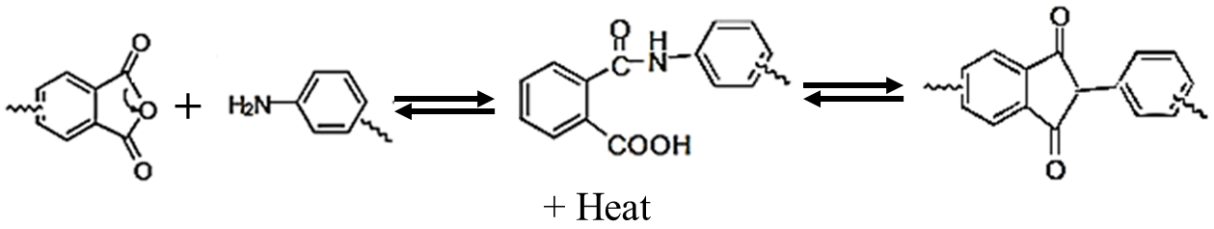

Figure 5-7: Reaction mechanism for formation of aromatic imide [275].

Poly(amic) acid formation is exothermic and the equilibrium is favored at lower temperatures, but at ambient conditions the equilibrium is shifted so far to the right that decreasing the temperature any lower does not result in any observable effects on the reaction. The monomer concentration also affects the reaction equilibrium; the forward reaction is bimolecular and the reverse reaction is unimolecular, and so increasing the monomer concentration results in high molecular weight products. This characteristic becomes particularly important in highly diluted solutions. Many factors can affect the successful synthesis of poly(amic) acid such as monomer reactivity, reaction conditions, solvent choice, and the control of side reactions involved in the synthesis [314]. However, it is widely accepted that the following factors favor the synthesis of poly(amic) acid: (1) High concentration of reacting species (ODA and PMD); (2) Successive addition of ODA and then PMD to the solution because when dianhydrate is added second, it reacts faster with the diamine than with the existing water; (3) Small deviations forming stoichiometric (excessive) amounts of dianhydrate are found to be helpful in synthesizing a higher molecular weight product. Using these pointers, the poly(amic) acid was synthesized and imidized using the following procedure [314].

First, 0.739 mole ODA (200.24 gr/mol) was dissolved in 4 ml DMAc by vigorous magnetic stirring in glovebox with less than 0.5 and 230 ppm water vapor and oxygen environment, respectively. The solution was stirred at room temperature for 30 min after which 0.743 mole PMD was added to the solution. Although the poly(amic) acid synthesis process (Figure 5-6) requires a similar molarity of ODA and PMD, as mentioned before, a small amount of excessive PMD can result in a higher molecular weight final product with better performance. Therefore, here a 5% excessive PMD was added to the ODA/DMAc solution. After stirring the solution for another half an hour, poly(amic) acid, which is a brown viscus liquid, was produced.

Finally the poly(amic) acid undergoes a step-by-step heat treatment to produce the Kapton polyimide. According to the literature, generally there are two paths for the imidization of poly(amic) acid. The first method involves a gradual increase in temperature to 250 °C – 350 °C [275,317,318], and the second method employs a step-wise imidization where first the poly(amic) acid is heated and held at 100°C for an hour, then heated to 200 °C and held for another hour and finally, heated and kept at 300 °C for another hour [319-322]. In this chapter, the second method is utilized. Figure 5-8a shows the temperature profile that was used to synthesize the Kapton polyimide. Increasing the temperature to 300 °C led to the imidization of the poly(amic) acid to produce a high molecular weight polyimide.

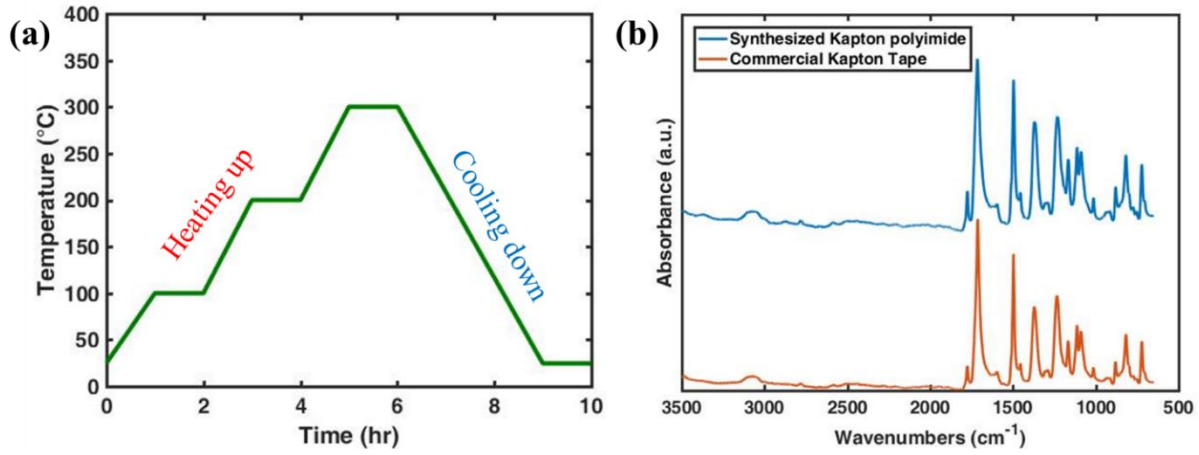

Figure 5-8: (a) Heat treatment process for imidization of poly(amic) acid. (b) FTIR spectra of the as synthesized and commercial Kapton polyimide.

The as synthesized polyimide was characterized by Fourier-transform infrared spectroscopy (FTIR) to analyses the purity and structure of the product. FTIR is the technique which is usually used for determination of organic compounds structures and it is useful for identifying the presence of certain functional groups. The FTIR spectra of the as synthesized Kapton polyimide is compared to that of commercial Kapton tape in Figure 5-8b. According to literature, the imide group exhibits five characteristic vibrational bands in FTIR, namely, the C-N-C transverse stretching, the imide carbonyl in-phase and out-of-phase stretching, the C-N-C out-of-plane bending, the C-N-C axial stretching, and the imide carbonyl out-of-phase stretching [323].

The two imide carbonyl absorptions can be explained in terms of an in-phase and out-of-phase coupling between the two carbonyl groups in the imide ring. This coupling produces a characteristic doublet with the out-of-phase mode absorbing at the higher wavelength, but with a much stronger intensity than the in-phase vibration [324]. In the FTIR characterization of polyimide, the in-phase vibration absorbs at 1774 cm^{-1}, while that of out-of-phase vibration absorbs at 1712 cm^{-1}. The vibration bands at 721, 1112, and 1371 cm^{-1} demonstrate the imide C-N-C out-of-plane bending, transverse stretching, and axial stretching modes, respectively [325].

Another important feature of Kapton polyimide as the matrix for high temperature nanocomposite energy harvesters is its ability to form graphite upon shining a low-power laser onto its surface (i.e. laser induced graphite, LIG) [326]. LIG is a cost effective and scalable method for fabrication of porous graphite with high electrical conductivity (Figure 5-9b). This method allows for the integration of highly conductive electrodes with superior thermal stability and conductivity [327] with the surface of a nanocomposite. When compared to other approaches such as conductive metal sputtering (like gold, Chapter 4), LIG offers a cheaper method with better adhesion to the matrix. Moreover, using LIG, any shape or form of electrodes can be directly printed onto the surface. Figure 5-9c shows the SEM micrograph of LIG on the surface of a polyimide. It shows a porous surface with nanostructured surface features (side view picture) that can be controlled by changing the laser power or dots per inch (DPI). Here, a uniform LIG electrode was printed on the polyimide surface by shinning a 3.2 W laser with 1000 DPI resulting in a surface conductivity of about 20 S cm^{-1}. The conductivity of the LIG surface can be increased by increasing the power or DPI of the laser, however, 20 S cm^{-1} is sufficiently conductive for piezoelectric energy harvester applications. It should also be noted that increasing the power or DPI further can cause uncontrollable carbonization of the polyimide and can result in debonding from its surface.

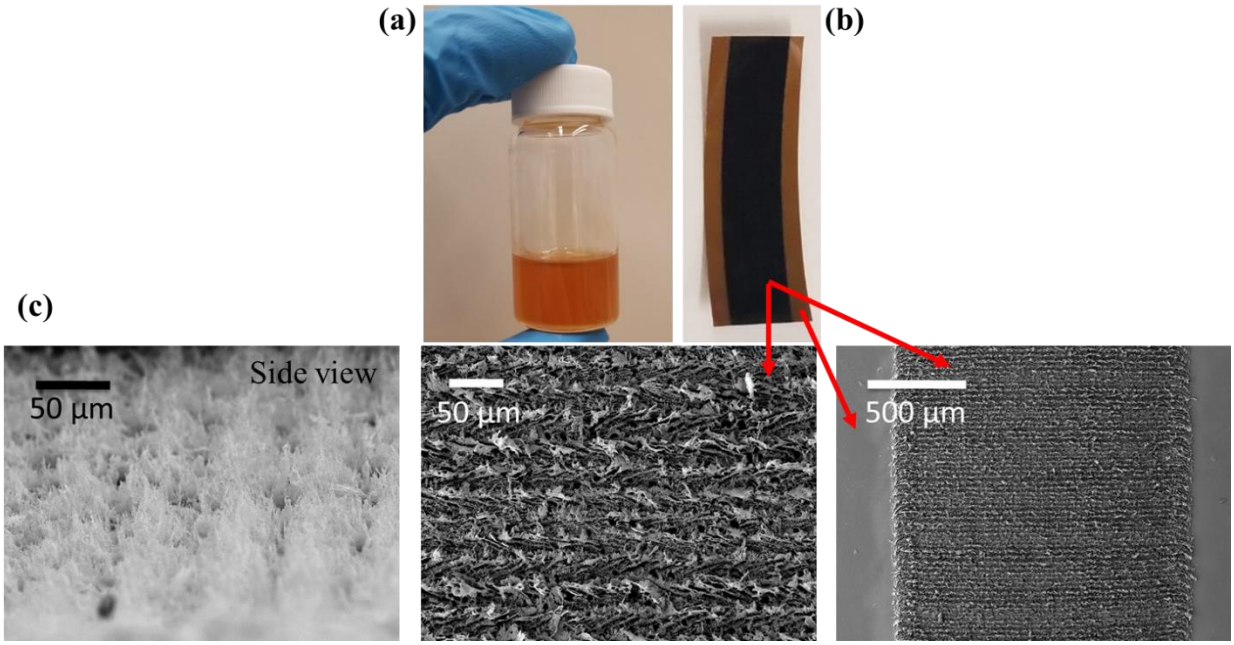

Figure 5-9: (a) As-synthesized poly(amic) acid. (b) A sample of imidized poly(amic) acid (Kapton, brown) with printed graphite electrode (black). (c) SEM micrographs of the printed graphite electrode on the surface of Kapton polyimide film (laser parameters: 3.2 W, 1000 DPI).

5.4.3. Fabrication of high temperature flexible energy harvester

Following the synthesis and heat treatment of freestanding PTO nanowires, they were dispersed in poly(amic) acid solution with an appropriate ratio to produce the target weight fraction using a magnetic stirring method for 1 hour. A speedmixer (3500 RPM, 15 min, FlackTek Inc) was used for further mixing the nanowires in the polymer. Finally, the nanowire suspension was sonicated using a horn sonicator for 5 min to produce a uniform dispersion of nanowires. Then the resulting nanocomposite ink was loaded into a syringe with a 20 gauge nozzle. The same Aerotech 3D printer equipped with a precision solution dispenser (as described in Chapter 4) was used for direct writing of the PTO/polyimide nanocomposite ink onto an aluminum sheet (25 µm thick) surface. This procedure resulted in highly aligned PTO nanowires in a polyimide matrix (Figure 5-10a). For comparison, another set of nanocomposites with randomly aligned nanowires were prepared using a solution casting method (Figure 5-10b). After printing, the nanocomposite were heat treated using the method described in Section 5.4.2 (Figure 5-8a) to produce a thermally resistant polyimide matrix for the nanocomposites.

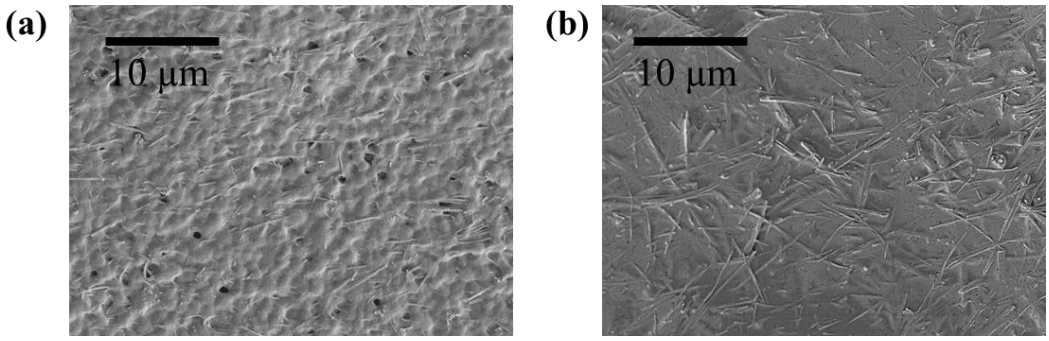

Figure 5-10: PTO nanowires/polyimide nanocomposite with (a) aligned (direct write method) and (b) randomly oriented nanowires (casting method)

Subsequently, the nanocomposites were detached from the aluminum substrate and rectangular LIG electrodes were printed on both sides (Figure 5-9b). Then the samples were directly poled with 300 V DC voltage at an elevated temperature of 250 °C. Finally, the samples were cooled down to room temperature while the poling field was applied thus resulting in poled nanocomposite energy harvesters. In the next section, the piezoelectric properties of the nanocomposites at various temperatures are studied. It is shown that using the aforementioned method results in highly effective flexible energy harvesters which can withstand extreme temperatures.

5.4.4. Electromechanical modeling and Electrical characterization

To model the effect of temperature on the electromechanical properties of the high temperature nanocomposite, the electromechanical coefficients of its constituents – both matrix and inclusions, as a function of temperature are needed. Those coefficients can be used to determine the effect of temperature on the nanocomposite as a whole. In the literature, only a few attempts have been made to measure the effect of temperature on the full electromechanical coefficients of piezoelectric material. For instance using IEEE standards, the full electromechanical matrix constants of $Pb(Mg_{1/3}Nb_{2/3})O_3$-$PbZrO_3$-$PbTiO_3$ crystals at room temperature all the way to 100 °C was investigated by Zhang *et al.* [328]. Kamiya *et al.* studied the effect of temperature on material parameters such as d_{31}, and k_{31} of a tetragonal and a rhombohedral PZTs using least squares fitting method however their data set is incomplete and its self-consistency is debatable [329]. Similarly, Sabat *et al.* reported the temperature dependence of

the full matrix material constants of PZTs by the resonant method. However, in all these reports, several different samples were used for their measurements, therefore the self-consistency of these coefficients was compromised [330]. Later, Tang *et al.* developed an experimental procedure for determining the full matrix material properties using resonant ultrasound spectroscopy. They only used one sample for their measurement and showed a guaranteed self-consistent system of electromechanical coefficients for PZTs and PTO as a function of temperature that can be used for computer simulations [331,332]. By fitting their experimental data, they came up with the following polynomial fits for the lead titanate stiffness matrix coefficients:

$$C_{11} = 137.65 + 78.24 \times 10^{-3}T - 17.78 \times 10^{-5}T^2 \ (GPa) \quad (5\text{-}3a)$$

$$C_{12} = 73.12 + 70.22 \times 10^{-2}\sqrt{T} - 34.8 \times 10^{-3}T \ (GPa) \quad (5\text{-}3b)$$

$$C_{13} = 74.70 + 86.90 \times 10^{-2}\sqrt{T} - 44.70 \times 10^{-3}T \ (GPa) \quad (5\text{-}3c)$$

$$C_{33} = 124.79 + 86.67 \times 10^{-3}T - 22.23 \times 10^{-5}T^2 \ (GPa) \quad (5\text{-}3d)$$

$$C_{44} = 27.31 + 22.84 \times 10^{-3}T(GPa) \quad (5\text{-}3e)$$

And the following relations were given for piezoelectric stress coefficients:

$$e_{15} = 11.28 + 1.779 \times 10^{-3}T - 7.066 \times 10^{-5}T^2 \ (C/m^2) \quad (5\text{-}4a)$$

$$e_{31} = -5.39 - 4.55 \times 10^{-3}T \ (C/m^2) \quad (5\text{-}4b)$$

$$e_{33} = 14.935 + 7.99 \times 10^{-3}T + 8.636 \times 10^{-5}T^2 \ (C/m^2) \quad (5\text{-}4c)$$

The temperature dependence of PTO's dielectric constant was investigated by Chaudhari [333] *et al.* They showed that dielectric constant of PTO is relatively constant at the room temperature to about 550 K and then starts to increase gradually and reaches the highest value at its Curie temperature which is a typical behavior ferroelectric materials. Therefore, in this chapter a constant value is considered for the dielectric constant of PTO. Figure 5-11a and b, illustrate the effect of temperature on stiffness (Eq. 5-3) and piezoelectric stress coefficients (Eq. 5-4), respectively. From this figure it is evident that all of these coefficients do not change significantly

with temperature in 25 to 250 °C range. Figure 5-11c show the evolution of dielectric constant with temperature at various frequencies and was adopted from ref. [333].

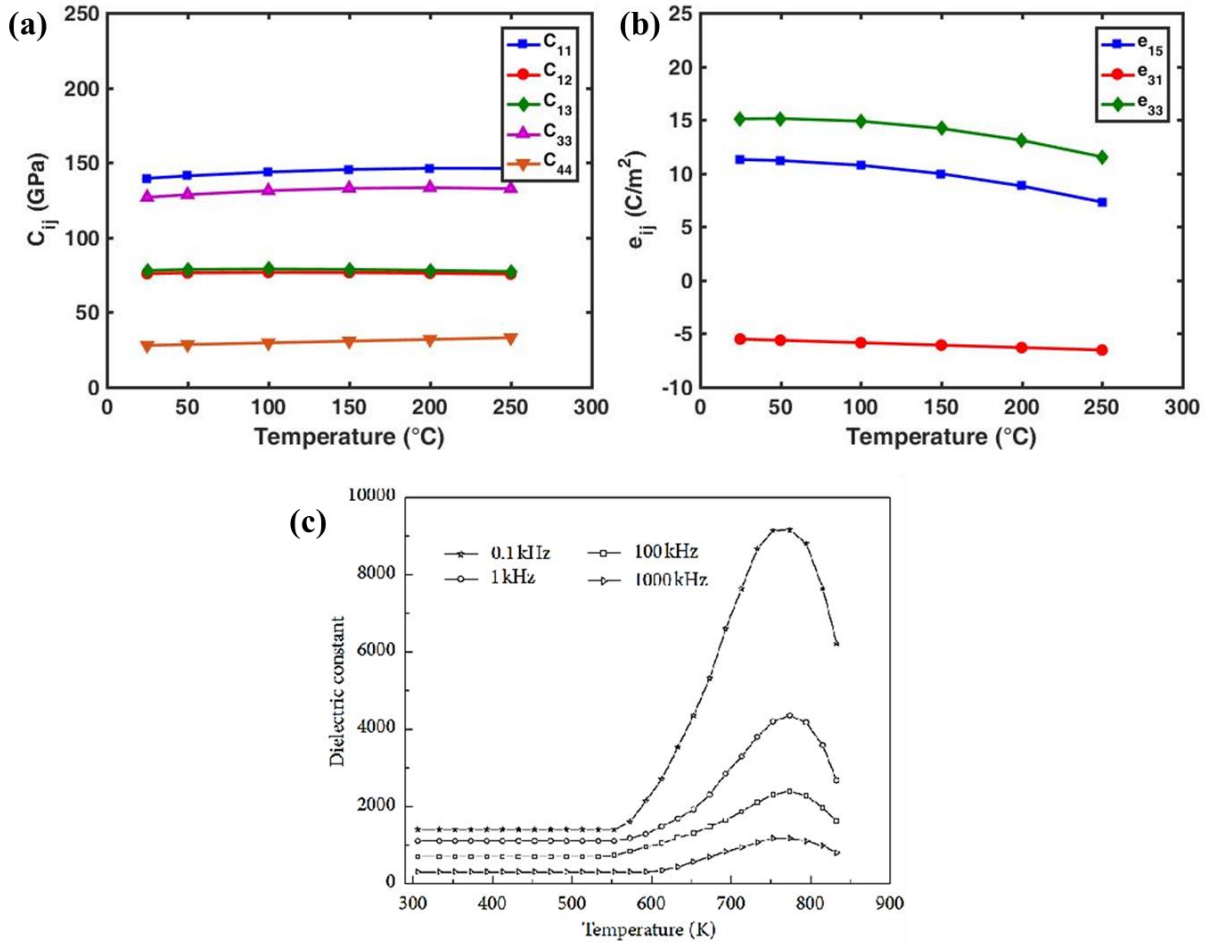

Figure 5-11: Interpolated (a) stiffness and (b) piezoelectric stress coefficients of PTO as a function of temperature based on Eqs. (5-3) and (5-4) [331,332]. (c) Dielectric coefficient of PTO vs. temperature (adapted from Ref. [333]).

Other important parameters required for calculation of piezoelectric properties of a nanocomposite is the Young's modulus and dielectric constant of the matrix. In this dissertation, both of these values were measured experimentally. The Young's modulus at each temperature was calculated using DMA by applying a controlled AC strain of 0.5% with 5 Hz frequency, and measuring the applied stress to the sample. The dielectric constant was measured via capacitance measurement using an LCR meter (Eq. 5-2) while the sample was kept in the temperature controlled furnace of DMA. Figure 5-12 show the results of these measurements which agrees well

with tensile modulus and dielectric constant of Kapton reported by Dupont™ with less than 10% error.

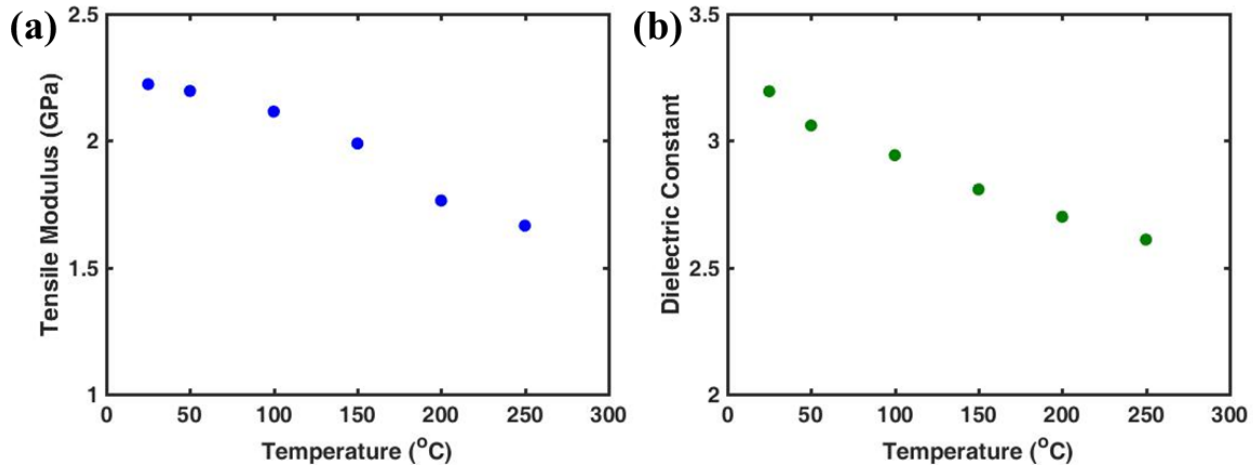

Figure 5-12: (a) The tensile modulus and (b) dielectric constant of the synthesized polyimide Kapton.

By feeding the aforementioned PTO and polyimide parameters into the FEM model developed in chapter 3 and 4, the effect of temperature in piezoelectric properties of the nanocomposite can be calculated. These results are experimentally verified by measuring the d_{31} piezoelectric strain coefficient of these nanocomposite. Figures 5-13a and b show the normalized d_{31} coefficient of aligned PTO nanowire/Polyimide nanocomposite at various volume fractions, temperature, aspect ratio, with LIG and gold (Au) electrodes, respectively. By comparing Figures 5-13a to 5-13b, it can be concluded that the devices with LIG electrodes perform better compared to the devices with gold electrodes at extreme temperatures with more stable response. This fact can be contributed to the integrated design and better thermal stability of the LIG electrodes. Since, LIG electrodes are cheaper, and easier to mask into complicated designs, and simultaneously more stable and versatile than gold electrodes, for the rest of this chapter only the devices with LIG electrodes are used.

According to Figure 5-13 that the FEM can be verified by experimental data at various volume fractions, temperatures, etc. It is shown that, the nanocomposites with higher volume fractions of aligned high aspect ratio nanowires have the highest d_{31} coefficients. Moreover, by increasing the aspect ratio of the nanowires from 10 to 20, the d_{31} coefficients can be enhanced by about 40% at various temperatures. But more importantly, these results prove that the PTO nanowires/polyimide

nanocomposite energy harvester can produce thermally stable output at different temperatures ranging from room temperature all the way up to 250 °C.

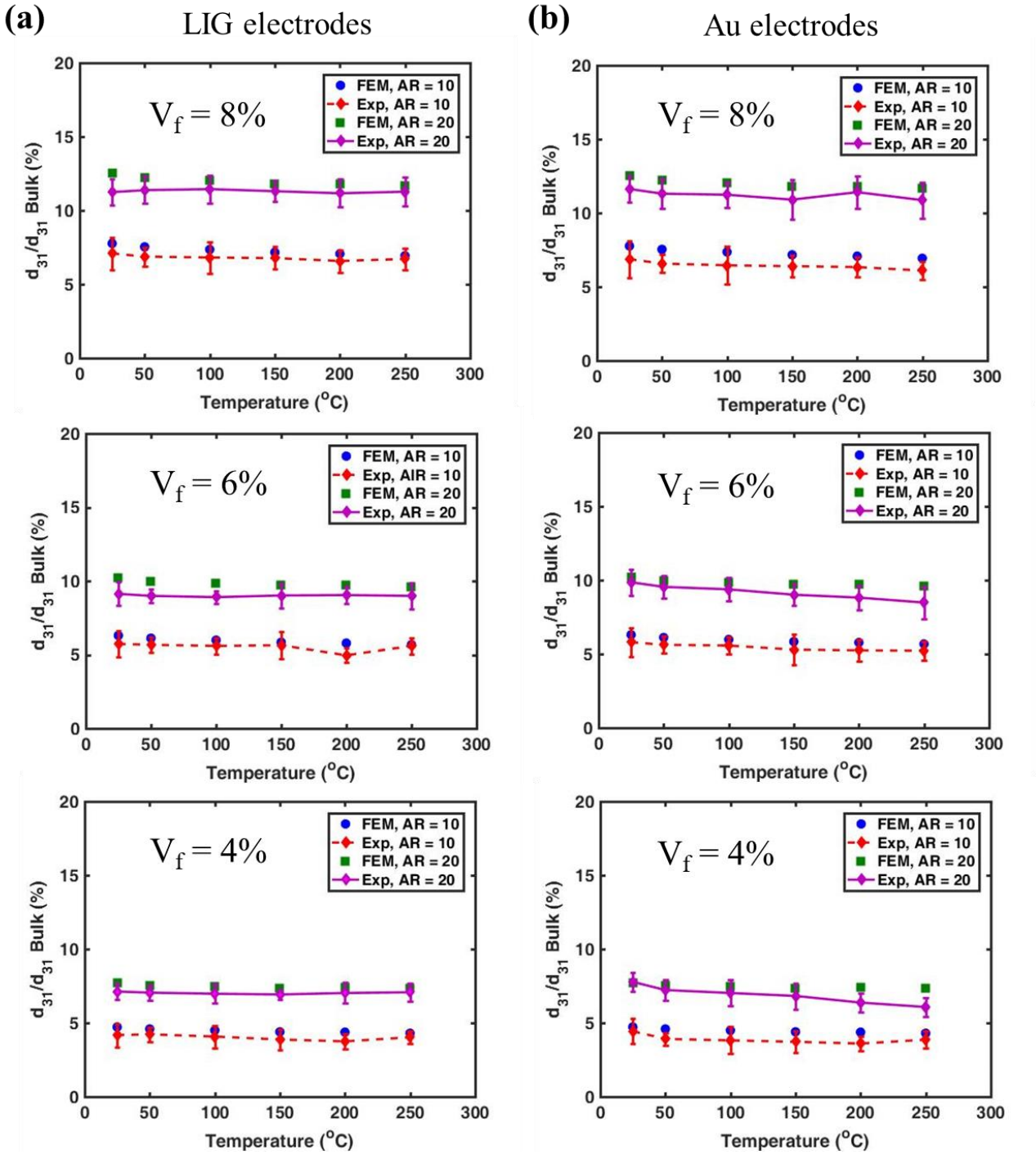

Figure 5-13: Normalized d_{31} coefficients of PTO nanowires/polyimide nanocomposite energy harvester at various volume fractions, aspect ratios, and temperatures.

After confirming that the LIG method lead to better energy harvesting performance, the power output of these devices were characterized using a similar method as mention in section 5.3.3 and Eq. (5-1). The optimal (maximum) power output of various devices with different volume fractions, aspect ratios and alignment is shown in Figure 5-14. According to Figure 5-14, all devices were able to maintain output electrical energy at temperatures spanning from room temperature to 250 °C. In all cases, a slight enhancement in power can be observed as the temperature is increased. This can be attributed to the reduction in dielectric coefficient of the nanocomposite. A well-known figure of merit (FOM) regarding the power output of a piezoelectric energy harvester which takes into account the piezoelectric strain and voltage coefficient is given by

$$FOM = g_{31}d_{31} = \frac{(d_{31})^2}{\kappa_{33}}. \tag{5-5}$$

According to Figure 5-13 the piezoelectric strain coefficient (d_{31}) of the nanocomposites are relatively constant with temperature. The dielectric coefficient (κ_{33}) of the nanocomposite is mainly affected by that of the polymeric matrix at low volume fractions ($V_f < 10\%$) [27]. As shown in Figure 5-12b, the dielectric coefficient of the polyimide matrix decrease with temperature. Therefore according to Eq. (5-5) the FOM enhances at higher temperatures, which can explain the slight increase in power shown in Figure 5-14. This figure also clearly demonstrate the effect of nanowires alignment and aspect ratio in output power. For example, at 250 °C a nanocomposite with $V_f = 6\%$ aligned nanowires and AR = 20 can produce more than 1.8 times power compared to that of AR = 10.

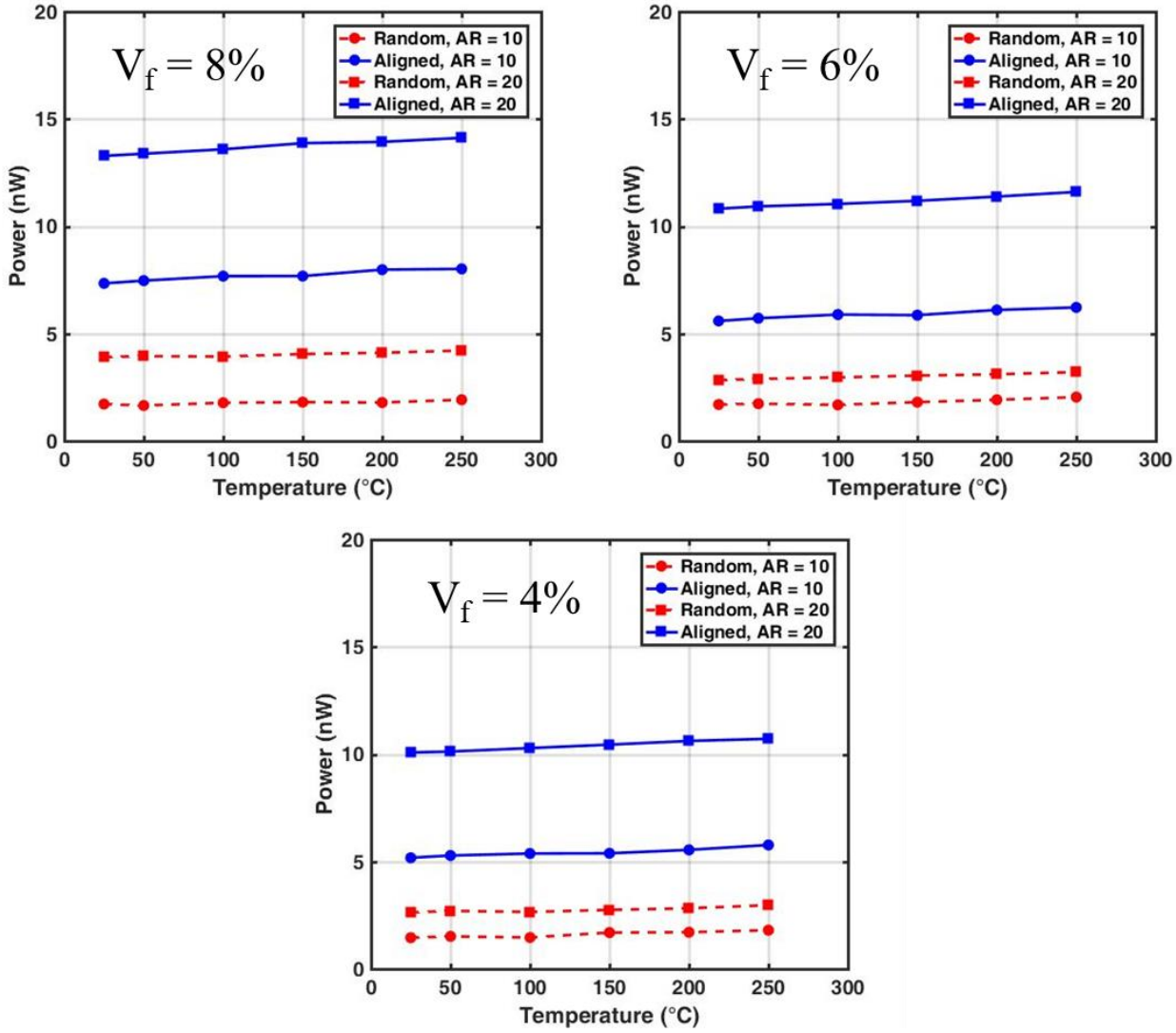

Figure 5-14: The power output characterization of PTO nanowires/polyimide nanocomposite energy harvester at various volume fractions, aspect ratios, alignment and temperatures.

5.5. Conclusions

In conclusion, a novel approach for the development of a high temperature energy harvester using high aspect ratio, vertically aligned PTO nanowire arrays is demonstrated. Its potential for harvesting vibrational energy at extreme temperatures (375 °C) has also been investigated. The open circuit voltage and power characterization analysis of the fabricated device under direct vibration excitation for various temperatures illustrates the extreme temperature range over which the device remains useful. The open circuit voltage and generated power of the device are

comparable to many NEMS and MEMS piezoelectric energy harvesters in the literature [85,190], but this novel approach has the added ability to generate these high power outputs at the highest temperatures reported for these devices. The results show that the fabricated energy harvester can generate stable open circuit voltage of about 0.6 V (peak-to-peak) at temperatures ranging from room temperature to 300 °C. Moreover, it is shown that the device can produce up to 22.3 mW m^{-2} at room temperature and up to 13 mW m^{-2} at 375 °C. Thus, the energy harvester provides sufficient energy density for many self-powered, extreme-temperature applications.

Furthermore, another type of high temperature energy harvester with added benefits of flexibility and control over alignment of the nanowires was fabricated. By synthesizing freestanding PTO nanowires and polyimide polymer, and the direct write approach developed in chapter 4, a thermally stable nanocomposite energy harvester capable of withstanding temperatures as high as 250 °C was fabricated. It was shown that it can provide electrical energy at temperatures spanning from 25 °C to 250 °C. In this chapter, the models developed in chapter 4 were modified to account for effects of temperature in piezoelectric performance of the nanocomposites which were then verified by experimental data. The findings of this chapter establishes a route towards mitigating the temperature constraint that existing sensing and power harvesting systems are limited by thus enabling additional capacity in the future design of self-powered systems.

Chapter 6: Conclusions

6.1. Summary of the findings and contributions

Composites composed of piezoelectric nanomaterials dispersed in a flexible polymer have emerged as promising materials for highly durable and flexible energy harvesters and sensors. Although piezoelectric materials in their bulk form have a high electromechanical coupling coefficient and can efficiently convert mechanical energy to electrical energy, the ceramic form has low fracture toughness and thus they are limited in certain applications due to difficulty in machining and conforming to curved surfaces. Recently, additive manufacturing processes such as direct write, have been developed to incorporate piezoelectric nanowires into a polymer matrix with controlled alignment to realize printed piezoelectrics. Given the multiphase structure of a nanocomposite, it is possible to control the material structure such that the piezoelectric coupling and dielectric properties can be varied independently. In this dissertation, experimentally validated finite element and micromechanics models were developed for calculation and optimization of the piezoelectric coefficient of a nanocomposite. It was shown that by using high aspect ratio nanowires with controlled alignment, high performance energy harvesters can be developed.

The micromechanical model used the Mori-Tanaka approach for calculation of electromechanical coefficients of a nanocomposite energy harvester. The results were then validated using FEM performed in COMSOL Multiphysics software. They show that for various nanowires aspect ratio, the nanocomposites with aligned nanowires have much higher piezoelectric strain coefficients compared to a nanocomposite with completely randomly oriented nanowires. Specifically, in a 40 %wt BTO nanowires in PDMS nanocomposite, the alignment of the nanowires with AR = 10 exhibit more than 100% enhancement in d_{31} and d_{33} coefficients. Furthermore, it was shown that using high aspect ratio nanowires even at low weight fractions, the nanocomposites exhibit high piezoelectric performance. The voltage coefficient (g_{31}) of the

nanocomposites was calculated and demonstrated that by utilizing nanowires with AR = 40, the voltage coefficient of the nanocomposite can outperform that of the bulk piezoelectric material by more than seven times due to the ability to vary the dielectric and coupling coefficients. It was found out that the g_{31} coefficient does not increase continuously with weight fraction of the nanowires. Rather, the highest possible g_{31} coefficient was realized at an optimal weight fraction (usually under 40 %wt). For example, the results showed that for nanocomposites with aligned nanowires with AR = 10, 20 and 40, the highest possible g_{31} coefficients coincide with WF = 35%, 27% and 24%, respectively. Furthermore, the effects of inclusions' misalignment were studied and it was determined that a nanocomposite with misalignment less than 20°, can outperform that of aligned inclusions due to its higher compliance.

The results of the models were verified using an ink-jet direct write method in which the nanocomposite ink was printed directly on to the substrates using a custom made 3D printer. The nanocomposite ink comprised of synthesized BTO nanowires with various aspect ratio mixed with PDMS polymeric matrix. By controlling the viscosity of the nanocomposite ink, the amount of shear forces acting on the nanowires were adjusted resulting in the controlled alignment of the printed nanowires. In other words, due to the high-shear environment inside the nozzle, the fillers progressively arrange themselves parallel to the printing nozzle which result in aligned fillers in the "written" composite. This method allows for fast fabrication of inexpensive and complex structures. By preparing various nanocomposites with different nanowires aspect ratio and alignment, for the first time the results of FEM and micromechanical models were experimentally verified.

Finally, the effects of operating temperature were taken into account by measuring the electromechanical coefficients of the nanocomposite's constituents. These values were incorporated into the models and the overall electromechanical coefficients of the nanocomposite at various temperature were calculated. The results were then verified experimentally. Two types of extreme temperature energy harvester were developed. In both devices lead titanate nanowires were chosen as the active material due to its high temperature stability. In the first type, a nonflexible cantilever-based energy harvester composed of vertically aligned arrays of lead titanate nanowire was fabricated. This device demonstrated the feasibility of energy harvesting at temperatures exceeding 300 °C using lead titanate. Then in the second type, freestanding lead

titanate nanowires were grown and mixed with synthesized polyimide matrix to produce a nanocomposite ink. Similarly, the morphology and aspect ratio of these nanowires were controlled by hydrothermal reaction parameters. Then, the aforementioned direct write approach was implemented to produce flexible nanocomposite energy harvester capable of generating stable power at temperatures ranging from ambient to 250°C. The electromechanical coefficients of these nanocomposite were measured and compared to that of the models and it was shown that the models can predict these coefficients accurately.

6.2. Recommendations for future work

This dissertation investigated the effects of geometrical properties of inclusion in nanocomposite energy harvesters via two independent modeling techniques and both of which were verified by experimental measurements. The two techniques used were micromechanics and FEM. The fundamental studies illustrated in this dissertation revealed several key findings in the field of nanocomposite energy harvesting and modeling. Different aspects of this research have resulted in a variety of interesting scientific contributions which can be implemented in many engineering applications. However, further improvements can be made in several aspects of this research.

The FEM method that was used for calculation of effective piezoelectric properties of a nanocomposite containing randomly oriented nanowires requires a large RVE with many inclusions, resulting in complicated computer programs that require long computation time. Moreover, the RSA method that was used in this dissertation cannot model a nanocomposite with volume fractions much more than 10%. Thus, a more computationally efficient FEM that can model higher concentrations of randomly oriented nanowires is needed. Recently, a method proposed by Islam *et al.* [334] coupled the RSA algorithm and dynamic FEM. It uses RSA to generate sparse inclusion assemblies of low volume fraction and subsequently utilizes dynamic FEM simulation for inclusion packing to achieve high volume fractions. This method can generate RVEs with volume fractions as high as 50%, depending on the inclusions' aspect ratio. Although this method has been used for fiber reinforced composites, it can be generalized to piezoelectric composites, and therefore model high concentration of randomly oriented nanowires in a piezoelectric nanocomposite.

The 3D printing method presented in this dissertation can also be improved by employing a fused filament fabrication technique in which the nanowires are dispersed in a filament made of the nanocomposite matrix. This method can increase the flexibility of the manufacturing and allows for improved cost-effectiveness and scaling of production. Furthermore, using the 3D printing method described in this dissertation, it is possible to print complex multifunctional structures with tailored piezoelectricity to be used as customizable sensors and actuators.

References

[1] M. Kimura, A. Ando, D. Maurya, S. Priya, Lead Zirconate Titanate-Based Piezoceramics, in: Anonymous Advanced Piezoelectric Materials, Elsevier, 2017, pp. 95-126.

[2] H. Tang, M.H. Malakooti, H.A. Sodano, Relationship between orientation factor of lead zirconate titanate nanowires and dielectric permittivity of nanocomposites, Appl. Phys. Lett. 103 (2013) 222901.

[3] Y. Lin, C. Andrews, H.A. Sodano, Enhanced piezoelectric properties of lead zirconate titanate sol-gel derived ceramics using single crystal PbZr 0.52 Ti 0.48 O 3 cubes, J. Appl. Phys. 108 (2010) 064108.

[4] S. Xu, Y. Wei, J. Liu, R. Yang, Z.L. Wang, Integrated multilayer nanogenerator fabricated using paired nanotip-to-nanowire brushes, Nano letters. 8 (2008) 4027-4032.

[5] J. Ma, J. Hu, Z. Li, C. Nan, Recent progress in multiferroic magnetoelectric composites: from bulk to thin films, Adv Mater. 23 (2011) 1062-1087.

[6] J. Hu, Z. Li, J. Wang, J. Ma, Y. Lin, C. Nan, A simple bilayered magnetoelectric random access memory cell based on electric-field controllable domain structure, J. Appl. Phys. 108 (2010) 043909.

[7] J. Ma, Z. Shi, C. Nan, Magnetoelectric Properties of Composites of Single Pb (Zr, Ti) O3 Rods and Terfenol-D/Epoxy With a Single-Period of 1-3-Type Structure, Adv Mater. 19 (2007) 2571-2573.

[8] I. Fujii, K. Nakashima, N. Kumada, S. Wada, Structural, dielectric, and piezoelectric properties of BaTiO3–Bi (Ni1/2Ti1/2) O3 ceramics, Journal of the Ceramic Society of Japan. 120 (2012) 30-34.

[9] J. Briscoe, S. Dunn, Piezoelectric nanogenerators–a review of nanostructured piezoelectric energy harvesters, Nano Energy. 14 (2015) 15-29.

[10] G. Zhu, A.C. Wang, Y. Liu, Y. Zhou, Z.L. Wang, Functional electrical stimulation by nanogenerator with 58 V output voltage, Nano letters. 12 (2012) 3086-3090.

[11] Y. Qi, M.C. McAlpine, Nanotechnology-enabled flexible and biocompatible energy harvesting, Energy & Environmental Science. 3 (2010) 1275-1285.

[12] Z.L. Wang, W. Wu, Nanotechnology-enabled energy harvesting for self-powered micro-/nanosystems, Angewandte Chemie International Edition. 51 (2012) 11700-11721.

[13] H.A. Sodano, D.J. Inman, G. Park, A review of power harvesting from vibration using piezoelectric materials, Shock Vib Dig. 36 (2004) 197-206.

[14] J. Lim, H. Jung, C. Baek, G. Hwang, J. Ryu, D. Yoon, J. Yoo, K. Park, J.H. Kim, All-inkjet-printed flexible piezoelectric generator made of solvent evaporation assisted BaTiO3 hybrid material, Nano Energy. 41 (2017) 337-343.

[15] C.D. Richards, M.J. Anderson, D.F. Bahr, R.F. Richards, Efficiency of energy conversion for devices containing a piezoelectric component, J Micromech Microengineering. 14 (2004) 717.

[16] F. Fan, L. Lin, G. Zhu, W. Wu, R. Zhang, Z.L. Wang, Transparent triboelectric nanogenerators and self-powered pressure sensors based on micropatterned plastic films, Nano letters. 12 (2012) 3109-3114.

[17] Z. Fan, J. Koruza, J. Rödel, X. Tan, An ideal amplitude window against electric fatigue in BaTiO3-based lead-free piezoelectric materials, Acta Materialia. 151 (2018) 253-259.

[18] F.R. Fan, W. Tang, Z.L. Wang, Flexible nanogenerators for energy harvesting and self-powered electronics, Adv Mater. 28 (2016) 4283-4305.

[19] S.K. Sanyal, Future of geothermal energy, (2010) 1-3.

[20] R. Turner, P.A. Fuierer, R. Newnham, T. Shrout, Materials for high temperature acoustic and vibration sensors: A review, Appl. Acoust. 41 (1994) 299-324.

[21] G. Meetham, High-temperature materials—a general review, J. Mater. Sci. 26 (1991) 853-860.

[22] A. Nafari, H.A. Sodano, Electromechanical modeling and experimental verification of a directly printed nanocomposite, 10596 (2018) 105960Z.

[23] A. Nafari, H.A. Sodano, Electromechanical modeling and experimental verification of a direct write nanocomposite, Smart Mater. Struct. (2018).

[24] C. Andrews, Y. Lin, H. Sodano, The effect of particle aspect ratio on the electroelastic properties of piezoelectric nanocomposites, Smart Mater. Struct. 19 (2010) 025018.

[25] K.Y. Lee, D. Kim, J. Lee, T.Y. Kim, M.K. Gupta, S. Kim, Unidirectional high-power generation via stress-induced dipole alignment from ZnSnO3 nanocubes/polymer hybrid piezoelectric nanogenerator, Advanced Functional Materials. 24 (2014) 37-43.

[26] Y. Zhang, H. Sun, C.K. Jeong, Biomimetic Porifera Skeletal Structure of Lead-Free Piezocomposite Energy Harvesters, ACS applied materials & interfaces. 10 (2018) 35539-35546.

[27] G.M. Odegard, Constitutive modeling of piezoelectric polymer composites, Acta materialia. 52 (2004) 5315-5330.

[28] J.H. Affdl, J. Kardos, The Halpin-Tsai equations: a review, Polymer Engineering & Science. 16 (1976) 344-352.

[29] M.L. Dunn, Micromechanics of coupled electroelastic composites: effective thermal expansion and pyroelectric coefficients, J. Appl. Phys. 73 (1993) 5131-5140.

[30] K. Yung, J. Wang, T. Yue, Modeling Young's modulus of polymer-layered silicate nanocomposites using a modified Halpin—Tsai micromechanical model, J Reinf Plast Compos. 25 (2006) 847-861.

[31] L. Liu, Z. Huang, A Note on mori-tanaka's method, Acta Mechanica Solida Sinica. 27 (2014) 234-244.

[32] T. Chen, G.J. Dvorak, Y. Benveniste, Mori-Tanaka estimates of the overall elastic moduli of certain composite materials, Journal of applied mechanics. 59 (1992) 539-546.

[33] T. Mori, K. Tanaka, Average stress in matrix and average elastic energy of materials with misfitting inclusions, Acta metallurgica. 21 (1973) 571-574.

[34] K.S. Maxwell, J.D. Whitcomb, Z. Ounaies, A. Barhoumi, Finite element analysis of a three-phase piezoelectric nanocomposite, J Intell Mater Syst Struct. 21 (2010) 1073-1084.

[35] C.C. Bowland, M.H. Malakooti, Z. Zhou, H.A. Sodano, Highly aligned arrays of high aspect ratio barium titanate nanowires via hydrothermal synthesis, Appl. Phys. Lett. 106 (2015) 222903.

[36] K. Park, S.B. Bae, S.H. Yang, H.I. Lee, K. Lee, S.J. Lee, Lead-free BaTiO 3 nanowires-based flexible nanocomposite generator, Nanoscale. 6 (2014) 8962-8968.

[37] K. Park, M. Lee, Y. Liu, S. Moon, G. Hwang, G. Zhu, J.E. Kim, S.O. Kim, D.K. Kim, Z.L. Wang, Flexible nanocomposite generator made of BaTiO3 nanoparticles and graphitic carbons, Adv Mater. 24 (2012) 2999-3004.

[38] J. Curie, P. Curie, Développement par compression de l'électricité polaire dans les cristaux hémièdres à faces inclinées, Bulletin de minéralogie. 3 (1880) 90-93.

[39] G. Lippmann, Principe de la conservation de l'électricité, ou second principe de la théorie des phénomènes électriques, Journal de Physique Théorique et Appliquée. 10 (1881) 381-394.

[40] W.P. Mason, Piezoelectricity, its history and applications, J. Acoust. Soc. Am. 70 (1981) 1561-1566.

[41] T. Meeker, Publication and proposed revision of ansi/ieee standard 176-1987" ansi/ieee standard on piezoelectricity", IEEE Transactions on Ultrasonics Ferroelectrics and Frequency Control. 43 (1996) 717-772.

[42] H. Janocha, K. Kuhnen, Real-time compensation of hysteresis and creep in piezoelectric actuators, Sensors and actuators A: Physical. 79 (2000) 83-89.

[43] C.C. Fuller, S. Elliott, P.A. Nelson, Active Control of Vibration, Academic Press, 1996.

[44] S.R. Moheimani, A.J. Fleming, Piezoelectric Transducers for Vibration Control and Damping, Springer Science & Business Media, 2006.

[45] C. Bowen, H. Kim, P. Weaver, S. Dunn, Piezoelectric and ferroelectric materials and structures for energy harvesting applications, Energy & Environmental Science. 7 (2014) 25-44.

[46] A. Lopes, J. Gutiérrez, J. Barandiarán, Direct fabrication of a 3D-shape film of polyvinylidene fluoride (PVDF) in the piezoelectric β-phase for sensor and actuator applications, European Polymer Journal. 99 (2018) 111-116.

[47] S. Garain, S. Jana, T.K. Sinha, D. Mandal, Design of in situ poled Ce3 -doped electrospun PVDF/graphene composite nanofibers for fabrication of nanopressure sensor and ultrasensitive acoustic nanogenerator, ACS applied materials & interfaces. 8 (2016) 4532-4540.

[48] S.R. Anton, H.A. Sodano, A review of power harvesting using piezoelectric materials (2003–2006), Smart Mater. Struct. 16 (2007) R1.

[49] N. Femia, G. Petrone, G. Spagnuolo, M. Vitelli, Power Electronics and Control Techniques for Maximum Energy Harvesting in Photovoltaic Systems, CRC press, 2012.

[50] C.R. Bowen, J. Taylor, E. LeBoulbar, D. Zabek, A. Chauhan, R. Vaish, Pyroelectric materials and devices for energy harvesting applications, Energy & Environmental Science. 7 (2014) 3836-3856.

[51] G. De Pasquale, E. Brusa, A. Soma, Capacitive vibration energy harvesting with resonance tuning, (2009) 280-285.

[52] C. Navau, J. Prat-Camps, A. Sanchez, Magnetic energy harvesting and concentration at a distance by transformation optics, Phys. Rev. Lett. 109 (2012) 263903.

[53] A. Nafari, H. Sodano, Surface morphology effects in a vibration based triboelectric energy harvester, Smart Mater. Struct. 27 (2017) 015029.

[54] B. Sothmann, R. Sánchez, A.N. Jordan, Thermoelectric energy harvesting with quantum dots, Nanotechnology. 26 (2014) 032001.

[55] Y. Lin, J. Song, Y. Ding, S. Lu, Z.L. Wang, Piezoelectric nanogenerator using CdS nanowires, Appl. Phys. Lett. 92 (2008) 022105.

[56] L. Lin, C. Lai, Y. Hu, Y. Zhang, X. Wang, C. Xu, R.L. Snyder, L. Chen, Z.L. Wang, High output nanogenerator based on assembly of GaN nanowires, Nanotechnology. 22 (2011) 475401.

[57] H. You, X. Ma, Z. Wu, L. Fei, X. Chen, J. Yang, Y. Liu, Y. Jia, H. Li, F. Wang, Piezoelectrically/pyroelectrically-driven vibration/cold-hot energy harvesting for mechano-/pyro-bi-catalytic dye decomposition of NaNbO3 nanofibers, Nano Energy. 52 (2018) 351-359.

[58] C. Chang, V.H. Tran, J. Wang, Y. Fuh, L. Lin, Direct-write piezoelectric polymeric nanogenerator with high energy conversion efficiency, Nano letters. 10 (2010) 726-731.

[59] I. Fujii, K. Nakashima, N. Kumada, S. Wada, Structural, dielectric, and piezoelectric properties of BaTiO3–Bi (Ni1/2Ti1/2) O3 ceramics, Journal of the Ceramic Society of Japan. 120 (2012) 30-34.

[60] J. Ma, Z. Shi, C. Nan, Magnetoelectric Properties of Composites of Single Pb (Zr, Ti) O3 Rods and Terfenol-D/Epoxy With a Single-Period of 1-3-Type Structure, Adv Mater. 19 (2007) 2571-2573.

[61] C. Huang, J. Song, C. Tsai, W. Lee, D. Lien, Z. Gao, Y. Hao, L. Chen, Z.L. Wang, Single-InN-Nanowire Nanogenerator with Upto 1 V Output Voltage, Adv Mater. 22 (2010) 4008-4013.

[62] Z.L. Wang, J. Song, Piezoelectric nanogenerators based on zinc oxide nanowire arrays, Science. 312 (2006) 242-246.

[63] Z. WANG, Commercial applications of nanogenerators as sustainable power source and active sensors, SCIENTIA SINICA Chimica. 43 (2013) 759-762.

[64] X. Wang, J. Song, J. Liu, Z.L. Wang, Direct-current nanogenerator driven by ultrasonic waves, Science. 316 (2007) 102-105.

[65] Y. Qin, X. Wang, Z.L. Wang, Microfibre–nanowire hybrid structure for energy scavenging, Nature. 451 (2008) 809-813.

[66] J. Zhang, M. Li, L. Yu, L. Liu, H. Zhang, Z. Yang, Synthesis and piezoelectric properties of well-aligned ZnO nanowire arrays via a simple solution-phase approach, Applied Physics A. 97 (2009) 869.

[67] C. Xu, X. Wang, Z.L. Wang, Nanowire structured hybrid cell for concurrently scavenging solar and mechanical energies, J. Am. Chem. Soc. 131 (2009) 5866-5872.

[68] B. Saravanakumar, R. Mohan, K. Thiyagarajan, S. Kim, Fabrication of a ZnO nanogenerator for eco-friendly biomechanical energy harvesting, RSC Advances. 3 (2013) 16646-16656.

[69] R. Yang, Y. Qin, L. Dai, Z.L. Wang, Power generation with laterally packaged piezoelectric fine wires, Nature nanotechnology. 4 (2009) 34.

[70] Z. Zhou, H. Tang, H.A. Sodano, Scalable synthesis of morphotropic phase boundary lead zirconium titanate nanowires for energy harvesting, Adv Mater. 26 (2014) 7547-7554.

[71] N.R. Alluri, A. Chandrasekhar, V. Vivekananthan, Y. Purusothaman, S. Selvarajan, J.H. Jeong, S. Kim, Scavenging biomechanical energy using high-performance, flexible BaTiO3 nanocube/PDMS composite films, ACS Sustainable Chemistry & Engineering. 5 (2017) 4730-4738.

[72] M.H. Malakooti, F. Julé, H.A. Sodano, Printed Nanocomposite Energy Harvesters with Controlled Alignment of Barium Titanate Nanowires, ACS applied materials & interfaces. 10 (2018) 38359-38367.

[73] S. Xu, Y. Qin, C. Xu, Y. Wei, R. Yang, Z.L. Wang, Self-powered nanowire devices, Nature nanotechnology. 5 (2010) 366-373.

[74] J. Kwon, W. Seung, B.K. Sharma, S. Kim, J. Ahn, A high performance PZT ribbon-based nanogenerator using graphene transparent electrodes, Energy & Environmental Science. 5 (2012) 8970-8975.

[75] W. Wu, S. Bai, M. Yuan, Y. Qin, Z.L. Wang, T. Jing, Lead zirconate titanate nanowire textile nanogenerator for wearable energy-harvesting and self-powered devices, ACS nano. 6 (2012) 6231-6235.

[76] Y. Lin, Y. Liu, H.A. Sodano, Hydrothermal synthesis of vertically aligned lead zirconate titanate nanowire arrays, Appl. Phys. Lett. 95 (2009) 122901.

[77] M.H. Malakooti, Z. Zhou, H.A. Sodano, Enhanced energy harvesting through nanowire based functionally graded interfaces, Nano Energy. 52 (2018) 171-182.

[78] S. Bai, Q. Xu, L. Gu, F. Ma, Y. Qin, Z.L. Wang, Single crystalline lead zirconate titanate (PZT) nano/micro-wire based self-powered UV sensor, Nano Energy. 1 (2012) 789-795.

[79] Y. Qi, N.T. Jafferis, K. Lyons Jr, C.M. Lee, H. Ahmad, M.C. McAlpine, Piezoelectric ribbons printed onto rubber for flexible energy conversion, Nano letters. 10 (2010) 524-528.

[80] X. Zhang, J. Chen, Y. Wang, Hierarchical PbZr x Ti1–x O3 Nanowires for Vibrational Energy Harvesting, ACS Applied Nano Materials. 1 (2018) 1461-1466.

[81] X. Ni, F. Wang, A. Lin, Q. Xu, Z. Yang, Y. Qin, Flexible nanogenerator based on single BaTiO3 nanowire, Science of Advanced Materials. 5 (2013) 1781-1787.

[82] R.W. Ward, The constants of alpha quartz, (1992) 3-4.

[83] R. Smith, F. Welsh, Temperature dependence of the elastic, piezoelectric, and dielectric constants of lithium tantalate and lithium niobate, J. Appl. Phys. 42 (1971) 2219-2230.

[84] D. Damjanovic, Materials for high temperature piezoelectric transducers, Current Opinion in Solid State and Materials Science. 3 (1998) 469-473.

[85] A. Koka, Z. Zhou, H.A. Sodano, Vertically aligned BaTiO 3 nanowire arrays for energy harvesting, Energy & Environmental Science. 7 (2014) 288-296.

[86] N. Abinnas, P. Baskaran, S. Harish, R.S. Ganesh, M. Navaneethan, K. Nisha, S. Ponnusamy, C. Muthamizhchelvan, H. Ikeda, Y. Hayakawa, 0.8 V nanogenerator for mechanical energy harvesting using bismuth titanate–PDMS nanocomposite, Appl. Surf. Sci. 418 (2017) 362-368.

[87] K. Xu, J. Li, X. Lv, J. Wu, X. Zhang, D. Xiao, J. Zhu, Superior piezoelectric properties in potassium–sodium niobate lead-free ceramics, Adv Mater. 28 (2016) 8519-8523.

[88] H. Zhang, S. Jiang, J. Xiao, K. Kajiyoshi, Low temperature preparation and electrical properties of sodium–potassium bismuth titanate lead-free piezoelectric thick films by screen printing, Journal of the European Ceramic Society. 30 (2010) 3157-3165.

[89] Y. Huan, X. Zhang, J. Song, Y. Zhao, T. Wei, G. Zhang, X. Wang, High-performance piezoelectric composite nanogenerator based on Ag/(K, Na) NbO3 heterostructure, Nano energy. 50 (2018) 62-69.

[90] J. Feenstra, H.A. Sodano, Enhanced active piezoelectric 0-3 nanocomposites fabricated through electrospun nanowires, J. Appl. Phys. 103 (2008) 124108.

[91] E.L. Tsege, G.H. Kim, V. Annapureddy, B. Kim, H. Kim, Y. Hwang, A flexible lead-free piezoelectric nanogenerator based on vertically aligned BaTiO 3 nanotube arrays on a Ti-mesh substrate, RSC Advances. 6 (2016) 81426-81435.

[92] C.K. Jeong, I. Kim, K. Park, M.H. Oh, H. Paik, G. Hwang, K. No, Y.S. Nam, K.J. Lee, Virus-directed design of a flexible BaTiO3 nanogenerator, ACS nano. 7 (2013) 11016-11025.

[93] J. Yan, Y.G. Jeong, High performance flexible piezoelectric nanogenerators based on BaTiO3 nanofibers in different alignment modes, ACS applied materials & interfaces. 8 (2016) 15700-15709.

[94] K. Park, S.B. Bae, S.H. Yang, H.I. Lee, K. Lee, S.J. Lee, Lead-free BaTiO 3 nanowires-based flexible nanocomposite generator, Nanoscale. 6 (2014) 8962-8968.

[95] Z. Lin, Y. Yang, J.M. Wu, Y. Liu, F. Zhang, Z.L. Wang, BaTiO3 nanotubes-based flexible and transparent nanogenerators, The journal of physical chemistry letters. 3 (2012) 3599-3604.

[96] K. Park, M. Lee, Y. Liu, S. Moon, G. Hwang, G. Zhu, J.E. Kim, S.O. Kim, D.K. Kim, Z.L. Wang, Flexible nanocomposite generator made of BaTiO3 nanoparticles and graphitic carbons, Adv Mater. 24 (2012) 2999-3004.

[97] N.R. Alluri, B. Saravanakumar, S. Kim, Flexible, Hybrid Piezoelectric Film (BaTi (1–x) Zr x O3)/PVDF Nanogenerator as a Self-Powered Fluid Velocity Sensor, ACS applied materials & interfaces. 7 (2015) 9831-9840.

[98] Y. Zhao, Q. Liao, G. Zhang, Z. Zhang, Q. Liang, X. Liao, Y. Zhang, High output piezoelectric nanocomposite generators composed of oriented BaTiO3 NPs@ PVDF, Nano Energy. 11 (2015) 719-727.

[99] C.K. Jeong, C. Baek, A.I. Kingon, K. Park, S. Kim, Lead-Free Perovskite Nanowire-Employed Piezopolymer for Highly Efficient Flexible Nanocomposite Energy Harvester, Small. 14 (2018) 1704022.

[100] X. Chen, X. Li, J. Shao, N. An, H. Tian, C. Wang, T. Han, L. Wang, B. Lu, High-performance piezoelectric nanogenerators with imprinted P (VDF-TrFE)/BaTiO3 nanocomposite micropillars for self-powered flexible sensors, Small. 13 (2017) 1604245.

[101] S. Siddiqui, D. Kim, M.T. Nguyen, S. Muhammad, W. Yoon, N. Lee, High-performance flexible lead-free nanocomposite piezoelectric nanogenerator for biomechanical energy harvesting and storage, Nano Energy. 15 (2015) 177-185.

[102] S. Shin, Y. Kim, J. Jung, M.H. Lee, J. Nah, Solvent-assisted optimal BaTiO3 nanoparticles-polymer composite cluster formation for high performance piezoelectric nanogenerators, Nanotechnology. 25 (2014) 485401.

[103] S. Shin, Y. Kim, M.H. Lee, J. Jung, J. Nah, Hemispherically aggregated BaTiO3 nanoparticle composite thin film for high-performance flexible piezoelectric nanogenerator, Acs Nano. 8 (2014) 2766-2773.

[104] Y. Hao, K. Bi, S. O'Brien, X. Wang, J. Lombardi, F. Pearsall, W. Li, M. Lei, Y. Wu, L. Li, Interface structure, precursor rheology and dielectric properties of BaTiO3/PVDF–hfp nanocomposite films prepared from colloidal perovskite nanoparticles, RSC Advances. 7 (2017) 32886-32892.

[105] M. Zhang, T. Gao, J. Wang, J. Liao, Y. Qiu, H. Xue, Z. Shi, Z. Xiong, L. Chen, Single BaTiO3 nanowires-polymer fiber based nanogenerator, Nano Energy. 11 (2015) 510-517.

[106] N. Hagood, A. Bent, Development of piezoelectric fiber composites for structural actuation, (1993) 1717.

[107] A. Safari, Development of piezoelectric composites for transducers, Journal de Physique III. 4 (1994) 1129-1149.

[108] W.A. Smith, Composite piezoelectric materials for medical ultrasonic imaging transducers-a review, (1986) 249-256.

[109] C.K. Jeong, I. Kim, K. Park, M.H. Oh, H. Paik, G. Hwang, K. No, Y.S. Nam, K.J. Lee, Virus-directed design of a flexible BaTiO3 nanogenerator, ACS nano. 7 (2013) 11016-11025.

[110] J. Yan, Y.G. Jeong, High performance flexible piezoelectric nanogenerators based on BaTiO3 nanofibers in different alignment modes, ACS applied materials & interfaces. 8 (2016) 15700-15709.

[111] V. Tomer, C. Randall, High field dielectric properties of anisotropic polymer-ceramic composites, J. Appl. Phys. 104 (2008) 074106.

[112] C. Bowen, R. Newnham, C. Randall, Dielectric properties of dielectrophoretically assembled particulate-polymer composites, J. Mater. Res. 13 (1998) 205-210.

[113] V. Tomer, G. Polizos, C. Randall, E. Manias, Polyethylene nanocomposite dielectrics: implications of nanofiller orientation on high field properties and energy storage, J. Appl. Phys. 109 (2011) 074113.

[114] H.A. Pohl, Dielectrophoresis, The behavior of neutral matter in nonuniform electric fields. (1978).

[115] F. Xu, J.W. Durham III, B.J. Wiley, Y. Zhu, Strain-release assembly of nanowires on stretchable substrates, ACS nano. 5 (2011) 1556-1563.

[116] Y. Huang, X. Duan, Q. Wei, C.M. Lieber, Directed assembly of one-dimensional nanostructures into functional networks, Science. 291 (2001) 630-633.

[117] B. Messer, J.H. Song, P. Yang, Microchannel networks for nanowire patterning, J. Am. Chem. Soc. 122 (2000) 10232-10233.

[118] G. Yu, A. Cao, C.M. Lieber, Large-area blown bubble films of aligned nanowires and carbon nanotubes, Nature nanotechnology. 2 (2007) 372.

[119] G. Yu, X. Li, C.M. Lieber, A. Cao, Nanomaterial-incorporated blown bubble films for large-area, aligned nanostructures, Journal of Materials Chemistry. 18 (2008) 728-734.

[120] A. Tao, F. Kim, C. Hess, J. Goldberger, R. He, Y. Sun, Y. Xia, P. Yang, Langmuir− Blodgett silver nanowire monolayers for molecular sensing using surface-enhanced Raman spectroscopy, Nano letters. 3 (2003) 1229-1233.

[121] J. Wang, C.S. Sandu, N. Setter, Large-scale fabrication of titanium-rich perovskite PZT submicro/nano wires and their electromechanical properties, IEEE Trans. Ultrason. Ferroelectr. Freq. Control. 56 (2009) 1813-1819.

[122] H. Tang, Y. Lin, H.A. Sodano, Enhanced energy storage in nanocomposite capacitors through aligned PZT nanowires by uniaxial strain assembly, Advanced Energy Materials. 2 (2012) 469-476.

[123] J.E. Smay, J. Cesarano, J.A. Lewis, Colloidal inks for directed assembly of 3-D periodic structures, Langmuir. 18 (2002) 5429-5437.

[124] J.A. Lewis, Direct ink writing of 3D functional materials, Advanced Functional Materials. 16 (2006) 2193-2204.

[125] B.G. Compton, J.A. Lewis, 3D-printing of lightweight cellular composites, Adv Mater. 26 (2014) 5930-5935.

[126] A.S. Gladman, E.A. Matsumoto, R.G. Nuzzo, L. Mahadevan, J.A. Lewis, Biomimetic 4D printing, Nature materials. 15 (2016) 413.

[127] G. Siqueira, D. Kokkinis, R. Libanori, M.K. Hausmann, A.S. Gladman, A. Neels, P. Tingaut, T. Zimmermann, J.A. Lewis, A.R. Studart, Cellulose nanocrystal inks for 3D printing of textured cellular architectures, Advanced Functional Materials. 27 (2017) 1604619.

[128] L. Cai, S. Zhang, Y. Zhang, J. Li, J. Miao, Q. Wang, Z. Yu, C. Wang, Direct printing for additive patterning of silver nanowires for stretchable sensor and display applications, Advanced Materials Technologies. 3 (2018) 1700232.

[129] M.K. Hausmann, P.A. Ruhs, G. Siqueira, J. Läuger, R. Libanori, T. Zimmermann, A.R. Studart, Dynamics of cellulose nanocrystal alignment during 3D Printing, ACS nano. 12 (2018) 6926-6937.

[130] van der Zande, Bianca MI, G.J. Koper, H.N. Lekkerkerker, Alignment of rod-shaped gold particles by electric fields, The Journal of Physical Chemistry B. 103 (1999) 5754-5760.

[131] K. Yamamoto, S. Akita, Y. Nakayama, Orientation and purification of carbon nanotubes using ac electrophoresis, J. Phys. D. 31 (1998) L34.

[132] G.M. Gratson, F. García-Santamaría, V. Lousse, M. Xu, S. Fan, J.A. Lewis, P.V. Braun, Direct-write assembly of three-dimensional photonic crystals: conversion of polymer scaffolds to silicon hollow-woodpile structures, Adv Mater. 18 (2006) 461-465.

[133] K.A. Seerden, N. Reis, J.R. Evans, P.S. Grant, J.W. Halloran, B. Derby, Ink-jet printing of wax-based alumina suspensions, J Am Ceram Soc. 84 (2001) 2514-2520.

[134] B. Tay, M. Edirisinghe, Investigation of some phenomena occurring during continuous ink-jet printing of ceramics, J. Mater. Res. 16 (2001) 373-384.

[135] M. Mott, J. Evans, Zirconia/alumina functionally graded material made by ceramic ink jet printing, Materials Science and Engineering: A. 271 (1999) 344-352.

[136] J.H. Song, M.J. Edirisinghe, J.R. Evans, Formulation and multilayer jet printing of ceramic inks, J Am Ceram Soc. 82 (1999) 3374-3380.

[137] E. Sachs, M. Cima, P. Williams, D. Brancazio, J. Cornie, Three dimensional printing: rapid tooling and prototypes directly from a CAD model, Journal of engineering for industry. 114 (1992) 481-488.

[138] S.L. Morissette, J.A. Lewis, P.G. Clem, J. Cesarano, D.B. Dimos, Direct-Write Fabrication of Pb (Nb, Zr, Ti) O3 Devices: Influence of Paste Rheology on Print Morphology and Component Properties, J Am Ceram Soc. 84 (2001) 2462-2468.

[139] I. Cesarano, R. Segalman, Robocasting provides moldless fabrication from slurry deposition. Ceramic Industry. 148 (1998) 94-100.

[140] J. Cesarano III, P. Calvert, US Patent 6 027 326, 2000. b) Q. Li, JA Lewis, Adv Mater. 15 (2003) 1639.

[141] J.E. Smay, J. Cesarano III, B.A. Tuttle, J.A. Lewis, Piezoelectric properties of 3-X periodic Pb (Zr x Ti 1− x) O 3–polymer composites, J. Appl. Phys. 92 (2002) 6119-6127.

[142] J.E. Smay, J. Cesarano, J.A. Lewis, Colloidal inks for directed assembly of 3-D periodic structures, Langmuir. 18 (2002) 5429-5437.

[143] D. Therriault, S.R. White, J.A. Lewis, Chaotic mixing in three-dimensional microvascular networks fabricated by direct-write assembly, Nature materials. 2 (2003) 265.

[144] G.M. Gratson, M. Xu, J.A. Lewis, Microperiodic structures: Direct writing of three-dimensional webs, Nature. 428 (2004) 386.

[145] D.W. Hutmacher, T. Schantz, I. Zein, K.W. Ng, S.H. Teoh, K.C. Tan, Mechanical properties and cell cultural response of polycaprolactone scaffolds designed and fabricated via fused deposition modeling, Journal of Biomedical Materials Research: An Official Journal of The Society for Biomaterials, The Japanese Society for Biomaterials, and The Australian Society for Biomaterials and the Korean Society for Biomaterials. 55 (2001) 203-216.

[146] G.M. Lous, I.A. Cornejo, T.F. McNulty, A. Safari, S.C. Danforth, Fabrication of piezoelectric ceramic/polymer composite transducers using fused deposition of ceramics, J Am Ceram Soc. 83 (2000) 124-128.

[147] D. Therriault, R.F. Shepherd, S.R. White, J.A. Lewis, Fugitive inks for Direct-Write assembly of Three-Dimensional microvascular networks, Adv Mater. 17 (2005) 395-399.

[148] G.M. Gratson, J.A. Lewis, Phase behavior and rheological properties of polyelectrolyte inks for direct-write assembly, Langmuir. 21 (2005) 457-464.

[149] M. Xu, G.M. Gratson, E.B. Duoss, R.F. Shepherd, J.A. Lewis, Biomimetic silicification of 3D polyamine-rich scaffolds assembled by direct ink writing, Soft Matter. 2 (2006) 205-209.

[150] J.E. Smay, G.M. Gratson, R.F. Shepherd, J. Cesarano III, J.A. Lewis, Directed colloidal assembly of 3D periodic structures, Adv Mater. 14 (2002) 1279-1283.

[151] R. Newnham, D. Skinner, L. Cross, Connectivity and piezoelectric-pyroelectric composites, Mater. Res. Bull. 13 (1978) 525-536.

[152] C.H. Zweben, Comprehensive Composite Materials, Elsevier, 2000.

[153] Q. Qin, Advanced Mechanics of Piezoelectricity, Springer Science & Business Media, 2012.

[154] H. Banno, Recent developments of piezoelectric ceramic products and composites of synthetic rubber and piezoelectric ceramic particles, Ferroelectrics. 50 (1983) 3-12.

[155] W.A. Smith, B.A. Auld, Modeling 1-3 composite piezoelectrics: thickness-mode oscillations, IEEE Trans. Ultrason. Ferroelectr. Freq. Control. 38 (1991) 40-47.

[156] A. Zaoui, Continuum micromechanics: survey, J. Eng. Mech. 128 (2002) 808-816.

[157] Z. Shu-Ang, A material multipole theory of elastic dielectric composites, Int. J. Solids Structures. 28 (1991) 423-447.

[158] W. Biao, Three-dimensional analysis of an ellipsoidal inclusion in a piezoelectric material, Int. J. Solids Structures. 29 (1992) 293-308.

[159] J. Aboudi, Mechanics of Composite Materials: A Unified Micromechanical Approach, Elsevier, 2013.

[160] A. Hershey, The elasticity of an isotropic aggregate of anisotropic cubic crystals, Journal of Applied mechanics-transactions of the ASME. 21 (1954) 236-240.

[161] E. Kröner, Kontinuumstheorie Der Versetzungen Und Eigenspannungen, Springer, 1958.

[162] Y. Benveniste, A new approach to the application of Mori-Tanaka's theory in composite materials, Mech. Mater. 6 (1987) 147-157.

[163] J.D. Eshelby, The determination of the elastic field of an ellipsoidal inclusion, and related problems, Proc.R.Soc.Lond.A. 241 (1957) 376-396.

[164] T. Mura, Micromechanics of Defects in Solids, Springer Science & Business Media, 2013.

[165] M. Taya, R.J. Arsenault, Metal Matrix Composites: Thermomechanical Behavior, Elsevier, 2016.

[166] M. Dunn, M. Taya, Micromechanics predictions of the effective electroelastic moduli of piezoelectric composites, Int. J. Solids Structures. 30 (1993) 161-175.

[167] C. Nan, F. Jin, Multiple-scattering approach to effective properties of piezoelectric composites, Physical Review B. 48 (1993) 8578.

[168] C. Nan, Effective-medium theory of piezoelectric composites, J. Appl. Phys. 76 (1994) 1155-1163.

[169] J. Aboudi, Micromechanical prediction of the effective coefficients of thermo-piezoelectric multiphase composites, J Intell Mater Syst Struct. 9 (1998) 713-722.

[170] P. Tan, L. Tong, Micromechanics models for non-linear behavior of piezo-electric fiber reinforced composite materials, Int. J. Solids Structures. 38 (2001) 8999-9032.

[171] A. Muliana, C. Lin, A multi-scale formulation for predicting non-linear thermo-electro-mechanical response in heterogeneous bodies, J Intell Mater Syst Struct. 22 (2011) 723-738.

[172] S.R. Anton, H.A. Sodano, A review of power harvesting using piezoelectric materials (2003–2006), Smart Mater. Struct. 16 (2007) R1.

[173] A. Harb, Energy harvesting: State-of-the-art, Renewable Energy. 36 (2011) 2641-2654.

[174] M.I. Tiwana, S.J. Redmond, N.H. Lovell, A review of tactile sensing technologies with applications in biomedical engineering, Sensors and Actuators A: physical. 179 (2012) 17-31.

[175] A. El Kacimi, E. Pauliac-Vaujour, J. Eymery, Flexible capacitive piezoelectric sensor with vertically aligned ultra-long GaN wires, ACS applied materials & interfaces. (2018).

[176] H.A. Sodano, D.J. Inman, G. Park, A review of power harvesting from vibration using piezoelectric materials, Shock Vib Dig. 36 (2004) 197-206.

[177] A. Nafari, C.C. Bowland, H.A. Sodano, Ultra-long vertically aligned lead titanate nanowire arrays for energy harvesting in extreme environments, Nano Energy. 31 (2017) 168-173.

[178] A. Nafari, C.C. Bowland, H.A. Sodano, Vertically Aligned Lead Titanate Nanowire Arrays for High Temperature Energy Harvesting, (2015) V002T07A018-V002T07A018.

[179] W. Obitayo, T. Liu, A review: Carbon nanotube-based piezoresistive strain sensors, Journal of Sensors. 2012 (2012).

[180] S. Stassi, V. Cauda, G. Canavese, C.F. Pirri, Flexible tactile sensing based on piezoresistive composites: A review, Sensors. 14 (2014) 5296-5332.

[181] K. Uchino, S. Nomura, L.E. Cross, R.E. Newnham, S.J. Jang, Electrostrictive effect in perovskites and its transducer applications, J. Mater. Sci. 16 (1981) 569-578.

[182] M. Lallart, P. Cottinet, D. Guyomar, L. Lebrun, Electrostrictive polymers for mechanical energy harvesting, Journal of Polymer Science Part B: Polymer Physics. 50 (2012) 523-535.

[183] J.M. Jani, M. Leary, A. Subic, M.A. Gibson, A review of shape memory alloy research, applications and opportunities, Materials & Design (1980-2015). 56 (2014) 1078-1113.

[184] Y. Heo, H.A. Sodano, Self-healing polyurethanes with shape recovery, Advanced Functional Materials. 24 (2014) 5261-5268.

[185] R.A. Ottaviani, J.C. Ulicny, M.A. Golden, Magnetorheological nanocomposite elastomer for releasable attachment applications. (2008).

[186] L. Yang, F. Duan, A. Eriksson, Analysis of the optimal design strategy of a magnetorheological smart structure, Smart Mater. Struct. 17 (2008) 015047.

[187] Z. Shi, T. Zhang, Static analyses for 2–2 multi-layered piezoelectric curved composites, Int. J. Eng. Sci. 45 (2007) 509-524.

[188] T. Zhang, Z. Shi, Bending behavior of 2–2 multi-layered piezoelectric curved actuators, Smart Mater. Struct. 16 (2007) 634.

[189] Z. Shi, Bending behavior of piezoelectric curved actuator, Smart Mater. Struct. 14 (2005) 835.

[190] Z. Zhou, H. Tang, H.A. Sodano, Scalable Synthesis of Morphotropic Phase Boundary Lead Zirconium Titanate Nanowires for Energy Harvesting, Adv Mater. 26 (2014) 7547-7554.

[191] J. Feenstra, H.A. Sodano, Enhanced active piezoelectric 0-3 nanocomposites fabricated through electrospun nanowires, J. Appl. Phys. 103 (2008) 124108.

[192] H. Tang, Y. Lin, C. Andrews, H.A. Sodano, Characterization of Nanocomposites Incorporating PZT Nanowires for Enhanced Energy Storage, (2010) 161-168.

[193] Z. Zhou, C.C. Bowland, M.H. Malakooti, H. Tang, H.A. Sodano, Lead-free 0.5 Ba (Zr 0.2 Ti 0.8) O 3–0.5 (Ba 0.7 Ca 0.3) TiO 3 nanowires for energy harvesting, Nanoscale. 8 (2016) 5098-5105.

[194] H. Kim, T. Fernando, M. Li, Y. Lin, T.B. Tseng, Fabrication and characterization of 3D printed BaTiO3/PVDF nanocomposites, J. Composite Mater. 52 (2018) 197-206.

[195] H. Kim, F. Torres, D. Villagran, C. Stewart, Y. Lin, T.B. Tseng, 3D printing of BaTiO3/PVDF composites with electric in situ poling for pressure sensor applications, Macromolecular Materials and Engineering. 302 (2017) 1700229.

[196] B. Jiang, D. Fang, K. Hwang, A unified model for piezocomposites with non-piezoelectric matrix and piezoelectric ellipsoidal inclusions, Int. J. Solids Structures. 36 (1999) 2707-2733.

[197] L.P. Khoroshun, B.P. Maslov, P.V. Leshchenko, Prediction of the effective properties of piezoactive composite materials, Kiev Izdatel Naukova Dumka. (1989).

[198] W. Voigt, Lehrbuch der Kristallphysik (Teubner, Leipzig, 1928), Google Scholar. (1908) 962.

[199] M. Huang, X. Gao, L.C. Brinson, A multivariant micromechanical model for SMAs Part 2. Polycrystal model, Int. J. Plast. 16 (2000) 1371-1390.

[200] R. Hill, The elastic behaviour of a crystalline aggregate, Proceedings of the Physical Society.Section A. 65 (1952) 349.

[201] V.Y. Topolov, C.R. Bowen, Electromechanical Properties in Composites Based on Ferroelectrics, Springer Science & Business Media, 2008.

[202] Y. Benveniste, G. Dvorak, T. Chen, On diagonal and elastic symmetry of the approximate effective stiffness tensor of heterogeneous media, J. Mech. Phys. Solids. 39 (1991) 927-946.

[203] M.F. Alhasadi, S. Federico, Relation between Eshelby stress and Eshelby fourth-order tensor within an ellipsoidal inclusion, Acta Mech. 228 (2017) 1045-1069.

[204] L. Jiang, E. Morelius, J. Zhang, M. Wolcott, J. Holbery, Study of the poly (3-hydroxybutyrate-co-3-hydroxyvalerate)/cellulose nanowhisker composites prepared by solution casting and melt processing, J. Composite Mater. 42 (2008) 2629-2645.

[205] M.H. Malakooti, H.A. Sodano, Multi-inclusion modeling of multiphase piezoelectric composites, Composites Part B: Engineering. 47 (2013) 181-189.

[206] D. Barnett, J. Lothe, Dislocations and line charges in anisotropic piezoelectric insulators, Physica Status Solidi (b). 67 (1975) 105-111.

[207] M.L. Dunn, M. Taya, An analysis of piezoelectric composite materials containing ellipsoidal inhomogeneities, 443 (1993) 265-287.

[208] C. Andrews, Y. Lin, H.A. Sodano, Effect of aspect ratio on the electroelastic properties of piezoelectric nanocomposites, 7289 (2009) 72891C.

[209] J. Schjødt-Thomsen, R. Pyrz, The Mori–Tanaka stiffness tensor: diagonal symmetry, complex fibre orientations and non-dilute volume fractions, Mech. Mater. 33 (2001) 531-544.

[210] M. Taya, Electronic Composites: Modeling, Characterization, Processing, and MEMS Applications, Cambridge University Press, 2005.

[211] Y. Mikata, Explicit determination of piezoelectric Eshelby tensors for a spheroidal inclusion, Int. J. Solids Structures. 38 (2001) 7045-7063.

[212] G.J. Rodin, Eshelby's inclusion problem for polygons and polyhedra, J. Mech. Phys. Solids. 44 (1996) 1977-1995.

[213] A. Gavazzi, D. Lagoudas, On the numerical evaluation of Eshelby's tensor and its application to elastoplastic fibrous composites, Comput. Mech. 7 (1990) 13-19.

[214] I. Johnston, D. McCluskey, C. Tan, M. Tracey, Mechanical characterization of bulk Sylgard 184 for microfluidics and microengineering, J Micromech Microengineering. 24 (2014) 035017.

[215] P. Du, X. Lin, X. Zhang, Dielectric constants of PDMS nanocomposites using conducting polymer nanowires, (2011) 645-648.

[216] M. Zgonik, P. Bernasconi, M. Duelli, R. Schlesser, P. Günter, M. Garrett, D. Rytz, Y. Zhu, X. Wu, Dielectric, elastic, piezoelectric, electro-optic, and elasto-optic tensors of BaTiO 3 crystals, Physical review B. 50 (1994) 5941.

[217] D. Liu, J. Li, The enhanced and optimal piezoelectric coefficients in single crystalline barium titanate with engineered domain configurations, Appl. Phys. Lett. 83 (2003) 1193-1195.

[218] T. Kanit, S. Forest, I. Galliet, V. Mounoury, D. Jeulin, Determination of the size of the representative volume element for random composites: statistical and numerical approach, Int. J. Solids Structures. 40 (2003) 3647-3679.

[219] M. Pindera, H. Khatam, A.S. Drago, Y. Bansal, Micromechanics of spatially uniform heterogeneous media: a critical review and emerging approaches, Composites Part B: Engineering. 40 (2009) 349-378.

[220] A. Drago, M. Pindera, Micro-macromechanical analysis of heterogeneous materials: macroscopically homogeneous vs periodic microstructures, Composites Sci. Technol. 67 (2007) 1243-1263.

[221] A. Jafari, A.A. Khatibi, M.M. Mashhadi, A. Ghazavizadeh, On the parameters influencing the effective properties of a piezoelectric nanocomposite film employing FEM, J. Composite Mater. 47 (2013) 1987-2003.

[222] A. Jafari, A.A. Khatibi, M.M. Mashhadi, Comprehensive investigation on hierarchical multiscale homogenization using representative volume element for piezoelectric nanocomposites, Composites Part B: Engineering. 42 (2011) 553-561.

[223] C. Poizat, M. Sester, Effective properties of composites with embedded piezoelectric fibres, Computational Materials Science. 16 (1999) 89-97.

[224] B. Widom, Random sequential addition of hard spheres to a volume, J. Chem. Phys. 44 (1966) 3888-3894.

[225] S. Williams, A. Philipse, Random packings of spheres and spherocylinders simulated by mechanical contraction, Physical Review E. 67 (2003) 051301.

[226] D. Duschlbauer, H.J. BÖhm, H.E. Pettermann, Computational simulation of composites reinforced by planar random fibers: homogenization and localization by unit cell and mean field approaches, J. Composite Mater. 40 (2006) 2217-2234.

[227] S. Kari, H. Berger, U. Gabbert, Numerical evaluation of effective material properties of randomly distributed short cylindrical fibre composites, Computational materials science. 39 (2007) 198-204.

[228] D. Coelho, J. Thovert, P. Adler, Geometrical and transport properties of random packings of spheres and aspherical particles, Physical Review E. 55 (1997) 1959.

[229] H.J. Böhm, A. Eckschlager, W. Han, Multi-inclusion unit cell models for metal matrix composites with randomly oriented discontinuous reinforcements, Computational materials science. 25 (2002) 42-53.

[230] Y. Pan, L. Iorga, A.A. Pelegri, Analysis of 3D random chopped fiber reinforced composites using FEM and random sequential adsorption, Computational Materials Science. 43 (2008) 450-461.

[231] Y. Xu, Ferroelectric Materials and their Applications, Elsevier, 2013.

[232] R.B. Meyer, L. Liebert, L. Strzelecki, P. Keller, Ferroelectric liquid crystals, Journal de Physique Lettres. 36 (1975) 69-71.

[233] R. Takayama, Y. Tomita, Preparation of epitaxial Pb (Zr x Ti1− x) O3 thin films and their crystallographic, pyroelectric, and ferroelectric properties, J. Appl. Phys. 65 (1989) 1666-1670.

[234] A. Glass, Dielectric, Thermal, and Pyroelectric Properties of Ferroelectric LiTa O 3, Physical Review. 172 (1968) 564.

[235] B. Dudem, D.H. Kim, L.K. Bharat, J.S. Yu, Highly-flexible piezoelectric nanogenerators with silver nanowires and barium titanate embedded composite films for mechanical energy harvesting, Appl. Energy. 230 (2018) 865-874.

[236] A. Koka, H.A. Sodano, High-sensitivity accelerometer composed of ultra-long vertically aligned barium titanate nanowire arrays, Nature communications. 4 (2013).

[237] V. Bornand, I. Huet, P. Papet, Multi-Step Growth of Oriented LiNbO 3 Thin Films, Integrated Ferroelectr. 45 (2002) 69-78.

[238] Y. Shouwen, Z. Liping, F. Xiqiao, Thermal effects of ferroelectric/magnetic materials under cyclic-electric loading, Journal of Thermal Stresses. 32 (2008) 149-164.

[239] T. Furukawa, G. Johnson, Measurements of ferroelectric switching characteristics in polyvinylidene fluoride, Appl. Phys. Lett. 38 (1981) 1027-1029.

[240] K. Schmitt, R. Herr, M. Schadt, J. Fünfschilling, R. Buchecker, X. Chen, C. Benecke, Strongly non-linear optical ferroelectric liquid crystals for frequency doubling, Liquid Crystals. 14 (1993) 1735-1752.

[241] S. Chu, T. Chen, I. Tsai, W. Water, Doping effects of Nb additives on the piezoelectric and dielectric properties of PZT ceramics and its application on SAW device, Sensors and Actuators A: Physical. 113 (2004) 198-203.

[242] X. Wang, C. Song, D. Li, K. Geng, F. Zeng, F. Pan, The influence of different doping elements on microstructure, piezoelectric coefficient and resistivity of sputtered ZnO film, Appl. Surf. Sci. 253 (2006) 1639-1643.

[243] A. Koka, Z. Zhou, H. Tang, H.A. Sodano, Controlled synthesis of ultra-long vertically aligned BaTiO3 nanowire arrays for sensing and energy harvesting applications, Nanotechnology. 25 (2014) 375603.

[244] A. Koka, H.A. Sodano, A Low-Frequency Energy Harvester from Ultralong, Vertically Aligned BaTiO3 Nanowire Arrays, Advanced Energy Materials. 4 (2014).

[245] H. Tang, Z. Zhou, H.A. Sodano, Relationship between BaTiO3 nanowire aspect ratio and the dielectric permittivity of nanocomposites, ACS applied materials & interfaces. 6 (2014) 5450-5455.

[246] P. Ayyub, V. Palkar, S. Chattopadhyay, M. Multani, Effect of crystal size reduction on lattice symmetry and cooperative properties, Physical Review B. 51 (1995) 6135.

[247] J. Varghese, R.W. Whatmore, J.D. Holmes, Ferroelectric nanoparticles, wires and tubes: synthesis, characterisation and applications, Journal of Materials Chemistry C. 1 (2013) 2618-2638.

[248] L. Liu, T. Ning, Y. Ren, Z. Sun, F. Wang, W. Zhou, S. Xie, L. Song, S. Luo, D. Liu, Synthesis, characterization, photoluminescence and ferroelectric properties of PbTiO3 nanotube arrays, Materials Science and Engineering: B. 149 (2008) 41-46.

[249] H. Liu, C. Hu, Z.L. Wang, Composite-hydroxide-mediated approach for the synthesis of nanostructures of complex functional-oxides, Nano Letters. 6 (2006) 1535-1540.

[250] D. Li, Y. Xia, Electrospinning of nanofibers: reinventing the wheel? Adv Mater. 16 (2004) 1151-1170.

[251] B. Parkinson, The emerging art of solid-state synthesis, Science. 270 (1995) 1157-1158.

[252] D. Guo, L. Zhao, Y. Sang, H. Liu, S. Liu, X. Sun, Al 2 O 3/yttrium compound core–shell structure formation with burst nucleation: a process driven by electrostatic attraction and high surface energy, RSC Advances. 4 (2014) 55400-55406.

[253] T. Hungria, J. Galy, A. Castro, Spark plasma sintering as a useful technique to the nanostructuration of piezo-ferroelectric materials, Advanced Engineering Materials. 11 (2009) 615-631.

[254] H. Maiwa, Preparation and properties of BaTiO3 ceramics by spark plasma sintering, Japanese Journal of Applied Physics. 47 (2008) 7646.

[255] T. Karaki, K. Yan, M. Adachi, Subgrain microstructure in high-performance BaTiO3 piezoelectric ceramics, Applied physics express. 1 (2008) 111402.

[256] H. Nonomura, M. Nagata, H. Fujisawa, M. Shimizu, H. Niu, K. Honda, Structural control of self-assembled Pb Ti O 3 nanoislands fabricated by metalorganic chemical vapor deposition, Appl. Phys. Lett. 86 (2005) 163106.

[257] L. Zhu, X. Liu, J. Meng, X. Cao, Facile sonochemical synthesis of single-crystalline europium fluorine with novel nanostructure, Crystal Growth and Design. 7 (2007) 2505-2511.

[258] R.E. Cohen, Origin of ferroelectricity in perovskite oxides, Nature. 358 (1992) 136.

[259] W.J. Dawson, Hydrothermal synthesis of advanced[electronic] ceramic powders, American Ceramic Society Bulletin. 67 (1988) 1673-1678.

[260] S. Ji, H. Liu, Y. Sang, W. Liu, G. Yu, Y. Leng, Synthesis, structure, and piezoelectric properties of ferroelectric and antiferroelectric NaNbO 3 nanostructures, CrystEngComm. 16 (2014) 7598-7604.

[261] S. Stassi, V. Cauda, C. Ottone, A. Chiodoni, C.F. Pirri, G. Canavese, Flexible piezoelectric energy nanogenerator based on ZnO nanotubes hosted in a polycarbonate membrane, Nano Energy. 13 (2015) 474-481.

[262] X.Y. Kong, Z.L. Wang, Polar-surface dominated ZnO nanobelts and the electrostatic energy induced nanohelixes, nanosprings, and nanospirals, Appl. Phys. Lett. 84 (2004) 975-977.

[263] X.Y. Kong, Z.L. Wang, Spontaneous polarization-induced nanohelixes, nanosprings, and nanorings of piezoelectric nanobelts, Nano letters. 3 (2003) 1625-1631.

[264] H. Lin, Y. Lu, H. Chen, H. Lee, S. Gwo, InGaN/GaN nanorod array white light-emitting diode, Appl. Phys. Lett. 97 (2010) 073101.

[265] A. Khan, M. Ali Abbasi, M. Hussain, Z. Hussain Ibupoto, J. Wissting, O. Nur, M. Willander, Piezoelectric nanogenerator based on zinc oxide nanorods grown on textile cotton fabric, Appl. Phys. Lett. 101 (2012) 193506.

[266] L. Liang, X. Kang, Y. Sang, H. Liu, One-Dimensional Ferroelectric Nanostructures: Synthesis, Properties, and Applications, Advanced Science. 3 (2016) 1500358.

[267] D. Hu, M. Yao, Y. Fan, C. Ma, M. Fan, M. Liu, Strategies to achieve high performance piezoelectric nanogenerators, Nano Energy. (2018).

[268] W. Jin, Z. Wang, H. Huang, X. Hu, Y. He, M. Li, L. Li, Y. Gao, Y. Hu, H. Gu, High-performance piezoelectric energy harvesting of vertically aligned Pb (Zr, Ti) O 3 nanorod arrays, RSC Advances. 8 (2018) 7422-7427.

[269] S. Muthukumar, N. Emanetoglu, G. Patounakis, C. Gorla, S. Liang, Y. Lu, Two-step metalorganic chemical vapor deposition growth of piezoelectric ZnO thin film on SiO 2/Si substrate, Journal of Vacuum Science & Technology A: Vacuum, Surfaces, and Films. 19 (2001) 1850-1853.

[270] C.C. Bowland, M.H. Malakooti, Z. Zhou, H.A. Sodano, Highly aligned arrays of high aspect ratio barium titanate nanowires via hydrothermal synthesis, Appl. Phys. Lett. 106 (2015) 222903.

[271] H. Tang, Y. Lin, H.A. Sodano, Synthesis of high aspect ratio BaTiO3 nanowires for high energy density nanocomposite capacitors, Advanced Energy Materials. 3 (2013) 451-456.

[272] C.A. Randall, N. Kim, J. Kucera, W. Cao, T.R. Shrout, Intrinsic and extrinsic size effects in fine-grained morphotropic-phase-boundary lead zirconate titanate ceramics, relation. 500 (1998) 6.

[273] A. Nafari, H. Sodano, Surface morphology effects in a vibration based triboelectric energy harvester, Smart Mater. Struct. 27 (2017) 015029.

[274] M. Gao, L. Li, W. Li, H. Zhou, Y. Song, Direct Writing of Patterned, Lead-Free Nanowire Aligned Flexible Piezoelectric Device, Advanced Science. 3 (2016).

[275] A. Tamang, S.K. Ghosh, S. Garain, M.M. Alam, J. Haeberle, K. Henkel, D. Schmeisser, D. Mandal, DNA-assisted β-phase nucleation and alignment of molecular dipoles in pvdf film: a realization of self-poled bioinspired flexible polymer nanogenerator for portable electronic devices, ACS applied materials & interfaces. 7 (2015) 16143-16147.

[276] Q. Guo, G. Cao, I. Shen, Measurements of piezoelectric coefficient d33 of lead zirconate titanate thin films using a mini force hammer, Journal of Vibration and Acoustics. 135 (2013) 011003.

[277] M. Pozzi, Impulse excitation of piezoelectric bimorphs for energy harvesting: a dimensionless model, Smart Mater. Struct. 23 (2014) 045044.

[278] P. Pillatsch, E. Yeatman, A. Holmes, A scalable piezoelectric impulse-excited energy harvester for human body excitation, Smart Mater. Struct. 21 (2012) 115018.

[279] J. Briscoe, N. Jalali, P. Woolliams, M. Stewart, P.M. Weaver, M. Cain, S. Dunn, Measurement techniques for piezoelectric nanogenerators, Energy & Environmental Science. 6 (2013) 3035-3045.

[280] X. Liu, J. Jeffries, R. Hanson, K. Hinckley, M. Woodmansee, Development of a tunable diode laser sensor for measurements of gas turbine exhaust temperature, Appl. Phy. B. 82 (2006) 469-478.

[281] A.D. Kersey, Optical fiber sensors for permanent downwell monitoring applications in the oil and gas industry, IEICE Trans. Electron. 83 (2000) 400-404.

[282] N. Sahoo, R.K. Peetala, Transient temperature data analysis for a supersonic flight test, Journal of Heat Transfer. 132 (2010) 084503.

[283] B. Kumar, S. Kim, Energy harvesting based on semiconducting piezoelectric ZnO nanostructures, Nano Energy. 1 (2012) 342-355.

[284] M. Gelabert, R. Laudise, R. Riman, Phase stability, solubility and hydrothermal crystal growth of PbTiO 3, J. Cryst. Growth. 197 (1999) 195-203.

[285] S. Zhang, F. Yu, Piezoelectric materials for high temperature sensors, J Am Ceram Soc. 94 (2011) 3153-3170.

[286] Y. Yang, X. Wang, C. Zhong, C. Sun, G. Yao, L. Li, Synthesis and growth mechanism of lead titanate nanotube arrays by hydrothermal method, J Am Ceram Soc. 91 (2008) 3388-3390.

[287] M. Schulz, J. Sauerwald, D. Richter, H. Fritze, Electromechanical properties and defect chemistry of high-temperature piezoelectric materials, Ionics. 15 (2009) 157-161.

[288] J. Hornsteiner, E. Born, G. Fischerauer, E. Riha, Surface acoustic wave sensors for high-temperature applications, (1998) 615-620.

[289] R. Fachberger, G. Bruckner, G. Knoll, R. Hauser, J. Biniasch, L. Reindl, Applicability of LiNbO/sub 3/, langasite and GaPO/sub 4/in high temperature SAW sensors operating at radio frequencies, IEEE Trans. Ultrason. Ferroelectr. Freq. Control. 51 (2004) 1427-1431.

[290] G. Ohlendorf, D. Richter, J. Sauerwald, H. Fritze, High-temperature electrical conductivity and electro-mechanical properties of stoichiometric lithium niobate, Diffus.Fundam. 8 (2008).

[291] H. Fritze, High temperature piezoelectric materials: Defect chemistry and electro-mechanical properties, Journal of electroceramics. 17 (2006) 625-630.

[292] J. Hornsteiner, E. Born, E. Riha, Langasite for high temperature surface acoustic wave applications, physica status solidi (a). 163 (1997) R3-R4.

[293] H. Fritze, H. Tuller, Langasite for high-temperature bulk acoustic wave applications, Appl. Phys. Lett. 78 (2001) 976-977.

[294] R.J. Kažys, A. Voleišis, B. Voleišienė, High temperature ultrasonic transducers, Ultragarsas. 63 (2008) 7-17.

[295] C. Lin, T. Yen, V.V. Felmetsger, M.A. Hopcroft, J.H. Kuypers, A.P. Pisano, Thermally compensated aluminum nitride Lamb wave resonators for high temperature applications, Appl. Phys. Lett. 97 (2010) 083501.

[296] T. Yen, C. Lin, X. Zhao, V.V. Felmetsger, D.G. Senesky, M.A. Hopcroft, A.P. Pisano, Characterization of aluminum nitride Lamb wave resonators operating at 600 C for harsh environment RF applications, (2010) 731-734.

[297] W.P. Mason, Physical Acoustics V4B: Principles and Methods, Elsevier, 2012.

[298] B. Jaffe, Piezoelectric Ceramics, Elsevier, 2012.

[299] S. Zhang, R. Xia, L. Lebrun, D. Anderson, T.R. Shrout, Piezoelectric materials for high power, high temperature applications, Mater Lett. 59 (2005) 3471-3475.

[300] Y. Chen, K. Uchino, M. Shen, D. Viehland, Substituent effects on the mechanical quality factor of Pb (Mg 1/3 Nb 2/3) O 3–PbTiO 3 and Pb (Sc 1/2 Nb 1/2) O 3–PbTiO 3 ceramics, J. Appl. Phys. 90 (2001) 1455-1458.

[301] J. Ryu, S. Priya, K. Uchino, High-T m relaxor ferroelectrics: 0.3 BiScO 3–0.6 PbTiO 3–0.1 Pb (Mn 1/3 Nb 2/3) O 3, Appl. Phys. Lett. 82 (2003) 251-253.

[302] S. Zhang, S. Rhee, C.A. Randall, T.R. Shrout, Dielectric and piezoelectric properties of high Curie temperature single crystals in the Pb (Yb1/2Nb1/2) O3–xPbTiO3 solid solution series, Japanese journal of applied physics. 41 (2002) 722.

[303] S. Zhang, C.A. Randall, T.R. Shrout, High Curie temperature piezocrystals in the BiScO 3-PbTiO 3 perovskite system, Appl. Phys. Lett. 83 (2003) 3150-3152.

[304] J. Herbert, Ferroelectric Transducers and Sensors; Gordon and Breach Science Publishers, New York. (1982).

[305] T. Shrout, S. Zhang, R. Eitel, C. Stringer, C. Randall, High performance, high temperature perovskite piezoelectrics, (2004) 126-129.

[306] W. Kuai, M. Zhao, C. Wang, L. Wang, J. Wang, Z. Gai, J. Zhang, N. Yin, Effect of composition on the structure and piezoelectricity of Na0. 5Bi4. 5Ti4O15-based flexoelectric-type polar ceramics, J. Alloys Compounds. 559 (2013) 76-80.

[307] P.A. Kralchevsky, K. Nagayama, Capillary forces between colloidal particles, Langmuir. 10 (1994) 23-36.

[308] E.R. Camargo, E. Longo, E.R. Leite, V.R. Mastelaro, Phase evolution of lead titanate from its amorphous precursor synthesized by the OPM wet-chemical route, Journal of Solid State Chemistry. 177 (2004) 1994-2001.

[309] H. Zhang, S. Jiang, G. Duan, J. Li, K. Liu, C. Zhou, H. Hou, Heat-resistant polybenzoxazole nanofibers made by electrospinning, European Polymer Journal. 50 (2014) 61-68.

[310] W.H. Mueller, D.N. Khanna, Heat resistant polybenzoxazole from bis-((aminohydroxyphenyl) hexafluoroisopropyl) diphenyl ether. (1990).

[311] E. Powers, G. Serad, History and development of polybenzimidazoles, in: Anonymous High Performance Polymers: Their Origin and Development, Springer, 1986, pp. 355-373.

[312] E.W. Neuse, Aromatic polybenzimidazoles. Syntheses, properties, and applications, in: Anonymous Synthesis and Degradation Rheology and Extrusion, Springer, 1982, pp. 1-42.

[313] J. Critchley, A review of the poly (azoles), Progress in Polymer Science. 2 (1970) 47-161.

[314] V. Ratta, Crystallization, morphology, thermal stability and adhesive properties of novel high performance semicrystalline polyimides. (1999).

[315] S. Ukishima, M. Iijima, M. Sato, Y. Takahashi, E. Fukada, Heat resistant polyimide films with low dielectric constant by vapor deposition polymerization, Thin Solid Films. 308 (1997) 475-479.

[316] B.J. Simonds, H.J. Meadows, S. Misra, C. Ferekides, P.J. Dale, M.A. Scarpulla, Laser processing for thin film chalcogenide photovoltaics: a review and prospectus, Journal of Photonics for Energy. 5 (2015) 050999.

[317] H. Stenzenberger, Addition polyimides, in: Anonymous High Performance Polymers, Springer, 1994, pp. 165-220.

[318] C. Sroog, Polyimides, Journal of Polymer Science: Macromolecular Reviews. 11 (1976) 161-208.

[319] M. Woodard, M. Rogers, D. Brandom, G. Wilkes, J. McGrath, Synthetic investigations of high Tg fluorinated polyimides, Polymer Preprints(USA). 33 (1992) 333-334.

[320] D.K. Brandom, G.L. Wilkes, Study of the multiple melting behaviour of the aromatic polyimide LaRC CPI-2, Polymer. 35 (1994) 5672-5677.

[321] V.L. Bell, B.L. Stump, H. Gager, Polyimide structure–property relationships. II. Polymers from isomeric diamines, Journal of Polymer Science: Polymer Chemistry Edition. 14 (1976) 2275-2291.

[322] M. Brink, D. Brandom, G. Wilkes, J. McGrath, Synthesis and characterization of a novel '3F'-based fluorinated monomer for fluorine-containing polyimides, Polymer. 35 (1994) 5018-5023.

[323] R. Dine-Hart, W. Wright, A study of some properties of aromatic imides, Die Makromolekulare Chemie: Macromolecular Chemistry and Physics. 143 (1971) 189-206.

[324] T. Matsuo, Carbonyl absorption bands in the infrared spectra of some cyclic imides with a five-membered ring, Bull. Chem. Soc. Jpn. 37 (1964) 1844-1848.

[325] Y. Yang, D. Yin, R. Xiong, J. Shi, F. Tian, X. Wang, Q. Lei, FTIR and dielectric studies of electrical aging in polyimide under AC voltage, IEEE Trans. Dielectr. Electr. Insul. 19 (2012) 574-581.

[326] J. Lin, Z. Peng, Y. Liu, F. Ruiz-Zepeda, R. Ye, E.L. Samuel, M.J. Yacaman, B.I. Yakobson, J.M. Tour, Laser-induced porous graphene films from commercial polymers, Nature communications. 5 (2014) 5714.

[327] M. Smith, D. Luong, T. Bougher, K. Kalaitzidou, J. Tour, B. Cola, Thermal conductivity enhancement of laser induced graphene foam upon P3HT infiltration, Appl. Phys. Lett. 109 (2016) 253107.

[328] S. Zhang, S. Lee, D. Kim, H. Lee, T.R. Shrout, Temperature dependence of the dielectric, piezoelectric, and elastic constants for Pb (Mg 1⁄3 Nb 2⁄3) O 3–Pb Zr O 3–Pb Ti O 3 piezocrystals, J. Appl. Phys. 102 (2007) 114103.

[329] T. Kamiya, R. Mishima, T. Tsurumi, M. Daimon, T. Nishimura, Mechanism of temperature dependence of piezoelectric properties for Pb (Zr, Ti) O3, Japanese journal of applied physics. 32 (1993) 4223.

[330] R. Georges Sabat, B.K. Mukherjee, W. Ren, G. Yang, Temperature dependence of the complete material coefficients matrix of soft and hard doped piezoelectric lead zirconate titanate ceramics, J. Appl. Phys. 101 (2007) 064111.

[331] L. Tang, W. Cao, Erratum:“Temperature dependence of self-consistent full matrix material constants of lead zirconate titanate ceramics”[Appl. Phys. Lett. 106, 052902 (2015)], Appl. Phys. Lett. 106 (2015) 199901.

[332] L. Tang, W. Cao, Temperature dependence of self-consistent full matrix material constants of lead zirconate titanate ceramics, Appl. Phys. Lett. 106 (2015) 052902.

[333] V.A. Chaudhari, G.K. Bichile, Synthesis, structural, and electrical properties of pure PbTiO3 ferroelectric ceramics, Smart Materials Research. 2013 (2013).

[334] M. Islam, G.J. Tudryn, C.R. Picu, Microstructure modeling of random composites with cylindrical inclusions having high volume fraction and broad aspect ratio distribution, Computational Materials Science. 125 (2016) 309-318.